elettra

ELETTRA HIGHLIGHTS > 07-08

2007-08

elettra

elettra

Publication of Elettra's Highlights occurs this year while our efforts to relaunch the Elettra Laboratory activities by upgrading the Elettra light source and constructing the new FERMI@Elettra fourth generation light source are nearing their peak. Several of the Elettra machine upgrade projects have been successfully completed in 2007, including construction of the Booster full-energy injector, upgrade of the RF plant, and installation of a Global Orbit Feedback. Full-energy injection has already been achieved at the time of this writing and top-up operation is scheduled for mid-2009.

We have mapped a strategy - in collaboration with our key partners and users - to take maximum advantage of the upgraded Elettra storage ring with top-up operating mode. Important steps included the successful workshop "New Frontiers in Insertion Devices" (November 20-21, 2006) and "The Future of Elettra" series (May 21 and December 2-3, 2007). The scope of the workshops was to review insertion devices at the most advanced synchrotron radiation facilities worldwide, the prospects for top-up operation at Elettra, as well as the different undulator/wiggler beamlines at Elettra and the related upgrade plans.

Several high performance beamlines were inaugurated at Elettra and/or opened to users, including the infrared microscopy and spectroscopy beamline SISSI in partnership with the University of Rome "La Sapienza" and INFM-CNR, the high-resolution photoemission beamline Bad-ELPH in partnership with the University of Augsburg, the powder diffraction beamline MCX in partnership with the University of Trento and the INSTM Consortium, and the scanning and imaging microscopy beamline TWINMIC. In addition, award of contracts by external public institutions made available significant resources for new development projects, such as the construction of a second structural biology beamline (and related support laboratories) and the upgrade of the SuperESCA and ESCAmicroscopy beamlines.

As far as the new free-electron laser (FEL) source, FERMI@Elettra, is concerned, the conceptual design phase was concluded successfully with the publication in February 2007 of the Conceptual Design Report (CDR), developed through scientific collaborations with the Lawrence Berkeley National Laboratory, the Massachusetts Institute of Technology, INFN and INFM, among others. The FERMI@Elettra project was included in the European Infrastructure Roadmap developed by ESFRI (the European Strategy Forum on Research Infrastructures), within the network of all FEL projects in Europe, and we received funding from the EU for the establishment of an European consortium of complementary FEL facilities (IRUVX).

The FERMI@Elettra construction phase started off with the restructuring of the management team and the hiring in February 2007 of managers experienced in the construction of FEL light sources. An international engineering group was retained to design all of the infrastructure of FERMI and manage the entire construction process. Since the Summer of 2007, several feasibility studies and preliminary civil engineering construction projects have been carried out. The photoinjector electron source has been completed with the installation of the beam transport and diagnostics. Furthermore, the main components of the photoinjector have been acquired from UCLA to perform the first tests on the beam in collaboration with MAX-Lab in Lund (Sweden), a partner of Elettra in the framework of the IRUVX Consortium.

Particularly relevant in 2007 was the award of a grant by the European Research Council (ERC) to Sincrotrone Trieste scientists for the construction of an inelastic scattering beamline for the FERMI@Elettra

source. The selection process by the ERC has been particularly strict: less than 3% of the submitted proposals have been funded to date.

The Booster project and the current upgrade of the beamlines will bring Elettra on par with the most advanced competitors and will at the same time emphasize the experience we have gained in the international arena. The FERMI@Elettra project, the first and, at present, only seeded FEL facility under construction worldwide, will enhance our international presence and attract new and highly qualified partners. These developments have been made possible by a major loan from the European Investment Bank (EIB), which recognizes the importance of the project at a pan-European level. All this strengthens the trend towards an internationalization of Sincrotrone Trieste, and its Elettra Laboratory.

We take this opportunity to thank our employees, our Partners and external Users for their enthusiasm and dedication over the years. We trust that with their help we will be able to meet the major challenge of fully exploiting an upgraded Elettra light source while developing the new FEL source FERMI@Elettra.

Alfonso Franciosi
Chief Executive Officer
Sincrotrone Trieste S.C.p.A.

TABLE OF CONTENTS

RESEARCH HIGHLIGHTS

FACILITY HIGHLIGHTS

FACTS & FIGURES

EVENTS

RESEARCH HIGHLIGHTS

LIFE SCIENCES

It is nowadays difficult to underestimate the role played in the life science field by protein crystallography and especially by synchrotron radiation: most protein crystals diffract poorly radiation from laboratory sources and many laboratories in the world rely on synchrotron beamlines, either for Multi- and Single-wavelength Anomalous Dispersion experiments or for routine data collection. Perhaps less well-known among life scientists, but equally relevant, is the contribution of small-angle x-ray scattering (SAXS) and infrared techniques. Three Elettra beamlines are devoted to this task, XRD1, SAXS and SISSI, and a new one, XRD2, is under construction.

Two of the beamlines (XRD1 and SAXS) have undergone significant changes in 2007. In particular, the optics of the single crystal X-ray diffraction beamline has been largely rebuilt, with the addition of a collimating mirror and the replacement of the focusing mirror. XRD1 was the first beamline to become operational and the upgrade, after more than 10 years of operation, was absolutely necessary. After a short stop the beamline became again fully operational, but in the second half of 2007 the entire synchrotron was stopped for the installation of the booster. All these modifications have been quite relevant for the users, since the new mirrors and the new monochromator crystal with an effective cooling system have improved the brilliance of XRD1 by at least a factor of ten and the stability of the beam. Other necessary improvements at the experimental station, in particular a robot for the automated mounting of frozen crystals, a new goniometer with kappa-geometry, a new detector and an automatic centering system are under way. Changes at XRD1 have also affected the SAXS beamline, since the enlargement of the experimental hutch of the former has allowed for the movement of the detector further away from the sample, significantly improving the maximum achievable resolution of the latter. Furthermore, the new XRD1 hutch is also fully compliant with a white beam experimental setup.

The installation of the booster is presently allowing full-energy mode injection, reducing the bottlenecks of the previous mode of procedure.

The upgrade of the beamlines performance has also brought (or brought back) new users: the over-subscription ratios (i.e., the number of shifts requested with respect to the total available) for the first semester of 2008 for XRD1 and SAXS were 2.3 and 2.6, respectively, whilst they were 1.6 and 2.3 in the same period of 2006 (we cannot consider the second semester of 2007, since the operations for the installation of the booster reduced the user's period to only 2 months). Among the international users, let us underline the presence of several groups from India, who are becoming important partners of Elettra.

The construction of a second X-ray diffraction beamline is under way and we hope to have it operational quite soon.

Finally, the Source for Imaging and Spectroscopic Studies in the Infrared (SISSI) beamline for spectroscopy, microspectroscopy and imaging applications, operational since 2006, has seen intensification and diversification of its application in the life science research field, including biochemistry, cell biology, biomedical diagnostics, time resolved IR and protein folding.

Giuseppe Zanotti

Giuseppe Zanotti graduated in chemistry in Padua in 1974 and he is now Full Professor at the Faculty of Sciences of the same University. Since the beginning of its scientific career he has worked at the determination of the structure of molecules and macromolecules through x-ray diffraction. He has worked on proteins that bind and transport small hydrophobic molecules, in the structural determination of protein kinase CK2/inhibitor complexes and, more recently, in that of proteins from pathogenic bacteria, in particular *H. pylori*. Giuseppe Zanotti has also been interested in theoretical aspects of the phase problem in crystallography and on the analysis and conformational aspects of the structure of globular proteins. Giuseppe Zanotti is the chairman of the Protein & Macromolecular Crystallography sub-committee at Elettra.

He is author of more than 140 publications on international journals and has deposited about 90 protein structures at the Protein Data Bank (http://www.rcsb.org).

THE FIRST STRUCTURE OF A BACTERIAL S-LAYER PROTEIN

T. Pavkov[1], E. M. Egelseer[2], M. Tesarz[2], D. I. Svergun[3], U. B. Sleytr[2], W. Keller[1]

[1] Institute of Molecular Biosciences, Structural Biology, University of Graz, Graz, Austria
[2] Center for Nanobiotechnology, University of Natural Resources and Applied Life Sciences, Vienna, Austria
[3] The European Molecular Biology Laboratory, Hamburg Outstation, Hamburg, Germany

E-mail: walter.keller@uni-graz.at

Figure 1.
Domain structure of rSbsC$_{(31-844)}$.
Domains I, II and III are shown in ribbon and domains IV, V and VI in surface representation, indicating partial disorder. Flexible linkers are shown in yellow.

Crystalline bacterial cell surface layers termed S-layers represent a first order self-assembly system which has been optimized in the course of evolution. It is estimated that the majority of bacteria and archaea produce S-layers. An intact "closed" S-layer on an average-sized, rod-shaped cell consists of approximately 5×10^5 monomers. Thus, at a generation time of about 20 min (e.g. for *Geobacilli*), at least 500 copies of a single polypeptide species with a molecular mass of approximately 100,000 Da have to be synthesized each second, translocated to the cell surface and incorporated into the S-layer lattice. S-layers provide organisms with a selective advantage by fulfilling various functions including protective coats, molecular sieves in the ultrafiltration range, ion and molecule traps, and structures involved in cell surface interactions and antifouling coats. In a great variety of archaea, they are involved in determining cell shape and they contribute to virulence when present in the component of cell walls of pathogens.

In spite of their biological importance for the functionality of prokaryotic cells, high resolution structural information of S-layer proteins is very scarce. The main reason for the absence of 3-D structural information resides in the tendency of S-layer proteins to self-assemble into 2-D crystalline lattices, thereby preventing the formation of 3-D crystals. Up to date, only 2 structures of archaeal recombinant S-layer fragments from *Staphylothermus marinus* [1] and *Methanosarcina mazei* [2] were reported.

Recently we determined the structure of the bacterial S-layer protein SbsC from *Geobacillus stearothermophilus* [3]. Various soluble N- and C-terminal deletion mutants were produced [4] of which rSbsC$_{(31-844)}$ and rSbsC$_{(31-443)}$ yielded crystals suitable for structure determination [3]. Combining the X-ray structures and a solution structure of rSbsC$_{(447-1099)}$ obtained by small angle X-ray scattering we observed a very elongated and flexible molecule. The crystal structure of rSbsC$_{(31-844)}$
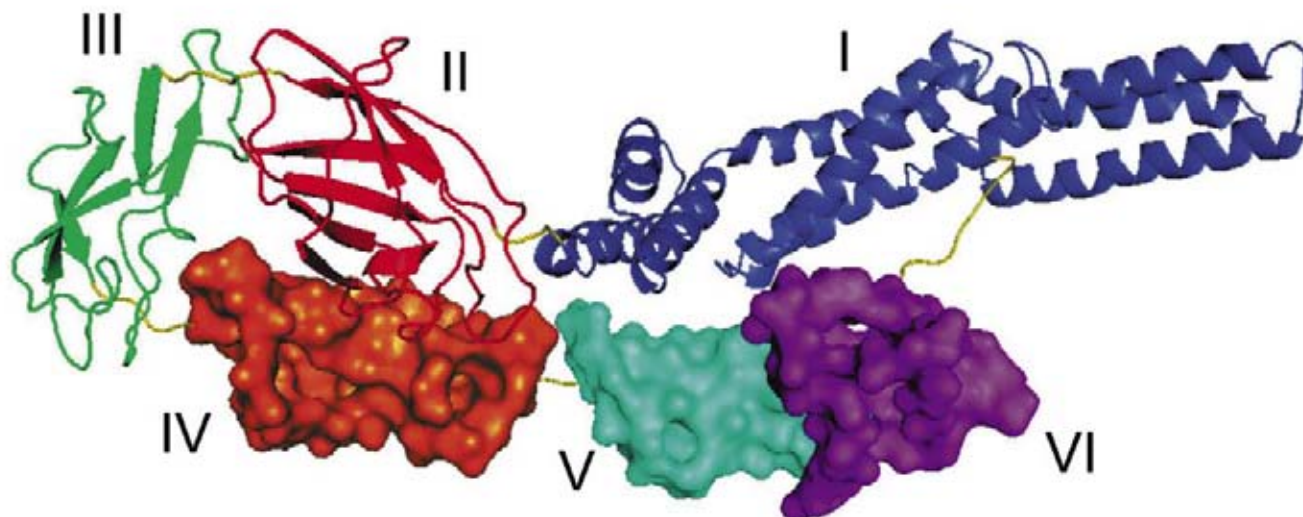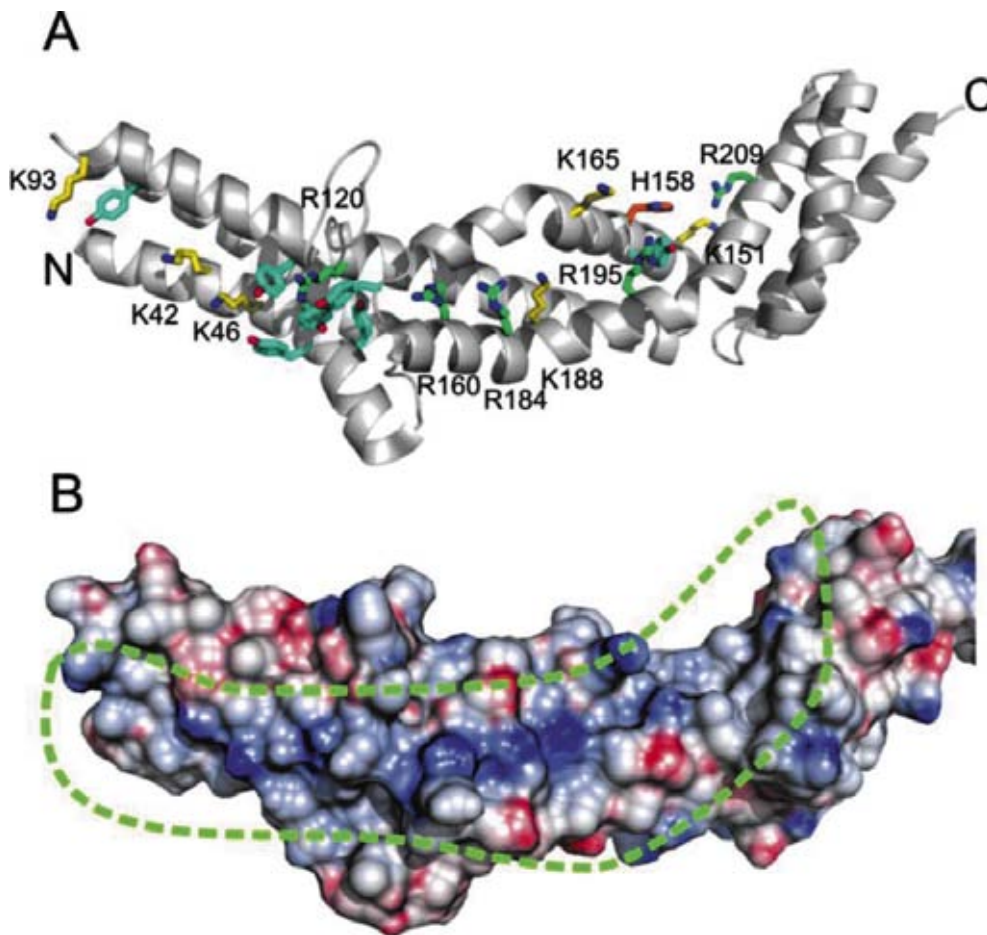
Figure 2.
Putative SCWP binding site.
(**A**) The ribbon diagram represents the structure of the SCWP binding domain including the residues of the putative ligand binding site (shown as stick model, Lys – yellow, Arg – green, Tyr – cyan, His – orange).
(**B**) The electrostatic potential mapped onto the surface of domain I shows a positively charged trace extending along the putative SCWP binding site (marked in green), which is preferentially targeting the negatively charged SCWP (adapted from Pavkov et al. [3]).

revealed a novel fold, consisting of six separate domains, which are connected by short flexible linkers (Figure 1). The N-terminal domain exhibits positively charged residues regularly spaced along the putative secondary cell wall polymer (SCWP) binding site (Figure 2). Upon SCWP binding, a considerable stabilization of the N-terminal domain occurs. These findings provide insight into the processes of S-layer attachment to the underlying cell wall and self-assembly, and also accommodate the observed mechanical strength, the polarity of the S-layer, and the pronounced requirement for internal flexibility inherent to cell growth and division. The SCWP-mediated anchoring of S-layer subunits to the rigid cell wall layer is crucial, since this step guarantees a defined orientation for incorporated S-layer proteins, while allowing enough flexibility for recrystallization of S-layer subunits to continuously assume a low free energy arrangement. In addition, the specific S-layer-SCWP interaction may play an important role in the regulated transport of the S-layer protein through the peptidoglycan layer.

The structure of the N-terminal part of SbsC provides the basis for detailed functional studies by site-directed mutagenesis for determining the exact interaction sites responsible for self-assembly, as well as specific binding of SCWP and other interacting proteins.

References

[1] J. Stetefeld, M. Jenny, T. Schulthess, R. Landwehr, J. Engel, R.A. Kammerer, *Nature Structural Biology* **7**, 772 (2000).
[2] H. Jing, J. Takagi, J.H. Liu, S. Lindgren, R.G. Zhang, A. Joachimiak, J.H. Wang, T.A. Springer, *Structure* **10**, 1453 (2002).
[3] T. Pavkov, E.M. Egelseer, M. Tesarz, D.I. Svergun, U.B. Sleytr, W. Keller, *Structure* **16**, 1226 (2008).
[4] M. Jarosch, E.M. Egelseer, C. Huber, D. Moll, D. Mattanovich, U.B. Sleytr, M. Sára, *Microbiology* **147**, 1353 (2001).

MERIOLINS, A NEW CLASS OF CELL DEATH–INDUCING KINASE INHIBITORS WITH ENHANCED SELECTIVITY FOR CYCLIN-DEPENDENT KINASES

K. Bettayeb[1], O. M. Tirado[2], S. Marionneau-Lambot[3], Y. Ferandin[1], O. Lozach[1], J. C. Morris[4], S. Mateo-Lozano[2], P. Drueckes[5,6], C. Schachtele[5], M. H. G. Kubbutat[5], F. Liger[7], B. Marquet[7], B. Joseph[7], A. Echalier[8], J. A. Endicott[8], V. Notario[2], L. Meijer[1]

[1] Centre National de la Recherche Scientifique, Cell Cycle Group & UPS2682, Station Biologique, Roscoff, Bretagne, France.

[2] Laboratory of Experimental Carcinogenesis, Lombardi Comprehensive Cancer Center, Georgetown University Medical Center, Washington, District of Columbia, USA

[3] Cancéropôle Grand Ouest, Nantes, France

[4] Department of Chemistry, School of Chemistry and Physics, University of Adelaide, Adelaide, Australia.

[5] ProQinase GmbH, Freiburg, Germany.

[6] Novartis Institutes for BioMedical Research, Expertise Platform Kinases, Basel, Switzerland.

[7] ICBMS, UMR 5246, Université Lyon 1, Laboratoire de Chimie Organique 1, Villeurbanne, France

[8] University of Oxford, Laboratory of Molecular Biophysics, Department of Biochemistry, Oxford, United Kingdom

E-mail: jane.endicott@biop.ox.ac.uk

A characteristic of many human diseases is an alteration in the pattern of protein phosphorylation. As a result, the last decade has witnessed an exponential growth in efforts to identify, optimize and evaluate small molecular weight, pharmacological inhibitors of numerous protein kinases [1]. Currently about 60 kinase inhibitors are undergoing clinical evaluation against cancers, inflammation, diabetes and neurodegenerative diseases. The success of Gleevec to treat chronic myelogenous leukemia (CML) patients attests to the potential importance of protein kinase inhibitors as drugs of the future.

Among the 518 human protein kinases, cyclin-dependent kinases (CDKs) have attracted considerable interest given their involvement in many essential physiological pathways and aberrant activities in multiple human diseases, especially cancer and neurodegenerative conditions. Sequential activation of CDK4/6 and CDK2 controls progression from G1 to S-phase of the cell cycle, and activation of CDK1 is essential for progression from G2 into M-phase [2]. All CDK inhibitors identified to date are ATP-competitive and tend to exhibit selectivity for particular members of the family as well as activity towards other protein kinases. For example, many CDK inhibitors also inhibit glycogen synthase kinase-3 and sometimes casein kinase 1.

ATP-competitive protein kinase inhibitors have been identified from a variety of sources. Though many are the result of library screening and medicinal chemistry programs several interesting compounds have also been extracted from natural products. Meridianins are a family of 3-(2-aminopyrimidine)indoles initially extracted from *Aplidium meridianum*, an Ascidian from the South Atlantic (South Georgia Islands) [2]. They were shown to have promise as a kinase inhibitory scaffold, and subsequently a number of derivatives were synthesized by various groups. However, although some meridianins inhibit various kinases such as CDKs, GSK-3, cyclic nucleotide-dependent kinases and CK1, they displayed only modest anti-proliferative effects.

Interestingly, meridianins share some structural similarity with variolins, another family of marine natural compounds containing a central pyrido[3',2':4,5]pyrrolo[1,2-c] pyrimidine core substituted with a 2-aminopyrimidine ring. Variolins were initially extracted from *Kirkpatrickia variolosa*, a rare and difficult to access Antarctic sponge, but subsequent total synthesis by Morris [4] and others provided further opportunity to examine the molecule's properties.

The chemical similarity between meridianins and variolins provided an opportunity to synthesize a hybrid structure, which was termed the meriolins. Surprisingly, selected meriolins were found to display potent inhibitory activity and relative selectivity towards CDKs, and also exhibited better anti-proliferative and pro-apoptotic properties in cell cultures than their "inspirational parent" molecules.

Figure 1. Details of the interactions of Meriolin 3 and Variolin B with the ATP binding pocket of CDK2/cyclin A. (A) Meriolin 3, (B) Variolin B. Selected CDK2 residues and the two inhibitors are drawn in ball and stick mode with CDK2 carbon, nitrogen and oxygen atoms colored yellow, blue and red respectively. Meriolin 3 and Variolin B bind in the CDK2 ATP binding site and carbon atoms are colored magenta and cyan respectively. Hydrogen bonds are drawn with dotted lines and two bound water molecules visible in the Variolin B-bound complex structure as red crosses.
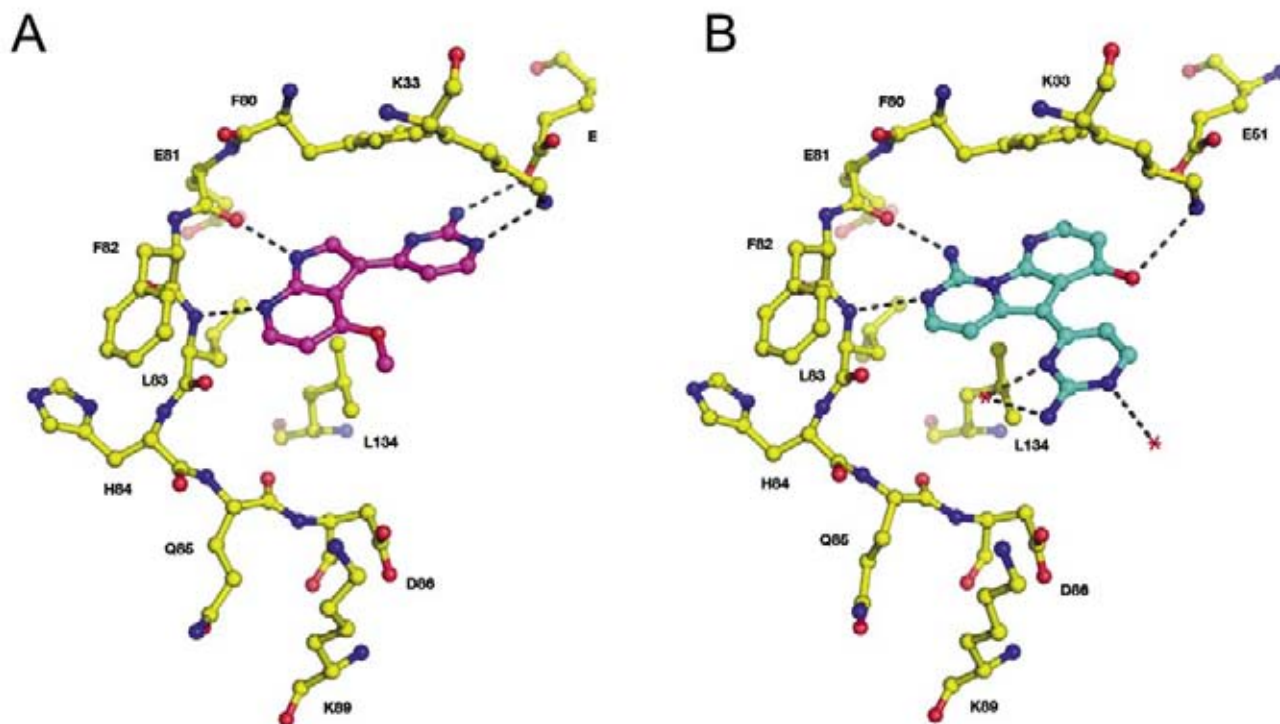
To elaborate the molecular interactions that mediate meriolin binding to the CDK active site, we determined the crystal structures of Meriolin 3 and Variolin B in complex with CDK2/cyclin A (Figure 1). These structures revealed that the two molecules bind in very different orientations in the CDK2 ATP-binding pocket. Meriolin 3 makes two hydrogen bonds to the CDK2 backbone within the hinge sequence that links the two lobes of the kinase and two further hydrogen bonds with the side chains of Lys33 and Glu51. Variolin B like Meriolin 3 makes two equivalent hydrogen bonds with the CDK2 hinge, and also interacts with the side chain of Lys33 through its hydroxyl group. In addition two ordered water molecules are discernible in the Variolin B-bound active site and it interacts with the Ile10 main chain amine. However, the presence of a third ring fused to the Variolin B indole system creates a planar structure that is too large to be accommodated at the back of the ATP binding site if Variolin B were to adopt the Meriolin 3 binding mode. As a result the indole moiety common to both inhibitors is flipped 180° between the two bound structures.

Further study of the meriolins in the neuroblastoma cell line SH-SY5Y showed that they prevent phosphorylation at CDK2-, CDK1- and CDK9-specific sites and induce rapid degradation of the survival factor Mcl-1. In addition, Meriolin 3 potently inhibits tumor growth in two mouse xenograft models: Ewing's sarcoma and LS174T colorectal carcinoma. Taken together, our results suggest that meriolins constitute a new kinase inhibitory scaffold with promising anti-tumor activity.

References

[1] M.E.M. Noble, J.A. Endicott, L.N. Johnson, *Science* **303**, 1800 (2004).
[2] M. Malumbres and M. Barbacid, *Nature Rev. Cancer* **1**, 222 (2001).
[3] M. Gompel, M. Leost, E. B. de Kier Joffe et al., *Bioorg Med. Chem. Lett*. **14**, 1703 (2004).
[4] R.J. Anderson, J.B. Hill, J.C. Morris, *J. Org. Chem*. **70**, 6204 (2005).

E-coli FRATAXIN: STRUCTURAL CHARACTERISATION OF ION BINDING SITES

M. Franzese[1], C. Pastore[3], P.A. Temussi[1,3], A. Pastore[3], F. Sica[1,2]

[1] Dipartimento di Chimica "Paolo Corradini", University of Naples, Italy
[2] Istituto di Biostrutture e Bioimmagini, CNR, Naples, Italy
[3] National Institute for Medical Research, London, United Kingdom

E-mail: filomena.sica@unina.it

The inherited human Friedreich's ataxia, a severe neuro- and cardio-degenerative disease, has been attributed to deficiency of the conserved mitochondrial protein frataxin (Fxn). Different and somewhat conflicting functions have been proposed for Fxn. Recent data suggest that the protein plays a key role in eukaryote cellular iron metabolism, particularly in the biosynthesis of mitochondrial heme and iron-sulphur cluster (FeS). Frataxin binds iron with features distinctly different from those of any other protein with this property: Fxn structural model does not contain cavities which could host iron or a suitable prosthetic group and, moreover, the frataxin sequences do not present conserved histidines and/or cysteines, which are the residues usually implicated in chelating iron. In agreement with these structural features, the Fxn affinity for iron has been shown to be very weak, being at the very best in the micromolar range [1]. NMR on the bacterial [1] and yeast ortholog of human frataxin has indicated that the iron ions bind at a semi-conserved negatively charged ridge which contains several Asp and Glu side chains. To gain a better insight on the iron binding, we have performed a crystallographic study on the protein from E-coli (CyaY) [2], whose structure has been previously determined by X-Ray diffraction and NMR. The molecule is folded in a α-β-sandwich motif with a negatively charged $\alpha 1$- $\beta 1$ region, where conserved acidic residues are clustered (Figure 1).

The study has been approached performing co-crystallization trials in different conditions of iron/ protein ratio, pH and precipitant agent, as well as soaking experiments. All trials with Fe(II) were performed under anaerobic conditions in a glove box. In all cases, the crystals were isomorphous with the native ones and they were tested by collecting a full set of diffraction data. The presence of metal ions was checked by calculating anomalous difference maps and observed difference Fourier maps. None of these maps indicated the presence of iron in the crystals.

Figure 1.
Ribbon model of CyaY structure. The anionic surface patch cluster of twelve acidic (-) residues localized in the α1-β1 region is shown.
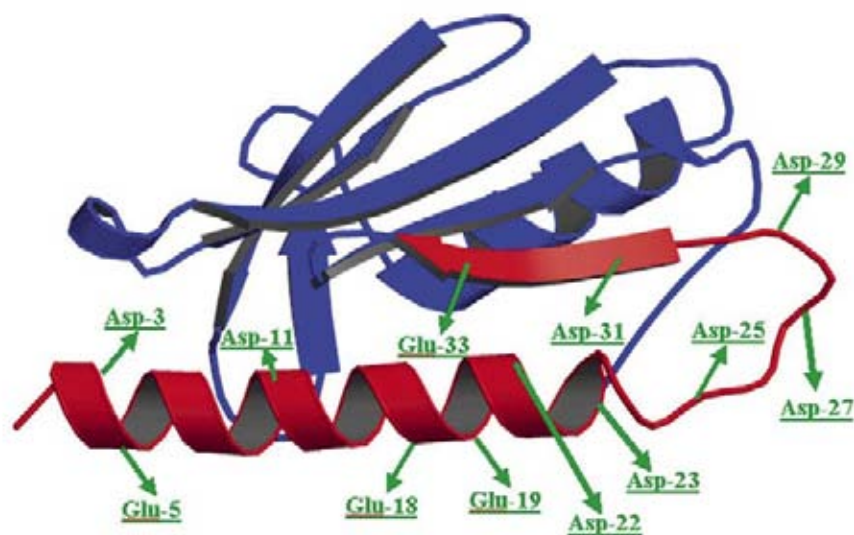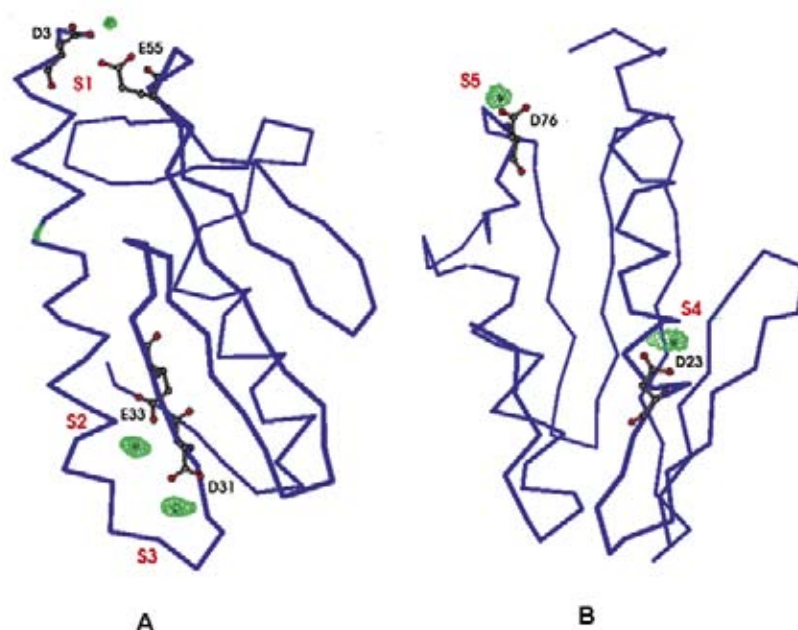
The binding of other positive ions were also studied using the same approach. In particular, Eu(III) was chosen as variant to Fe(III), whereas Ca(II) and Co(II) were used to mimic Fe(II) This choice was suggested by NMR results that indicate that these ions behave very similar to Fe(III) and Fe(II), respectively [1]. Crystal derivatives with Co(II) (CyaY-Co) and Eu(III) (CyaY-Eu) were obtained and their structures refined at 1.75 and 1.42 Å resolution, respectively. In both cases, the protein moiety is very similar to the wild type structure as evidenced by the very small root mean square deviations for the main chain atoms.

Both the anomalous difference maps and the observed difference Fourier maps calculated for the Eu(III) complex contain five strong peaks (Figure 2). The europium ion in the S1 site is coordinated with an approximate octahedral geometry to the protein residues D3 and E55 and to four water molecules. In the S2 site, the ion is bound to E33 and to four solvent molecules in a distorted octahedral geometry, with the sixth ligand not well defined. A strong peak on the density map (S3) was also assigned to an Eu(III) ion and is located at only 6.1 Å from S1; in this case two water molecules form a bridge between the two ions. The protein residues involved in the binding to this third metal ion are D29 and D31, which adopt a different conformation with respect to the apo-form. Four water molecules complete the coordination sphere. Finally, the remaining two sites involve residues whose side chains are partially disorde-

red in the apo structure. In particular, Eu(III) in S4 is coordinated to the two carboxylate oxygens of D23 and to E19 and to two water molecules. The binding in S5 has an octahedral geometry and is stabilized by the side chains of D76 and D27 of a symmetry related molecule and by four water molecules.

For CyaY-Co, only the sites S1 and S2, which display a coordination similar to that observed for the CyaY-Eu structure, are occupied.

These results show that all the binding sites of CyaY with the metals are on the external protein surface (Figure 2) and involve few protein residues and several water molecules. The interaction of CyaY with the metals does not induce main chain conformational variations and only three side chains change orientations to accommodate the ligands. Surprisingly, the iron derivatives of the protein could not be obtained. This might have been caused by the crystallization conditions that could interfere with the iron binding; alternatively, it may suggest that the capacity to bind the iron is associated to an aggregated form of the protein, present at low concentration in solution.

References

[1] M. Nair, S. Adinolfi, C. Pastore, G. Kelly, P.A. Temussi, A. Pastore, *Structure*, **12**, 2037 (2004).
[2] C. Pastore, M. Franzese, F. Sica, P.A. Temussi, A. Pastore, *FEBS Journal*, 274, 4199 (2007).

X-RAY STRUCTURE ANALYSIS OF tRNA^{Gly} ACCEPTOR STEM MICROHELICES: COMPARISON OF STRUCTURE AND HYDRATION

C. Förster[1], A. Zerressen-Harte[1], J.P. Fürste[1], M. Perbandt[2], Ch. Betzel[2], V.A. Erdmann[1]

[1] Institute of Chemistry and Biochemistry, Free University Berlin, Berlin, Germany
[2] Institute of Biochemistry and Molecularbiology, University of Hamburg, c/o DESY, Hamburg, Germany

E-mail: erdmann@chemie.fu-berlin.de

Figure 1.
Tertiary tRNA structure, derived from [4], with the acceptor stem region pointed out showing the E.coli and the human tRNA^{Gly} sequences.

tRNA identity elements assure the correct aminoacylation of tRNAs by the aminoacyl-tRNA synthetases with the cognate amino acid. The tRNA^{Gly} / glycyl-tRNA synthetase is a member of the so-called 'class II system' in which the tRNA determinants consist of rather simple elements [1]. The glycine system is a special case within 'class II': there exists a large divergence between eukaryotes/archaebacteria and eubacteria. Not only the glycyl-tRNA synthetases differ to great extent in protein structure and sequence motifs, also the tRNA identity elements differ [2]. These are located in the aminoacyl stem of tRNA^{Gly}, with additionally the discriminator base, that strictly has to be adenosine in the eukaryotic/archaebacterial but uracil in the eubacterial case [2,3]. Due to these differences a unique evolutionary divergence is discussed in the literature for this system.

Recently, we solved the crystal structures of the Escherichia coli and the human tRNA^{Gly} aminoacyl stem microhelices (PDB-IDs: 2VAL, 2V7R). Here we present a comparative crystal structure analysis of the tRNA^{Gly} acceptor stem microhelices and of their surrounding hydration patterns.

The E.coli and human tRNA^{Gly} acceptor stem microhelices show sequence homology within the first three base pairs (Fig.1), which contain the C2-G71 identity element [2,3]. Both tRNA^{Gly} helices crystallize at different conditions and the crystals show different morphology, space groups, crystal packing and resolution of X-ray diffraction data. The E.coli tRNA^{Gly} acceptor stem crystallizes in the space group P3$_2$21 with the unit cell parameters a=b=35.35 Å, c=130.82 Å, γ=120.00° and diffracts to 2.0 Å resolution. The asymmetric unit contains two RNA duplexes, 55 defined water molecules and one magnesium atom. The two E.coli tRNA^{Gly} microhelices show minimal differences in their local and overall geometric parameters. The hydrated magnesium ion is bound to helix A in vicinity of the second and third base pair (data not shown). Helix B contains no magnesium. Slight deviations in the helical parameters might represent a magnesium-bound and a magnesium-free state of the tRNA^{Gly} microhelix. The human tRNA^{Gly} aminoacyl stem crystallizes in the monoclinic space group C2 with the cell constants: a=37.12 Å, b=37.49 Å, c=30.38 Å, β=113.02°. The crystals diffract to 1.2 Å resolution and contain one molecule in the asymmetric unit. A total of 85 water molecules could be assigned per RNA and no further ligand or metal ion could be detected.
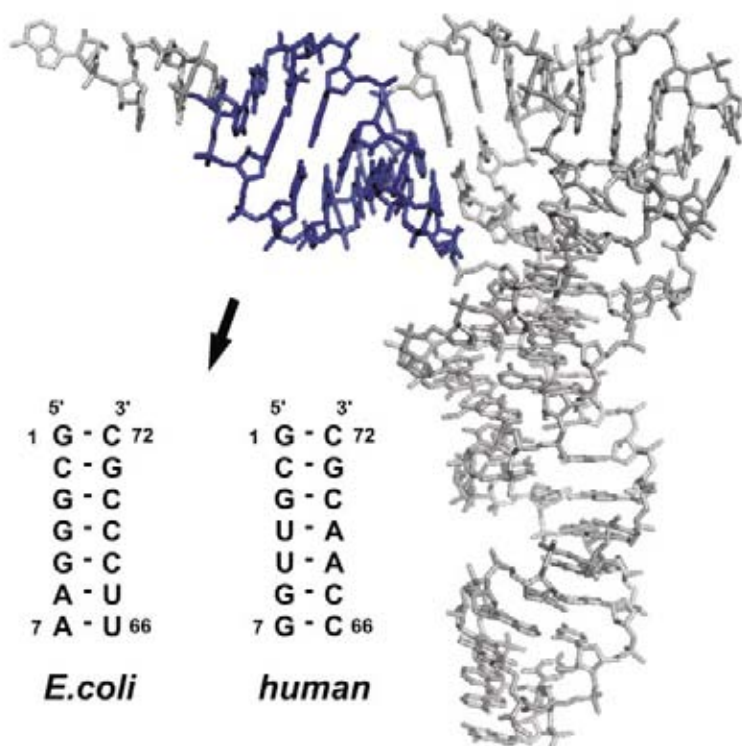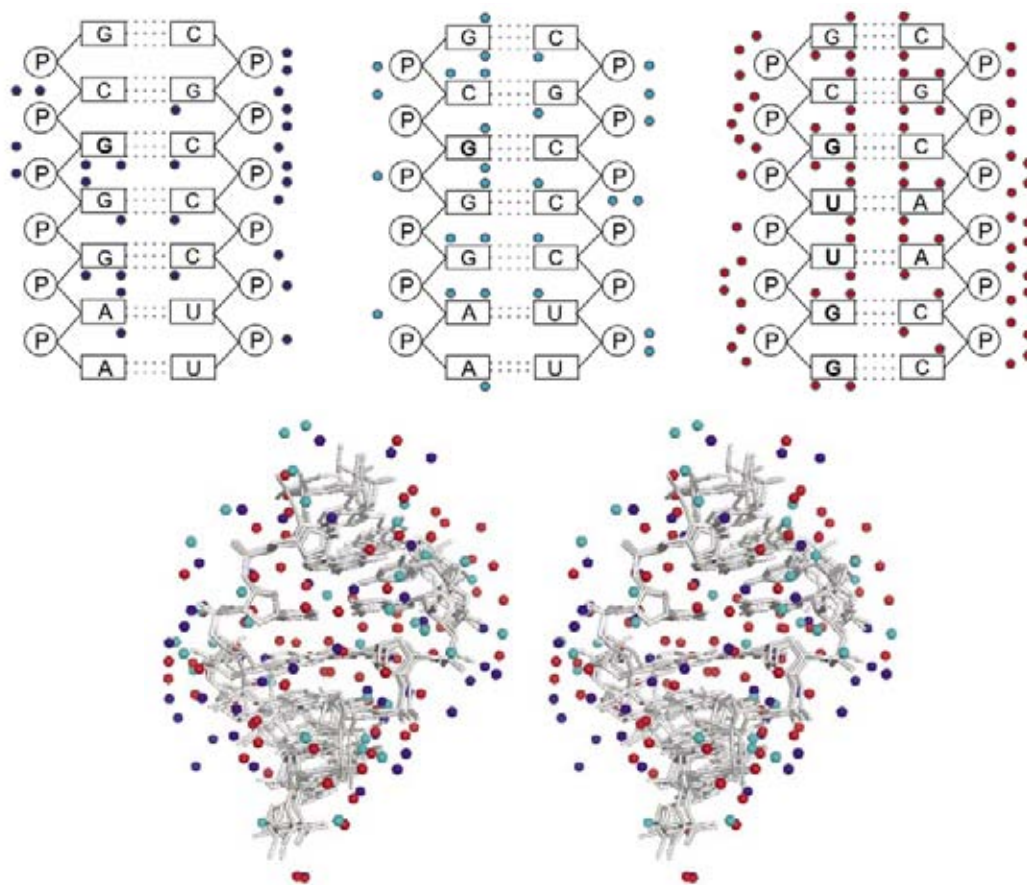
Figure 2.
(a) Schematically drawn hydration patterns of the E.coli tRNA^{Gly} microhelix A, the magnesium-bound RNA (water shown as blue dots) and B, the magnesium-free RNA (cyan dots) and of the human tRNA^{Gly} microhelix, which is magnesium-free (red dots).
(b) Superposition (stereo presentation) of the different hydration layers surrounding the two E. coli and the human tRNA^{Gly} microhelices: The water molecules are shown as dots with the colours corresponding to the ones described above.

All tRNA^{Gly} acceptor stems form the standard A-type RNA, respectively. The values for the local helical parameters of the three RNAs like twist, slide, tilt, rise and χ-displacement lie in the expected values known for the canonical A-type RNA. The sugar puckering of the three RNAs is distributed in the 2'-exo conformation for all nucleotides. The backbone phosphate-phosphate distances also demonstrate the canonical A-form RNA structure. The phosphate backbone α/γ torsion angles all adopt the (-)gauche/(+)gauche conformation whereas the β torsion angles show the anti conformation around +/-180 degrees.

A comparative analysis of the hydration patterns surrounding the RNAs is demonstrated in figure 2, which schematically shows the assignment of the water molecules to the nucleobases and phosphates of the RNAs. We observed different pictures for all three hydration patterns. This observation is highlighted by an overlay of the three RNA helices in figure 2b, showing the tRNA^{Gly} microhelices with similar helical geometry which are accompanied by a large variability in their hydration patterns.

Further experiments will have to clarify a possible specificity of hydration in RNAs. Repetitive crystallization and structure analysis with identification and comparison of water molecules will help to further investigate this question. Regarding RNA–protein interactions, the hydration layer might be the first contact site and play an important role for recognition, like for example in combination with tRNA identity elements.

References

[1] G. Eriani, M. Delarue, O. Poch, J. Gangloff and D. Moras, Nature **34**, 203 (1990).
[2] K. Shiba, Glycyl-tRNA Synthetases. "The Aminoacyl-tRNA Synthetases", Landess Bioscience, Georgetown, Texas, U.S.A. Chapter **13**, 125 (2005).
[3] W.H. McClain, K. Foss, R.A. Jenkins and J. Schneider, Proc. Natl. Acad. Sci. U.S.A. **88**, 6147 (1991).
[4] H. Shi and P.B. Moore, RNA **6**, 1091 (2000).

HIGH RESOLUTION STRUCTURE OF A PLANT CELL WALL DEGRADING ENZYME VARIANT AND SHORT STRONG HYDROGEN BONDS IN PROTEINS

A. Langkilde[1§], L. Lo Leggio[1], A. Mølgaard[1], S. Larsen[1,2]

[1]*Department of Chemistry, University of Copenhagen, Copenhagen, Denmark*
[2]*European Synchrotron Radiation Facility (ESRF), Grenoble, France*
[§]*Present address: Department of Medicinal Chemistry, University of Copenhagen, Copenhagen, Denmark*

E-mail: ael@farma.ku.dk

Hydrogen bonds play a pivotal role for the structure and function of proteins in shaping secondary structure, protein-ligand interactions and catalytic activity. The very short O-H…O hydrogen bonds formed between carboxylic acid and carboxylate groups are among the strongest. Many textbooks present aspartate and glutamate as the charged species, in accordance with the pK_a values of the free acids (3.9 and 4.2, respectively). The local chemical environment in a protein can however change the microscopic pKa value of a carboxylic acid group significantly, keeping the carboxylic acid residues protonated at higher pH. It is noteworthy that Asp and Glu are not generally considered as possible hydrogen bond donors in programs employed in the analysis of protein structures, therefore hydrogen bonds between carboxylic acid and carboxylate groups may be overlooked.

The formation of short, strong hydrogen bonds with partially covalent character causes deshielding of the involved proton giving rise to ^{1}H NMR chemical shifts above 18 ppm. Such low field proton signals and their relation to Low Barrier Hydrogen Bonds (LBHB) considered to be important for catalysis have been extensively studied and debated. Serine proteases with a catalytic Asp-His-Ser triad containing a short Asp-His hydrogen bond were among the best investigated systems in relation to LBHBs [1]. A virtually identical catalytic Asp-His-Ser triad was also found in rhamnogalacturonan acetylesterase (RGAE), and the esterase catalysis is assumed to follow a similar mechanism [2].

An extreme low field signal (at approximately 18 ppm) in the ^{1}H NMR spectrum of rhamnogalacturonan acetylesterase (RGAE) showed the presence of a short strong hydrogen bond in the protein. This signal was also present in the mutant RGAE D192N. This was unexpected as this variant could not form the short His-Asp hydrogen bond which in serine proteases gives rise to the signal around 18 ppm.

To elucidate this aspect the structure of RGAE D192N variant has been determined by X-ray crystallography using data collected to 1.33 Å resolution at Elettra. The high resolution data (99.5 % complete, average redundancy of 9, and R_{merge}=3.2 %) enabled structure refinement in SHELXL including modeling of disordered side chains and inclusion of anisotropic displacement parameters on non H atom (R=11.57 %, R_{free}=15.34 %).

The high resolution structure permitted a thorough analysis of the short hydrogen bonds, as the estimated standard deviation on the donor-acceptor distances of these hydrogen bonds were in the 0.01-0.03 Å range. A careful analysis and comparison of the structure of RGAE D192N and the wild-type structure known to a resolution of 1.12 Å [3], was conducted with the purpose of identifying possible candidates for the short hydrogen bond with the 18 ppm deshielded proton. An examination of the short hydrogen bonds in the RGAE, the calculated pK_a values, and solvent accessibilities identified a buried carboxylic acid carboxylate hydrogen bond between Asp75-Asp87 as the likely origin of the 18 ppm signal, supported by theoretical calculations of the chemical shift values [4].

Despite the precedents in the literature our results show that the low-field signals observed in some ^{1}H NMR experiments on proteins can not be assigned to active site hydrogen bonds without additional evidence. In the present case, the 18 ppm ^{1}H NMR signal in RGAE

(Research Highlights) LIFE SCIENCES

Figure 1. The overall structure of RGAE D192N is shown excluding Thr79 and Ser80 which could not be located in the density maps. Terminal residues, Thr1 and Leu233, are labeled. The three residues that correspond to the catalytic triad (Ser9-His195-Asn192) are colored green. The N-acetyl-D-glucosamine and acetate ion are illustrated by spheres and the shortest hydrogen bonds are shown as dashed lines.
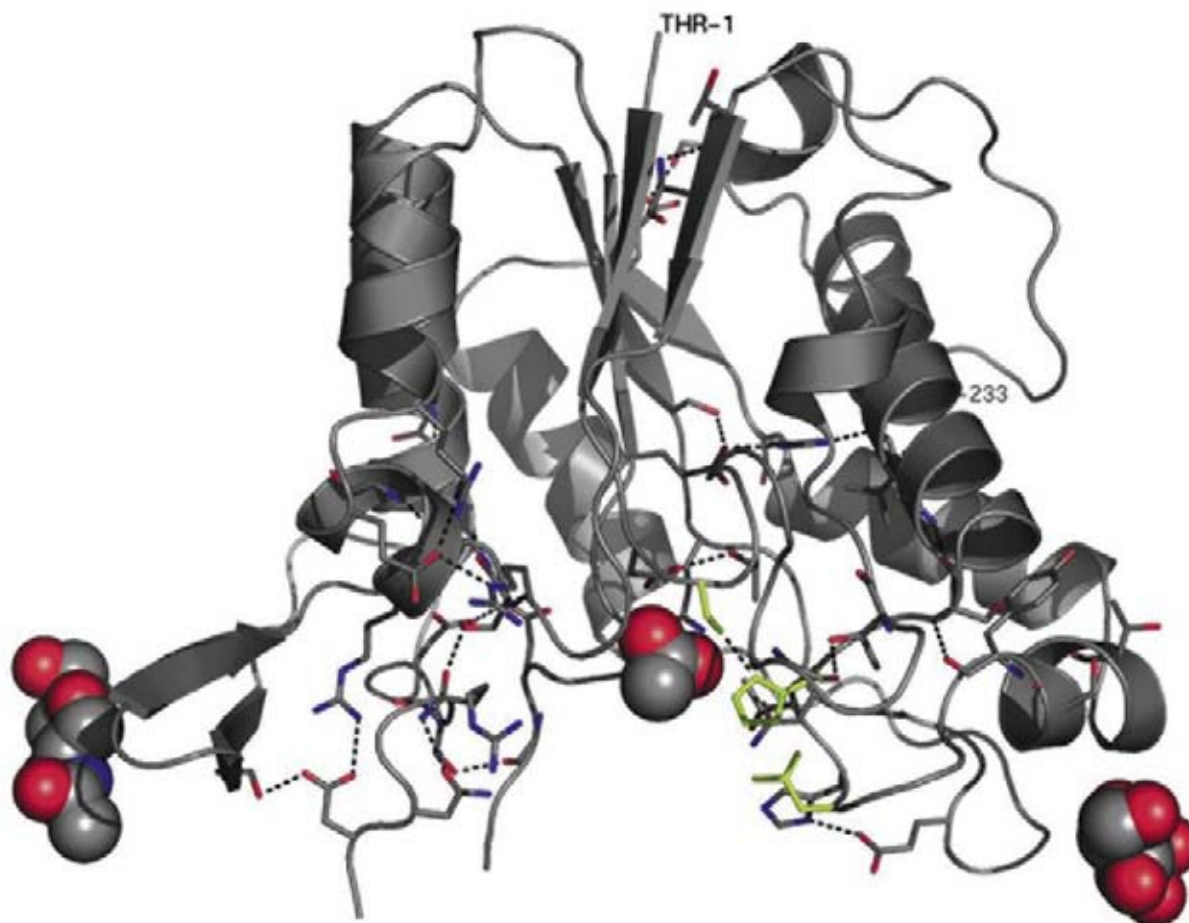
cannot be assigned to the hydrogen bond between the residues in the catalytic triad.

Our analysis of RGAE structures revealed furthermore that all the short hydrogen bonds in this enzyme are located close to the active site indicating a role in the enzymatic function. Interactions between carboxylic acid side-chains are not rare. A search in a PDB subset revealed short contacts between carboxylic acid side-chains in 16 % of the protein chains. Many of the shortest contacts involve residues that are putative catalytic residues or residues close to the active site, which emphasize the importance of including Asp and Glu as possible hydrogen bond donors in protein structure analysis.

References

[1] W. W. Cleland, P. A. Frey, J. A. Gerlt, *J. Biol. Chem.* **273**, 25529 (1998).

[2] A. Mølgaard, S. Kauppinen, S. Larsen, *Structure* **8**, 373 (2000).

[3] A. Mølgaard, S. Larsen, *Acta Cryst.* D **58**, 111 (2002).

[4] A. Langkilde, S. M. Kristensen, L. Lo Leggio, A. Mølgaard, J. H. Jensen, A. R. Houk, J.-C. N. Poulsen, S. Kauppinen, S. Larsen, *Acta Cryst.* D **64**, 851(2008).

STRUCTURE AND MEMBRANE INTERACTION MODES OF THE DEFENCE PEPTIDE LL-37 AND ITS ANALOGUES

F. Morgera[1,2], L. Vaccari[1], S. Pacor[2], N. Antcheva[2], D. Scaini[1], L. Casalis[1], A. Tossi[2]

[1] Sincrotrone Trieste S.C.p.A., Trieste, Italy
[2] Department of Life Sciences, University of Trieste, Italy

E-mail: francesca.morgera@elettra.trieste.it

Co-evolution of humans and pathogens has led to multiple defence mechanisms. They are commonly defined as innate and adaptive immunity, respectively the non specific first line of defence and the inducible specific one. The human peptide LL37 is a small natural protein belonging to the "Host Defence Peptides" group (HDPs) and has multiple roles in immunity, acting either as direct antimicrobial molecule or as an immunomodulating agent [1]. Increasing antibiotic resistance and the urgent need for alternative approaches to infection management has lead to the systematic study of the mode of action of HDPs so as to identify the main structure-activity requirements for developing new potential therapeutic agents. Within this framework, we have analysed the effects of structural variations on membrane interactions for LL-37 and its chimpanzee orthologue (*mmu*RL37), using

several complementary biophysical and biochemical methods. Transmission and ATR-FTIR spectroscopy in solution and on model membranes respectively provided information on both peptide and membrane structure variations upon interaction. In particular, we focused on the backbone amide vibrations (amide I & II; 1500-1700 cm^{-1}), widely used to study the conformations of proteins. Moreover, AFM was performed at Nanostructure Laboratory @ Elettra on the same supported membranes as used for IR measurements, giving insights on the morphology and phase status. The study of the biological activity on bacterial cells (not shown) allowed a complete overview of peptide mode of action, highlighting the structural requirements necessary for a selective activity against pathogens. FTIR transmission spectroscopy in D$_2$O provided information on the confor-
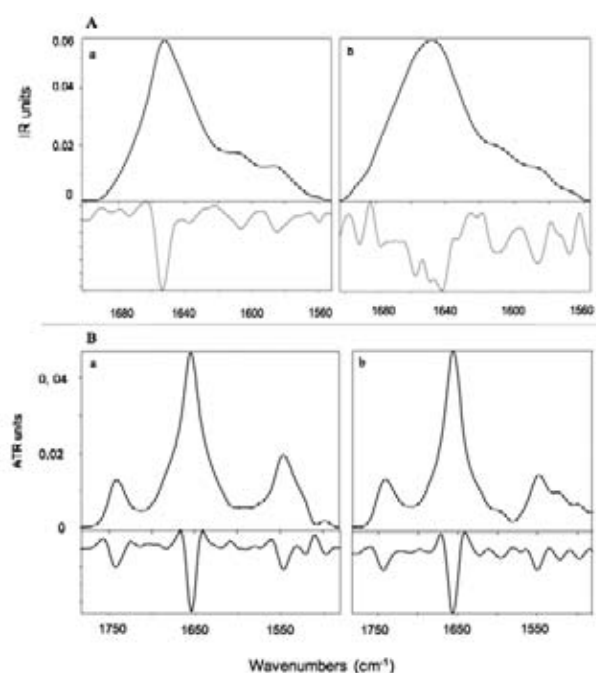
Figure 1.
Transmission (A) and ATR- FTIR (B) amide I & II spectra of LL37 (a) and *mmu*RL37 (b). The bottom panels show the respective spectra 2nd derivatives.
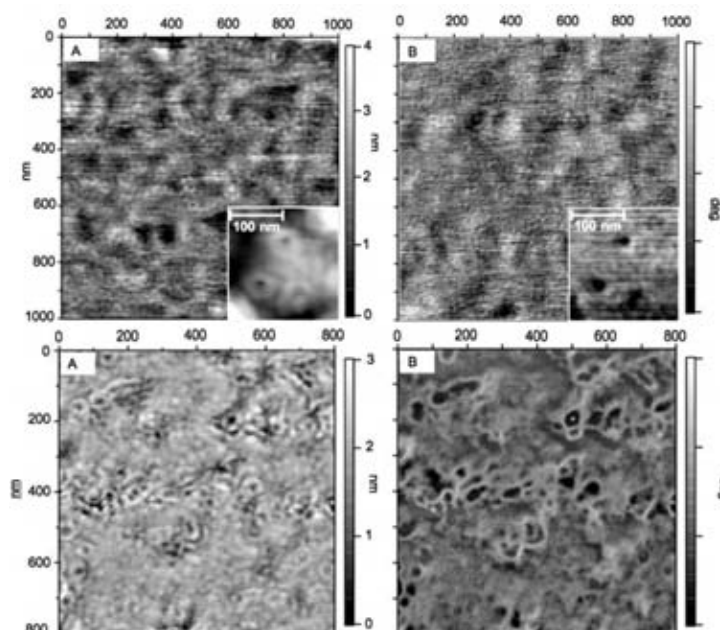
Figure 2.
AFM topographic (A) and phase (B) images of lipid bilayer upon interaction with LL-37 (top), and *mmu*RL37 (bottom). Insets are respectively the topography and phase images at a higher resolution of the lipid bilayer upon LL-37 interaction.

mational states of the HDPs in solution at higher concentrations, which may reflect those reached at the bacterial membrane surface (Figure 1A). Spectra of LL-37 carried out after complete H/D exchange, indicate a stable helical structure, whereas *mmu*RL37 shows a broader, more composite amide I band, indicative of a more random structure even under these high concentration conditions. ATR-FTIR experiments in the presence of a Germanium supported egg phosphatidyl glycerol (PG) bilayer gave insights on how the peptides bind to this anionic membrane, a simple model for bacterial membranes (Figure 1B). In particular, it shows LL-37 in contact with the bilayer after dehydration, revealing a sharp band centred at 1652 cm^{-1}, typically assigned to a α-helical structure. In this case, the ATR amide I and II bands for RL-37 confirm that in the presence of anionic lipids, it gives rise to a strong α-helical signal. The frequency of this band is red-shifted (to 1656 cm^{-1}) with respect to LL-37, possibly indicating a deeper insertion of the helical segment into the hydrophobic environment of the membrane. This is consistent with the greater effect exerted by RL-37 on the lipid acyl bands (not shown), with a more marked shift in the CH$_2$ stretching frequencies (from 2920 to 2924 cm^{-1} and from 2850 to 2854 cm^{-1} for the antisymmetric and symmetric modes) [2]. AFM images of dehydrated PG bilayers upon LL-37 or *mmu*RL-37 interaction are shown in Figure 2., indicating the latter peptide causes a generalized perturbation in the bilayer,

resulting in lesions of varying sizes and with a more amorphous appearance. LL-37 instead generates a defined pattern of perturbations consistent with the formation of many holes of roughly the same size that are visible only at higher resolution. The topography of these holes suggests they may be toroidal in nature, being characterized by a positive curvature of the membrane resulting from accumulation of AMPs at the bilayer surface. Our conclusions are further corroborated by AFM-phase imaging, which provides information on physical variations beyond morphology. These show that the lipid bilayer preserves its phase homogeneity upon LL-37 interaction, while it becomes inhomogeneous upon *mmu*RL37 interaction. This could be explained assuming an important perturbation of the lipid order induced by *mmu*RL-37, which is not appreciable for the human peptide. In conclusion, the comparison of these structural data with the biological ones has suggested a different mode of action for the two orthologs. In fact, it would appear that the evolution of the primate peptide has led to sequence variations, resulting in different modes of membrane interaction and membrane lesions.

References

[1] R.E. Hancock et al., *Nat. Biotechnol.* **24**, 1551 (2006).
[2] L. Tamm et al., *Quarterly Reviews of Biophysics* **30**, 365. UK, Cambridge University Press (1997).

TRACKING IMPLANTED MAMMALIAN CELLS *IN-VIVO* USING SYNCHROTRON X-RAY IMAGING

C. J. Hall[1], E. Schültke[2], R. Menk[3], F. Arfelli[4], B. Juurlink[2]

[1] *Monash University, Monash Centre for Sychrotron Science, Melbourne, Australia*

[2] *The University of Saskatchewan, Dept. of Anatomy and Cell Biology, Saskatoon, Canada*

[3] *Sincrotrone Trieste S.C.p.A., Trieste, Italy*

[4] *Physics Department, University of Trieste, Italy*

E-mail: Chris.Hall@sync.monash.edu.au

X-ray imaging (radiography) is currently the most common method of producing medical images. The mature technology behind both the production and detection of x-ray photons has enabled relatively inexpensive, but high quality x-ray imaging systems to be made available to health services worldwide. One advantage that x-rays have over other photons used for imaging is their high penetration. This quality allows x-ray fluxes to be used to image organs inside the body making visible both tissue morphology and with appropriate contrast agents, function. Recently there has been considerable interest in the use of biomedical x-ray imaging at spatial resolutions of less than 50 microns. This effort has been largely led by groups using synchrotron sources or with recently developed x-ray tubes having a very fine electron focal spots.

Our work on the SYRMEP beam line attempts to combine phase contrast radiography with novel contrast markers for cells. The hope is that low dose, high contrast images can be produced which would simultaneously show anatomy and marked function. With the high fidelity x-ray beams available at Elettra, fruitful research into novel x-ray markers has become possible. One method used to enhance the contrast of implanted cells against the background of endogenous tissue is to engineer extrinsic cells in a way that allows a highly specific uptake of a contrast agent on a temporary basis. This method is already used extensively in optical microscopy and medical radiography. An alternative approach which is more suited to gene therapy for instance, is that extrinsic cells are loaded with a contrast marker before implantation. In this case the contrast agent is designed to reside in the cells for long periods of time. The technique requi-res a marker that is chemically inert, non-toxic, and does not interfere with the normal functioning of the cells. Colloidal gold fits the requirements of this second type of methodology very well.

Gold is one of the least reactive of the elements making it potentially useful as an inert marker. Furthermore the surfaces of gold nano-particles created in colloids can be coated with a variety of proteins to provide functional behaviour in a biological environment. These features provide it with good prospects as an agent for a variety of biological systems research [1]. For instance gold colloid has been used recently as a vascular x-ray contrast agent in animal radiology [2]. The use of gold labelled proteins as a cell tagging technique in electron microscopy is not new but so far little investigation has been made into using gold colloids for functional x-ray imaging. Our team has embarked on a study to investigate ways of exploiting gold nano-particles as a means to trace movement of marked cells *in-vivo*. We are using both projection x-ray radiography and computed micro-tomography (μCT) on SYRMEP[3]. The initial disease model we have chosen is an aggressive malignant brain tumour: *glioblastoma multiforme*, modelled in rats. Propagated C6 glioma cells were encouraged to phagocytose gold nano-particles by including gold labelled serum proteins in their growth medium[4]. A number of gold loaded cells were subsequently implanted in the brains of laboratory animals and allowed to develop into tumours. X-ray imaging performed at Elettra was used to visualise the morphology and distribution of the resulting cancers. Results have been very encouraging with the clusters of gold loaded cells quite clearly visible in the x-ray images. To investigate

(Research Highlights) LIFE SCIENCES
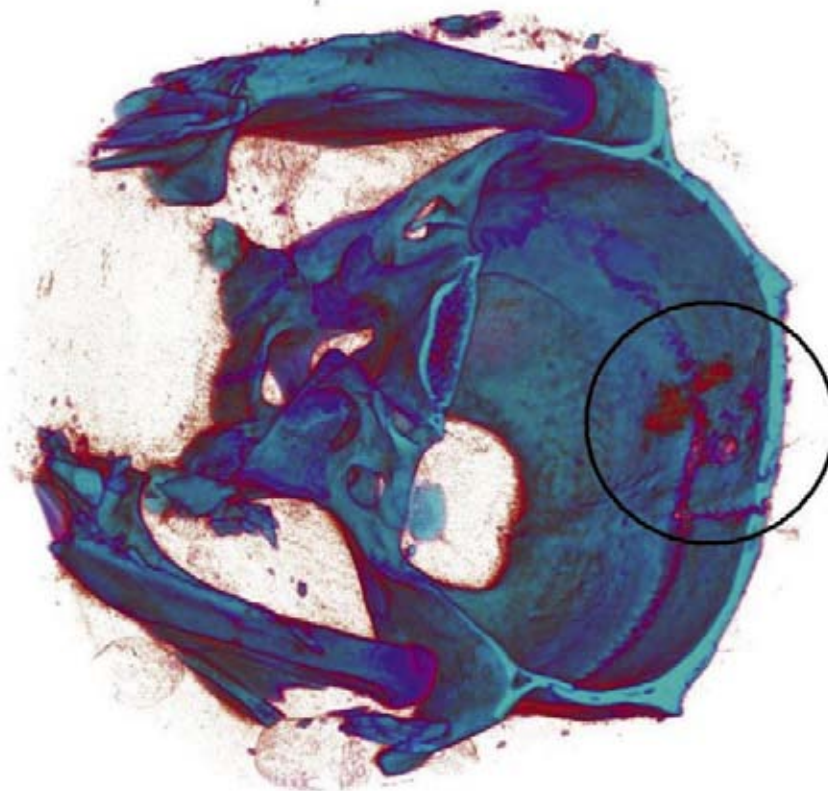
Figure 1.
A screenshot of one of the rat head tomographs. The was data taken on the SYRMEP beam line with a monochromatic beam of 25 keV. The projection images were sampled with 28 micron pixels and reconstructed using filtered back-projection. The burr hole drilled in the skull when the cells were introduced is visible on the top of the skull. Underneath this within the brain cavity, the lesion formed by the marked Glioma cells is visible as a radio opaque cloud.

the potential for the idea to work with non synchrotron sources we also made images with the Tomolab facility at Elettra using the same specimens. Initial results suggest that although the contrast of the lesion is not as good as with the synchrotron source, the images are of sufficient quality to be useful in neurological research.

The first paper on this work will be published this year in the European Journal of Radiology.

References

[1] B.H. Juurlink, R.M. Devon, *Experientia* **47**, 75 (1991).

[2] J.F. Hainfeld et al., *Br. J. Radiol.* **79**, 248 (2006).

[3] M.J. Paulus et al., *Neoplasia* **2**, 62 (2000).

[4] B. H. J. Juurlink, W. Walz, *Neural cell culture techniques* in *Neuromethods Vol. 33: Cell Neurobiology Techniques*, A. A. Boulton, G. B. Baker, A. N. Bateson, Editors, Humana Press, Totowa, NJ, p. 53 (1998).
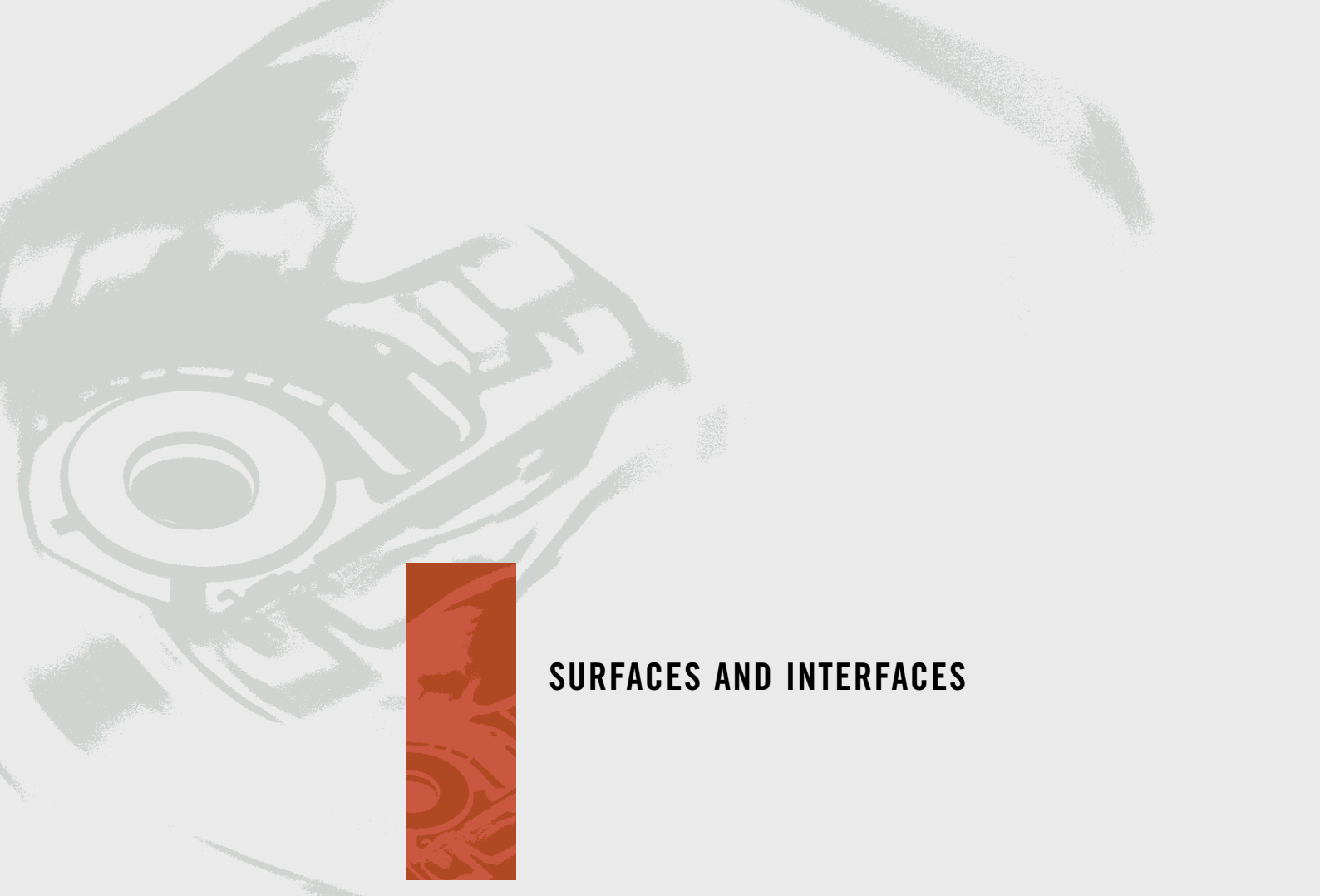
SURFACES AND INTERFACES
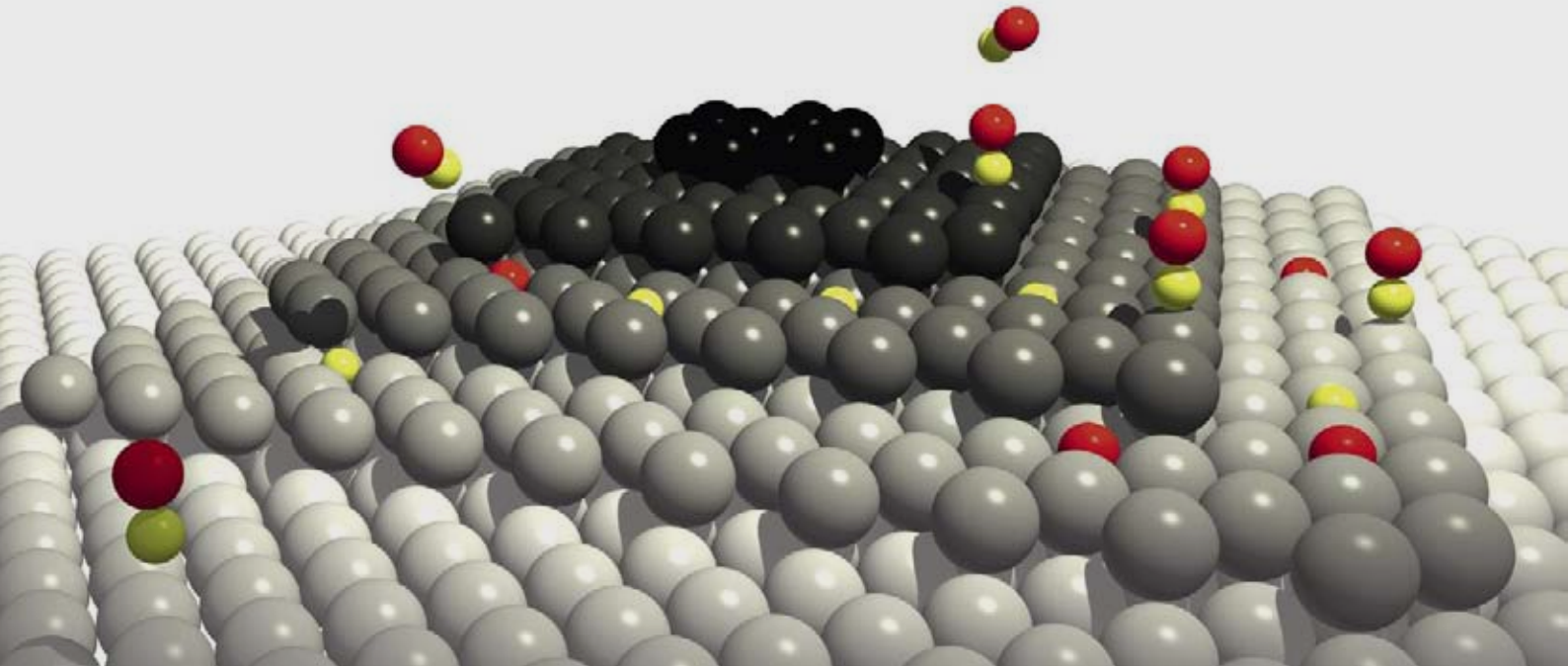
In the Surfaces and Interfaces section, systems at the nano-scale are attracting increasing attention, from the traditional sense of the outermost layers of a surface to the specific properties of nanometer localisation. The issues tackled by the scientific community selected here, constitute the basis for further research fully exploiting synchrotron radiation (SR) and eventually exploiting the characteristics of new light sources, accompanied by complementary experimental techniques and theoretical efforts.

A major effort is devoted to the study of organic molecule self-assembling on model inorganic surfaces. The sulfur-gold interaction of alkanethiols on gold, competing with the weak van der Waals forces between the radical chains, has been shown to drive molecular self-assembling, whose specific structure has been brilliantly solved by grazing-incidence x-ray diffraction (GIXRD). Surface diffraction also solved the structure of planar pi-conjugated aromatic molecules interacting with metal surfaces. Other contributions show that polarization-dependent near-edge x-ray absorption spectroscopy (NEXAFS) is not only used as a straightforward probe for molecular orientation, but it is also exploited to enlighten the modification of empty states upon adsorption, whose interface state dispersion is outlined by high-resolution angular-resolved photoemission (ARPES). All these are brilliant examples of geometric, structural and electronic structure determination.

ARPES is widely used for fundamental surface and interface phenomena, enlightening the formation of one-dimensional 3d-bands in Cu nanowires constructed on a Pt vicinal surface, and disentangling the very nature of the $\sqrt{3}$ Sn/Si structure, also corroborated by scanning-tunneling spectroscopy data, showing an insulating Mott-Hubbard ground state.

One major issue for the facility is structural and magnetic nano-imaging. Quantitative information on the surface stress exerted by adsorbed oxygen islands on tungsten, and stress-induced stripes disordering at high temperature with the same behaviour of finite-size Ising lattices, are brought to light by photoemission and low energy electron microscopy (LEEM). Rotation of magnetic domain walls is clearly detected and imaged in NiFe magnetically soft layers, enlightening the role of spectroscopic imaging of magnetic systems at the nanoscale, one of the major trends in SR.

Furthermore, nano-sized oxides for storage and reduction and bimetallic catalysts were studied under reaction with gases by high-resolution core-level photoemission, while resonant photoelectron diffraction allows identification of defect states on titania surfaces. Catalytic activity in more realistic environments (temperature, pressure) may be definitely envisaged as a further potential research objective with SR and new-generation light sources.

Carlo Mariani

Carlo Mariani is professor of Condensed Matter Physics at the Roma "La Sapienza" University since 2001. Previously, at University of Modena, Université Pierre et Marie Curie (Paris), Italian National Research Council (CNR) in Frascati, Fritz-Haber-Institut der Max Planck Gesellschaft in Berlin.
Research activity focused on the experimental study of low-dimensional systems, surfaces and nano-structures, with a variety of experimental approaches, also exploiting synchrotron radiation. Study of model two-dimensional (2D) surface and interface systems, ordered 1D nano-wires, size-confinement, self-organized nano-structured organic molecules on surfaces and hybrid systems. Author of more than 130 refereed papers on international journals, several proceedings, and communications to conferences. Referee of major international journals and of EU research projects. Member of Scientific and Organizing Committees of international conferences. President of the Italian Society for Synchrotron Radiation and member of the Elettra scientific review panel.

THE STRUCTURE OF ALKANETHIOLS MONOLAYERS SELF-ASSEMBLED ON GOLD

A. Cossaro[1], R. Mazzarello[2], R. Rousseau[2], L. Casalis[3], A. Verdini[1], A. Kohlmeyer[4], L. Floreano[1], S. Scandolo[5], A. Morgante[1,6], M. L. Klein[4], G. Scoles[2,3,7]

[1] Laboratorio Nazionale TASC, INFM-CNR, Trieste, Italy
[2] SISSA - Scuola Internazionale Superiore di Studi Avanzati, Trieste, Italy
[3] Sincrotrone Trieste S.C.p.A., Trieste, Italy
[4] Department of Chemistry, University of Pennsylvania, Philadelphia, PA, USA
[5] International Center for Theoretical Physics and INFM/Democritos, Trieste, Italy
[6] Department of Physics, University of Trieste, Trieste, Italy
[7] Department of Chemistry, Princeton University, NJ, USA

E-mail: floreano@tasc.infm.it

We have determined the structural configuration of Alkanethiols [$(CH_2)_nCH_3SH$] on gold, a puzzling issue that was raised almost 15 years ago in Princeton and that we have finally solved in Trieste by a concerted experimental and theorethical effort. Alkanethiols on gold represent the archetypal among self-assembled monolayers (SAMs), since they form a strong link to the metal substrate through the thiol head-group, while the tail-group can be easily functionalized to tailor the SAM properties, such as wetting, corrosion, adhesion, lubrication and conductivity. At the same time, gold, being unreactive and bio-compatible, can be easily patterned, and obtained as a colloid, as nanoclusters and as a thin film. In the latter case, the surface of the individual grains prevalently displays the high symmetry (111) crystal face.

Common to all alkanethiols on Au(111) is the formation of an ordered SAM displaying a hexagonal ($\sqrt{3}\times\sqrt{3}$) symmetry, corresponding to the adsorption of one standing-up molecule each three Au atoms. Long-chain alkanethiols display an additional modulation of the ($\sqrt{3}\times\sqrt{3}$) structure, yielding a c(4×2) superlattice with the same molecular concentration. These densely packed ordered phases can be equivalently obtained by adsorption from the vapor-phase or in dilute solution, which explains the widespread employment of this system in many research fields. [1]

Even if alkanethiols on Au(111) are by far the most studied SAMs, the exact determination of the adsorption site of sulphur gave rise to a longstanding controversy. First, ab initio calculations were supporting the adsorption of thiols with S in between two Au atoms (bridge site), whereas experiments of photoelectron and photon interference between S and Au atoms rather indicated the presence of sulphur on-top of single Au atoms. Second, the formation of the c(4×2) superlattice implies that the SAM must be formed by molecules adopting two different orientations or adsorption sites.

Recently we have studied the SAM structure of methylthiol (CH_3SH), MT, the simplest and yet the most disputed one. By a recursive comparison between diffraction measurements (x-rays and photoelectrons) and molecular dynamics calculations, we have found a model consistent with ours and former experiments, where the simple ($\sqrt{3}\times\sqrt{3}$) structure results from the dynamical equilibrium between thiols adsorbed in two different, but interchangeable configurations. One configuration is formed by a thiol in a bridge site, the other is formed by two thiols that pull an Au atom out of the surface yielding a staple structure, where the S atoms are laterally linked to the common Au adatom, but they sit almost on-top of a surface Au atom. This novel structure is made energetically competitive with the bridge site by the presence of vacancies. [2]

Due to the fast Au surface diffusion, the Au vacancies produced by the staples are rapidly delocalized over the surface. The vacancy diffusion favors the interchange between bridge and staple configurations (on a picosecond timescale at room temperature). The dynamical disorder due to diffusing vacancies and thiol interchange prevents the establishment of a long range correlation between the bridge and staple thiols, yielding an average ($\sqrt{3}\times\sqrt{3}$)

Research Highlights SURFACES AND INTERFACES
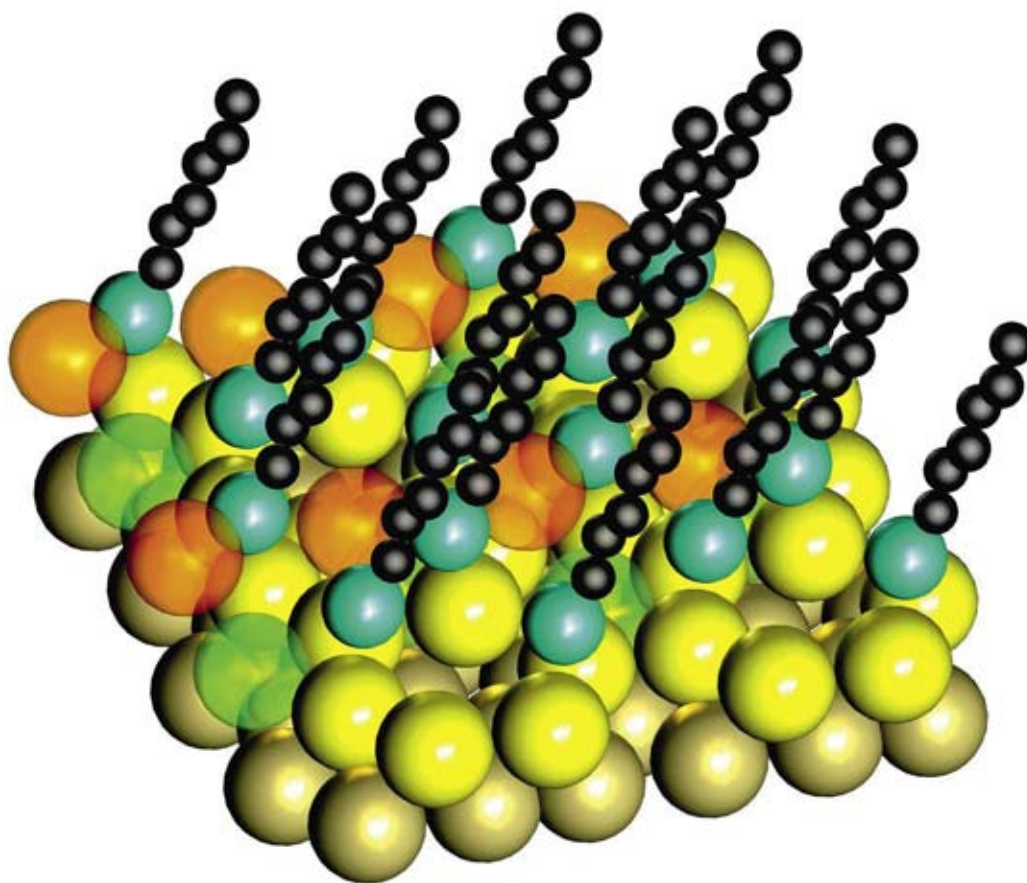
Figure 1.
3D pictorial of the c(4x2) structural model resulting from x-ray diffraction fit. Hexanethiols (S in light-blue, C in black) in bridge and staple configurations are shown; surface Au atoms in yellow, Au adatoms in orange. Partially occupied Au positions are indicated by transparent atoms (surface atoms in green, adatoms in orange).

symmetry, that simply leads to an MT coverage of one molecule every three surface Au atoms. [2]

Once verified for the case of methylthiol, we tested the predictive strength of our model on long-chain alkanethiol SAMs, which display the more complex c(4×2) superlattice. We have considered the case of hexanethiol [$(CH_2)_5CH_3SH$], HT, which intermediate length yields a SAM with coexisting ($\sqrt{3}\times\sqrt{3}$) and c(4×2) phases. Both molecular dynamics calculations and x-ray diffraction measurements indicate that the HT SAM contains the same ingredients of the MT one, i.e. Au vacancies, Au adatoms, and thiols, in both bridge and staple configuration. In this case, however, the dynamical disorder at the surface is strongly hampered by the van der Waals' interaction among the tails of the HT molecules. Calculations predict an effective slowing of the interchange mechanism. With respect to MT, the longer living staple and bridge HT configurations allow the establishment of a correlation among them and the vacancies, that gives rise to the c(4×2) symmetry phase. Experimentally, the atomic disorder of the surface layer is partially quenched yielding a vacancy delocalization much lower than in the MT case. The adatoms in the staple configuration are found to line-up yielding the characteristic zig-zag arrangement of the molecules (Figure 1). [3]

In conclusion, thiols on the Au(111) surface are found to adsorb in two different geometric configurations and to produce a dynamical disorder by creating adatoms and vacancies that rapidly diffuse over the surface. The van der Waals' interaction among the tails of long chain alkanethiols drives the ordering of the thiols, hence reducing the dynamical disorder on the Au surface.

References

[1] C. Love, L.A. Estroff, J.K. Kriebel, R.G. Nuzzo, G.M. Whitesides, *Chem. Rev.* **105,** 1103 (2005).
[2] R. Mazzarello, A. Cossaro, A. Verdini, R. Rousseau, L. Casalis, M.F. Danisman, L. Floreano, S. Scandolo, A. Morgante, G. Scoles, *Phys. Rev. Lett.* **97,** 016102 (2007).
[3] A. Cossaro, R. Mazzarello, R. Rousseau, L. Casalis, A. Verdini, A. Kohlmeyer, L. Floreano, S. Scandolo, A. Morgante, M.L. Klein, G. Scoles, *Science* **321,** 946 (2008).

MOLECULAR CHARGE DISTRIBUTION AND DISPERSION OF ELECTRONIC STATES IN THE CONTACT LAYER BETWEEN PENTACENE AND Cu(119) AND BEYOND

E. Annese[1], J. Fujii[1], C. Baldacchini[2], B. Zhou[1], C.E. Viol[1], I. Vobornik[1], M.G. Betti[2], G. Rossi[1,3]

[1] Laboratorio Nazionale TASC, INFM-CNR, Trieste, Italy

[2] Physics Department, University La Sapienza, Roma, Italy

[3] Physics Department, University of Modena and Reggio Emilia, Modena, Italy

E-mail: annese@tasc.infm.it

The demand for novel devices exploiting the physical and chemical properties of organic films is rapidly increasing. One of the most promising molecules in organic electronics is pentacene, because of its planar structure and conductive properties. The properties of π-conjugated organic films are controlled by the energy position of the molecular states with respect to the Fermi level, in particular the highest occupied and the lowest unoccupied molecular orbitals (HOMO and LUMO). Recent spectroscopy experiments provided evidence of the formation of hybrid electron states at the interface between organic molecules and noble metal surfaces [1-2]. The delocalization of the electronic states at the interface remains an open issue.

We observed significant difference in the electronic states of the pentacene molecules in direct contact with the Cu(119) substrate and the overlayer pentacene molecules by the analysis of STM (scanning tunnelling microscopy) and ARPES (angle resolved photoelectron spectroscopy with polarized synchrotron radiation) results in ultrathin [~monolayer (ML)] pentacene films. Both ARPES and STM data were measured at the APE-INFM beamline at Elettra.

Photoelectrons were excited by photons linearly polarised either perpendicular (see Figures 1a and 1b) or parallel (Figure 1c) to the long molecular axis. The ARPES results are presented in Figure 1a for 1 ML and for 2 ML coverages and compared to the spectrum of the clean Cu(119) surface. The molecular adsorption of a single pentacene layer on Cu (119) induces a spectral density increase at the Fermi edge (I_1). Two pentacene-induced features can be singled out at 1 eV (I_2) and at 1.45 eV (I_3) (Figure 1a). I_1 peak shows a k-depen-

Figure 1.
ARPES spectra at hν=18 eV;
a) Angle integrated spectra around $\bar{\Gamma}$ for pentacene on Cu(119): clean substrate (grey shaded), monolayer (ML) and ~2 ML :
b) Molecular interface state, I_2, and the residual substrate sp band dispersing along $\bar{\Gamma}'$–$\bar{X}'$.
c) I_1 (close to EF) and HOMO derived spectral features, I_3, along the $\bar{\Gamma}'$–$\bar{X}'$ direction.

(Research Highlights) SURFACES AND INTERFACES
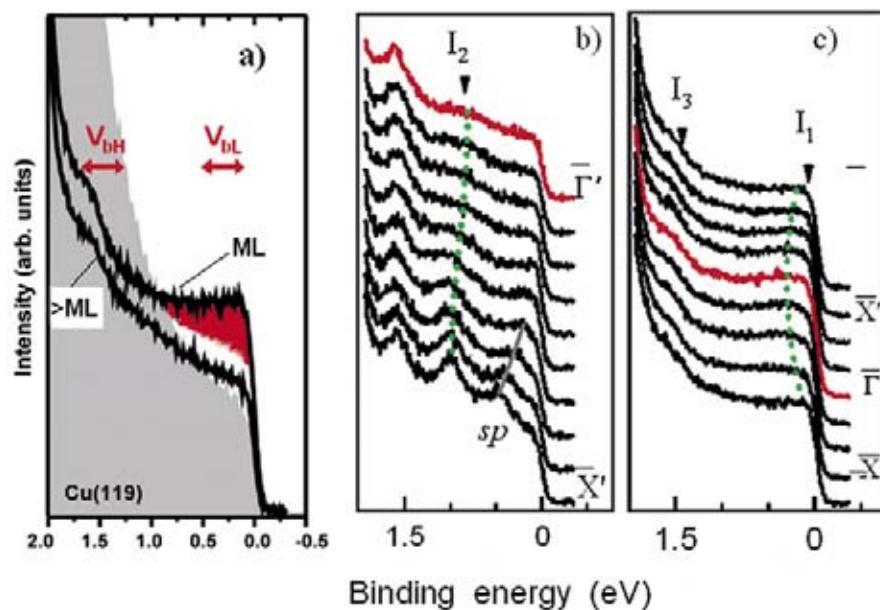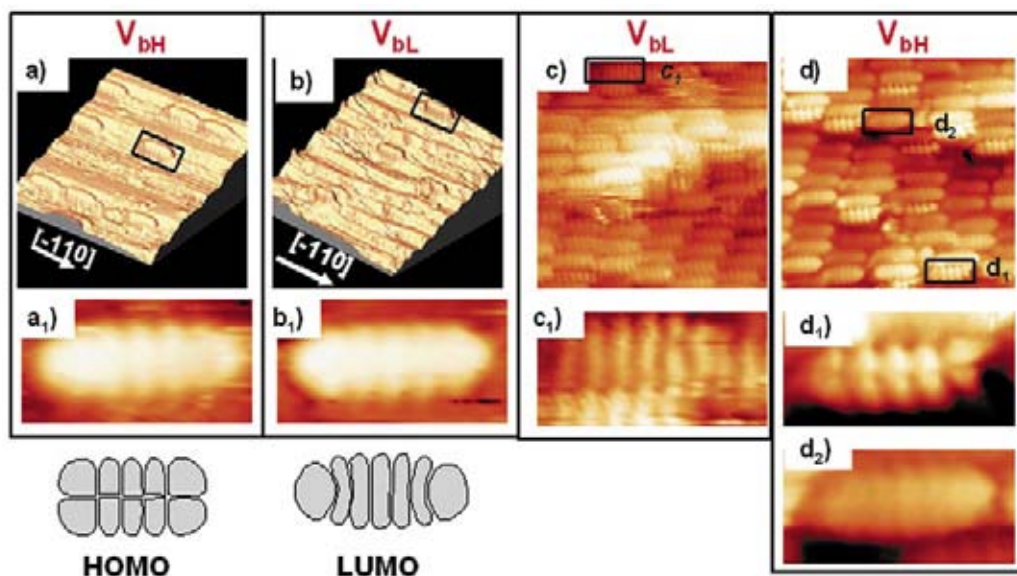
Figure 2.
(a-d) Bias-dependent STM images of pentacene on Cu(119) at submonolayer coverage (a, b) and 1.1 ML coverage (c, d); size: 9.1×10 nm^2; in a) and c) the bias corresponds to LUMO derived features (V_{bL}), in b) and d) the bias corresponds to HOMO derived features (V_{bH}); (a$_1$, b$_1$, c$_1$, d$_{1-2}$) are zoom-in to the selected molecules in the images (a-d); The insets are the HOMO and LUMO calculated electronic density distributions.

dent intensity modulation in this energy region 0–1.5 eV along $\bar{\Gamma}$ -$\bar{X}$. The peak I_2 disperses from $\bar{X}$ to $\bar{\Gamma}$. The energy dispersion along $\bar{\Gamma}$ -$\bar{X}$ can be ascribed to the charge delocalization along the pentacene chains, which is mediated by the metallic substrate at the interface. As the molecular layers pile up, at higher pentacene coverages, I_1 and I_2 are not detected, while the HOMO-derived peak I_3 increases in intensity.

Interacting molecules, in contact with copper, generate dispersive electronic states associated to a perturbed electron charge density distribution of the molecular orbitals (Figure 2). The STM images were acquired with atomic resolution at the relevant values of the bias voltages $|V_{bL}|$, $|V_{bH}|$, which correspond to the binding energies of the molecular interface states I_1 and I_3 (Figure 1a).

In Figure 2 are imaged both isolated pentacene molecules (0.05 mol/nm^2) (Figure 2 a-b) and molecules on a coverage exceeding the monolayer (1.1 ML ~ 0.80 mol/nm^2) (Figure 2c-d). The individual adsorbed pentacene molecule shows seven protrusions charge pattern at both V_{bL} and V_{bH}. In particular the molecule in Figure 2a$_1$) differs from the charge electron distribution of the HOMO of the free molecules, giving the signature of the interaction between pentacene and substrate. A charge pattern similar to that in Figure 2 a$_1$) could also be observed at the higher pentacene density when imaging at V_{bL} Figure 2c) and at V_{bH} for interface layer molecules. At V_{bH} a different type of molecular charge pattern can be distinguished. These correspond to the top-

most molecules, not surrounded by other molecules besides the ones underneath (Figure 2d$_1$) mimicking the HOMO features of the free molecule.

We have identified a peculiar charge density distribution of the pentacene molecules in contact with the Cu(119) surface. The perturbed molecular orbitals are strictly limited to the contact layer. The second layer molecules are weakly bound to the contact layer but preserve the in-plane orientation, the alignment along the substrate template and a charge density distribution mimicking free pentacene molecular orbitals. In the reciprocal space, the molecular charge distortion gives rise to the electronic states localized at the interface, with a tiny dispersion along the pentacene long molecular axis.

References

[1] A. Ferretti *et al*, *Phys. Rev. Lett.* **99**, 046802 (2007).

[2] C. Baldacchini *et al*, *Phys. Rev.* B **76**, 245430 (2007).

PERIODIC ARRAYS OF Cu-phthalocyanine CHAINS ON Au(110)

L. Floreano[1], A. Cossaro[1], R. Gotter[1], A. Verdini[1], A. Morgante[1,2], F. Evangelista[3], A. Ruocco[3], G. Bavdek[1,4], D. Cvetko[1,4]

[1] Laboratorio Nazionale TASC, INFM-CNR, Trieste, Italy

[2] Physics Department, University of Trieste, Italy

[3] Physics Department and CNISM, University of Roma III, Italy

[4] Physics Department, University of Ljubljana, Slovenia

E-mail: floreano@tasc.infm.it

Metal-Phthalocyanines (M-Pc) are aromatic dyes formed by four pyrrolic and four benzene macrocycles arranged around a central metal atom in a planar geometry. This family of molecules is widely employed in organic-based electronic devices (OEDs), due to the easy trimming of its optical response by simple replacement of the central metal species (Cu-Pc is the basic consitituent of hemoglobine, Mg-Pc that of chlorophyll, etc).

The electronic properties of real OEDs deviate from those of pristine active material because of the interface formed between the organic film and the electrodes. In fact, a proper overlap between the electron orbitals at the interface is required for optimal charge injection. Moreover molecular reorientation at the interface can induce topological defects, thus inhibiting the charge transport. [1] Most of poly-aromatic molecules, like Cu-Pc, adsorb flat on metal surfaces, but the presence of defects and the atomic structure underneath affect the azimuthal orientation of the molecules as well as their spacing, which drive the orientation of next layers, i.e. the device performances.

Figure 1.
Different probing depths of GIXRD, LEED, and HAS schematically represented in the three panels, from left to right, respectively. The sketch represents a single organic overlayer on top of a metal crystal. Reproduced with permission from ref. [2]. Copyright 2008 American Chemical Society.

The Au(110) surface is well suited for a thorough study of the atomistic processes that govern the growth of Cu-Pc on gold. The surface exhibits a large atomic reconstruction in its ground state, the so-called *missing row* (1×2)-Au(110) phase. This phase is formed by narrow (111) microfacets, i.e. the same symmetry planes exposed by poly-crystalline gold electrodes. The channels between such facets determine a marked uniaxial anisotropy, which influences surface diffusion and molecular orientation. Reconstructions of higher order *missing row* type are energetically accessible by adsorption of atoms/molecules.

We exploited the complementary probing depth and chemical sensitivity of the different investigation techniques available at the Aloisa beamline (Figure 1) to fully characterize the ordered growth of Cu-Pc on the (1×2)-Au(110) surface, from the early stage of deposition up to the saturation of the first monolayer. The deposition has been monitored in real time by helium atom scattering (HAS) and low energy electron diffraction (LEED). The corresponding molecular orientation has been studied by variable polarization absorption spectroscopy (NEXAFS), whereas the Au substrate structure has been determined by out-of-plane surface X-ray diffraction (SXRD).

Several ordered molecular phases may be produced in the submonolayer range that involve large rearrangements of the Au(110) substrate. Common to all submonolayer phases appears a quasi unidimensional character of the overlayer ordering, where Cu-Pc molecules line up edge-to-edge into extended chains. Such chains are aligned along the Au missing row direction and display an intrachain commensurate 5-fold periodicity of 14.4 Å. An effective interchain repulsion mecha-
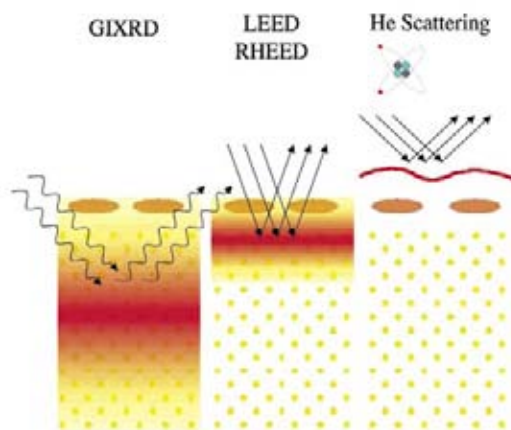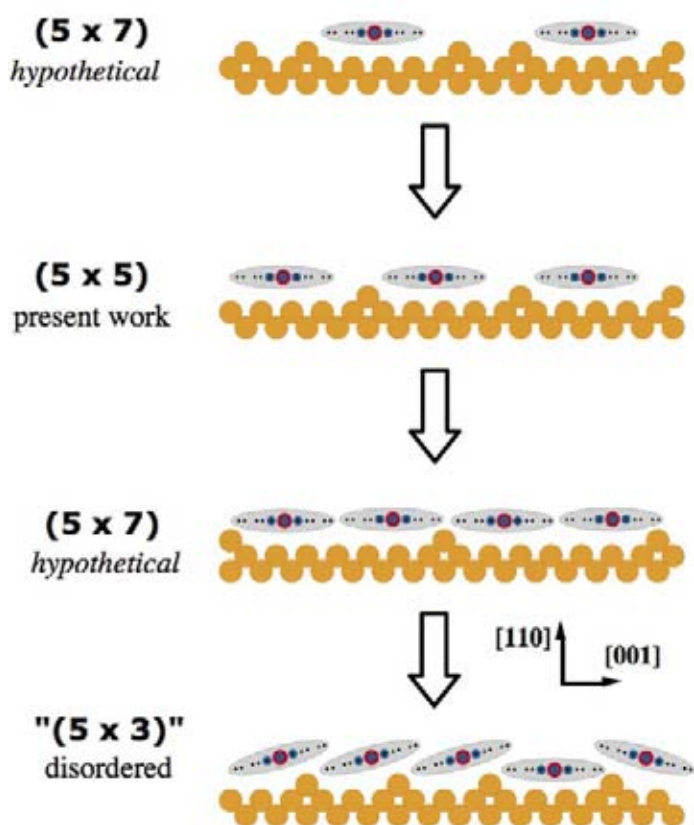
Figure 2. Sideview of the model for four consecutive phases of Cu-Pc on Au(110). The (5×5) and "(5×3)" are drawn from NEXAFS and SXRD analysis. The low coverage (5×7) phase (3/7 ML) has been drawn on the basis of the observed domain wall proliferation leading to the formation of the (5×5) phase. The high coverage (5×7) phase (6/7 ML) has been drawn from the assumption that Cu-Pc molecules have the tendency to lie flat on the substrate. Reproduced with permission from ref. [2]. Copyright 2008 American Chemical Society.

nism drives the formation of regular arrays of parallel Cu-Pc chains, whose spacing along [001] varies with the molecular coverage [2].

Cu-Pc molecules are found to relieve the *missing row* geometry of the Au substrate inducing a shallow reconstruction beneath the chains. Molecules are found to lie flat on the surface for the (5×5) phase, whereas they are slightly tilted off the surface in the laterally compressed "(5×3)" monolayer phase, where they coexist with a large number of point defects. In fact, the "(5×3)" monolayer phase yields a clear diffraction pattern as seen by LEED and SXRD, whereas only diffuse scattering can be detected by HAS because of the large cross-section of these defects. [3] The large substrate reconstructions are characterized by *added rows* aside the Cu-Pc chains, thus mimicking the monoatomic steps on the Au(111) surface, that are also known to drive the azimuthal reorientation of Cu-Pc [4].

From comparison of the (5×5) and "(5×3)" structural determinations, we can draw a sketch of the surface evolution through the intermediate symmetry phases, as shown in Figure 2. Regular arrays of Cu-Pc chains with the desired spacing can be thus obtained by simply tuning the coverage and substrate temperature.

References

[1] C.D. Dimitrakopoulos, P.R.L. Malenfant, *Adv. Mater.* **14**, 99 (2002).

[2] L. Floreano, A. Cossaro, R. Gotter, A. Verdini, G. Bavdek, F. Evangelista, A. Ruocco, A. Morgante, D. Cvetko, *J. Phys. Chem. C* **112**, 10794 (2008).

[3] A. Cossaro, D. Cvetko, G. Bavdek, L. Floreano, R. Gotter, A. Morgante, F. Evangelista, A. Ruocco, *J. Phys. Chem. B* **108**, 14671 (2004).

[4] I. Chizov, G. Scoles, A. Kahn, *Langmuir* **16**, 4358 (2000).

PENTACENE NANORAILS ON Au(110)

G. Bavdek[1,2], **A. Cossaro**[1], **D. Cvetko**[1,2], **A. Morgante**[1,3], **C. Africh**[1], **C. Blasetti**[1,3], **F. Esch**[1], **L. Floreano**[1]

[1] *Laboratorio Nazionale TASC, INFM-CNR, Trieste, Italy*
[2] *Physics Department, University of Ljubljana, Slovenia*
[3] *Physics Department, University of Trieste, Italy*

E-mail: floreano@tasc.infm.it

Among the organic molecules employed for the fabrication of organic electronic devices (OEDs), Pentacene is one of the few having reached the consumer market, thanks to its electronic properties (large charge mobility), as well as due to its large thermal and mechanical stability. Nowadays, the realization of single layer molecular devices has definitely entered in the prototypical stage and the molecular nanomanipulation let us envisage the last step towards device miniaturization. As a consequence, the possibility to fabricate by self-assembly regular molecular arrays in non-trivial configurations becomes of interest also for OEDs fabrication.

Strongly anisotropic substrates are used as templates to pursue the self-assembly of nano-patterned organic overlayers. The highly corrugated (1×2)-Au(110) surface is generally well suited for driving the accomodation of poly-conjugated molecules, thanks to its large instability towards higher order reconstructions. [1] We have found that Pentacene deposition on Au (110) follows a Stranski-Krastanov regime of growth, i.e. 3D islands, with standing up molecular orientation, grow on top of a first layer of standing flat molecules. The corresponding phase diagram (Figure 1) has been drawn from real time acquisition of photoemission spectra (XPS) together with He diffraction patterns (HAS). [2]

We have characterized in detail the adsorption geometry of the pentacene monolayer phases by means of near-edge X-ray absorp-

Figure 1.
Phase diagram of pentacene films on Au(110).
The '(6×3)' phase is quoted since it has not a well-defined equilibrium coverage. The completion of the first monolayer is conventionally assigned in between the (3×6) and (6×8) phases. Reproduced with permission from ref. [2]. Copyright 2006 American Chemical Society.

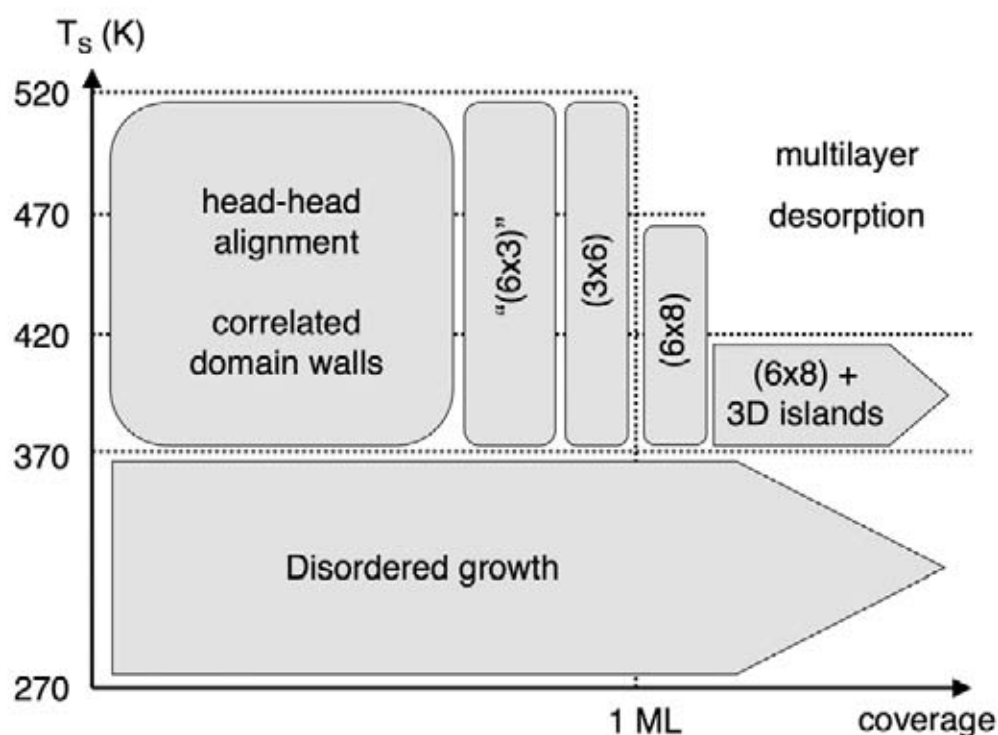**Figure 2.** The (3×6) phase (left) is formed exclusively by flat-laying molecules (one molecule per unit cell), which align into chains extending in the [1$\bar{1}$0] direction. The (6×8) phase (right panel) also contains flat chains, as the (3×6) phase, but they are separated by chains of on-edge molecules, forming regular arrays of nanorails (three molecules per unit cell). The cells are indicated by rectangles (thick lines). Reproduced with permission from ref. [3]. Copyright 2008 American Chemical Society.
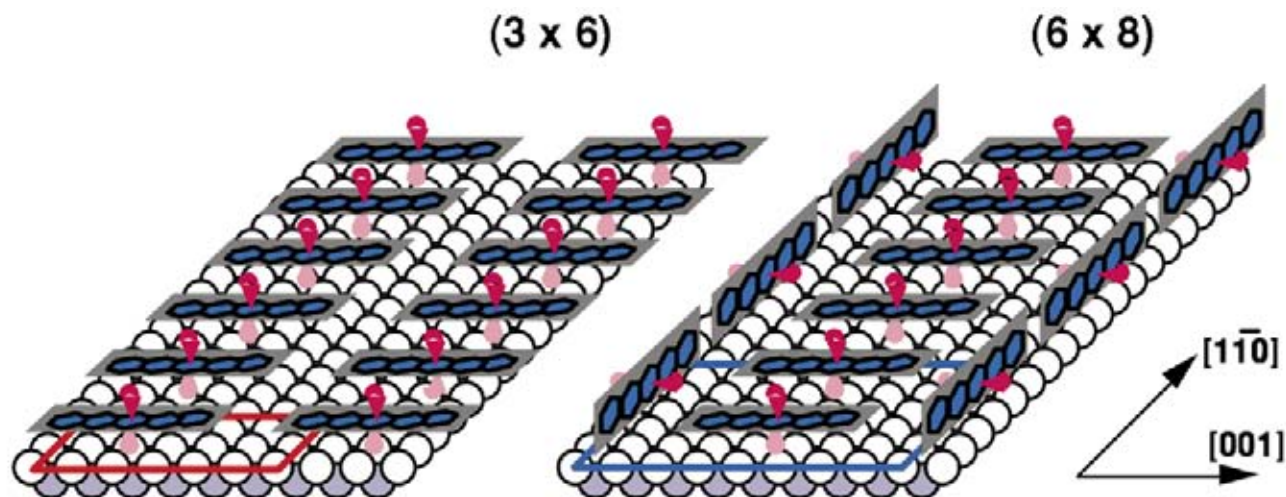
tion spectroscopy (NEXAFS) at the carbon *K*-shell and scanning tunneling microscopy (STM). As the coverage increases the molecules undergo some azimuthal reorientations. In particular, we succeeded in preparing a peculiar phase at the saturation of the first monolayer, displaying a strongly anisotropic template formed by two types of electronically and orientationally unequivalent pentacene molecules, mimicking regular arrays of nanorails (Figure 2).

Flat-lying molecules, aligned side-by-side with the long molecular axis along the [001] direction, form long crosstie chains extending in the [1$\bar{1}$0] direction. In between the adjacent flat chains, additional on-edge molecules, i.e. tilted by 90° around their molecular axis, line up head-to-tail into rails extending along [1$\bar{1}$0]. These molecules are only weakly hybridized with the substrate, as indicated by their lowest unoccupied molecular orbitals, which closely resemble those of the free molecule. The nanorail structure is found to be stable up to 420 K in vacuum and also to remain in place after exposure to air, thus being a template well suited for further self-assembly of organic heterostructures. [3]

The same molecule thus displays two geometrically and electronically unequivalent configurations within the same monolayer phase. It is particularly important to have

available regular and stable arrays of quasi-free pentacene molecules (the rail chains) for further lateral coupling to other molecules or molecular assemblies, for example to enhance the charge transfer in donor-acceptor heterojunctions for photovoltaic applications. At the same time, 2/3 of the molecules (the crosstie chains) are in an optimal configuration for mediating the charge transport towards the metallic substrate. According to the most recent studies on the annealing of intermixed active layers in organic photovoltaic cells, [4] the high degree of order of the nanorails is also expected to further enhance the efficiency of a possible heterojunction.

References

[1] S. Prato, L. Floreano, D. Cvetko, V. De Renzi, A. Morgante, S. Modesti, F. Biscarini, R. Zamboni, C. Taliani, *J. Phys. Chem. B* **103**, 7788 (1999).

[2] L. Floreano, A. Cossaro, D. Cvetko, G. Bavdek, A. Morgante, *J. Phys. Chem. B* **110**, 4908 (2006).

[3] G. Bavdek,, A. Cossaro, D. Cvetko, C. Africh, C. Blasetti, F. Esch, A. Morgante, L. Floreano, *Langmuir* **24**, 767 (2008).

[4] A.C. Mayer, M.T. Lloyd, D.J. Herman, T.D. Kasen, G.G. Malliaras, *Appl. Phys. Lett.* **85**, 6272 (2004).

CHARGE TRANSFER AT THE ZnPcCl$_8$/Ag(111) INTERFACE PROBED BY A COMBINED PHOTOEMISSION AND X-RAY ABSORPTION STUDY

L. Giovanelli[1,2], **P. Amsalem**[1,2], **J. M. Themlin**[1,2], **Y. Ksari**[1,2], **M. Abel**[1,2], **L. Nony**[1,2], **F. Bondino**[3], **E. Magnano**[3], **M. Mossoyan-Deneux**[1,2], **L. Porte**[1,2]

[1] *Aix-Marseille Université, IM2NP, Centre Scientifique de Saint-Jérôme, Marseill, France*
[2] *Centre National de la Recherche Scientifique, Marseille-Toulon, France*
[3] *Laboratorio Nazionale TASC, INFM-CNR, Trieste, Italy*

E-mail: luca.giovanelli@im2np.fr

The study of the interface formation between molecular thin films and well ordered inorganic surfaces has elicited increasing scientific interest. In fact, the performance improvements of future electronic devices based on organic molecules will strongly depend on the advances made in the fundamental understanding of the physical phenomena taking place at these interfaces and during the organic thin film growth [1]. More recently, the possibility of designing original low-dimensional systems based on self-assembled functionalized organic molecules has further spurred the surface science community in getting a deeper understanding of the intermolecular and molecule-substrate interaction [2]. Within the rich field of molecular self-assembly, the study of model systems with an increasing degree of complexity is highly desirable.

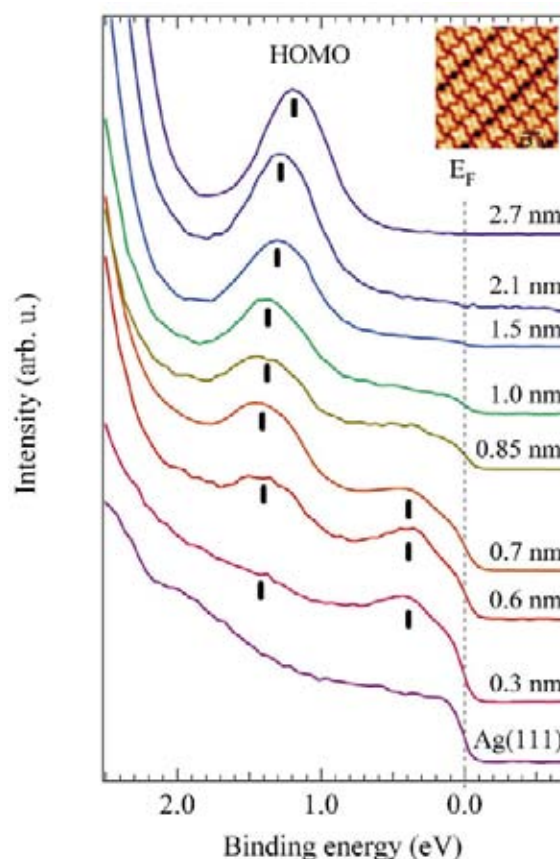**Figure 1.**
Valence band spectra of ZnPcCl$_8$/Ag(111) as a function of molecular film thickness. Thick markers evidence the HOMO of the thick film molecules and of the interface molecules (former LUMO). A high resolution STM image of 1 ML ZnPcCl$_8$/Ag(111) is shown in the inset.

Following that purpose, a detailed study of zinc-phthalocyanine (Zn-Pc) derivatives deposited on Ag(111) has recently been undertaken [3,4]. By substituting eight outermost hydrogens with halogen atoms (Cl and F), the two-dimensional self-assembling properties reveal a rich behavior through the appearance of various two-dimensional phases. The presence of regularly-spaced fault-lines in the 1 ML structure suggests that the molecule-substrate interaction plays a key role in the self-organization phenomenon. In the present study, the evolution of the electronic structure of a thin film of $ZnPcCl_8$ grown on Ag(111) has been investigated. We compare the occupied and unoccupied electronic states measured when the surface coverage is less than one monolayer (sub-ML) to those of a thin film of increasing thickness.

The valence band (VB) was studied by Ultaviolet Photoemission Spectroscopy from the earliest stages of adsorption up to a thick molecular layer. Figure 1 shows the spectra measured in the region close to the Fermi level (E_F). The VB in this region is modified after the first deposition. There is an overall enhancement of the energy distribution curve, and a new density of states grows up as a strong spectral feature centered at 0.4 eV. On the basis of the evolution at higher coverage, it is clear that this feature is distinct from the electronic states originating from the HOMO orbital of the isolated molecule. When the thickness is raised beyond 0.6 nm, the intensity of the new feature close to E_F diminishes and eventually disappears. This behaviour is the clear sign of an interface character. To explain this feature, we put forward a charge transfer from the metal substrate to the first molecular layer with the consequent creation of occupied interface states at the expense of unoccupied molecular states.

Figure 2 displays the nitrogen near-edge X-ray absorption fine structure (NEXAFS) spectra of a multilayer (top) and a sub-ML of $ZnPcCl_8$/Ag(111) measured at the beamline BACH. The NEXAFS spectra are closely related to the density of unoccupied states of the system, under the additional influence of a core hole. The spectrum of the multilayer is representative of the (weakly-interacting) $ZnPcCl_8$ molecules and up to 401 eV the spectral features are due to optical transitions to empty states of π character, the lowest in energy being due to the LUMO. The spectrum of the sub-ML is noticeably different. One easily recognizes all the main features but there is a general redistribution of their intensities and
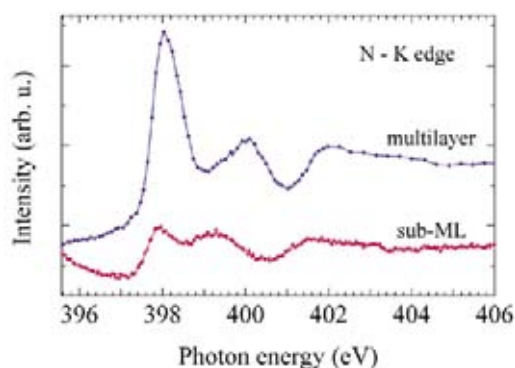
Figure 2.
N K edge X-ray absorption spectra of a thick layer of $ZnPcCl_8$ (top) and a sub-ML of $ZnPcCl_8$/Ag(111) (bottom).

relative energy positions. Most remarkably, the intensity ratio between the first two features has considerably changed, the first one being reduced with respect to the second. This evidence corroborates the charge-transfer scenario and further indicates that the LUMO of the first-layer molecules becomes partially filled. Nevertheless, the lack of a sizeable density of states at E_F suggests that more complicated mechanisms of intra- or extra-molecular charge redistribution may be important to understand the full picture.

In conclusion, our measurements give further insight into the mechanism of interface formation between a metal and a planar conjugated organic molecule. The molecular adsorption is accompanied by the formation of some intense interface states: a charge transfer from the substrate fills in a previously unoccupied molecular orbital with a possible hybridization with the substrate states. Accordingly, a reduction (filling) of the lowest unoccupied molecular orbital (LUMO) and a redistribution of higher unoccupied states take place.

References
[1] D. Cahen *et al.*, *Materials Today* **8**, 32 (2005).
[2] T. Yokoyama *et al.*, *Nature* **413**, 619 (2001).
[3] M. Abel *et al.*, *ChemPhysChem* **82**, 7 (2006).
[4] L. Giovanelli *et al.*, *J. Phys. Chem.* C **112**, 8654 (2008).

A TWO-DIMENSIONAL MOTT-HUBBARD INSULATOR:
Sn/Si(111)-(√3x√3)R30°

S. Modesti[1,2], L. Petaccia[1,3], G. Ceballos[1], I. Vobornik[1], G. Panaccione[1], G. Rossi[1,4], L. Ottaviano[5], R. Larciprete[3,6], S. Lizzit[3], A. Goldoni[3]

[1] Laboratorio Nazionale TASC, INFM-CNR, Trieste, Italy

[2] Dipartimento di Fisica, Università di Trieste, Trieste, Italy

[3] Sincrotrone Trieste S.C.p.A., Trieste, Italy

[4] INFM, Dipartimento di Fisica, Università di Modena e Reggio Emilia, Modena, Italy

[5] Università degli Studi dell'Aquila, Coppito-L'Aquila, Italy

[6] CNR-Istituto dei Sistemi Complessi, Monterotondo-Roma, Italy

E-mail: modesti@tasc.infm.it

A Mott-Hubbard insulator is a system with an odd number of electrons per unit cell where the tendency of the electrons to be spatially localized to minimize Coulomb repulsion prevails on the tendency to be delocalized to minimize the cost in kinetic energy from spatial confinement. In three-dimensional material the tendency to delocalize usually wins and solids with an odd number of electrons per unit cell conduct, as predicted by the band theory. In systems with a lower number of dimensions there is less freedom for the motion of the electron and the correlations caused by the

Coulomb repulsion have a stronger effect. An example are the high-temperature superconductors, quasi-two-dimensional solids that conduct when the doping is above a minimum value, and are Mott-Hubbard insulators below this value. The electron correlation effects play a fundamental role also in the metallic and superconducting phases in these materials, but the full understanding of their effects is difficult to reach because of the complexity of these systems.

Simpler strictly two-dimensional (2D) systems are easier to study and can provide a

Figure 1.
(a) Filled state STM image of the Sn/Si(111)-(√3x√3)R30° surface consisting in 1/3 of a monolayer of Sn atoms on the Si(111) surface in a triangular lattice. All the Sn atoms are equivalent and the Sn layer is not rippled. The dark-bright region on the left is a defect. The image has been taken at 4 K.
(b) Average tunneling spectra of the same surface measured far from the defects at different temperatures,
(c) Single conductance spectra at 5 K. The normalized conductance mimics the local density of states. A narrow gap across the Fermi level – 0 sample voltage – opens below 70 K.
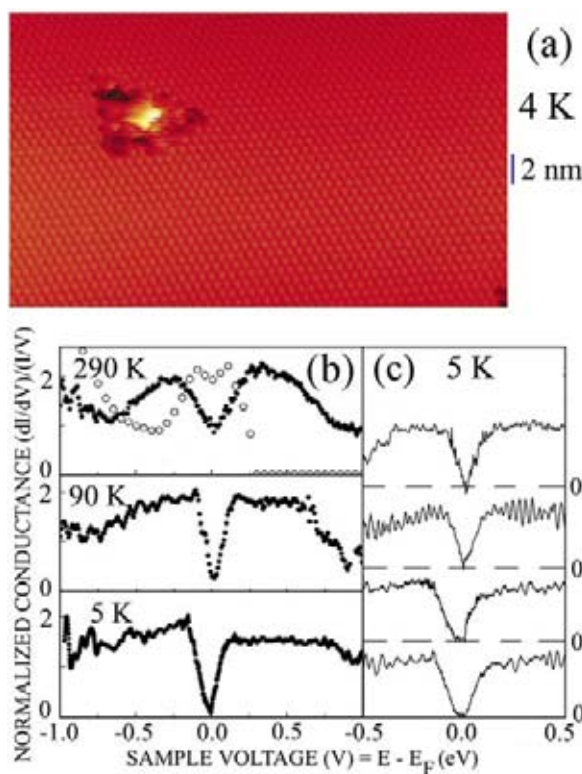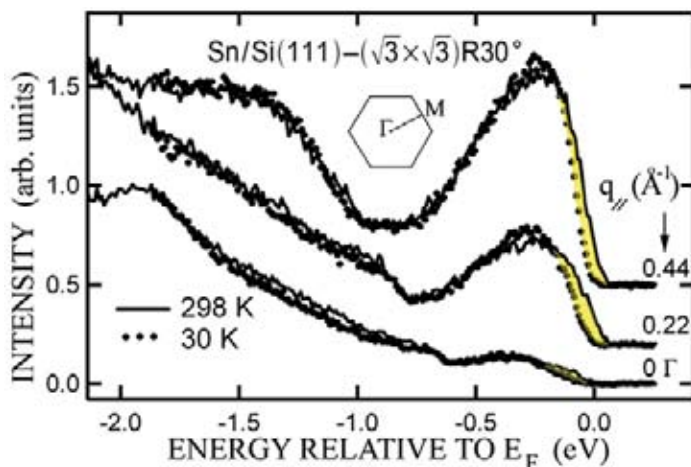
Figure 2.
Photoemission spectra at 298 K and 30 K along the ΓM direction of the surface √3 × √3 Brillouin zone for different values of the parallel wave vector. The the M point is at 0:56 Å⁻¹. Also shown for comparison is the Fermi edge measured on polycrystalline Ta at 30 K. The yellow marks the region where the spectral intensity decreases at low temperature and the Mott-Hubbard gap opens. The energy width of this region is comparable to that measured by STS.

useful aid to the understanding of the physics of the high temperature superconductors. Mott insulators have been created over the past decade on the surfaces of common semiconductors (SiC, GaAs, Si, Ge) by absorption of suitable atoms in order to get systems with an odd number of electron per unit cell and narrow bands. We have demonstrated that one third of a monolayer of Sn in a triangular lattice on Si(111), despite having a half-filled surface band, is a narrow gap insulator below 70 K and a bad metal above this temperature [1]. Our experimental results are in agreement with LSDA+U calculations that predict an antiferromagnetic Mott-Hubbard insulating ground state [2]. This system is an interesting playground for the rich physics of 2D triangular Mott insulators.

The structure of 1/3 of a monolayer of Sn on Si(111) in a triangular lattice has been determined by scanning tunnelling microscopy (STM) at 4 K and photoelectron diffraction (PED) from the Sn 4d core levels at 30 K measured at the SuperESCA beamline. The data indicate that all the Sn adsorbed atoms have the same bonding geometry – they are bonded to three surface Si atoms - and the same height with respect to the Si surface plane. Since the photoelectron diffraction is a fast process on the time scale of the atomic motions, the PED data provide a snapshot of the structure and confirm that absence of ripple in the Sn layer observed by STM is not a time averaging effect – like in the isoelectronic Sn/Ge(111) system,- but is real.

The electronic properties of the system have been determined by scanning tunnelling spectroscopy (STS) from 300 K to 4 K and by angle resolved photoemission spectroscopy down to 30 K (APE beamline). Both techniques show a decrease of the spectral intensity in a ~200 meV window across the Fermi level from 300 K and 70 K, and the opening of a ~50 meV gap below 70 K.

These results are not compatible with a band-theory picture since because by electron counting the ground state of the system should be metallic. All LDA calculations predict a metallic state. On the contrary, LSDA+U calculations [2], that take into account part of the correlation effects neglected by LDA, find an antiferromagnetic insulating ground state that without buckling, in the limit of the LSDA+U approximation, in a strong indication of a Mott-Hubbard ground state. The magnitude of the predicted gap and the spectral functions are in good agreement with the experimental results. According to the calculations the antiferromagnetic coupling is strong enough to induce spin ordering at least on a local scale. The challenge is now to find experimental evidences of the antiferromagnetic (local) order.

References
[1] S. Modesti et al., *Phys. Rev. Lett.* **98**, 126401 (2007).
[2] G. Profeta and E. Tosatti, *Phys. Rev. Lett.* **98**, 086401 (2007).

PROBING ELECTRONIC CHARGE LOCALISATION IN SEMICONDUCTORS BY RESONANT PHOTOELECTRON DIFFRACTION

P. Krüger[1], S. Bourgeois[1], B. Domenichini[1], H. Magnan[2], D. Chandesris[3], P. Le Fèvre[3], A. M. Flank[3], J. Jupille[4], L. Floreano[5], A. Cossaro[5], A. Verdini[5], A. Morgante[5]

[1] ICB, UMR 5209 CNRS-Université de Bourgogne, Dijon, France
[2] SPCSI, CEA Saclay, Gif-sur-Yvette, France
[3] Synchrotron SOLEIL, Gif-sur-Yvette, France
[4] Institut des NanoSciences de Paris, CNRS, Paris
[5] Laboratorio Nazionale TASC, INFM-CNR and Sincrotrone Trieste S.C.p.A., Trieste, Italy

E-mail: pkruger@u-bourgogne.fr

Many properties of semiconductors and oxides depend crucially on defects and impurities. The whole field of microelectronics hinges on the possibility to switch between electron and hole transport by appropriate doping. Another example is solid state catalysis where in many cases surface defects are the active sites of the catalytic reaction. Defects so strongly modify the transport and chemical properties of the semiconductor because they introduce new electronic states in the band gap. Detailed knowledge of these "defect states" is crucial for the understanding of the material properties. Titanium dioxide is a wide-gap semiconductor used for many technological applications. TiO_2 can easily be electron doped by reduction which produces oxygen vacancies and a defect state in the band gap. This state is occupied by the "excess" electrons that are left behind upon vacancy formation at O^{2-} anion sites ($O^{2-} \rightarrow \frac{1}{2} O_2 + 2e^-$). A major question is: where are these excess electrons localized, or in other words: what is the spatial distribution of the defect charge? At the most stable surface of TiO_2, rutile(110), O vacancies preferentially form at O1 sites (Figure 1). It is known that the excess electrons occupy Ti-3d orbitals, but the important question on *which* Ti sites they are located could never been answered by experiment. On the theoretical side many studies have been reported but the results obtained with different approaches are strongly conflicting [1].

Figure 1.
Model of the TiO_2 (110) surface. Small blue (big red) balls are titanium (oxygen) atoms. An oxygen vacancy is indicated as V.

Figure 2. Experimental photoelectron diffraction pattern from the defect state in TiO$_2$ (110) excited at the Ti-2p-3d resonance. The azimuthal anisotropy, I(θ,ϕ)/I$_0$(θ)-1, is shown as a stereographic projection for $\theta<80°$. On the right, relevant interatomic directions are indicated in the irreducible quarter of the pattern.
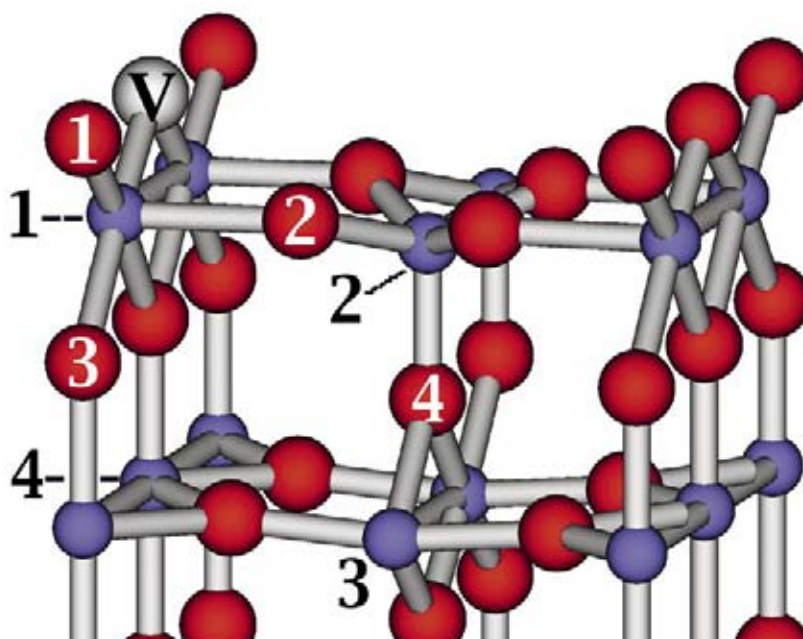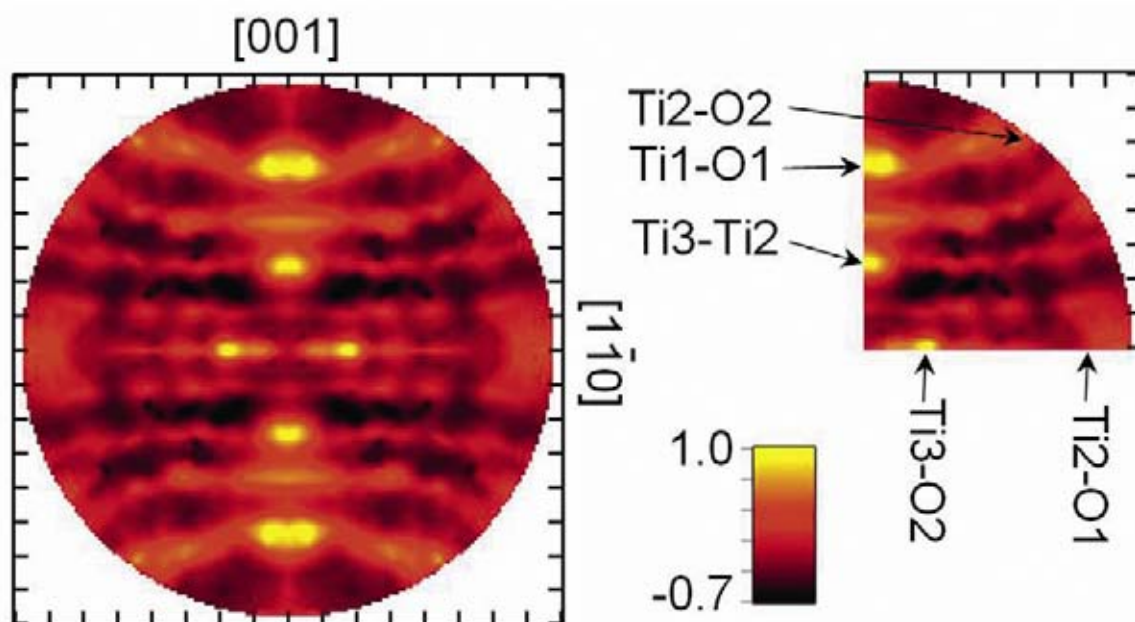
Recently, we have studied the charge distribution of the defect state using a novel synchrotron based technique: resonant photoelectron diffraction [2]. In a photoelectron diffraction (PED) experiment one measures the angular distribution of the photoelectrons emitted from a single crystal surface for fixed photon and electron energy. The angular modulation of intensity, called PED pattern, is produced by the diffraction of the photoelectron wave that is emitted from a certain atom and scattered at the neighbouring atoms. The PED pattern thus reflects the local environment around the emitter atoms. This is routinely exploited in core-level PED, a well-established structural technique. Here we have analysed photoelectrons from the defect state in the valence band rather than from a core-level. In this case the only emitter atoms are those that carry some excess charge. By analysing the PED pattern we succeeded in identifying these atoms. Due to the low defect concentration of a few percent of a monolayer, the count rate of such a defect state PED experiment is, in general, very low. This is why we have done the experiment in a resonant mode, by tuning the x-ray energy to the Ti-L$_2$ adsorption edge. The photoemission intensity of the defect state could thereby be enhanced by two orders of magnitude. The resonant PED pattern, as measured at the Aloisa beamline, is shown in Figure 2. Bright spots correspond to directions of high photoemission intensity. Due to the focussing effect of electron-atom scattering, high intensity can be expected along interatomic

directions from an emitter to a neighbour atom. It can be seen that all bright spots agree well with interatomic directions from sites Ti1, Ti2 and Ti3, which indicates that all these three sites carry some defect charge. For a quantitative analysis we have simulated the PED patterns of all possible emitter sites using first-principle multiple scattering calculations. The relative weights of the different sites were then obtained by a least square fit to the experimental pattern. The result is that about two thirds of the defect charge is located on the sub-surface site Ti3. The remaining one third of the charge is shared between the surface layer sites Ti1 and Ti2. These findings are in good agreement with DFT calculations but in contradiction with some competing theoretical approaches [1]. In conclusion we have shown that resonant PED can be used to measure the charge localisation of defect or impurity states in semiconductors and that it provides element- and site-specific information on the valence electronic structure of surfaces.

References

[1] M. V. Ganduglia-Pirovano et al*., Surf. Sci. Rep.* **62**, 219 (2007).
[2] P. Krüger et al*., Phys. Rev. Lett.* **100**, 055501 (2008).

ONE-DIMENSIONAL 3*d* ELECTRONIC BANDS OF MONATOMIC Cu CHAINS

P. H. Zhou[1], P. Moras[2], L. Ferrari[3], G. Bihlmayer[4], S. Blügel[4], C. Carbone[2]

[1] *International Center for Theoretical Physics, Trieste, Italy.*

[2] *Istituto di Struttura della Materia, Consiglio Nazionale delle Ricerche, Trieste, Italy.*

[3] *Istituto dei Sistemi Complessi, Consiglio Nazionale delle Ricerche, Roma, Italy.*

[4] *Institut für Festkörperforschung, Forschungszentrum Jülich, Germany.*

E-mail: zhouph@lsu.edu

By mean of nanoscale structuring and self-organization processes at surfaces, metallic systems can be tailored with given geometry, suitable periodicity, and large lateral coherence. In the synthesis of nanomaterials, vicinal surfaces are suitable templates for forming one-dimensional structures with a high degree of order and characteristic electronic properties of confined geometries. A number of peculiar phenomena, such as Peierls transitions, periodic lattice distortions, and charge density waves, have been observed on the *sp*-states of these one-dimensional systems. Compared with *sp*-electrons, *d*-states have wave functions more localized near the atomic core, experience a larger correlation effect, and present much smaller energy dispersions and group velocities. This imposes constraints on the degree of coherence to shorter length scales, as well as on the required sensitivity of the measurements in probing smaller bandwidths.

In an angle-resolved photoemission experiment, carried out on the VUV-beamline at Elettra [1], we examined the *3d*-bands of arrays of Cu wires, artificially constructed by self-assembling on the vicinal Pt(997) surface, which presents a regular sequence of monatomic steps and eight atom wide terraces [2]. The resulting structure can be regarded as a dense one-dimensional superlattice of one to eight atom wide Cu wires separated by narrow Pt terraces.

Figure 1 shows photoemission intensity plots as a function of the in-plane wave vector for eight chains of Cu on Pt(997), forming a full monolayer on the Pt substrate. The location of the extremal points in the band dispersion indicates that the Cu atoms are hexagonally packed with the bulk Pt-Pt interatomic distance of 2.77 Å. The *3d*-states of the monolayer display a two-dimensional character with a significant energy dispersion along and perpendicular to the direction of the substrate steps.

When the width of the Cu wires reduces the electronic structure of the system tends to acquire a one-dimensional character. Figure 2
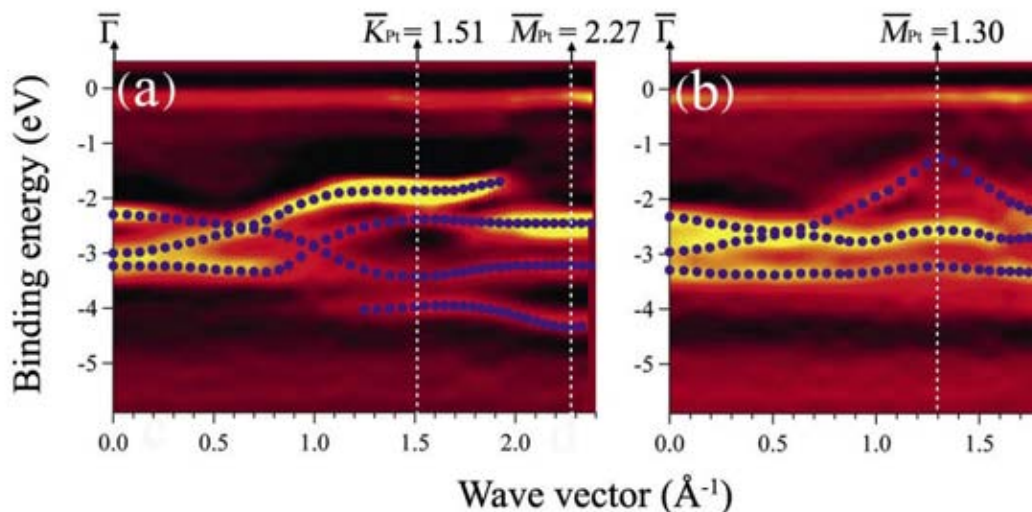
Figure 1. Photoemission intensity plot of the dispersion of eight chains on Pt(997) along the [1$\bar{1}$0] and [1$\bar{1}$2] directions of the Pt(997) substrate which correspond the directions (a) parallel to and (b) perpendicular chains directions, respectively.

shows the electronic states of monatomic Cu chains in the directions (a) along and (b) perpendicular to the chains. Along the chain directions the data exhibit two band states which display detectable dispersion. In contrast, for both bands no significant binding energy changes are observed as a function of the in-plane wave vector perpendicular to the chain axis. This qualitatively different behavior along the two directions clearly highlights the strongly anisotropic character of the *3d* electronic states in the chain array geometry.

The photoemission results are interpreted on the basis of *ab-initio* calculations of Cu monatomic chains on a Pt stepped surface, based on the full potential linearized augmented plane wave method. In figure 2 c) it can be seen that the calculated band structure compares well to the experimental bands of the Cu/Pt(997) system. Detailed analyses of band symmetry and charge density distribution indicate that the Cu *3d*-states do not significantly bind to the substrate at the center and at the boundaries of the Brillouin zone, while they weakly hybridize with Pt *5d*-states in the middle of the zone. The one-dimensional confinement of the Cu *3d* electronic states thus mainly arises from a vanishing interaction between the chains and a weak degree of electronic coupling to the metallic substrate. While the Cu *3d*-states form dispersing bands along the chain axis, because of the electron hopping due to the overlapping *d*-wave functions at neighboring sites, they do not to delocalize across the Pt terraces.

Interestingly, the band structure displays a periodicity which corresponds to the lateral arrangement of the Cu chains array. Indeed, the lateral periodicity given by the ordered sequence of decorated steps and terraces manifests itself also introducing new zone boundaries along the chain axis. In conclusion, the one-dimensional geometry of the monatomic chains results in the localization of the Cu *3d*-states, with band dispersion of one-dimensional character and periodicity defined by the specific arrangement of the superlattice.

References

[1] P. H. Zhou, P. Moras, L. Ferrari, G. Bihlmayer, S. Blügel, and C. Carbone, *Phys. Rev. Lett.* **101**, 11268 (2008).

[2] P. Gambardella, M. Blanc, H. Brune, K. Kuhnke, and K. Kern, *Phys. Rev. B* **61**, 2254 (2000).

Figure 2. Electronic band dispersion of Cu monatomic chains, (a) along and (b) perpendicular to chain direction. (c) Comparison of the experimental data with *ab initio* calculations of the band structure of monatomic Cu chains on Pt(664). Open red circles represent states with substantial charge density on Cu atoms at the step edge. Blue spheres represent data from the experimental results of Cu/Pt(997).
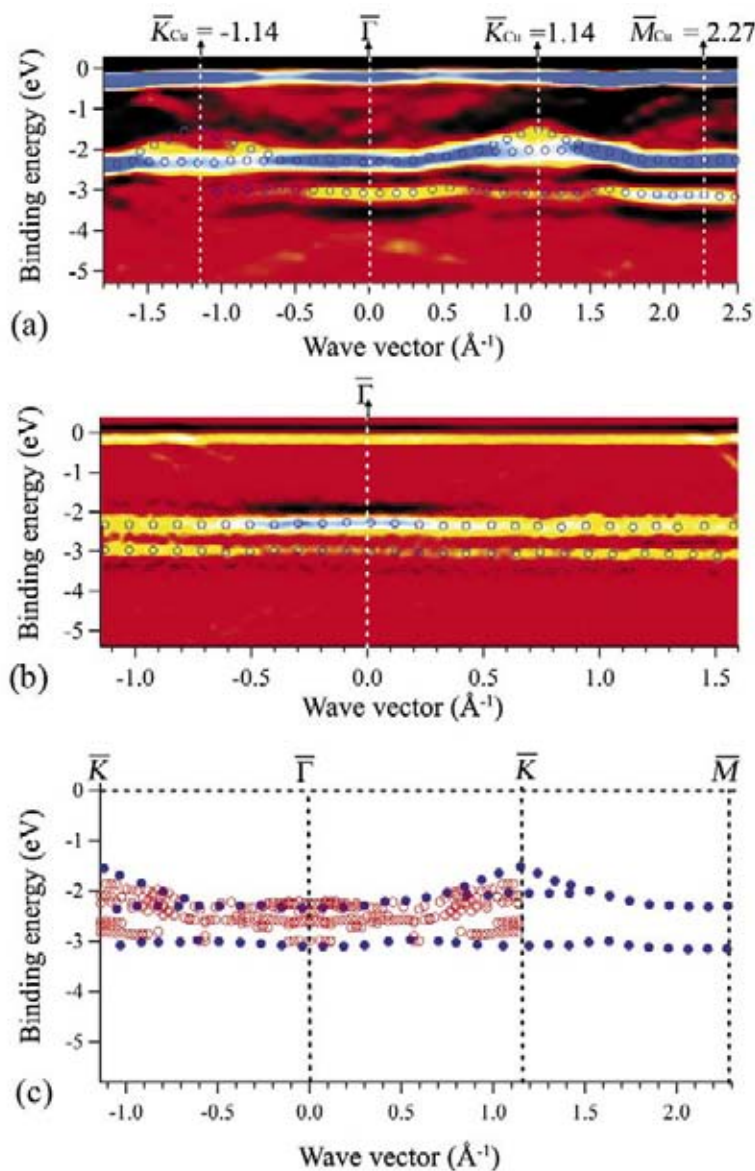
SURFACE STRESS DETERMINATION USING LOW-ENERGY ELECTRON DIFFRACTION

T.O. Menteş[1], N. Stojić[2,3], N. Binggeli[4], M.Á. Niño[1], A. Locatelli[1], L. Aballe[5], M. Kiskinova[1], E. Bauer[6]

[1] *Sincrotrone Trieste S.C.p.A., Trieste, Italy*

[2] *Scuola Internazionale Superiore di Studi Avanzati (SISSA), Trieste, Italy*

[3] *Theory@Elettra Group, INFM-CNR DEMOCRITOS, Trieste, Italy*

[4] *Abdus Salam International Centre for Theoretical Physics and INFM-CNR DEMOCRITOS National Simulation Center, Trieste, Italy*

[5] *CELLS-ALBA Synchrotron Light Facility, C3 Campus Universitat Autónoma de Barcelona, Barcelona, Spain*

[6] *Department of Physics, Arizona State University, Tempe, Arizona, USA*

E-mail: tevfik.mentes@elettra.trieste.it

The modified interactions on solid surfaces as compared to those in the bulk often result in surface stress. The surface atoms prefer to be closer together or further apart than the bulk lattice spacing, putting them under tensile or compressive stress, respectively [1].

Although the presence of surface stress is a well known phenomenon, its quantitative determination is still a challenge, both experimentally and theoretically. The most common experimental approach is based on measuring the bending of a thin sample upon adsorption of a foreign species on one side. This macroscopic effect is directly related to the change in the surface stress, but the method suffers from the averaging over the whole area. On the theoretical side, density-functional theory (DFT) calculations give reliable results for the bulk elastic parameters, while the studies of surface elasticity are complicated by the large supercells and demanding convergence criteria.

Our work shows that careful low-energy electron diffraction (LEED) measurements can give quantitative information on the surface stress [2]. The analysis is based on the lattice relaxations upon stress release at a boundary. Previously, a change in unit volume observed in small crystallites had been attributed to strain relaxation. In a similar fashion, we followed the changes in the average lattice constant in small *two-dimensional* oxygen islands on W(110), and combined the diffraction analysis with DFT calculations [2].

Oxygen adsorbed on a W(110) surface orders into a p(1×2) structure for coverages below 0.5 ML. At low coverages, the oxygen adatoms pack into islands, which grow in size with increasing coverage. At 0.5 ML, the whole surface is covered with the p(1×2)-ordered oxygen, whereas higher coverages result in structures with higher packing density.

Figure 1a displays the microspot-LEED pattern showing the two rotational p(1×2) domains (measured in a 2 micron diameter area with a single atomic step). The width of the diffraction spots gives the average island size (or domain size at higher coverage). We found that the half-order spot separations change systematically as the oxygen coverage is increased and the spots get sharper. This corresponds to a variation in the average distance between the oxygen atoms. The fractional changes in the spot separation have an inverse relation with the island size, as shown in Figure 1b. This inverse scaling is explained by a finite-length Frenkel-Kontorova chain, with the magnitude of the lattice relaxations proportional to the surface stress change across the island boundary [2]. Using calculated force constants, we obtained $\Delta\tau$ = -6.5 N/m along $[1\bar{1}0]$ as the stress difference between the oxygen covered and the clean tungsten surfaces.

For comparison, we performed DFT pseudopotential calculations using the PWSCF code. We utilized a thick symmetric slab to simulate the clean and oxygen covered tungsten surface. The structural parameters and the surface energy from our calculation showed good agreement with the data from the literature [2].

The calculated surface stress change between oxygen covered and clean W was found to be $\Delta\tau$ = -4.72 N/m, in fair agreement with the experiment despite the approximations in the experimental model. The level of this agreement is highlighted by a comparison

with the existing crystal-bending data [3], which lead to significantly lower values. We attribute the difference to the macroscopic nature of the crystal-bending measurement, which is avoided in our microspot diffraction data. Clearly the calculation does not take into account any surface defects, and a quantitative comparison is only possible with an experiment using a defect-free surface.

In addition to the surface stress values, the calculation gave further insight into our experimental observations. As seen in Figure 1c, the mismatch in the oxygen lattice along [001] scales with a higher power of the inverse island size. The calculations predict a very small stress change along the [001] direction, which is not sufficient to cause any significant lattice relaxation. However, stretching the calculation slab along [1$\bar{1}$0], a small stress is induced along [001]. This stress-strain coupling between orthogonal directions gives an explanation to the experimentally observed higher-order scaling along the [001] direction.

In conclusion, we show that, using low-energy electron diffraction, it is possible to extract quantitative information on surface stress. We expect our analysis to be of general use, beyond the specific O/W(110) adsorbate system studied here

References

[1] H. Ibach, *Surf. Sci. Rep.* **29**, 195 (1997).
[2] T. O. Menteş, N. Stojić, N. Binggeli, M. A. Niño, A. Locatelli, L. Aballe, M. Kiskinova, E. Bauer, *Phys. Rev. B* **77,** 155414 (2008).
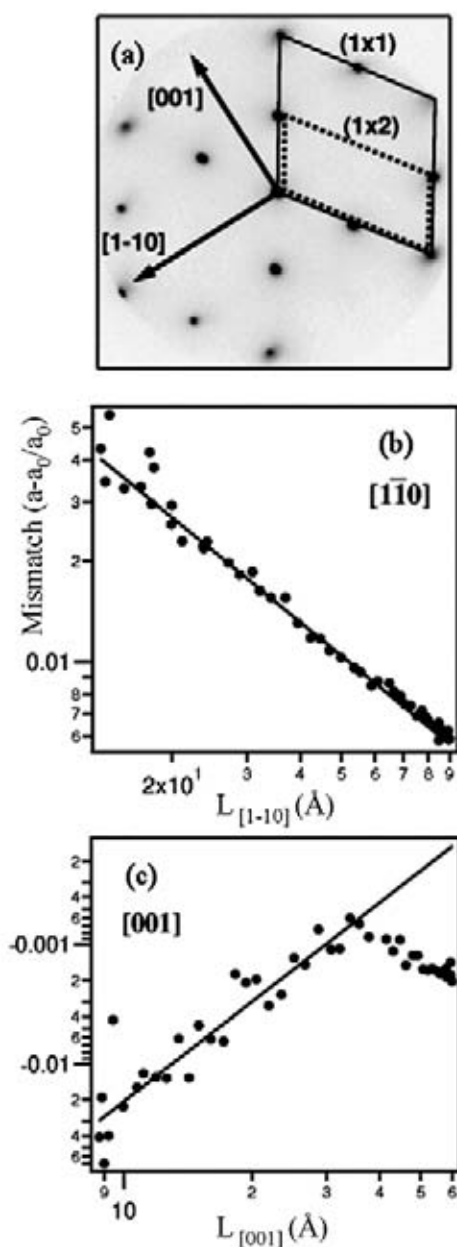[3] D. Sander, A. Enders, J. Kirschner, *Europhys. Lett.* **45**, 208 (1999).

Figure 1.
(a) LEED pattern of the p(1×2) oxygen covered surface.
(b) and (c) the evolution of the average oxygen lattice as a function of average island size along [1$\bar{1}$0] and [001], respectively.

ORDER-DISORDER TRANSITION AT THE MESOSCOPIC SCALE: Pd STRIPES ON W(110)

T.O. Menteş[1], A. Locatelli[1], L. Aballe[2], E. Bauer[3]

[1]Sincrotrone Trieste S.C.p.A., Trieste, Italy
[2]CELLS-ALBA Synchrotron Light Facility, C3 Campus Universitat Autónoma de Barcelona, Barcelona, Spain
[3]Department of Physics, Arizona State University, Tempe, Arizona, USA

E-mail: tevfik.mentes@elettra.trieste.it

Spontaneous formation of patterns is a common occurrence in nature. From the Turing patterns during chemical reactions to the wavy stripes of sand dunes, one can find a plethora of examples with almost periodic shapes and forms. In addition to their aesthetically pleasant regularity, such patterns usually appear at length scales surprisingly larger than their building blocks (like the dunes made of small sand particles). This is generally due to the interplay between opposing processes, which may extend to long distances.

Most commonly, the pattern is formed out of equilibrium, and is kept in a steady-state by a driving force (the wind for sand dunes, a thermal gradient for convection patterns, etc) [1]. On the other hand, in some cases quasi-periodic structures can be observed in thermodynamic equilibrium, that is at the minimum of the free-energy. The mesoscopic order is stabilized by competing interactions with different range of influence. Short distance interaction can be bonding (in the case of atoms and molecules) or exchange between constituents, whereas at the long-range we generally find electrostatic, dipolar or elastic type interactions.

In this study we illustrate the formation of adlayer patterns induced by the elastic interaction between adlayer steps. Surface stress had already been shown to cause a periodic ordering of atomic steps on crystal surfaces [2]. The competition, which determines the pattern period, is between the energy cost of step creation due to bond breaking, and the elastic energy gain due to stress relaxation at the step. The period depends exponentially on the interaction parameters and easily reaches mesoscopic length scales above 100 nanometers.

Using low-energy electron microscopy (LEEM), a method which allows imaging structure of surfaces with a lateral resolution of about 10 nanometers, we have observed that a small amount of palladium (less than a single atomic layer) on W(110) spontaneously orders into monolayer stripes at high temperatures [3]. A series of images of Pd stripes on W(110) at different temperatures is shown in Figure 1. The alternating bright and dark areas correspond to regions covered with a Pd monolayer and those covered with a dilute Pd lattice gas, respectively. The pattern period and the contrast sharply decrease with increasing temperature.

The variation of the period as a function of temperature is plotted in Figure 2a. We have shown in ref [3] that this variation is due to the broadening of the stripe boundaries. As the boundary gets smeared out with increasing temperature, the energy cost of step creation decreases. However, the same broadening also reduces the elastic relaxation energy, counterbalancing the influence of the boundary energy at the highest temperatures before the stripes disorder. The pattern disorders at $T_c = 1170$ K.

Figure 1.
LEEM image series of Pd stripes on W(110) surface as a function of temperature. Regions covered with the Pd monolayer are bright. Image size is 2×2 μm². Temperature increases from left to right (1100 K, 1120 K, 1130 K, 1145 K and 1160 K). The curved lines correspond to monatomic steps on the tungsten substrate.
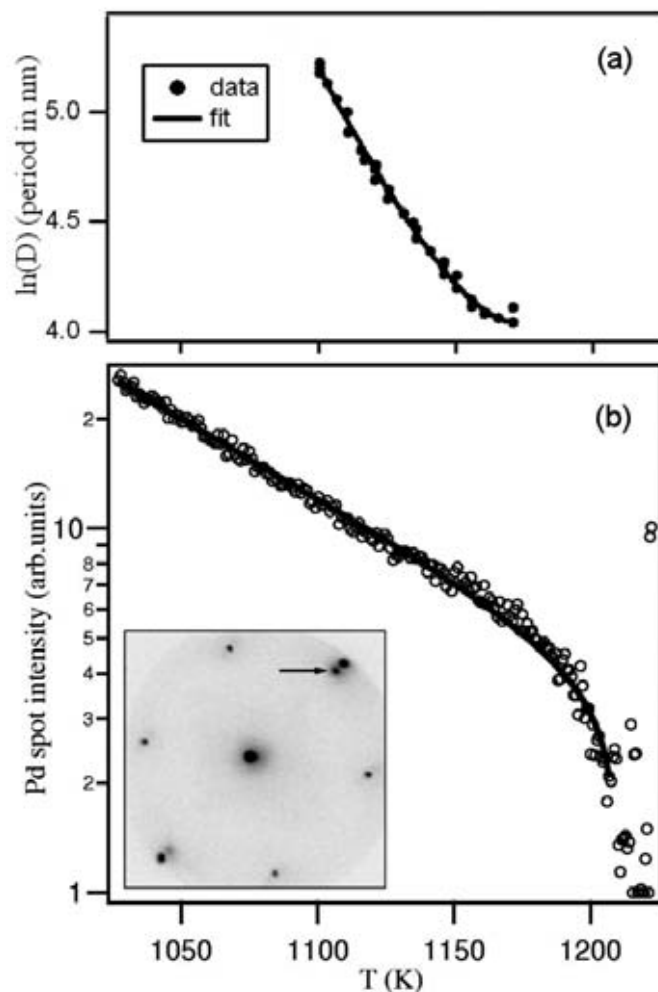
Figure 2.
The logarithm of the stripe period as a function of temperature is displayed in panel (a). Panel (b) shows the temperature dependence of the Pd low-energy electron diffraction spot intensity. The LEED pattern is seen in the inset.

We have shown that the temperature dependence of the pattern period can be described using the results from the two-dimensional Ising model [3]. As shown in Figure 2a, the variation is reproduced very well. On the other hand, the critical temperature found by fitting the stripe period, $T^0_c = 1202$ K, is considerably higher than the stripe disordering temperature T_c. This apparent discrepancy finds an explanation when we consider the order at the atomic scale. Condensed regions of Pd show a distinct diffraction spot, as marked by an arrow in the inset of Figure 2b. With increasing temperature, the intensity of the Pd spot decreases, as a consequence of Pd atoms subliming from condensed regions into the lattice gas. However, the spot is present, although increasingly weak and diffuse, all the way up to about T^0_c, as can be expected from the Ising model without long range interaction.

Our experiment is a direct confirmation that the short-range order at the atomic scale survives at temperatures higher than the disordering temperature of the mesoscopic pattern. Moreover, the difference between T_c and T^0_c depends on the ratio of the short and long range interaction parameters. These observations are relevant for order-disorder transitions in all pattern forming systems.

References

[1] M. C. Cross and P. C. Hohenberg, *Rev. Mod. Phys.* **65**, 851 (1993).
[2] O. L. Alerhand, D. Vanderbilt, R. D. Meade, and J. D. Joannopoulos, *Phys. Rev. Lett.* **61**, 1973 (1988).
[3] T. O. Menteş, A. Locatelli, L. Aballe, and E. Bauer, *Phys. Rev. Lett.* **101**, 085701 (2008).

GENERATION OF 360° DOMAIN WALLS IN MAGNETIC TUNNEL JUNCTIONS

F. Montaigne[1], M. Hehn[1], N. Rougemaille[2], S. El Moussaoui[3], F. Maccherozzi[3], R. Belkhou[3], D. Lacour[1]

[1] Laboratoire de Physique des Matériaux, Nancy-Université, CNRS, Vandœuvre lès Nancy, France
[2] Institut Néel, CNRS and Université Joseph Fourier, Grenoble, France
[3] Synchrotron SOLEIL, Gif-sur-Yvette, France

E-mail: daniel.lacour@lpm.u-nancy.fr

Magnetic tunnel junctions (MTJ) are probably one of the most studied devices in the so called spintronics research field. Their active part is composed of two ferromagnetic electrodes separated by a thin insulating layer. This layer is that thin (0,5 – 3 nm) that a tunnel current exist between the two electrodes. The tunnel conduction depends on the density of states in each electrode, and therefore for a ferromagnetic material on the spin. This leads to the most attractive property of MTJs: their electrical resistance varies strongly with the magnetic configuration of the electrodes. The resistance can vary from more than 100% between a parallel and an antiparallel alignement of the two magnetizations. The Magnetic Random Access Memories (MRAM) and the read heads of hard drive disks take benefits from this property. In the MRAM case, the parallel or antiparallel alignment of the electrodes magnetizations is used to store a bit. Measuring the MTJs resistance gives access to its magnetic configuration and consequently to the stored data bit. In the case of read heads, magnetic fields originating form the hard drive disk change the relative angle between the two electrodes magnetizations. This leads to a resistance variation directly linked to the magnetic bits stored in the hard drive. Mainly to increase storage capacity, smaller and smaller MTJs have to be realized. Size effect starts then to play an important role and can affect drastically the electrodes magnetic properties. By combining high resolution magnetic imaging at Elettra and micromagnetic simulations, we have demonstrated the strong influence of a dipolar magnetic coupling on the magnetization reversal of MTJs [1].

Understanding the domain wall formation process is crucial since it affects both the magnetic and electrical properties of MTJs. For example, when the MTJs are structured in micrometer sized elements, an antiferromagnetic coupling tends to align the magnetization of each electrode in an antiparallel configuration. This coupling originates from the magnetic stray field at the nanostructures edges (see red arrows in Figure 1). We have studied the case of MTJs patterned in ellipses. First, magnetic multilayers have been deposited by sputtering on silicon substrates. Then, by combining electron beam lithography and

Figure 1.
Schematic representation of our MTJs. The two magnetic electrodes, composed of a nickel/iron alloy and of cobalt, are respectively represented in green and purple. They are separated by 2 nm thick layer of oxidized aluminium (not represented for clarity reason). The magnetic stray field sketched in red tends to align the magnetization each electrode in an antiparallel configuration.
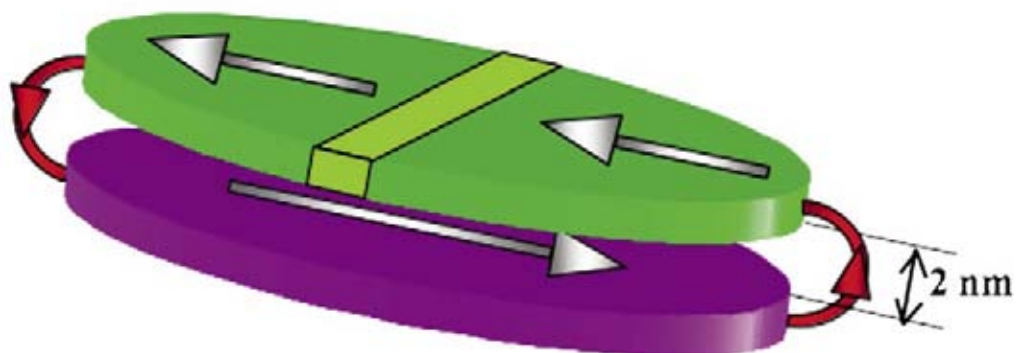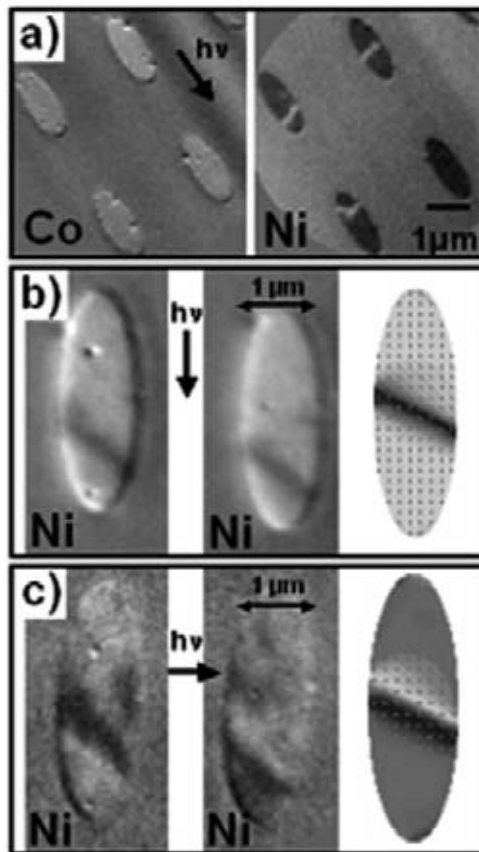
Figure 2.
(a) XMCD-PEEM images of 4 ellipses recorded at the Co and at the Ni edges. The photons incidence direction is aligned along the ellipses long axis from the top left corner. The white and black contrasts correspond to magnetization components aligned along the long ellipses axis. XMCD-PEEM images of 2 ellipses (1 μm x 3 μm) measured at the Ni edge. The grey level distribution corresponds to the scalar projection of the local magnetization with respect to the light incidence: (b) parallel and (c) perpendicular to the ellipses long axis.

dry etching, ellipses with an aspect ratio of 1:3 and lateral dimensions of 1 µm have been defined. They are composed of the following stack: Ta(5nm)/Co(4nm)/Al$_2$O$_3$(2nm)/Fe$_{20}$Ni$_{80}$(4nm)/Ru(2nm). We have used the high spatial resolution of the X-ray Photoemission Electron Microscopy (X-PEEM) combined to X-ray Magnetic Circular Dichroism (XMCD) available at the Nanospectroscopy beamline to image the magnetic configuration of our MTJs. This powerful technique allows imaging independently the magnetic configuration in each electrode, provided that the electrodes are composed of different elements. Figure 2(a) shows that, when no magnetic field is applied, both layer magnetizations are mainly in an antiparallel configuration. Moreover, if the Co layer magnetization is uniform, surprisingly this is not always the case in the NiFe layer. The (b) and (c) parts of Figure 2 present images obtained in geometries where the technique is sensitive to the magnetization component either along the ellipses long axis (b) or along the ellipses short axis (c). The combination of this imaging technique with *in-silico* modelling (right part of the Figure 2b and 2c) allows understanding the nature and the formation process of the non-uniform magnetization distribution in the NiFe layer. In this region, the magnetization rotates continuously by 360°, forming an object separating two regions of uniform magnetization. This magnetic object is called a 360° domain wall. By simulations, only one chirality is obtained for the wall, although three different cases can be observed experimentally: no wall and two chiralities (Figure 2). This difference has been attributed to local magnetic anisotropy fluctuations at the ellipses extremities, which drive the magnetization curling direction during the reversal process.

References

[1] M. Hehn *et al*., *Appl. Phys. Lett.* **92**, 072501 (2008).

SYNERGETIC EFFECTS OF THE Cu/Pt(110) SURFACE ALLOY: ENHANCED REACTIVITY OF WATER AND CARBON MONOXIDE

M. J. Gladys[1], O. R. Inderwildi[1], S. Karakatsani[1], V. Fiorin[1], G. Held[1,2]

[1] *Department of Chemistry, University of Cambridge, Cambridge, UK*
[2] *Department of Chemistry, University of Reading, Reading, UK*

E-mail: g.held@reading.ac.uk

Figure 1.
a) Adsorption geometry for (OH+H) on 0.5ML Cu/Pt{110}-(1×2).
b) Potential energy diagrams for water adsorbed onto clean Pt{110}-(1×2) (blue) and water on a Cu adatom on 0.5ML Cu/Pt{110}-(1×2) (red).

The demand for an alternative energy economy is becoming increasingly pressing. One way of replacing fossil fuels is through fuel cell technology which requires efficient methanol or hydrogen production on an industrial scale. In these processes the water-gas shift (WGS) reaction, $CO + H_2O \rightarrow H_2 + CO_2$, is an essential reaction step, for which typically binary alloy catalysts are used. Adding a second metal to a catalyst surface either provides the opportunity for several reactions to occur in parallel, each catalysed by a different surface constituent individually, or generates synergetic characteristics beyond either of the individual constituents. In this context, copper is a promising material, whose catalytic potential was appreciated very early and has since been studied extensively. Pure Cu is used in hydrocarbon synthesis reactions, such as methanol production, however due to its low melting temperature it is susceptible to sintering and therefore rarely used in other industrial processes [1]. It is used, however, as additive to other catalytically active metals, e.g. providing protection from coking (carbon deposits) during reactions [1,2].

We have studied the adsorption characteristics and reactivity of the WGS reactants, water and CO, on the bimetallic Cu/Pt{110} surface using high resolution X-ray photoelectron spectroscopy in combination with *ab initio* model calculations [3]. The clean Pt{110} surface has a (1×2) "missing row reconstruction" (every second row of surface atoms is missing) and is known for its high catalytic activity [4]; when covered with 0.5 ML Cu, the copper atoms fill the troughs of the missing rows and form nanowires (Figure 1a), which are stable up to 830K. This has dramatic consequences for the reactivity of this surface. While water adsorbs intact on clean Pt{110}, the bimetallic 0.5ML Cu/Pt{110}-(1×2) surface induces partial dissociation at temperatures above 170K, as can be seen by the appearance of a second peak in the O1s photoelectron spectrum (Figure 2a). *Ab initio* calculations show that water dissociation occurs via the Cu surface atoms. When the molecules adsorb on top of Cu atoms the dissociation barrier is only 0.53eV, low enough for dissociation at 170K into a mixed OH+H layer as shown in Figure 1a. The

a)

b)
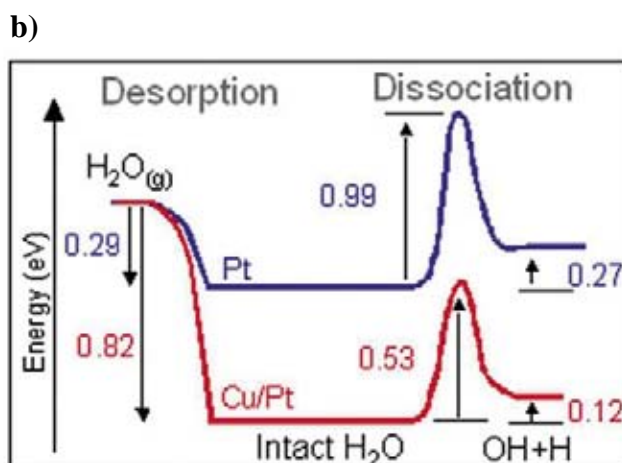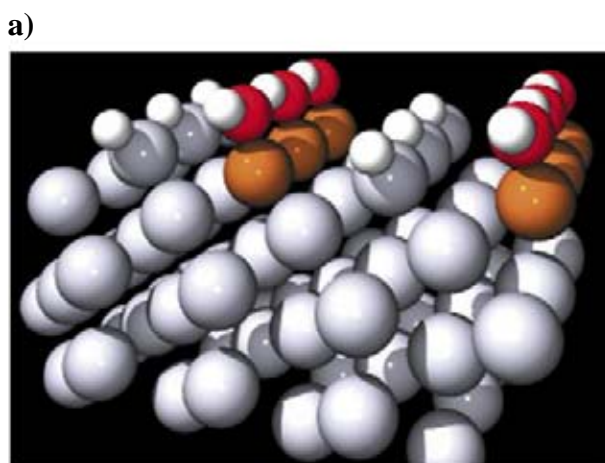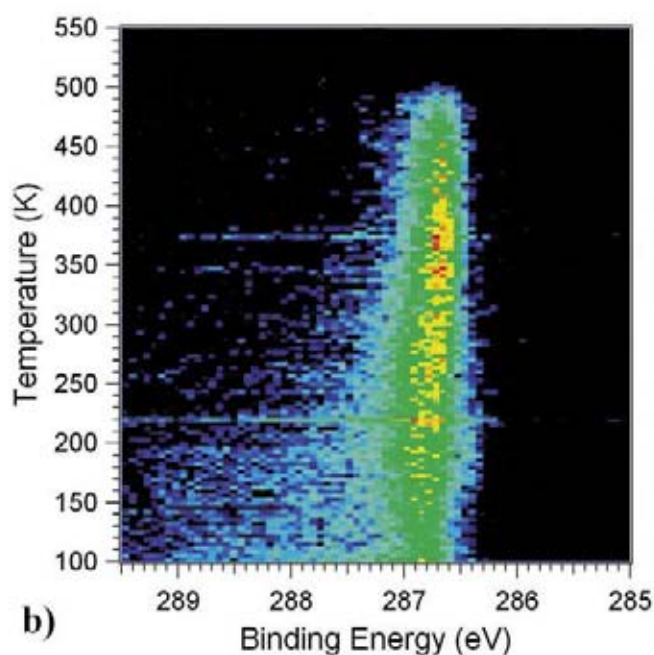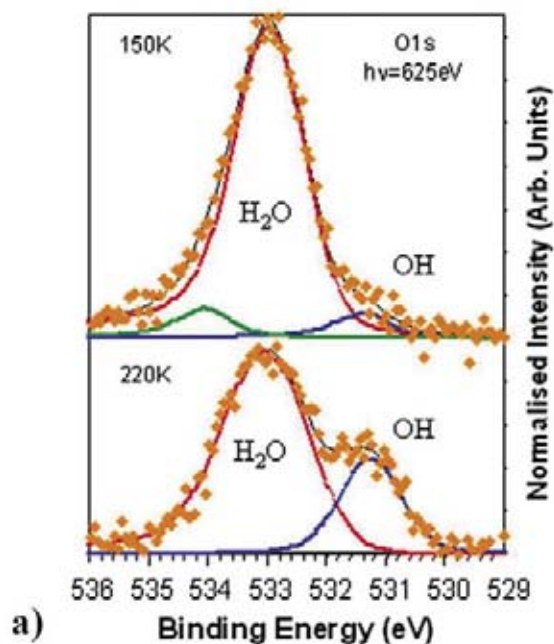
potential energy diagrams (Figure 1b) for this reaction clearly show that the barrier is lower and the adsorption energy of the dissociated layer is higher for the bimetallic surface. The OH molecules stay near the Cu atoms and block the adsorption of further water, thus dissociation will stop as soon as all Cu atoms are covered. This explains why the experimental results indicate that dissociation terminates already when half the Cu atoms are covered by OH. Hydrogen bonds with intact water molecules will additionally stabilise the OH molecules.

CO does not dissociate on this surface but the adsorption energy is enhanced with respect to, both Pt and Cu{110} surfaces. Figure 2b represents a series of temperature programmed (TP) C1s spectra (100K–550K) after CO was adsorbed on the 0.5ML Cu/Pt{110} surface at 100K. Up to about 300K, we observe satellite structure in the low binding energy range (287-289eV), which is typical for CO bonding to Cu surface atoms. The C1s signal at higher temperatures (peak at 286.7eV) is typical for adsorption on Pt atoms and very similar to CO on clean Pt{110}, however, the maximum desorption temperature is 30K higher. Our *ab initio* calculations in combination with the experimental valence band spectra reveal that the Cu 3d-band is narrowed and shifted upwards with respect to the Cu{110}. This causes electron donation from the Cu to the Pt surface atoms and explains the observed increase in the CO-Pt bond strength.

Our study shows that this bimetallic Cu/Pt surface has superior catalytic activity for water activation as compared to pure Cu and Pt, however, CO poisoning is still a potential problem. The high effective diffusion barrier for Cu atoms would allow high working temperatures for this system, which is an advantage over pure Cu catalysts currently in use.

References

[1] J. Sinfelt, *Bimetallic Catalysis*; Wiley, New York, 1983.
[2] J. A. Rodriguez, *Surf. Sci. Rep.* **24**, 223 (1996).
[3] M. J. Gladys, *et al.*, *J. Phys. Chem. C* **112**, 6422 (2008).
[4] G. Ertl, *Surf. Sci.* **299/300**, 742 (1994) and references therein.

Figure 2.
a) O1s XPS signal after water was dosed on the 0.4ML Cu/Pt{110} surface at 150K (top, essentially intact water layer with a small X-ray induced OH signal) and 220K (bottom, two well resolved peaks assigned to H_2O, red, and OH, blue); b) TP-XPS C1s spectra (peak intensity vs binding energy and sample temperature; 100K–550K; 0.1K/s; 5K/spectrum) of CO adsorbed on the 0.5ML Cu/Pt{110}-(1×2) at 5×10^{-9} mbar for 300s at 100K.

INVESTIGATION OF NO$_x$ STORAGE PROCESSES ON BARIUM OXIDE BASED SINGLE-CRYSTAL MODEL CATALYSTS

T. Staudt[1], A. Desikusumastuti[1], M. Happel[1], J. Libuda[1], E. Vesselli[2], A. Baraldi[2], S. Gardonio[3], S. Lizzit[3], F. Rohr[4]

[1] Lehrstuhl für Physikalische Chemie II, Friedrich-Alexander-Universität Erlangen-Nürnberg, Erlangen, Germany
[2] Physics Department and Center of Excellence for Nanostructured Materials, Trieste University, Trieste, Italy,
 and Laboratorio Nazionale TASC, INFM-CNR, Trieste, Italy
[3] Sincrotrone Trieste S.C.p.A., Trieste, Italy
[4] Umicore AG & Co. KG, Hanau-Wolfgang, Germany

E-mail: libuda@chemie.uni-erlangen.de

An improved level of understanding and manipulation of the structural and chemical properties of catalytically active surfaces at the microscopic level may open up novel routes towards a rational improvement of heterogeneous catalysts [1]. In particular, the integration of storage functionalities into catalytic materials represents an intriguing and versatile tool to improve the selectivity and activity of heterogeneous catalysts under non-stationary reaction conditions. A prominent example in the field of exhaust gas aftertreatment in lean-burn engines, is the NO$_x$ storage and reduction (NSR) catalyst, where barium based materials represent the key storage component [2].

Lean-burn engines, i.e. combustion engines operating under air-rich conditions, provide the advantage of substantially higher fuel and CO$_2$ efficiency. However they give rise to the emission of toxic gases, in particular NO$_x$. The NSR concept circumvents the problem by converting the NO$_x$ to nitrates and storing them as Ba(NO$_3$)$_2$ during lean operation. During fuel-rich operations, the nitrate decomposes and is reduced to nitrogen. Due to the complexity of the catalytic systems, the underlying surface chemistry, however, remains poorly understood at the microscopic level; a typical problem which is commonly denoted as the "material gap between heterogeneous catalysis and surface science". The development of model systems with increasing degree of complexity represents one possible strategy to bridge this gap. The use of single crystal based model catalysts provides the possibility to apply the full spectrum of surface science experimental methods, and, thus, to obtain a detailed understanding of the underlying processes that control reactivity and microkinetics.

In order to model NO$_x$ storage materials, single-crystal-based model catalysts are prepared by deposition of barium and subsequent oxidation on ordered Al$_2$O$_3$ films (prepared on a NiAl(110) surface). The size of the particle can be controlled over a large range via the amount of Ba deposited. Accordingly, two different experimental situations were selected in the present study, corresponding to smaller and larger Nanoparticles (see [3] for details).

Using the high-resolution photoelectron spectroscopy (HR-PES) capabilities at the Elettra SuperESCA beamline, the first synchrotron radiation based investigation of a NSR model system was performed. The composition of the model catalysts, the interaction between the catalytically active barium oxide particles and the support and their reactivity and storage capability during interaction with NO$_2$ was analysed.

On the pure alumina support, exposure to NO$_2$ at room temperature, leads to slow formation of surface nitrite species, accompanied by further oxidation of the support and an increasing thickness of the Al$_2$O$_3$ film. At large exposures, two very slow processes occur, the formation of a small amount of surface nitrates and the decomposition to aluminum oxynitrides (for details see [4]).

During preparation of the nanoparticles, intermixing of Ba^{2+} and Al^{3+} ions occurs, yielding to the formation of mixed oxide aluminate-like particles (BaAl$_{2x}$O$_{1+3x}$), even at 300 K. This process is accompanied by a continuous increase of the aluminum oxide film thickness. Whereas intermixing is nearly complete for small particles at room temperature, there are kinetic limitations towards aluminate formation for larger particles. These, however, can be overcome by annealing the model catalyst in O$_2$. The for-

Figure 1. Sequence of photoelectron spectra of the Al 2p, Ba 4d and N 1s region for smaller (A) and larger particles (B). For Al 2p, the black lines indicated the pristine Al_2O_3 film, the spectra shown in blue were taken after barium deposition and spectra in red were acquired after subsequent annealing to 800 K in O_2. The thin dotted lines show a fit for the clean Al_2O_3/NiAl(110) sample, indicating the different components comprising the Al 2p signal. Two STM images are shown in the insets for both sample after annealing to 800 K in O_2 (150 nm^2, U = 2.7 V, I = 0.17 nA). The N 1s spectra (right) were measured after stepwise exposure to NO_2 at 300 K. The insets show the intensity of the features as a function of NO_2 exposure.
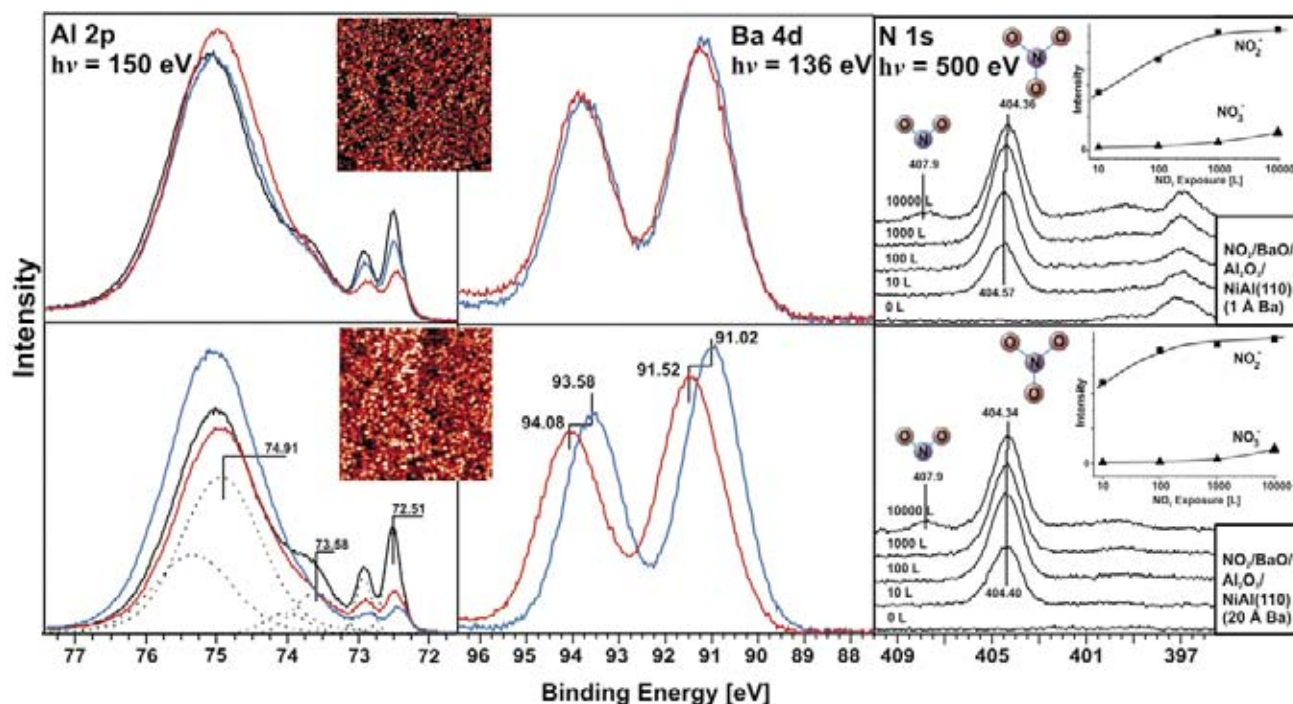
mation of mixed Ba-Al oxides, eventually resulting in the formation of barium aluminates, is well known from NSR powder catalysts, but was not yet proven directly for model catalysts. The present results provide direct evidence for the facile formation of mixed oxide particles, displayed in Figure 1 [4].

Upon exposure of the mixed oxide particles to NO_2, the formation of surface nitrites occurs, at a notably higher rate than for the pristine Al_2O_3 film (Figure 1, right). Surface nitrate formation completely saturates at NO_2 exposures around 1000 L for both types of particles (see inset in Figure 1 right). Afterwards, surface nitrates are generated, suggesting transformation of nitrites to nitrates. During the interaction with NO_2, further oxidation of the support occurs, leading to an increasing thickness of the $BaAl_{2x}O_{1+3x}$ particles and/or the Al_2O_3 film.

In summary, the results underline the great potential of synchrotron radiation based HR-PES measurements on complex model catalysts. In the present case, the investigations shown that numerous elementary processes on NSR systems can be reproduced on thin-film based model NSR catalysts in an ideal UHV environment.

References

[1] G. Ertl, H. Knoezinger, J. Weitkamp (eds), *"Handbook of heterogeneous catalysis"*, VCH: Weinheim (1997) and references therein.

[2] N. Takahashi *et al.*, *Catal. Today* **27**, 63 (1996).

[3] A. Desikusumastuti *et al.*, *Catal. Lett.* **121**, 311 (2008).

[4] T. Staudt *et al.*, *J. Phys. Chem. C* **112**, 9835 (2008).

ELECTROCHEMICAL OXIDATION OF C_{60} AND GROWTH OF p- AND n-DOPABLE FULLERENE FILMS

C. Bruno[1], M. Marcaccio[1], D. Paolucci[1], C. Castellarin-Cudia[2], A. Goldoni[2], A. V. Streletskii[3], T. Drewello[3], S. Barison[4], A. Venturini[5], F. Zerbetto[1], F. Paolucci[1]

[1]INSTM Sezione di Bologna, Dipartimento di Chimica "G. Ciamician", Università di Bologna, Italy
[2]Sincrotrone Trieste S.C.p.A., Trieste, Italy
[3]Department of Chemistry, University of Warwick, Coventry, England
[4]IENI – CNR, Padova, Italy
[5]ISOF – CNR, Bologna, Italy

E-mail: francesco.paolucci@unibo.it

The facile reduction of fullerenes, exemplified by the electrochemical stepwise reversible addition of up to six electrons to C_{60} and C_{70} [1], contrasts with their difficult oxidation [2]. We recently succeeded in obtaining the cyclic voltammetric reversible generation of C_{60}^{2+} and C_{60}^{3+} [3]. This was allowed by the adoption of ultra-dry solvents and electrolytes with very high oxidation resistance and low nucleophilicity which ultimately led to the serendipitous discovery that C_{60} may be oxidatively electropolymerized [4] thus forming stable conducting polymeric films able to transport both holes and electrons, a feature that is not possessed by many organic systems.

Figure 1A shows multi-scan cyclic voltammetric (CV) curves of a dichloromethane solution of C_{60} run between 0 and 2.20 V, i.e. corresponding to the generation of C_{60}^{2+} [3]. The curves show the appearance of new peaks and an overall progressive current increase due to the formation of a redox-active deposit on the electrode. The electrochemical response is strongly reminiscent of that observed in textbook examples of conducting polymers.

Despite of the formation of a thick film ($\geq$ 500 nm) on the electrode, the CV curves shown in Figure 1A are still largely dominated by the diffusion-controlled voltammetric peaks typical of pristine C_{60} in solution. The voltammetric response of the film changes significantly in a blank electrolyte solution (Figure 1B): while the peaks due to C_{60} in solution are no longer observed, the curve displays a reversible behavior that comprises very broad reversible peaks located in the same potential regions where pristine C_{60} undergoes either oxidation or reduction. The film retains the electroactive properties of the pristine fullerene, with significant differences that may be attributed to the formation of a bonded structure where charge may be injected and transported. This is inferred from the observation that the CV peaks of pristine C_{60} in Figure 1A are only slightly affected by the presence of the film except for a large increase in intensity, in turn associated to an increase of the electroactive surface area. The separation between forward and reverse peaks has not greatly increased even in the presence of thick films

Figure 1.
(A) Cyclic voltammetric curves of a 0.15 mM solution of C_{60} in dichloromethane; the solution is 0.05 M in (TBA)AsF$_6$. Scan rate: 1.0 V. The multi-scan cyclic voltammetric curves show progressive film growth.
(B) Cyclic voltammetric curves (1st and 50th cycles) of a film-modified Pt electrode in a 0.05 M blank (TBA)AsF$_6$ dichloromethane solution. The film displays both cathodic and anodic behaviour (highly reproducible over repetitive cycling). Scan rates: 0.4 V/s. T = 298 K.
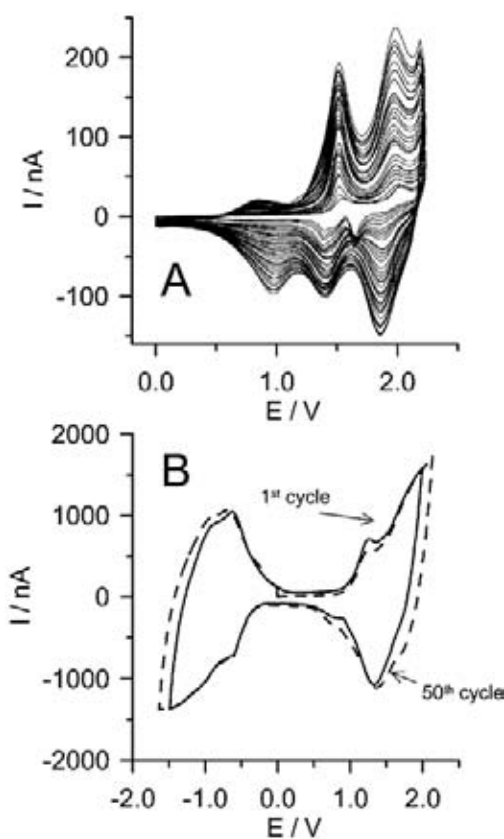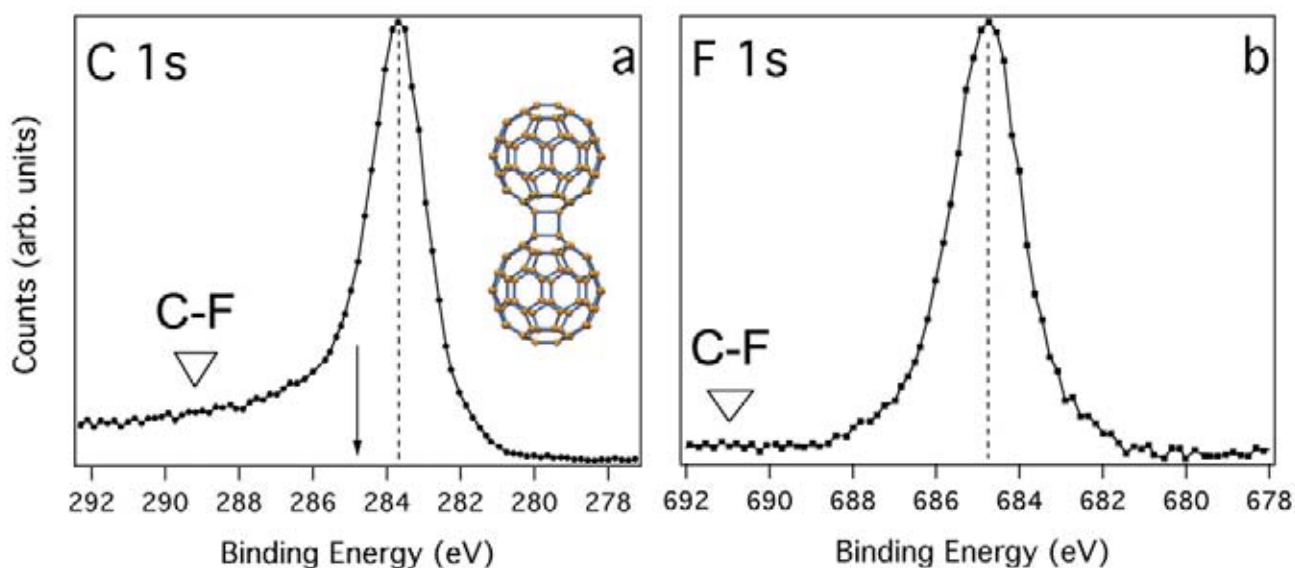
thus suggesting that the film resistivity is negligible. Quantum chemical calculations at B3LYP/6-31G* level suggest that sp^3 carbon centers form at the site of polymerization, thus preventing the formation of a fully conjugated structure. Charge transport should occur in the polymer via a hopping mechanism.

Physical-chemical characterizations of the film were carried out with atomic force microscopy, Raman, infrared and X-ray-photoelectron (XPS) spectroscopies, secondary ion mass spectrometry (SIMS), scanning electron microscopy, energy-dispersive X-ray analysis (EDX) and matrix-assisted laser desorption/ionization [4]. For example, figure 2a shows the C 1s measured with XPS. Compared to pristine C_{60} films, the shift and lineshape of the measured C 1s peak is consistent with the formation of a conducting polymer. Importantly, XPS measurements evidenced that there is no reaction between the counter-ions and C_{60}. The addition of F atoms from AsF_6^- onto the fullerene cage was in fact a possible drawback of the present anodic electropolymerization route. Fingerprints of the C-F bonds are expected at higher energy than the observed binding energies. The F 1s binding energy (Figure 2b) and the atomic ratio F:As ~ 6 are consistent with the presence of supporting electrolyte $(TBA)AsF_6$ entrapped into the polymer. This was also confirmed by EDX and SIMS.

The neutral films exposed to air and solvents showed a remarkable stability and did not undergo any significant degradation under electrochemical oxidation or reduction conditions, provided that highly aprotic and non-nucleophilic conditions were used. Finally,

Riccò *et al.* prepared solid-state $C_{60}(AsF_6)_2$ and using powder X-rays diffraction, they showed that C_{60} molecules develop interconnections *via* coupled intermolecular bonds (2+2 cycloaddition) forming 1D chains with zigzag arrangements.

References

[1] Q. Xie *et al.*, *J. Am. Chem. Soc.* **114**, 3977 (1992); Y. Oshawa *et al*, *J. Chem. Soc., Chem. Commun.* 781 (1992).
[2] Q. Xie *et al.*, *J. Am. Chem. Soc.* **115**, 9818 (1993).
[3] C. Bruno *et al.*, *J. Am. Chem. Soc.* **125**, 15738 (2003).
[4] C. Bruno *et al.*, *J. Am. Chem. Soc.* **130**, 3788 (2008).

Figure 2.
XPS of the C 1s (a) and F 1s (b) core levels. A possible structure of polymeric double linked $(C_{60})_2^{2+}$ is shown. The arrow indicates the binding energy of undoped non-polymeric C_{60} films. The energy where the peak corresponding to C-F bond should be expected is shown with a triangle.
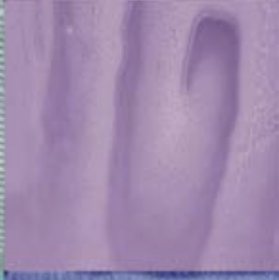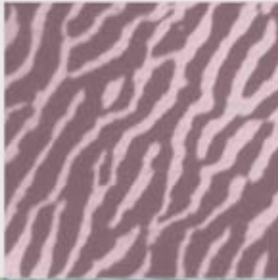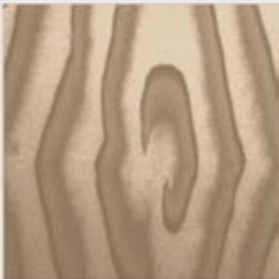
MATERIALS SCIENCE

Condensed matter science over the last several decades has been driven mainly by the discovery of new materials exhibiting exotic properties. Starting from the end-seventies, one can recall the discoveries of "valence fluctuation" phenomenon, heavy fermions, quasi-crystals, high temperature cuprate superconductors, fullerenes, carbon nanotubes, other exotic superconductors, inorganic nanomaterials, colossal magnetoresistive materials, and graphene, to name just a few.

Materials Physics and Chemistry are now accepted, distinct and one of the most vibrant sub-branches of science where the study of such materials and their properties have led us to many largely unexplored and little understood frontiers of science. This necessitated, as well as was helped along by, tremendous progress both in terms of experimental and theoretical tools over these decades. Therefore, it is not surprising to find that activities within Elettra reflect this global trend, with about one third of over 200 publications listed in the Elettra data base for 2007 can be classified as materials science research. Reflecting the wide spectrum of investigations under the broad banner of materials science, Elettra-based research covered areas ranging from magnetism to electronic properties, from atomic structure to bulk structures via the mesoscopic scale, from fundamentally important issues to issues with great technological implications. In keeping with the technological innovations that have given rise to increasingly sophisticated experimental possibilities, Elettra has responded to this ever-increasing challenge by designing and commissioning new and sophisticated beamlines to probe novel properties of matter, while continuously upgrading several of the older beamlines to keep their competitive edge. In this context, it is worthwhile to note that materials science, more than any other single discipline, requires the most diverse range of techniques to elucidate the complex range of properties of matter it deals with; for example, a reasonable understanding of a single system may require addressing its electronic and magnetic properties, its long-range geometric structure as well as its local structure (that may be distinctly different from the global structure), shape and ordering (when probing finite size systems), etc. Therefore, it does not come as a surprise that materials science research at Elettra accesses the widest range of beamlines, totaling more than a third of the beamlines here, including photon scattering, absorption and photoemission techniques with photon energies varying from a few meV to several keV.

While it is difficult to select a "representative" set of examples for such a wide range of activities and applications of Elettra facilities to investigate materials science, in the following, a limited set of investigations is highlighted to give a glimpse of the diversity of issues addressed and techniques employed.

Dipankar Das Sarma

Educated at IIT Kanpur for MSc Physics in 1977 and at IISc Bangalore for PhD degree in 1982, Dipankar Das Sarma is author of more than 300 research publications with an H-index of 41 and over 6000 citations. Fellow of all three major Academies in India and also a Fellow of the American Physical Society and of TWAS. Recipient of most major awards and recognitions within India and several international prizes. Adjunct or Visiting Professor at several important institutions. Member of the Editorial Board or Advisory Board of about 8 scientific journals in Physics and Chemistry. Presently, MLS Chair Professor of Physics and Chairman, Centre for Advanced Materials at Indian Association for the Cultivation of Science. Member of several national and international committees, including Chairman, Proposal Review Committee at Elettra.

BURNING MATCH OXIDATION PROCESS ON CHIRAL SILICON NANOWIRES

P. De Padova[1], C. Quaresima[1], P. Perfetti[1], B. Olivieri[2], C. Leandri[3], B. Aufray[3], S. Vizzini[3], H. Oughaddou[4], G. Le Lay[3]

[1] CNR-ISM, Roma, Italy

[2] CNR-ISAC, Roma, Italy

[3] CRMCN-CNRS, Marseille, France

[4] Commissariat à l'energie Atomique, Laboratoire SIMA, DSM-IRAMIS-SPCSI, Gif sur Yvette, France, and Département de
 Physique, Université de Cergy Pontoise, France

E-mail: paola.depadova@ism.cnr.it

Silicon nanowires (SiNWs) are one of the most stimulating structures in nanoscience due to the central function played by Si in the world of semiconductor industry and in the fundamental physics. The high resolution (HR) photoemission spectroscopy (PES) experiments on self-aligned straight SiNWs on the silver (110) surface were carried out at the VUV beam line of ELETTRA in Trieste, whereas the STM and STS observations of the SiNWs were performed at the CINaM in Marseille [1,2].

Figure 1a displays HR Si $2p$ PES spectrum measured at $\vartheta_{e-}=0°$ of 0.5 ML Si deposited on Ag(110) surface at room temperature (RT). This peak is composed of four (spin-orbit splitted) components S_1, S_2, S_3 and S_4 attributed to different Si atoms located at the SiNWs. The spectrum is completely dominated by the S_2 component. Its full width at half maximum (FWHM) is 130 meV, which is the narrowest Si $2p$ line shape ever reported in a solid phase photoemission experiment. Another important result arises from the fit of the Si $2p$ spectra, which imposes two significantly different values of the Lorentzian FWHMs $\Gamma_{1/2} = 40$ meV and $\Gamma_{3/2} = 25$ meV respectively for the Si $2p_{1/2}$ and Si $2p_{3/2}$ lines, which have a common Gaussian FWHM of just 95 meV. The evidence of the extra broadening of the $2p_{1/2}$ Lorentzian FWHM points to a non-radiative Coster-Kronig Auger LLV transition, forbidden in semiconducting Si (Si gap: 1.12 eV), but allowed in a metallic state.

Figure 1b shows a 10.2 x 10.2 nm^2 filled-states STM image of 0.5 ML Si/Ag(110) deposited at RT. The $x2$ periodicity of the SiNWs parallel to the Ag direction and a misalignment

Figure 1.
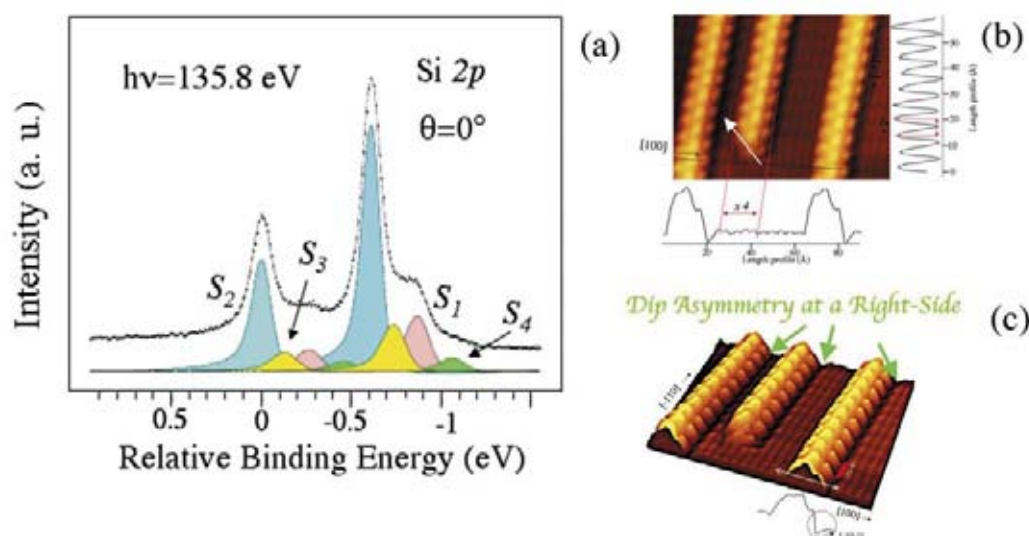(a) Normal emission convoluted Si $2p$ core level for SiNWs after the deposition of 0.5 ML of Si on Ag(110). (b) 10.2x10.2 nm^2 filled-states STM image. (c) 3D view of 10.2x10.2 nm^2 filled-states STM image: dip asymmetry at right-side.
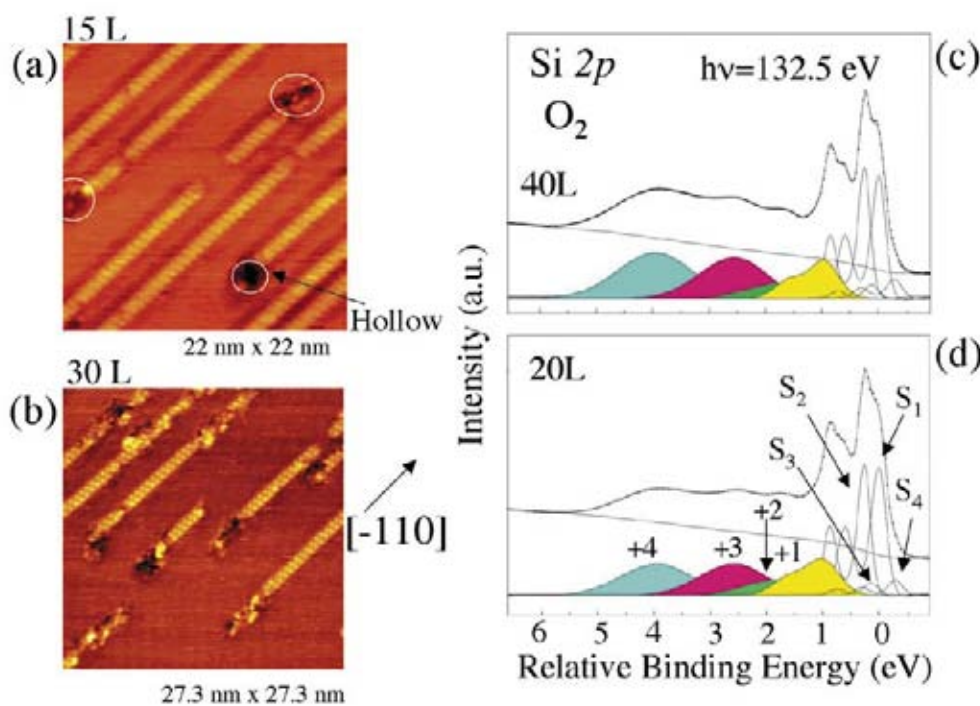
Figure 2.
Filled-states STM images of Si NWs on Ag(110) at different oxygen doses: (a) 22 x 22 nm² at 15 *L*. (b) 27.3x27.3 nm² at 30 *L*. Convoluted Si *2p* core levels of SiNWs grown on Ag(110) and exposed to O₂ at: (c) 20 *L* and (d) 40 L.

between the right and left side protrusions corresponding to a glide of one $a_{Ag[-110]}$ lattice parameter are evidenced. The line profile along the [100] direction assigns a lateral size of ~ 1.6 nm for every single SiNW, i.e. an *x4* width of $4a_{Ag[100]}$, while the height is about 0.2 nm. The nanostructures are never terminated along the [100] Ag direction, but along the [3-34] direction of the Ag(110) surface. This fact confers to NWs an asymmetric morphology with respect to the plane perpendicular to the (110) surface. The asymmetric transverse shape of the SiNWs is evidenced by the 3D view reported in Figure 1c of the previous STM image, where a dip is clearly noticeable on the right side of each NW. On other extended areas there is the reverse situation where the dip is always situated on their left side and the nanostructures are terminated along the [-334] direction. Hence the two types of symmetry breaking NWs phase separate in large "magnetic-like" domains of opposite "spin" to recover the overall mirror symmetry of the bare surface.

Figures 2a and 2b display a 22 x 22 nm² and 27.3 x 27.3 nm² filled-states STM images of 0.5 ML Si deposited at RT on the Ag(110) surface exposed to a 15 *L* and 30 *L* doses of O₂. The termination-sides of the clean Si NWs are drastically modified, showing apparently some black voids or hollows (circled images in Figure 2a that announce the onset of the oxidation process. These termination-sides are involved at first in the oxidation process, whereas the almost totality of the Si NWs is

not affected by the O₂ atoms. At higher oxygen exposure, the oxidation of the Si NWs proceeds progressively from their extremities along the [–110] direction maintaining an atomic structure preferably developed along the one-dimension of the wires. This is clearly observed in the Figure 2b at 30 *L* and at higher oxygen exposure. The oxidation behaves according to a *match–burning* process, where the extremities of the Si NWs are considered as the head of a match, which reacts with oxygen.

These characteristic features discovered through the HR STM observations of the oxidized Si NWs find their corresponding signatures in spectroscopy measurements. Figures 2c and 2d report the Si *2p* core-level spectra measured on the Si NWs, after 20 and 40 *L* of O₂ exposure. The virgin part of the Si NWs on Ag(110) reveals the four doublets, S_1, S_2, S_3 and S_4, and the oxidized part at higher binding energy further four new peaks S^{1+}, S^{2+}, S^{3+} and S^{4+} assigned to the +1, +2, +3 and +4 oxidation states of Si.

References

[1] P. De Padova, C. Quaresima, P. Perfetti, B. Olivieri, C. Leandri, B. Aufray, S. Vizzini, G. Le Lay, *Nano Lett.* **8**, 271 (2008).

[2] P. De Padova, C. Leandri, S. Vizzini, C. Quaresima, P. Perfetti, B. Olivieri, H. Oughaddou, B. Aufray and G. Le Lay, *Nano Lett.* **8**, 2299 (2008).

SURFACE SCIENCE APPROACH TO UNDIVIDUAL QUASI-1D NANOSTRUCTURES: SPEM, X-PEEM, LEEM AND LEED ON SnO$_2$ NANOSTRUCTURES

A. Kolmakov[1], S. Potluri[1], T. O. Mentes[2], M. A. Nino[2], A. Locatelli[2], A. Barinov[2], L. Gregoratti[2], M. Kiskinova[2]

[1] Southern Illinois University at Carbondale, Illinois 62901-4401, USA
[2] Sincrotrone Trieste S.C.p.A., Trieste, Italy

E-mail: akolmakov@physics.siu.edu

Figure 1.
(a) LEEM image (FOV 20 µm) and the micro-LEED pattern, corresponding to the (010) facet of the nanostructure
(b) XANES spectrum (violet) taken from individual SnO$_2$ nanowire, which contains features characteristic for the SnO (yellow) and SnO$_2$ (blue) compounds. The energy scale is offset with respect to the first maximum of Sn 3d$_{5/2}$.

Metal oxide quasi one-dimensional nano-structures such as wires, belts rods and tubes are in the focus of intense research due to their unique potential for applications in the nano-(opto)electronics, chemical sensing and catalysis [1,2]. Due to the high surface-to-bulk aspect ratio of these materials, the surface structural and electronic properties play a dominant role, which has motivated the current rapidly growing communities exploring the modification of these properties by varying the size, defects density, doping level etc. In this respect surface sensitive electron spectroscopies are among the most appropriate methods, but they needed to step into microscopic world in order to probe *individual* nanostructures. Thanks to the ultra-bright and tunable photon beams provided by the synchrotron facilities the Scanning PhotoElectron Microscopy (SPEM) and X-ray Photoelectron Emission Microscopy (XPEEM) have become amenable with the size domain of the nano-structures (10-100 nm) [3,4].

Using the SPEM and XPEEM instruments at Elettra in combination with structural sensitive Low Energy Electron Microscopy (LEEM) we explored the surface structure and chemical states of individual SnO$_2$ nano-wires and nanobelts [4]. Figure 1a shows the LEEM image of a SnO$_2$ nanobelt and the micro-LEED pattern, which manifests the (010) structure of side facets comparable to the ones observed for SnO$_2$ rutile crystals. Figure 1b shows the XANES spectrum (violet) of the SnO$_2$ nanobelt, which contains overlapping features of SnO$_2$ and SnO phases, indicative for certain degree of oxygen deficiency. This was confirmed by Sn 3d and O 1s spectra measured on individual nanobelts with SPEM [4]. We also demonstrated the possibility to use SPEM for probing electron transport properties by imaging in-situ the
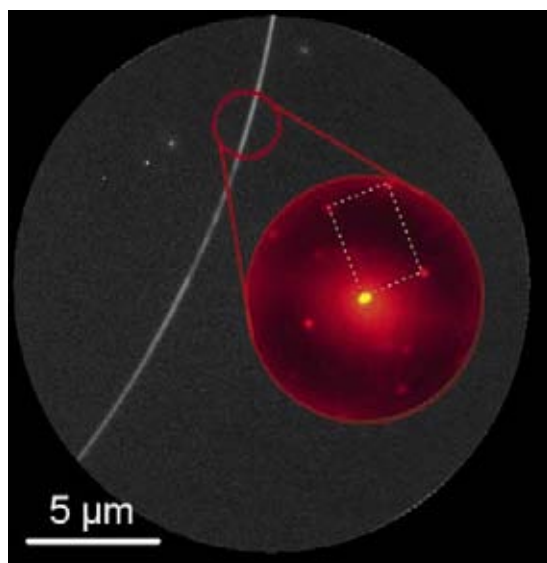
(a)
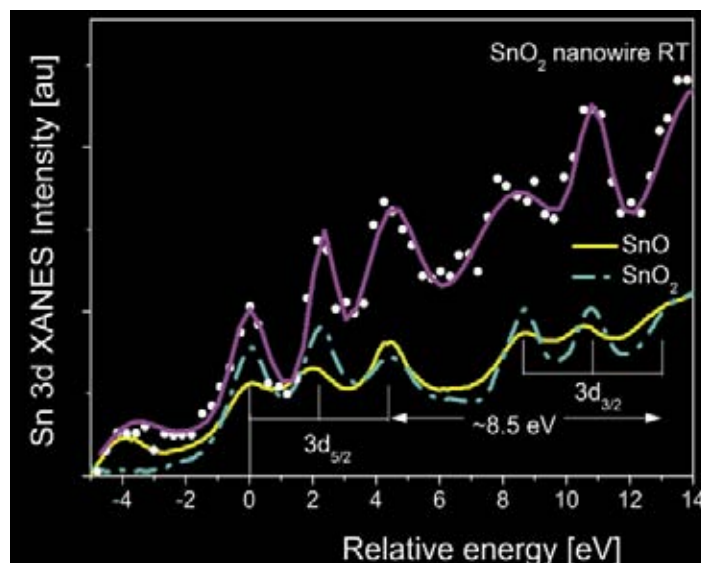
(b)

Figure 2. (a) Sketch of the device and the SPEM set-up for imaging the Sn 4d emission from the SnO_2 nanowire mats under variable bias conditions. (b) Sn 4d maps of the chemiresistor of percolating nanowires taken with grounded electrodes (top) and with right electrode biased at -8 V (bottom). The differences in the Sn 4d images are due to the presence of highly resistive nodes (marked with white circles), which impede even potential distribution along the nanowires. The caused rigid electron energy shift is beyond the energy window of the analyzer, tuned to the Sn 4d emission with grounded electrodes, which results in strong attenuation of the signal from certain nanowires.

(a)

(b)
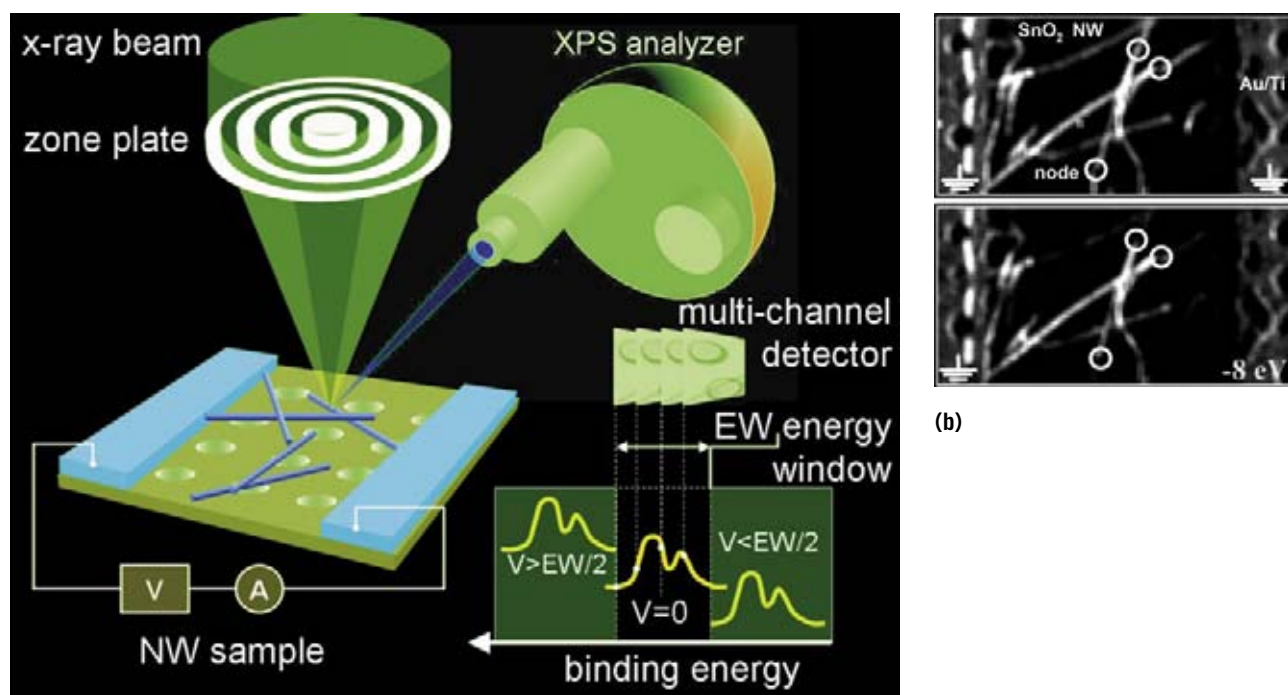
nanostructures wired as active element of the chemiresistor device. Figure 2a shows a sketch of the fabricated chemiresistor gas sensing device: the SnO_2 nanowire network contacted by two electrodes. The support is a Si_3N_4 membrane with periodic holes, allowing the nanowires placed over the holes to be locally probed. The potential of SPEM for analyzing the charge distribution and transport properties is based on the correlation between the applied potential and kinetic energy of the emitted photoelectrons. The Sn 4d images in Figure 2b demonstrate that we can monitor the percolating character of the conductivity: the strong attenuation of the signal from certain wires when biasing one of the electrodes indicates their higher resistivity.

These pioneering results are opening new avenues to explore the effect of size and environment (e.g. gases and temperature) on the surface activity, electronic properties and functionality of nano-materials.

References
[1] A. Kolmakov, *Int. J. Nanotechn.* **5**, 250 (2008).
[2] A. Kolmakov, X. Chen, M. Moskovits, *J. Nanosci. Nanotechn.* **8**, 111 (2008).
[3] S. Günther, B. Kaulich, L. Gregoratti, M. Kiskinova, *Prog. Surf. Sci.* **70**, 187 (2002).
[4] A. Kolmakov, S. Potluri, A. Barinov, T. Mentes, L. Gregoratti, M. Nino, A. Locatelli, M. Kiskinova, *ACS Nano* 2008 in press.

FABRICATION OF X-RAY PATTERNABLE MESOSTRUCTURED SILICA FILMS

P. Falcaro[1], S. Costacurta[1,2], L. Malfatti[2], T. Kidchob[2], M.F. Casula[3], M. Piccinini[4], A. Marcelli[4], B. Marmiroli[5], H. Amenitsch[5], M. Takahashi[6], P. Innocenzi[2]

[1] Associazione CIVEN Venezia Marghera, Italy
[2] Laboratorio di Scienza dei Materiali e Nanotecnologie (LMNT), Università di Sassari, Alghero, Italy
[3] Dipartimento di Scienze Chimiche, Università di Cagliari, Monserrato, Italy
[4] Laboratori Nazionali di Frascati – INFN, Italy
[5] Institute of Biophysics and Nanosystems Structure Research, Austrian Academy of Sciences, Graz, Austria
[6] Institute for Chemical Research, Kyoto University Gokasho, Japan

E-mail: falcaro@civen.org

Mesoporous films have aroused great interest because of the high ordered porosity, chemical compositional control, high thermal stability, possibility to use inorganic or hybrid porous matrix to grow or embed functional molecules or active nanoparticles [1,2]. Prospected applications in advanced devices have be raised, among which, for instance, ultralow-k dielectric or photonic materials, sensing and solar cell devices, photonic and catalysis applications, etc.

Until now, research on mesostructured films has been focused intensively on the control of geometric factors, such as the symmetry and the degree of order of the mesostructure, chemical composition, sensing properties. To produce a device based on mesoporous films another step is required: the capability to control the shape and geometry (scale of micron or millimetre). Acquiring the technology for designing devices is the key to engineering the materials and fabricate nano-devices [3].

We have successfully developed a highly-integrated patterning technology based on the response to X-ray radiation of mesostructured materials; we have combined different synchrotron technologies for in situ characterization, processing control and final material production.

Deep X-ray Lithography (DXRL) has been used to pattern mesostructured silica thin films. This lithographic approach is based on selective template removal and silica polycondensation induced by synchrotron radiation. The areas of the film that are not exposed to radiation can be selectively etched owing to a lower crosslinking degree of the inorganic network. An important advantage of this method is the possibility to simultaneously remove the surfactant and to induce condensation of the silica network in a single-step process. Small-angle X-ray Scattering (SAXS), DXRL and IR microimaging beamlines at Elettra have been employed during the same experiment. For the first time X-ray patternable mesostructured silica films have been fabricated; this experiment opens the route to new technologies for functional applications.

Block copolymer surfactant Pluronic F127, bis(4-tert-butylphenyl)iodonium p-toluenesulfonate (PG), and ethanol (EtOH) were purchased from Aldrich and used as-received. P-type/boron doped, (100) oriented, 400mm thick silicon wafers (Si-Mat) were employed as the substrates. A stock sol was prepared, containing 3.1 mL of ethanol, 4.3 mL of tetraethylorthosilicate, and HCl (0.355 mL, 0.77M). This sol was left to react under stirring in a closed vessel for 1 h at room temperature. A templating solution was prepared dissolving Pluronic F127 (1.3 g) in ethanol (15 mL), HCl (1.5 mL, 0.06M) and 0,6 bis(4-tert-butylphenyl)iodonium p-toluenesulfonate. Silicon substrates were dip-coated in the precursor sol at the withdrawal speed of 2.3 mm s^{-1} and at 40% relative humidity (RH). The as-deposited films were patterned by DXRL 3 h after deposition. The samples were exposed through X-ray masks containing test patterns of different size, shape, and geometry (5 to 500 mm). The masks had a gold absorber. After this procedure, the films were chemically etched to remove the unirradiated parts of the mesostructure. The samples were sonicated in a developing solution (mixture of ethylene glycol and ethanol), and then dried under an air flow. The films, after the lithographic process, were thermally treated at 150 °C for 1 h.
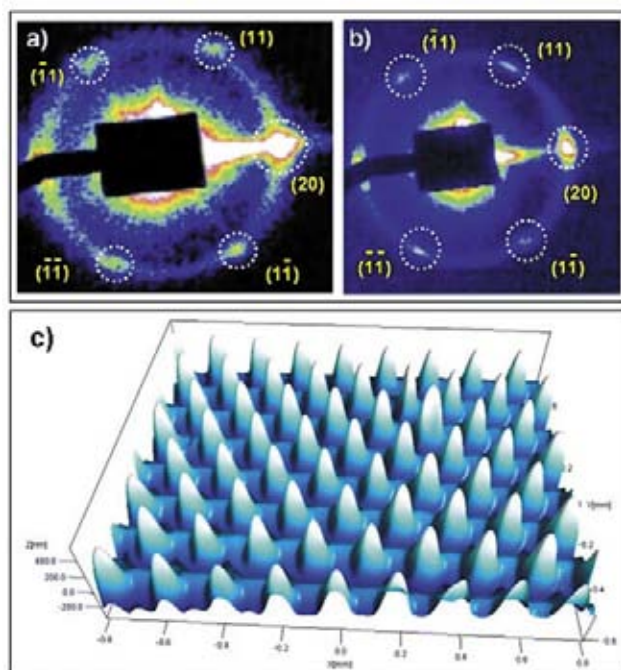
In order to perform GISAXS tests, as-deposited mesostructured films were exposed to synchrotron radiation through a mask that covered half of the film, so that a large area of the sample could be investigated by the probing beam. GISAXS experiments showed that in both the irradiated and the masked regions, the mesostructure has 2D hexagonal symmetry (space group p6m) [4]. TEM measurements have confirmed a p6m mesostructure with cylindrical micelles. A comparison between the GISAXS patterns with and without mask has shown that no substantial change in spot position and sharpness occurred, leading to conclude that no change in mesostructure symmetry took place upon deep X-ray patterning (Figures 1a and 1b). The exposure of the films to X-rays did not cause, therefore, any structural changes in mesophase or mesostructure damage.

The regions that were not exposed to X-ray radiation could be easily etched. This developing process is fast and effective, and optical profilometry measurements have revealed that the masked areas of the samples were completely removed by etching. Figure 1c shows portions of a mesoporous film patterned with pillars subsequently etched. We have also evaluated if the etching process affects the mesostructure, because in the etching procedure the whole film is immersed into the solution: this could cause a partial degradation of the Si–O–Si network resulting in loss of order or collapse of the inorganic walls with mesostructure disruption.

This work shows the possibility to pattern mesostructured films in order to control geometry and to fabricate functional devices. No change in the diffraction patterns of the etched film has been detected, indicating that the mesostructure is retained upon etching. Mesostructure preservation is very important from the viewpoint of applications, in that the properties associated with the order (e.g., high specific surface area, pore accessibility) must be retained to ensure the functionality of the material.

References

[1] P. Falcaro, S.; Costacurta, G. Mattei, H. Amenitsch, A. Marcelli, M. C. Guidi, M. Piccinini, A. Nucara, L. Malfatti, T. Kidchob, P. Innocenzi. *J. Am. Chem. Soc.* **127**, 3838, (2005);

[2] a) D. Buso, P. Falcaro, S. Costacurta, M. Guglielmi, A. Martucci, P. Innocenzi, L. Malfatti, V. Bello, G. Mattei, C. Sada, H. Amenitsch, I. Gerdova, A. Haché. *Chem. Mater.* **17**, 4965, (2005); b) S. Costacurta, L. Malfatti, P. Innocenzi, H. Amenitsch, A. Masili, A. Corrias, M. F. Casula *Microporous and Mesoporous Mater.*, in press (2008) DOI:10.1016/j.micromeso. 2008.02.003

[3] P. Innocenzi, T. Kidchob, P. Falcaro, M. Takahashi, *Chem. Mater.* **20**, 607, (2008).

[4] D. Grosso, Galo J. de A. A. Soler-Illia, F. Babonneau, C. Sanchez, P.A. Albouy, A. Brunet-Bruneau, A. Ruud Balkenende, *Adv. Mater.*, **13**, 1085, (2001).

TIME-RESOLVED *IN SITU* SMALL-ANGLE X-RAY DIFFRACTION EXPERIMENTS FOR A BETTER UNDERSTANDING OF THE FORMATION OF SURFACTANT-TEMPLATED SILICA

N. Baccile[1], C. V. Teixeira[2], H. Amenitsch[3], F. Villain[4], M. Lindén[2], F. Babonneau[1]

[1] *Laboratoire de Chimie de la Matière Condensée de Paris (LCMCP), Université Pierre et Marie Curie-Paris 6 and CNRS, Paris, France*
[2] *Department of Physical Chemistry, Åbo Akademi University, Turku, Finland*
[3] *Institute of Biophysics and Nanosystems Research, Austrian Academy of Sciences, Graz, Austria*
[4] *Chimie Inorganique et Matériaux Moléculaires (CIM2), Université Pierre et Marie Curie-Paris 6 and CNRS, Paris, France*

E-mail: niki.baccile@mKpiKg.mpg.de

Nanoscience is a relatively new discipline in which common interest arose worldwide in the past 20 years. The two main approaches, which are used to build and control matter, are generally referred to as *top-down* and *bottom-up*. Top-down approach mainly consists in casting matter into nano-objects by using patterning techniques, like in the fabrication of transistors and microchips. On the contrary, the bottom-up approach consists in building nano-objects atom-by-atom, starting from single atom to groups of molecules and finally to materials with given nanostructures. This communication deals with the formation of nanomaterials with ordered porosity via a bottom-up approach. These materials are obtained through assemblies of two types of objects: surfactant molecules (e.g. cetyltrimethylammonium bromide, $C_{16}H_{33}N^+(CH_3)_3Br$, CTAB) which have a tendency to form oil droplets in water, around which silica precursor (e.g., tetraethoxysilane, $Si(OEt)_4$, TEOS) will react to form a silica layer (Figure 1). The growth of the silica layers will then lead to the formation of silica-based powders in which the oil droplets are trapped in ordered arrays. Then upon calcination, the organic phase can be eliminated to give a silica powder with a controlled and ordered porosity, which can find many applications in the field of catalysis, sensors, drug delivery, depollution devices.
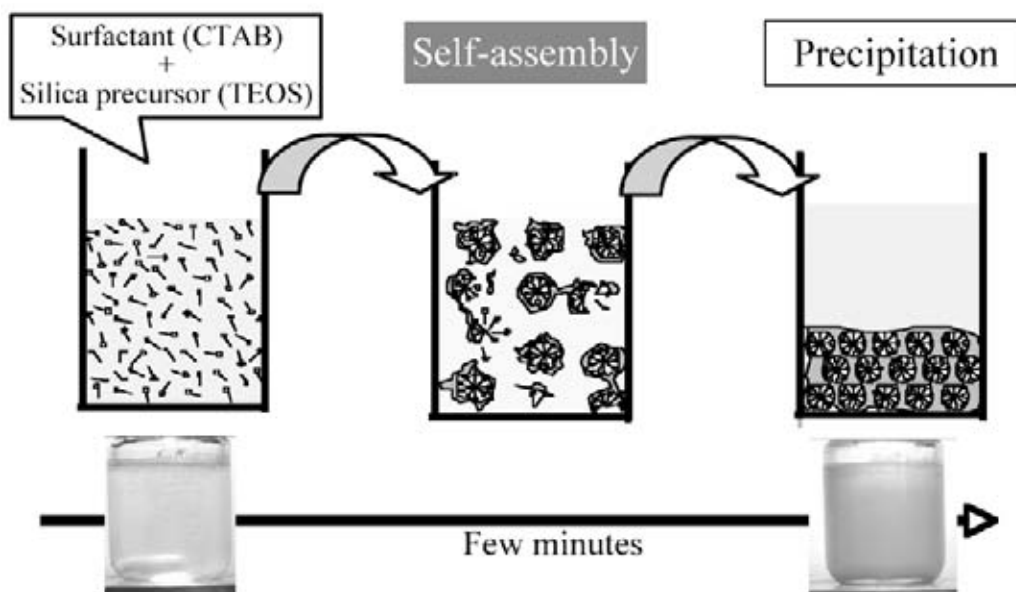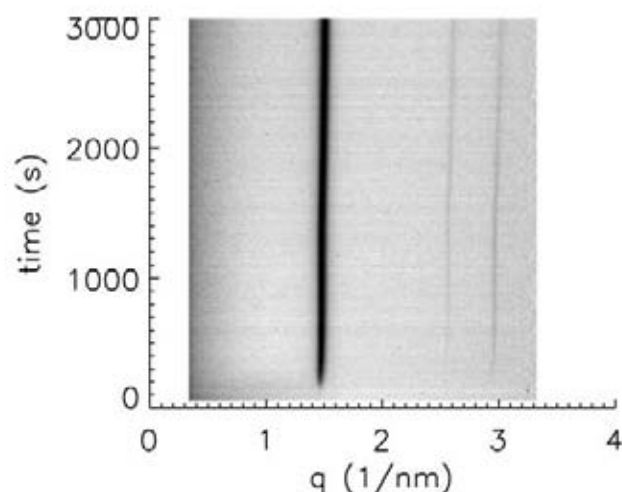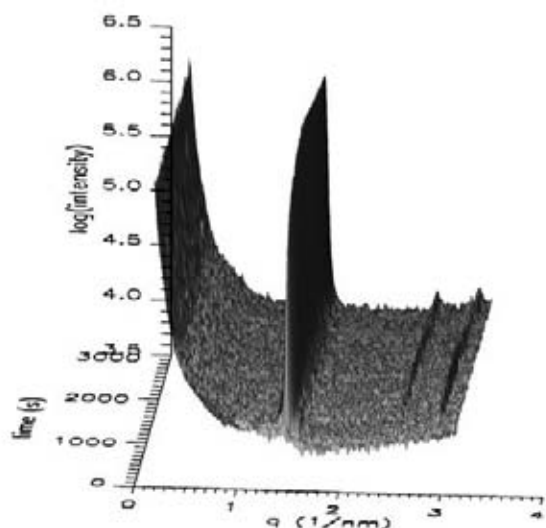

Figure 1.
Scheme representing our time-resolved *in situ* approach to study the formation of surfactant-templated silica powder.

The objective of this communication is to better understand the formation of such silica-surfactant assemblies governed by complex self-assembly mechanism between organic and inorganic moieties. We follow in real time the development of the ordered silica-surfactant phase using Small Angle X-ray Diffraction. Similar studies exist for systems prepared under basic conditions. Here, strongly acidic conditions are used that modify the charge on the growing silica species, and thus the type of interactions with the surfactants.

The whole reaction takes place in a conventional glass beaker at 25°C and atmospheric pressure. At time zero, the surfactant molecules (CTAB) are homogeneously dispersed in water together with the silica precursor (TEOS). Once in contact with water, TEOS reacts through hydrolysis and condensation to form silica. During the reaction, the solution mixture is continuously pumped out of the beaker in a closed circuit through a capillary tube placed in front of the X-ray beam. The X-ray diffraction patterns are thus collected regularly on an image plate.

Three different systems are studied with a constant TEOS/CTAB ratio (1:0.12) and various water concentrations. Figure 2 shows the time-resolved evolution of the X-ray patterns obtained for one system (TEOS:CTAB:HCl:H_2O = 1:0.12:9.2:130).

For each system, one diffraction peak appears first at increasing reaction times with dilution (from 100 s to 300 s). At longer times, two additional diffraction peaks are observed at higher *q-values*, which indicate an increase in the ordering of the scattering objects which can be described as surfactant micelles covered with a silica layer. The *q-value* is actually related to the distance between micelles,

which is around 4 nm. The associated distances for each peak allow us to identify that they originate from a two-dimensional hexagonal close packing array of cylinders. The main result extracted from these experiments is the direct formation of this hexagonal phase in each case, with no other transient phase. The time evolution of the main peak in the XRD pattern – namely its associated d-spacing and its full-width-at-half-maximum - shows two distinct stages which are also strongly dependent on the sol composition. There seems to be a co-existence of an ordered phase and a disordered one for longer times under experimental conditions (acidic pH) compared to the usual ones (basic pH), indicating that the ordering process is clearly slower in our case.

These results were also coupled to complementary Raman scattering experiments (not reported here) to follow also in real time, before precipitation, the hydrolysis of TEOS. This technique is sensitive to the vibration mode of the molecule, and here to the symmetric breathing mode of the $Si(OEt)_4$ tetrahedron. Once one Si-OEt group is hydrolyzed and replaced by one Si-OH group, the perfect symmetry is disrupted and the intensity of the Raman signal decreases. These experiments confirm the increasing rate of the hydrolysis reaction with TEOS concentration, and more interestingly, demonstrate the acceleration of the hydrolysis rate in presence of CTAB micelles due to micellar solubilization and surfactant stabilization of emulsion droplets.

Reference

[1] N. Baccile, *et al., Chem. Mater.* **20**, 1161 (2008).

TWO-BAND PARALLEL CONDUCTIVITY AT TERAHERTZ FREQUENCIES IN THE SUPERCONDUCTING STATE OF MgB$_2$

P. Dore[1], A. Perucchi[2], M. Ortolani[3], D. Di Castro[1], S. Lupi[1,2], V. Ferrando[4], M. Putti[4], I. Pallecchi[4], C. Ferdeghini[4], X. X. Xi[5]

[1] CNR-INFM Coherentia and Dipartimento di Fisica, Università di Roma La Sapienza, Rome, Italy

[2] Sincrotrone Trieste S.C.p.A., Trieste, Italy

[3] CNR-Istituto di Fotonica e Nanotecnologie, Rome, Italy

[4] CNR-LAMIA and Università di Genova, Genoa, Italy

[5] Department of Physics Pennsylvania State University University Park, USA

E-mail: paolo.dore@roma1.infn.it

The recent discovery of superconductivity in MgB$_2$ has raised a large interest [1] because of an unprecedentedly high T_C ($\approx$40 K) in a conventional BCS superconductor, in which the phononic origin of the superconducting pairing has been established. Furthermore, MgB$_2$ clearly shows the existence of two electronic bands (π and σ) which origin two distinct energy gaps (Δ_σ and Δ_π) in the superconducting state. Since the two-band superconductivity is an intriguing phenomenon that, although addressed theoretically, had been never observed before, MgB$_2$ gives a unique opportunity for testing theoretical models of BCS superconductivity in the two-band case.

Infrared spectroscopy can have an important role in studying the low-energy electrodynamics of complex systems. In particular, reflectance measurements at terahertz (THz) frequencies on a superconducting system at temperatures below the critical temperature T_C can allow the determination of the superconducting energy gap Δ in a non-invasive way. For example, in a isotropic s-wave BCS superconductor, the reflectance R(ω) for T$<<$ T_C abruptly approaches the unity at ω=2Δ (optical gap), thus giving a maximum in the ratio R$_S$/R$_N$, where R$_S$ and R$_N$ are the reflectances in the superconducting and normal states, respectively.

In the THz spectra of the two-band MgB$_2$ superconductor, only a feature at $\omega\approx2\Delta_\pi$ was generally seen with no evidence of the σ-gap [2]. On the contrary, the effect of the σ-gap is dominating in a realistic two-gap modelling based on the generally employed two-band parallel conductivity assumption (i.e., independent BCS responses of the two bands). This inconsistency raises an important pro-

blem, suggesting that this assumption can be questioned when applied at THz frequencies.

We performed reflectance measurements on high-quality MgB$_2$ epitaxial films [3] at the infrared beamline SISSI. Since MgB$_2$ quickly degrades in air, each film was sealed under vacuum in a quartz ampoule after growth and the optical experiments were continuously performed in vacuum. In the THz range (frequency ν <4 THz or ω<130 cm^{-1}, photon energies below 16 meV) we measured the intensity reflected by the sample by cycling the temperature in the 5-50 K range. We thus obtained R(T)/R(42) (i.e., for T<T$_C$, R$_S$/R$_N$) spectra with high accuracy ($\pm$ 0.1%). Measurement performed on an ultra-clean MgB$_2$ film with T$_C$=41 K show that R(50 K))/R(42 K) is flat within experimental uncertainties, as expected, while, on decreasing temperature below T$_C$, the R(T)/R(42) increases and a clear edge structure becomes evident at T=5 K (Figure 1a). We remark that only the high accuracy of the present synchrotron measurements allows the detection of an effect as small as 0.5%. The grey line in Figure 1a is the 5 K model spectrum computed on the basis of the two-band parallel conductivity assumption by employing independently obtained parameters (plasma frequencies Ω_σ and Ω_π, relaxation rates γ_σ and γ_π, energy gaps Δ_σ and Δ_π) to model the BCS response of each band. The resemblance of the model spectrum with the data is highly significant, and the edge structure observed in both model and measured spectra around 14 meV can be attributed to the σ-gap. This finding, obtained in a ultra-clean MgB$_2$ film, is a crucial result, since it allows us to reconcile THz observations with the predictions of BCS calculations.
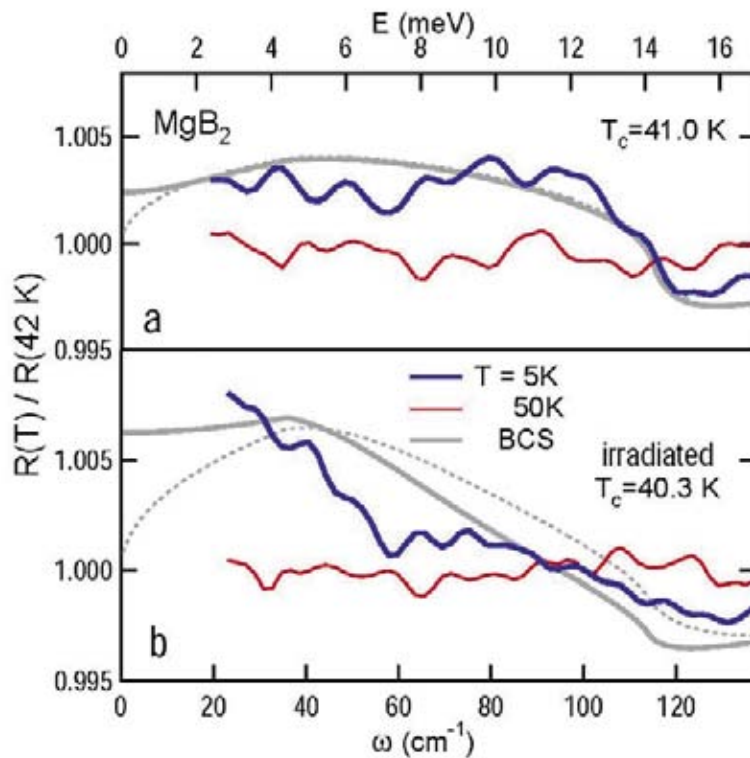
Figure 1.
Reflectivity ratios R(T)/R(42 K) in the THz range. The 5 K data are compared to BCS calculations (thick gray line, film thickness 200 nm; dotted line, semi-infinite medium) as obtained, on the basis of the two-band parallel conductivity assumption, by using plasma frequencies Ω_σ = 3.8 eV, Ω_π = 5 eV (from our measurements of the absolute reflectance in the entire infrared range), relaxation rates γ_σ=11 meV (γ_σ = 37 meV in (b)], γ_π = 7.2 meV, and gap values Δ_σ =7.2 meV, Δ_π =2.3 meV (from tunnelling spectroscopy measurements [4]).

To investigate the effect of the impurity level, we performed R(T)/R(42 K) measurements on a second film (T_C=40.3 K), previously irradiated with a low fluence of thermal neutrons which only induces a slight increase of the impurity scattering rates, in particular of γ_σ [4]. In this case an edge in the R(5 K)/R(42 K) is observed around 7 meV (Figure 1b). The model spectrum obtained by employing the ultra-clean film parameters, with the exception of γ_σ increased by about a factor 3, is in general agreement with the data (Figure 1b).

In conclusion, our results (M. Ortolani, P. Dore *et al.*, Phys. Rev. B **77**, 100507, 2008) show that the R_S/R_N spectrum measured at THz frequencies on a ultra-clean film gives evidence of the σ-gap and can be well described on the basis of the two-band parallel conductivity assumption. In a film with an impurity level slightly higher than that of the ultra-clean film, only the effect of the π-gap is well evident, thus explaining the inconsistency between theory and previous THz experiments in terms of different impurity levels. The proof that the two-band parallel conductivity assumption can well describe the electrodynamic response of MgB$_2$ at THz frequencies is of general interest since MgB$_2$ epitaxial films are being extensively investigated for possible applications in superconducting devices and terahertz electronics.

References

[1] Comprehensive reviews on the MgB$_2$ properties are reported in *Physica C*, **456** (2007)

[2] For a review of infrared studies on MgB$_2$, see: A.B. Kuzmenko, *Physica C* **456**, 63 (2007)

[3] A.V. Pogrebnyakov *et al.*, *Phys. Rev. Lett.* **93**, 147006 (2004).

[4] V. Ferrando *et al.*, *J. Appl. Phys.* **101**, 043903 (2007).

ANGLE RESOLVED PHOTOEMISSION AND THE PHYSICS OF CoO$_2$ TRIANGULAR PLANES

M. Zacchigna[1], A. Nicolaou[2,3], V. Brouet[2], A. Tejeda[3], P. Lejay[4], S. Hébert[5], H. Muguerra[5], D. Grebille[5], F. Parmigiani[6]

[1] Laboratorio Nazionale TASC, INFM-CNR, Trieste, Italy

[2] Lab. Physique des Solides, UMR 8502, Université Paris-Sud, Orsay, France

[3] Synchrotron SOLEIL, Gif-sur-Yvette, France

[4] Institut Néel, Grenoble, France

[5] Lab. CRSIMAT, UMR6508, CNRS et Ensicaen, Caen, France

[6] Sincrotone Trieste S.C.p.A., Trieste and Dipartimento di Fisica, Università di Trieste, Italy

E-mail: Michele.Zacchigna@elettra.trieste.it

Studies on transition metals oxides have been the source for some of the most interesting discoveries in solid state physics in the last decades, due to the richness of the phenomena that these compounds can provide. In the case of cobaltates, one is looking at layered metals, where a triangular plane of Co ions (embedded in CoO$_2$ slabs) can accommodate a varying number of electrons. Recently, the Na$_x$CoO$_2$ family gained a double interest. On one hand, it is promising for industrial applications, because of its high thermoelectric power. On the other hand, its behaviour attracted interest of the solid state community for its rich phase diagram [1]: magnetic transitions, unusual metal-insulator transitions, and, as if it was not enough, superconductivity were discovered within this family. The superconducting phase, appearing in what can be seen as a doped Mott insulator, reminds of the case of cuprates and triggered even more interest. This called for a detailed determination and understanding of the electronic structure.

Figure 1 displays the Fermi Surface (FS) measured by ARPES of Na$_{0.82}$CoO$_2$, one of the magnetic phases. Its hexagonal shape is characteristic of the triangular symmetry of the CoO$_2$ slab and agrees well with other ARPES studies of Na cobaltates [2,3]. Because ARPES is very surface sensitive and the Na environment of the surface after cleaving is somewhat ill-defined, one can however wonder how the

Figure 1.
(a) Comparison of the structures of Na and misfit cobaltates. The same CoO$_2$ slabs are present in the two families, but separated either by Na or Rock-Salt layers.
(b) Fermi Surface of Na$_{0.82}$CoO$_2$ measured on the BACH beamline at 100eV and 20K. Red points indicate the trace of the BiBaCoO FS.

(a)   (b)

BiBaCoO

Na_xCoO_2
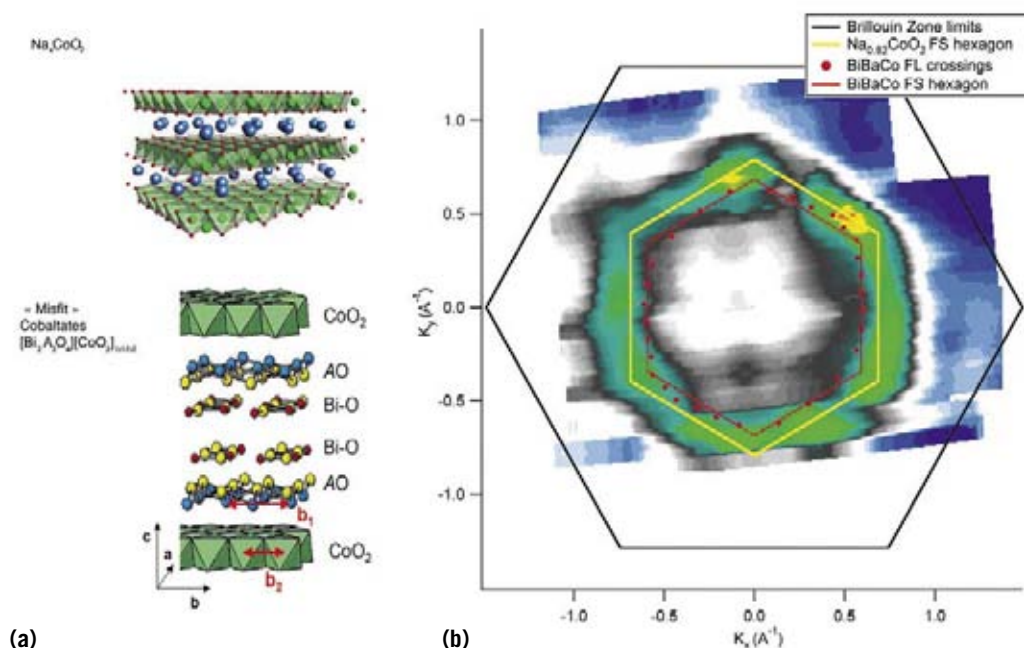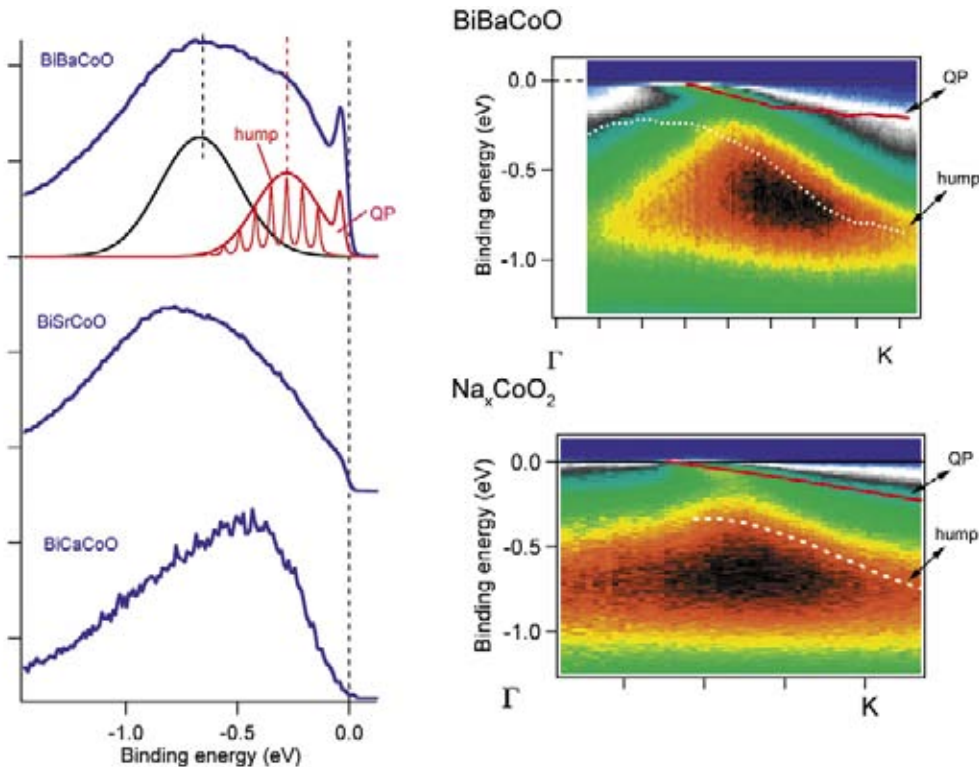
Figure 2.
Lineshapes at k_f for BiBaCoO, BiSrCoO and BiCaCoO. The QP peak forms a narrow (~100meV) band followed by a broad "hump", superimposed to the contribution from other bands and/or incoherent background. This structure is universal to cobaltates, as show by the comparison of the dispersions for BiBaCo and $Na_{0.82}CoO_2$. Red line and dotted white lines sketched the dispersion of QP and hump, respectively.

surface of these materials is representative of the bulk properties. In this framework, we decided to extend our interest to the bigger family of misfit cobaltates, where an inert Bi-O plane "protects" the CoO_2 plane, much like in Bi cuprates (see Figure 1). The rationale here is also to evaluate the role of the structure surrounding the CoO_2 planes. We demonstrated [4] that the electronic structure of the misfit cobaltate $[Bi_2Ba_2O4]$. $[CoO_2]_{~2}$ (BiBaCoO) is very similar to that of Na_xCoO_2. In particular, the FS periodicity is the one dictated by the triangular lattice. The FS crossings for this compound are reported as red points on the FS map of $Na_{0.82}CoO_2$ (Figure 1), evidencing the identical hexagonal shape. The careful analysis of the Fermi velocity (v_f), lineshape and size of the FS (k_f value) allows a more detailed comparison. Assuming a rigid band filling of the a_{1g} band, the size of the FS in BiBaCoO corresponds to x~0.7. One would then expect a smaller FS in $Na_{0.82}CoO_2$, contrary to the observation of Figure 1. This signals a deviation from the rigid band filling picture, which remains to be clearly understood. It could be attributed to a lower doping at the surface than bulk, but it is also interesting to discuss in connection with the inhomogeneous charge distribution observed by other experiments for this doping range.

In a series of experiments at the BACH and APE beamlines at Elettra and the SIS beamine at the SLS, we have performed an extensive study of different misfit phases. Unexpectedly, we observed a progressive decrease in the intensity of the quasiparticle (coherent) peak near k_f (Figure 2), when the structure of the intercalated Rock-Salt planes is shrinked by use of Ba, Sr or Ca, i.e. the doping is increased from x~0.7 to x~0.8. We showed that this change should not be interpreted as a shift of the band below the Fermi level but rather to a transfer of spectral weight to a hump (incoherent feature) at higher binding energy [4]. The implication of this is of key importance for the interpretation of the lineshape. It emphasizes its peak-dip-hump nature, which is also present in Na_xCoO_2. We attribute this to a strong (polaronic) coupling to collective excitations (see sketch of Figure 2), which is found to increase with x.

References

[1] M.L. Foo *et al., Phys. Rev. Lett.* **92**, 247001 (2004) and ref. therein.

[2] H-B. Yang *et al., Phys. Rev. Lett.* **95**, 146401 (2005).

[3] D. Qian *et al., Phys. Rev. Lett.* **96**, 216405 (2006).

[4] V. Brouet *et al., Phys. Rev. B* **76**, 100403 (2007).

THE ROLE OF METAL CONTACT IN THE SENSITIVITY OF SINGLE WALLED CARBON NANOTUBES TO NO_2

R. Larciprete[1,2], L. Petaccia[2], S. Lizzit[2], A. Goldoni[2]

[1] CNR- Institute of Complex Systems, Italy
[2] Sincrotrone Trieste S.C.p.A., Trieste, Italy

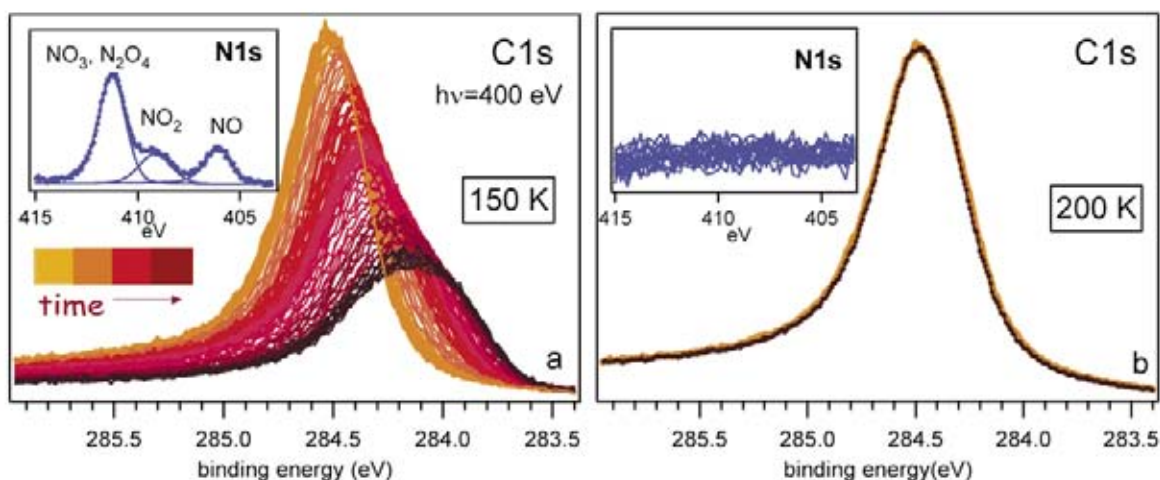**E-mail: rosanna.larciprete@isc.cnr.it**

Figure 1.
(a) Sequence of C1s spectra measured while dosing SWCNTs with 150 L of NO_2 at 150 K; inset: N1s spectrum measured at the end of the up-take.
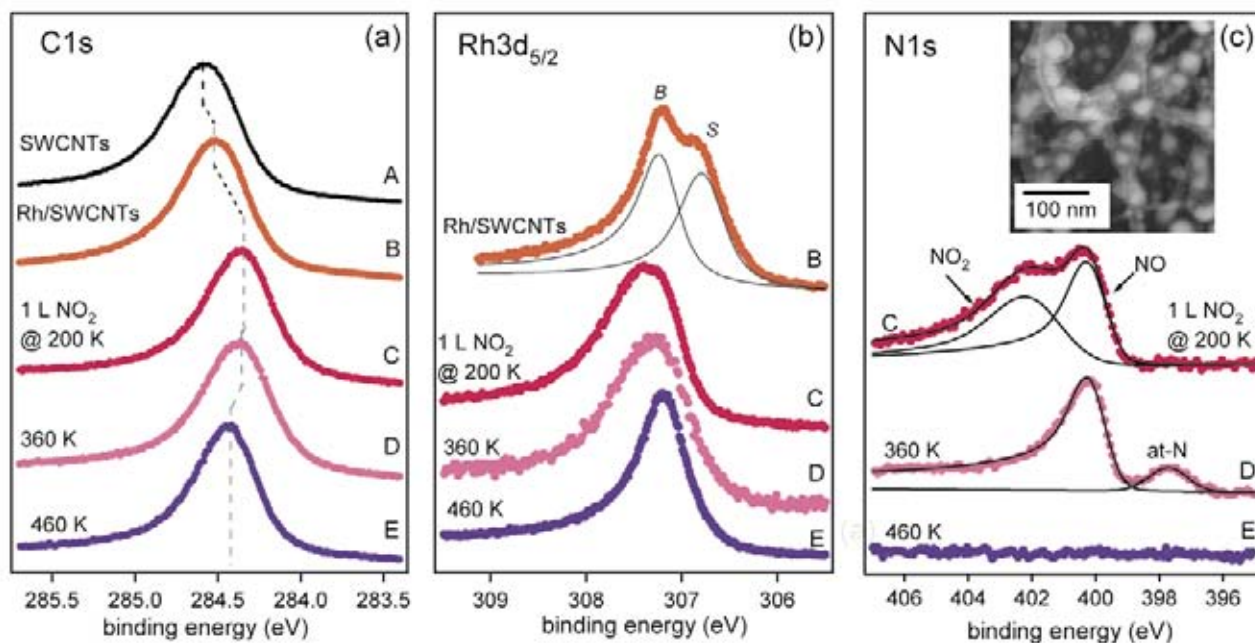**(b)** C1s spectra measured on SWCNTs before (black) and after (yellow) the exposure to 400 L of NO_2 at 200 K; inset: sequence of N1s spectra measured while dosing the gas.

In the last years an intrinsic sensitivity of carbon nanotubes (CNTs) has been reported [1] for diverse gases at room temperature (RT), with particular emphasis on NO_2, because of its importance in environmental pollution. For the latter, a detection level on the order of ppm has been measured at RT for CNT based sensors. In general the mechanism believed to regulate the response of single walled nanotubes (SWCNTs) to adsorbed NO_2 is identified in the electron transfer from semiconducting CNTs to the oxidising adsorbates, ($\sim$0.1 electrons per molecule) [2], which increases the hole carrier density in *p-type* tubes. However, what is still under debate is if there is at all the possibility to adsorb NO_2 on CNTs at RT, as the calculated NO_2-CNT binding energies of $0.11 \div 0.79$ eV^2 correspond to desorption temperature ranging between 45 K and 320 K.

In this study we show that whereas NO_2 adsorbs on SWCNTs at low temperature (150 K), at T$\geq$200 K there is no interaction between the tube lattice and NO_2 molecules or fragments. Thus any change in the CNT transport properties observed at RT can only be the result of external effects, such as NO_2 adsorption on metals in contact with CNTs (residual contaminants, catalyser particles, metal contacts). We used high energy resolution X-ray photoemission spectroscopy at the SuperESCA beamline of ELETTRA to follow the adsorption of NO_2 on SWCNTs at different temperatures [3,4]. Figure 1a shows the results obtained at 150 K: the C1s peak intensity diminishes with increasing NO_2 dose due to the building up of an adsorbed layer; moreover the binding energy (BE) shift to lower values, undoubtedly indicates the occurrence of charge withdrawal from the C lattice by the NO_2 adsorbate. After a dose of 150 L the N1s spectrum exhibits three peaks at 401.5, 404.5 and 407 eV, assigned to NO_3 (and/or NO_2 multilayer), NO_2 and NO species, respectively. On the contrary the N1s spectra measured while dosing NO_2 ($\sim$ 400 L) at 200 K remain flat and simultaneously no sign of C1s attenuation and line shape changing is revealed (Figure 1b). Thus NO_2 molecules do not interact with SWCNTs at T$\geq$200 K. The effect of NO_2 adsorption on SWCNTs covered by a uniform

Figure 2.
(a-c) C*1s*, Rh*3d*$_{5/2}$ and N*1s* core level spectra measured on SWCNTs (curve A), on the Rh/SWCNTs before (curves B) and after (curves C) the exposure to 1 L of NO$_2$ at 200 K, and after sample annealing (curves D-E). The inset in (c) displays the SEM image of the SWCNTs decorated with the Rh clusters.

distribution of Rh clusters (inset in Figure 2c) is illustrated in Figure 2. The C*1s* spectra measured before and after the addition of Rh (Figure 2a) indicate that the adsorbed metal atoms only determine a down BE shift of ~ 60 meV, which has to be attributed to the charge transfer across the Rh-SWCNTs junction. The corresponding Rh*3d*$_{5/2}$ spectrum (B in Figure 2b) exhibits two components at 307.19±0.01 eV (*B*) and 306.75±0.01 eV (*S*) attributed to Rh adatoms located below and at the surface sites. The effect on the C*1s* spectrum of 1 L of NO$_2$ is a further down shift of 145 meV (C in Figure 2a), undoubtedly mediated by the presence of the Rh nanoclusters which get oxidized. Bonding of NO$_2$ to Rh atoms is witnessed by the Rh*3d*$_{5/2}$ spectrum (C in Figure 2b), in which the surface component has vanished and the remaining peak is broadened due to the Rh atoms bonding to adsorbates. These are NO and NO$_2$, - the former originated from the NO$_2$ dissociation- as attested by the N*1s* components at 400.2 and 402.3 eV (C in Figure 2c). The N*1s* spectrum measured at increasing temperature shows the progressive desorption of the NO$_x$ (x=0-2) adspecies. At the same time the Rh*3d* core level narrows, whereas the C*1s* peak moves back towards the original BE position.

Lacking any direct interaction between NO$_2$ and CNTs, the C*1s* peak shifts have to be related to adsorbate induced variations of the Rh work function, which in turn modify the line up of the CNT bands at the metal-nano-

tube junction. Likely, NO$_x$ adsorption on the Rh nanoclusters is responsible of changing the height of the Schottky barrier at the Rh-semiconductive CNT contact. Thus the effect of NO$_2$ on the nanotubes is not a direct doping but a modification of the alignment of the CNT bands, which indirectly affects the sensitivity of CNTs to adsorbates. If not considered adequately, it can be taken as a reversible direct interaction between SWCNTs and gas molecules, which at T≥200 K does not exist.

References
[1] J. Kong *et al*., *Science* **287**, 622 (2000)
[2] S. Peng *et al*., *Chem. Phys. Lett.* **387**, *271 (2004)*
[3] A. Goldoni et al*., J. Am. Chem. Soc.* **125**, 11329 (2003)
[4] R. Larciprete *et al*., *J. Phys. Chem. C* **111**, 12169 (2007)

SYNTHESIS OF UNEXPECTED LARGE QUANTITIES OF SINGLE-WALLED ALUMINOGERMANATE NANOTUBES

C. Levard[1,2], J. Rose[1,2], A. Masion[1,2], E. Doelsch[3], D. Borschneck[1,2], L. Olivi[4], C. Dominici[5], O. Grauby[6], J.C. Woicik[7], J.-Y. Bottero[1,2]

[1] CEREGE, Aix-Marseille University Aix en Provence, France
[2] CNRS, CEREGE (UMR-6635, FR ECCOREV), Aix en Provence, France
[3] CIRAD, Environmental Risks of Recycling Research Unit, Aix-en-Provence, France
[4] Sincrotrone Trieste S.C.p.A., Trieste, Italy
[5] CP2M, Aix-Marseille University, Marseille, France
[6] CRMC2, Campus de Luminy, Marseille Cedex 09, France
[7] NIST, Gaithersburg, USA

E-mail: levard@cerege.fr

Over the past two decades, there has been increasing interest in non-carbon based nanotubes and their unique properties, such as reactivity and a highly specific surface area. Since 1992 and the synthesis of tungstene disulfide nanotubes [1], synthesis of such tubular structures from different inorganic materials such as SiO_2, MoO_3, V_2O_5 and Al_2O_3, TiO_2, GaN, etc., has increased. These years of research gave rise to multiple applications such as electronics, catalysis, gas storage. In parallel, many synthesis methods have been explored, e.g. template processes, reverse micellar systems, vapor depositions and electrochemical reactions. The low rate of nanotube production is a recurrent shortcoming of these complex processes. The production of a high quantity of material can be long and expensive and is a real challenge for industrial-scale applications.

Imogolite ($Al_2SiO_3(OH)_4$), a natural aluminosilicate nanotube (formation that occur in nature at ambient pressure and low temperature), appears to be easy to synthesize. These aluminosilicates nanotubes were obtained by coprecipitation of aluminum and silicon monomers in aqueous solution with an initial millimolar concentration yielding to very small

Figure 1.
Structure of imogolite (Ø=2 nm, L= few tens to several hundred of nanometers). Imogolite is composed of a curved gibbsite ($Al(OH)_3$) layer on the outer surface and Si monomers linked to 6 Al inside the tube
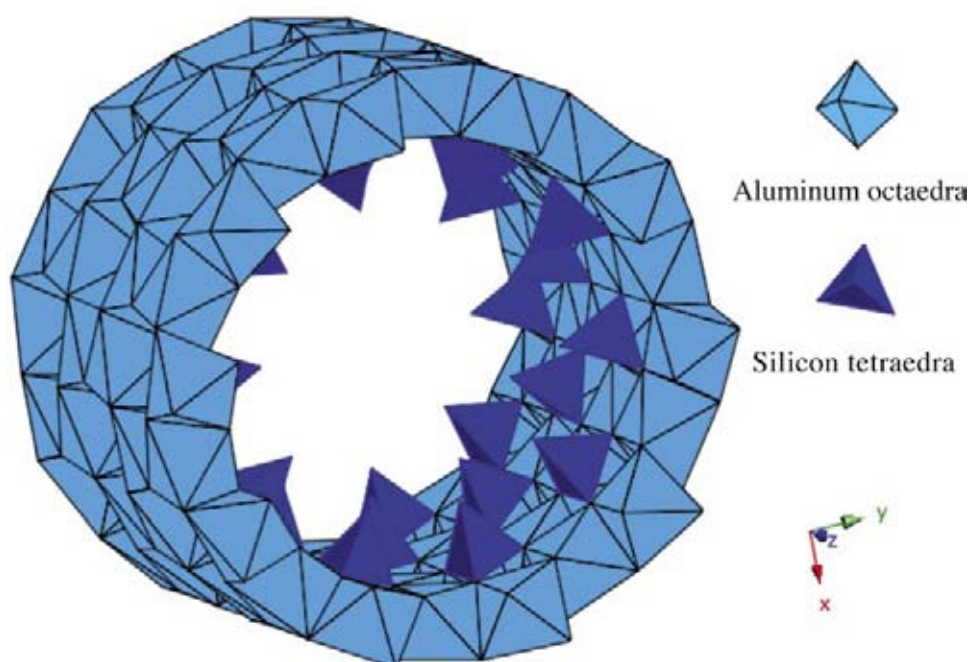
Aluminum octaedra

Silicon tetraedra

Figure 2. Caracterization of the Ge-imogolite structure. Pseudo-radial distribution function of Ge-imogolite synthesized from a decimolar concentration and comparison with the Ge-imolite reference synthesized from a millimolar concentration (A). TEM picture of Ge-imogolite synthesized from a decimolar concentration (B).
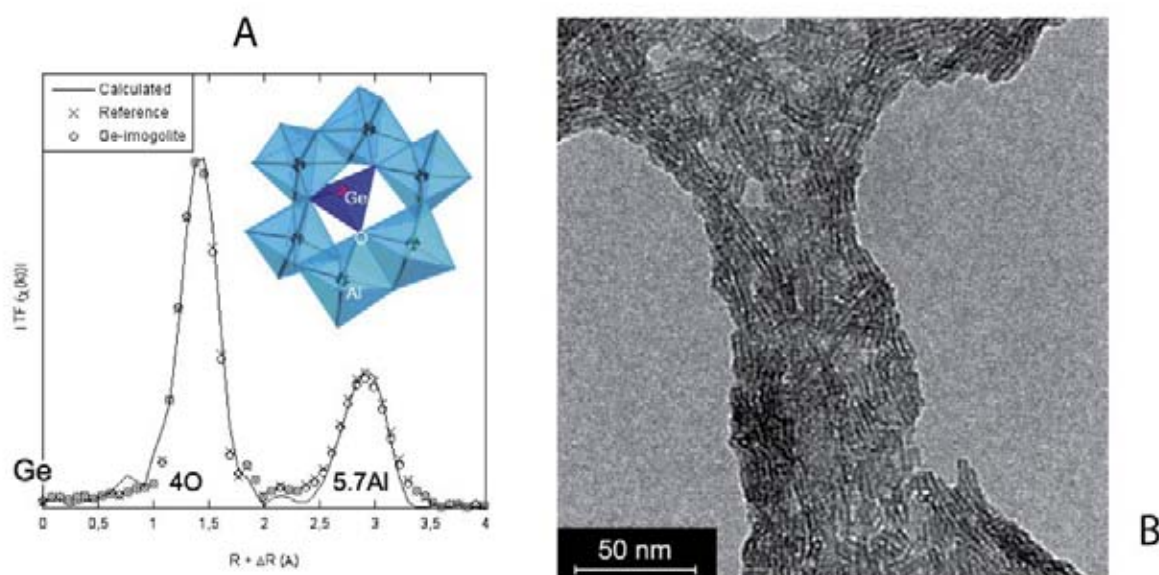
amount of material [2]. Attempts to synthesize imogolite from more concentrated (decimolar) solutions failed [3].

In the present paper, we report the case of single-walled aluminogermanate nanotubes, analogous to natural imogolite ($Al_2GeO_3(OH)_4$). These inorganic nanotubes were mass synthesized by replacing silicon by germanium in decimolar concentration [4]. The proposed new protocol increased the production by two orders of magnitude. The Aluminogermanate nanotubes were characterized using a multiscale approach.

The Ge local environment has been investigated using X-ray Absorption Spectroscopy (XAS) (Figure 2-A). Ge was in tetrahedral coordination and linked to the Al layer by about 6 Al atoms, characteristic to the imogolite local structure.

TEM images (Figure 2-B) confirmed the fiber structure of the aluminogermanate nanotubes synthesized from a decimolar concentration. The aluminogermanate nanotubes aggregated in a fibrous network. A picture analysis revealed an average diameter of 3.03 nm ± 0.11 nm. The small standard deviation indicated a very homogeneous diameter size distribution.

We have synthesized aluminogermanate nanotubes, with a structure analogous to natural imogolite, in high quantities. The Ge-imogolite structure was confirmed by a multimethod characterization. The Ge-imogolite synthesis efficiency was considerably increased (x 85 in wt.) compared to "standard" methods. Considering the mild synthesis conditions (aqueous solution, low temperature), this is encouraging with respect to potential industrial applications of these nanotubes.

References

[1] R. Tenne, L. Margulis, M. Genut, G. Hodes, *Nature* **360**, 444 (1992).

[2] V.C. Farmer, A.R. Fraser, J.M. Tait, *J. Chem. Soc. Chem. Comm.* 462, *(*1977)

[3] R. Nakanishi, S. I. Wada, M. Suzuki, M. Maeda, *J. Fac. Agr. Kyushu Univ.* **52**, 147 (2007).

[4] C. Levard, J. Rose, A. Masion, E. Doelsch, D. Borschneck, L. Olivi, C. Dominici, O. Grauby, J.C. Woicik, J.-Y. Bottero, *J. Am. Chem. Soc.* **130**, 5862 (2008).

ON THE ATTENUATION LENGTH OF LOW ENERGY ELECTRONS IN SOLIDS

F. Offi[1], S. Iacobucci[1,2], P. Vilmercati[3,4], A. Rizzo[1], A. Goldoni[3], L. Petaccia[3], M. Sacchi[5], G. Panaccione[6]

[1] CNISM and Dipartimento di Fisica, Università Roma Tre, Rome, Italy

[2] CNR, Istituto dei Sistemi Complessi, Monterotondo Scalo, Italy

[3] Sincrotrone Trieste S.C.p.A., Trieste, Italy

[4] Dipartimento di Fisica, Università degli Studi di Trieste, Italy

[5] Synchrotron Soleil, F-91142 Gif-sur-Yvette, France and Laboratoire de Chimie Physique - Matière et Rayonnement, Université P. et M. Curie, Paris, France

[6] Laboratorio Nazionale TASC, INFM-CNR, Trieste, Italy

E-mail: offi@fis.uniroma3.it

In photoemission spectroscopy (PES) electrons are excited in vacuum after absorption of a photon. The analysis of the energy-, angular-, and spin-distribution of the emitted photoelectrons has allowed over the years to obtain precise information about electronic properties of materials. Photoemission spectra from solid systems provide information only from a limited material depth, since the excited electrons suffer scattering events inside the material and may be lost before being emitted. The electron scattering probability depends, first of all, on the electron energy E and, for the typical PES energy range, is relatively high, such that PES is a very surface sensitive technique, with an information depth of only about 20-50 Å (Figure 1a) [1]. It is however often desirable to retrieve the photoemission signal from deeper in the solid, such as for systems having surface electronic properties different from the bulk ones (e.g., several superconductors) or when a capping layer is used to protect surfaces from contamination. It was suggested that the electron scattering probability is very low at low electron energy ($E<10$ eV), with the result that electrons could travel long distance before a collision [1]. In such cases, a photoemission signal from a larger depth in solids could be obtained, resulting in a bulk sensitive technique for the investigation of the materials electronic properties (Figure 1b). In our experiment we verified
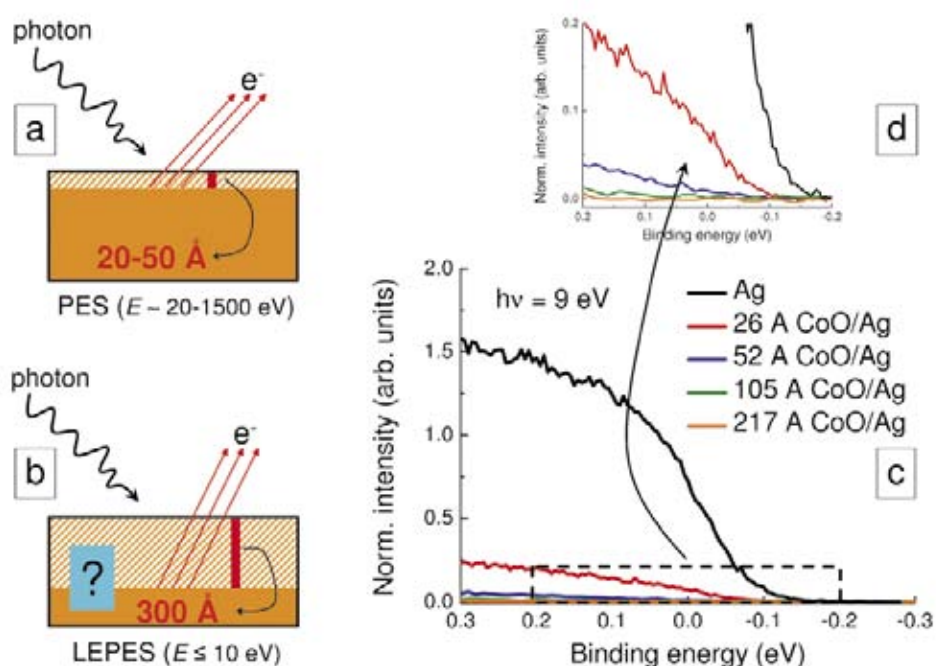

Figure 1.
Information depth in a PES experiment with $E\sim$20-1500 eV (a) and in LEPES experiment with $E\leq10$ eV (b); (c) LEPES spectra taken close to the Fermi level at a photon energy hν=9 eV from a Ag(001) surface for increasing CoO thickness; (d) zoom in of the spectra of panel (c).
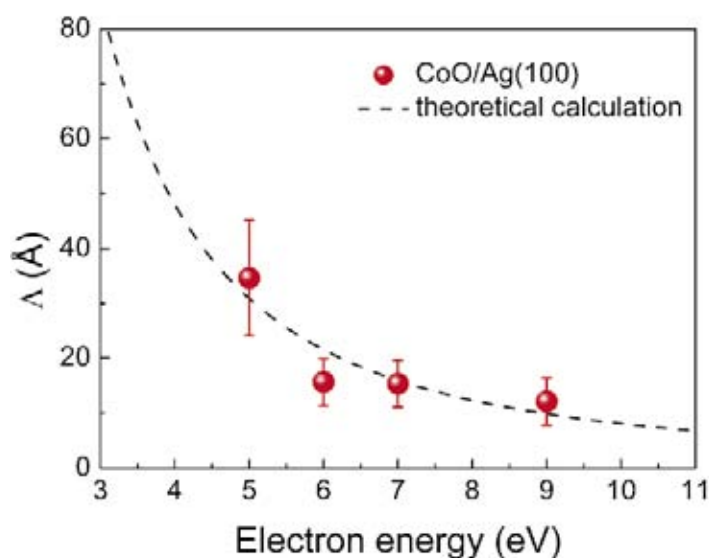
Figure 2.
Electron attenuation length Λ is plotted as symbols with error bars versus electron energy. The superimposed dashed line is a theoretical calculation of electron attenuation length resulting from a fit of the experimental data with a curve suggested in Ref. [1] reduced by a scaling factor of 6.0.

such hypothesis, obtaining that indeed the information depth of low energy photoemission spectroscopy (LEPES) is increasing when lowering electron energy, but considerably less than expected. Given the recent renewed interest in LEPES experiments [2], our results set a firm limit on the values and limitations of the technique.

In order to investigate the information depth of LEPES we used the photon supplied at the BaD ElPh beamline, where high intensity flux is available for energy between about 5 and 20 eV. We detected the electrons excited by such photons in an Ag substrate for increasing thickness of a CoO overlayer [3]. For different photon energies, we acquired the photoemission intensity close to the Ag Fermi edge (zero binding energy) looking at its progressive attenuation for increasing overlayer thickness (the insulator CoO makes no contribution in the intensity at the Fermi level). Figure1c is an example for a photon energy hν = 9 eV: the Ag intensity steadily decreases upon increasing CoO thickness, until, for overlayer thicker than 52 Å, the intensity is extremely weak, as seen in the zoom in of Figure 1d. From such data we can evaluate the information depth of the technique by computing the electron attenuation length Λ. We integrated the photoemission signal intensity in the energy interval ±0.2 eV with respect to the Fermi level and we fitted the results with an exponential decay function of the kind $I_d = I_0 e^{-d/\Lambda}$, where I_d is the integrated intensity corresponding to the CoO thickness d and I_0 is the integrated intensity for overlayer thickness d=0 (bare Ag substrate). The obtained values of Λ are plotted in Figure 2 (solid circles with error bars) versus the electron energy measured in respect to the Fermi level.

Superimposed to the experimental points is a theoretical calculation (dashed line) adapted from the curve proposed in Ref. [1] for the attenuation length of electrons in inorganic compounds. Such curve is generally used for substantiating the very large attenuation length of low energy electrons, and it is still cited as an indication of the bulk sensitivity of LEPES. We fitted the curve to our experimental data having only a scale factor as a free parameter. The best fit, shown in Figure 2, was obtained by dividing the curve from Ref. [1] by a 6.0 factor. Therefore, while our data reproduce the Λ versus electron energy dependence as suggested by the Seah-Dench curve [1], the absolute value obtained is much smaller than earlier suggested.

Our results thus indicate a moderate increase of the bulk-sensitivity in photoemission spectroscopy with very low energy electrons. While care must be taken in analysing spectral change versus photon energy [3], LEPES may therefore unravel the electronic properties in many solid systems with complicated surface behaviour when combined with the high energy resolution available at modern synchrotron radiation beamline.

References

[1] M. P. Seach and W. A. Dench, *Surf. Interf. Analysis* **1**, 2 (1979).
[2] T. Kiss, F. Kanetaka, T. Yokoya, T. Shimojima, K. Kanai, S. Shin, Y. Onuki, T. Togashi, C. Zhang, C. T. Chen, and S. Watanabe, *Phys. Rev. Lett.* **94**, 057001 (2005).
[3] F. Offi, S. Iacobucci, P. Vilmercati, A. Rizzo, A. Goldoni, M. Sacchi, and G. Panaccione, *Phys. Rev. B* **77**, 201101(R) (2008).
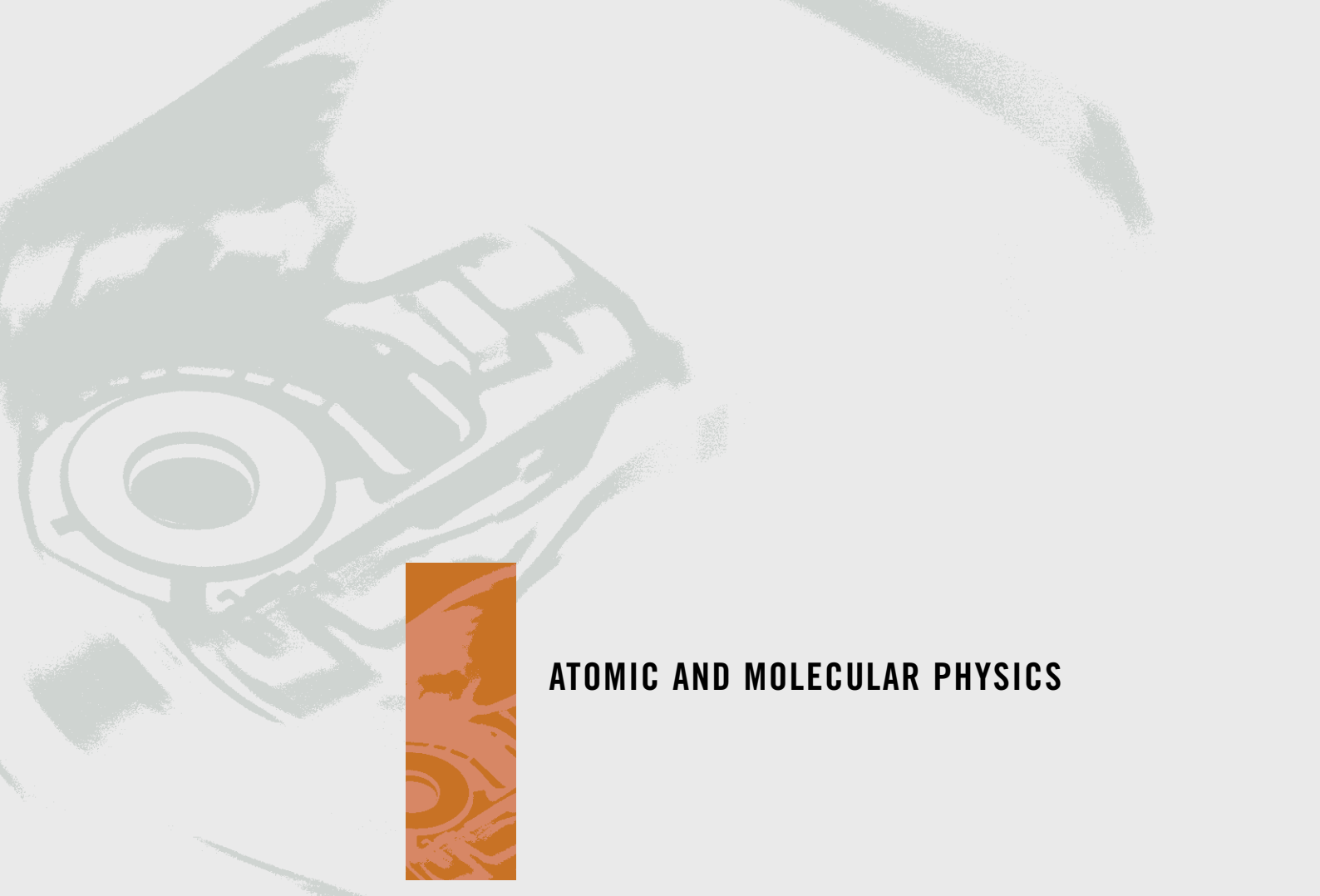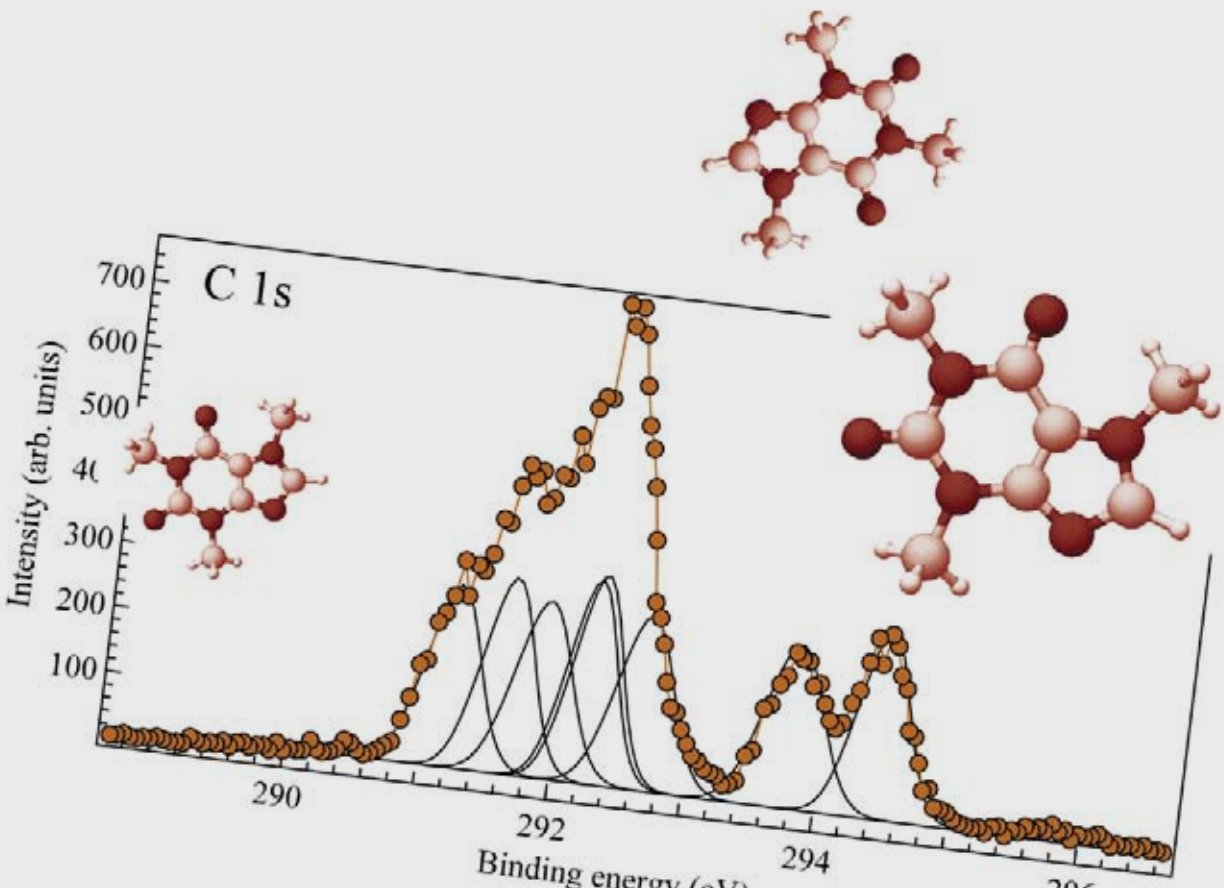
As a member of the program committee A (Gas Phase) at Elettra for the last 10 years, I have been able to follow the development of science in this field over time. The quality of the research has grown during the years, as researchers have become more experienced and one can also see the gradual increase of international commitment.

In the present highlights these trends are very visible. There are studies of very fundamental processes such as the kinetic energy release in the double photo ionization of H_2. Taking away two electrons from this molecule leaves two protons interacting and the report deals with the physical interpretation of the "kinetic energy release effect". Two protons in interaction is the absolutely simplest molecular ion one can think of. Nevertheless there is a lot of physics to deal with!

There are two very nice results from instrument development efforts. A new ECR ion trap has been installed at the gas phase beamline and the results show that this method to study cross sections gives very good conditions. I have during the years followed cross section measurements both at Daresbury and at LURE. The ECR ion trap is a very nice contribution to the field. A laser synchronized to the SR-beam has been installed and the first results are very nice.

Finally, Elettra has during the last years developed a very solid research programme concerning studies of molecular radicals. These studies are important and the report in this year's Highlights represents the state-of-the-art in the field.

As chairman of the gas phase PAC I would also like to point out that these results would never have been achieved without the hard work of the in-house responsible scientist and of the Elettra staff. Several of them are co-authors of the reports and the combination of international presence with high quality in-house research is obviously promising for the future.

Svante Svensson

Svante Svensson graduated 1976 in the well known ESCA group in Uppsala headed by the Nobel Laureate Kai Siegbahn. He has been active in synchrotron radiation based research since 1981 and has specialized on high resolution electron spectroscoopy on atoms, molecules, clusters and liquids. Recently he has also taken up high kinetic energy photoelectron spectroscopy. Beamline development and end station instrumentation have been important issues in his research.
Prof. Svensson has several international commitments apart from his activity in the PAC at ELETTRA. He is coordinator of a Nordic Research Network and also coordinator of the contributions to MAX in IRUVX. He is co-author of 270 articles. At the moment he spends a year as visiting professor at the Triangle de la Physique in Paris, where he will take part in the commissioning and startup of the PLEIADES beam line.

TRACKING THE FULL BREAK-UP OF H₂ MOLECULES

T. J. Reddish[1], J. Colgan[2], P. Bolognesi[3], L. Avaldi[3], M. Gisselbrecht[4], M. Lavollée[4], M. S. Pindzola[5], A. Huetz[4]

[1] *Department of Physics, University of Windsor, Windsor, Ontario, Canada*

[2] *Theoretical Division, Los Alamos National laboratory, Los Alamos, New Mexico, USA*

[3] *CNR-IMIP, Area della Ricerca di Roma 1, Monterotondo Scalo, Italy*

[4] *CNRS- Universitè Paris Sud, LIXAM, Orsay, France*

[5] *Department of Physics, Auburn University, Auburn, USA*

E-mail: lorenzo.avaldi@imip.cnr.it

Figure 1.
Schematic potential energy diagram of the initial and final states for PDI of H₂. During double ionization the ground vibrational state is projected onto the upper repulsive curve, whose dissociation limit is at 31.67 eV, resulting in a broad range of kinetic energies for the final proton pair.

The fate of a molecule after absorption of a photon with sufficient energy to break it apart is of fundamental importance for the comprehension of several natural phenomena and for an efficient handling of many industrial processes. Indeed when bonds are broken neutral and charged radicals are formed and react with neighbouring molecules. The greater the energy absorbed, the greater the number of possible reactions and the "damage" produced on the molecule itself and its environment. In H_2 when the energy absorbed is large enough to remove the two electrons, the molecule then explodes due to the repulsive interaction between the two protons.

$$h\nu + H_2 \rightarrow H^+ + H^+ + e_1 + e_2$$
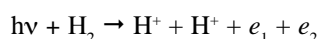
The probability to remove two electrons is about two orders of magnitude lower than the one to eject only one electron, because it is dominated by the interaction between the electrons themselves (i.e. they have to be considered a "correlated pair"). Thus intense VUV sources of radiation and efficient spectrometers that enable the time correlated detection of few charged particles are needed to investigate this process. These requirements have been met by an experiment at ALS [1] and a series of experiments [2,3] at the Gasphase beamline at Elettra. In these experiments a uniform electric field guides the positive and negative charges produced in the break-up in opposite directions from the interaction region to the detectors, while a magnetic field ensures that the fast electrons are detected as well. For each particle the position of impact on the detector and its time-of-flight are measured. From these quantities the initial momenta of the four particles are reconstructed and, due to the high velocity of the protons in the Coulomb explosion (i.e. the protons fly away in a time shorter than the molecular rotation), the alignment of the molecular axis with respect to the polarization of incident light is determined. Thus a 3D "photograph" of the Coulomb explosion can be taken.

In an earlier work [2], we studied how the spatial distribution of one escaping electron, having fixed the direction of the other one, depends on the alignment of the molecular axis with respect to polarization of the incident radiation. Here we report the results of a study that unravels the dependence of the electron spatial distribution on the internuclear separation R. The purely repulsive character of the H_2^{2+} potential curve results in a proton kinetic energy release, KER, whose value (Figure 1) depends on R at the moment of the
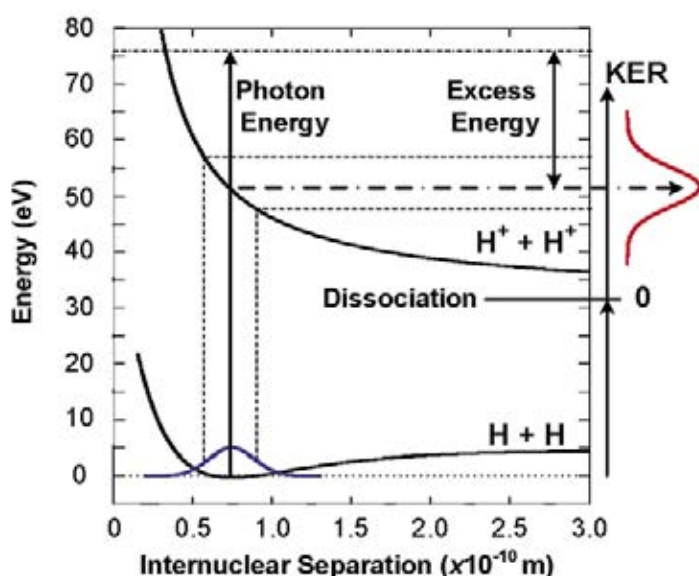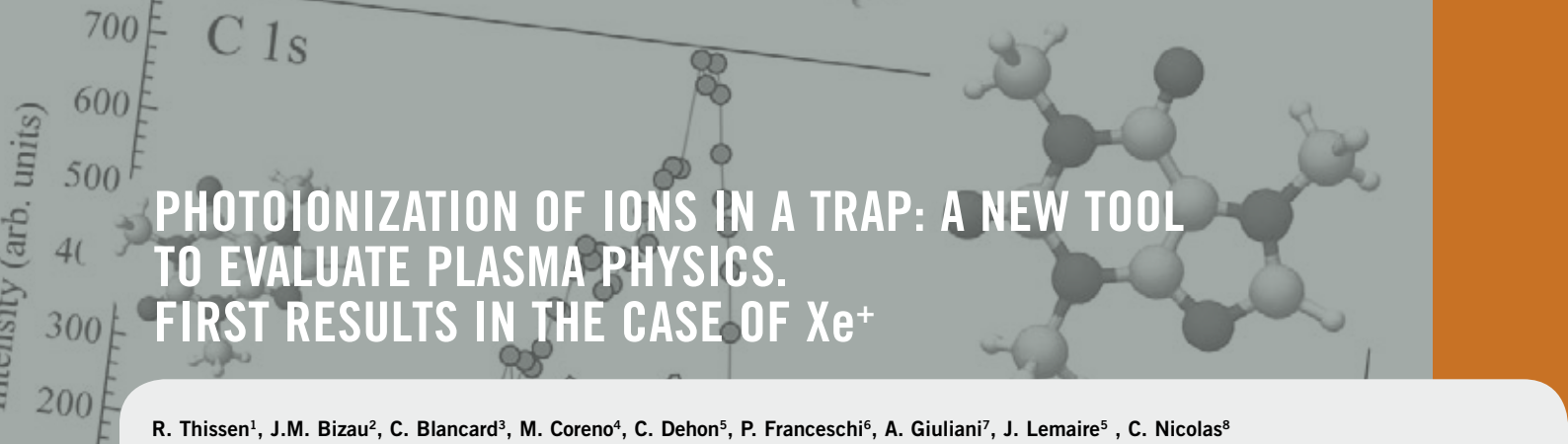
double ionization. Selection of the KER allows one to probe the interplay between the electronic and nuclear motion in the process. The experiment was performed at 76.09 eV, ~25 eV above the double ionisation threshold at the equilibrium internuclear distance, with the Elettra ring operated in the four bunch mode. A selection of the measured fully differential cross sections, FDCS, is reported in figure 2. The two columns correspond to FDCS in which the two photoelectrons are measured in coincidence with ions whose KERs are 16.5 and 23.5 eV, respectively. These KERs correspond approximately to R = 1.6 and 1.2 a_0. The FDCSs display a noticeable variation with the direction of the fixed electron (indicated by the arrows in Figure 2), with the alignment of molecular axis and with R. The experimental observations are in very good agreement with the calculations of the Time Dependent Close-Coupling (TDCC) method [4] performed at different R. TDCC calculations of the FDCS for each final M state accessed in the transition, where M = 0 (Σ), ±1 (Π) is the total magnetic quantum number in a reference frame aligned with the molecular axis. The FDCS results from the contributions of the Σ, Π components and their cross term. This analysis allows one to establish that the Π component, slowly varying with R, gives the main contribution to the FDCS while the Σ component is responsible of the variation with R. The cross term, with its constructive/destructive interference between the two components, amplifies the changes in R of the pure Σ component. The analogy of these findings with the those for the photoionization of H_2^+[3], where electron-electron correlations are completely absent, leads to the conclusion that the observed R-dependent trends in the photodouble ionization of H_2 are due to the electron-ion, rather than electron-electron, interactions. Therefore the Σ electronic states which lie near the internuclear axis, in contrast to the Π states concentrated in the plane between the nuclei, are more sensitive to variations in R.

References

[1] T. Weber *et al., Nature* **431**, 437 (2004).
[2] M. Gisselbrecht *et al., Phys. Rev. Lett.* **96**, 153002 (2006).
[3] T.J. Reddish *et al., Phys. Rev. Lett.* **100**, 193001 (2008).
[4] J. Colgan, M.S. Pindzola and F. Robicheaux, *Phys. Rev. Lett.* **98**, 153001 (2007).

Figure 2. FDCSs in the 'coplanar' geometry for $E_1 = E_2 = 12.5 \pm 10$ eV: (a) direction of the fixed electron $\theta_1 = 60°$ and of the molecular axis $\theta_N = 20°$, (b) $\theta_1 = 60°$, $\theta_N = 160°$ and (c) $\theta_1 = 90°$, $\theta_N = 20°$. Two KER values, 16.5 (left) and 23.5 eV (right) corresponding to approximately R = 1.6, 1.2 a_0, respectively, are shown. The experimental data are arbitrarily normalized to the TDCC results convoluted over the experimental bandwidths (solid); unaveraged TDCC results for the stated values (dashed) have the scaling factors indicated. See [3] for more details.
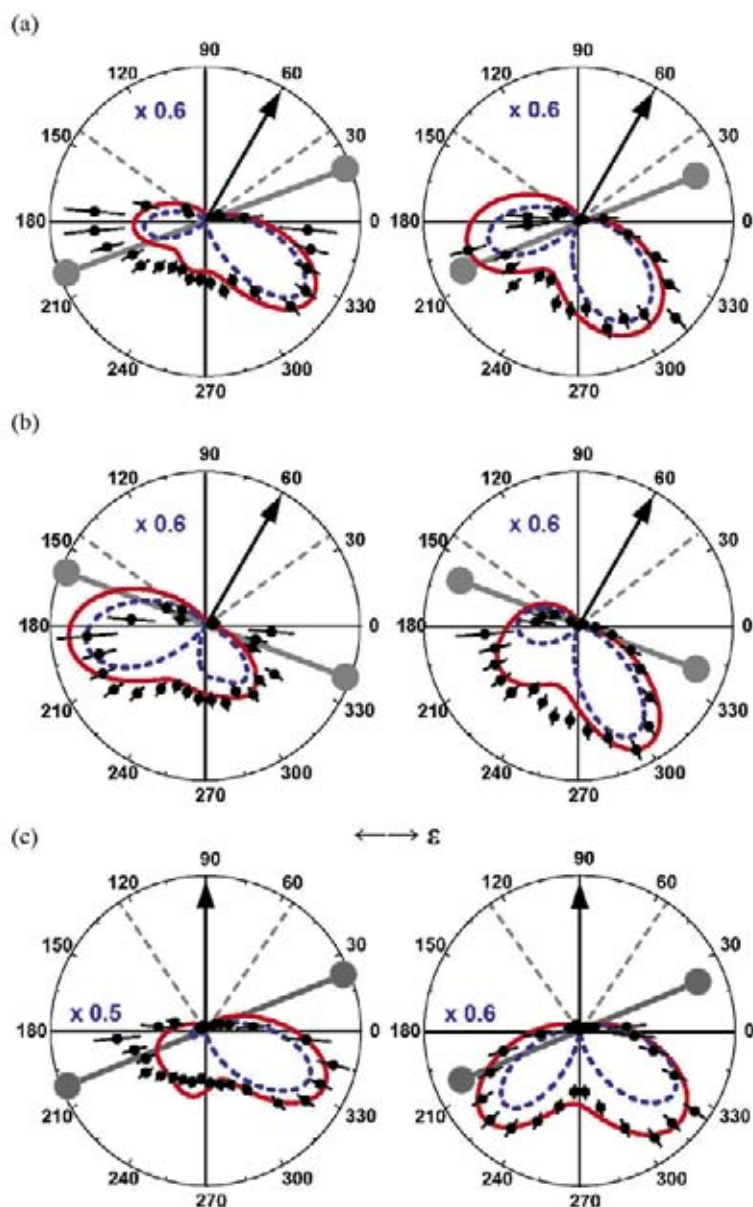
PHOTOIONIZATION OF IONS IN A TRAP: A NEW TOOL TO EVALUATE PLASMA PHYSICS. FIRST RESULTS IN THE CASE OF Xe+

R. Thissen[1], J.M. Bizau[2], C. Blancard[3], M. Coreno[4], C. Dehon[5], P. Franceschi[6], A. Giuliani[7], J. Lemaire[5] , C. Nicolas[8]

[1] Laboratoire de Planétologie de Grenoble, UJF, Bât. D de Physique, Grenoble, France

[2] Laboratoire d'Interaction des Rayons X avec la Matière (LIXAM), Université Paris-Sud, Orsay cedex, France

[3] CEA DAM Ile-de-France, DPTA, Bruyères-le-Châtel Cedex, France

[4] CNR-IMIP, Rome branch and Gas Phase Beamline@Elettra, Trieste, Italy

[5] Laboratoire de Chimie Physique, Bât. 350, Université Paris Sud, Orsay, France

[6] Sincrotrone Trieste S.C.p.A., Trieste, Italy

[7] Cepia, Institut National de la Recherche Agronomique (INRA), Nantes Cedex 3, France

[8] Synchrotron SOLEIL, L'Orme des Merisiers, Saint Aubin, Gif-sur-Yvette cedex, France

E-mail: roland.thissen@obs.ujf-grenoble.fr

The "Fourth State of Matter", often called plasma, differs from the solid, liquid and gas state by its significant number of electrically charged particles which affect its electrical properties and behaviour. Besides being inherent in our daily lives through many aspects, plasmas make up more than 99 percent of the visible universe.

An ordinary gas is electrically "neutral". Indeed, in each atom the positive charges of the nucleus are balanced by an equal number of negatively charged electrons. A gas turns into plasma when insertion of heat or of other energy can induce the release of some or all electrons from a significant number of atoms, so that the electrical characteristics of the gas are macroscopically affected. Atoms being left with a positive charge, the detached negative electrons are free to move about and both atoms and the resulting electrically charged gas are said to be "ionized."

Atomic spectroscopy is a powerful tool for characterizing plasma properties such as their thermodynamic state and transport. The determination of the populations and degree of ionization of species inside the plasma requires knowledge of the production rates (cross sections) for many atomic processes. Beyond their fundamental interest, photoionization of ions is particularly important for such different fields as astrophysics, planetary sciences and, more generally, all applications of energetic plasmas (food processing, waste disposal, fusion research, X-ray laser, electronic etching or implantation). Photoabsorption cross sections are fundamental information needed for the description of radiation transfer, the main way for energy to diffuse inside the plasma.

The main obstacle to experimental studies in this field is the difficulty to produce clean targets of multiply-charged ions with density high enough to compensate for both the relatively low flux of the available XUV photon sources and the low value of photoionization cross sections. One technique allowing for the measurement of absolute photoionization cross sections on a large variety of ion samples was implemented during the 80's in Daresbury [1]. It consists in merging two beams: one of mass-selected ions and one of energy-selected synchrotron radiation. The major limitation of this method is that the ionic target is often composed of a mixture of ions in different excited states, as the time of flight of the ions between the source and the interaction region is very short (typically a few μsec). The determination of the population of ions in the different states present in the target usually requires theoretical data.

We propose [2] a new method to measure the photoionization cross sections of the pure ground level of ionic species: *store ions in a trap and wait for a time long enough for excited states to radiatively decay to the ground state before their irradiation*. To this purpose, we installed the MICRA [3] (Mobile Ion Cyclotron Resonance Analyzer) Penning ion trap on the low energy branch of the Gas Phase Beam-Line, in order to analyze the change of the photoion population as a function of photon energy.
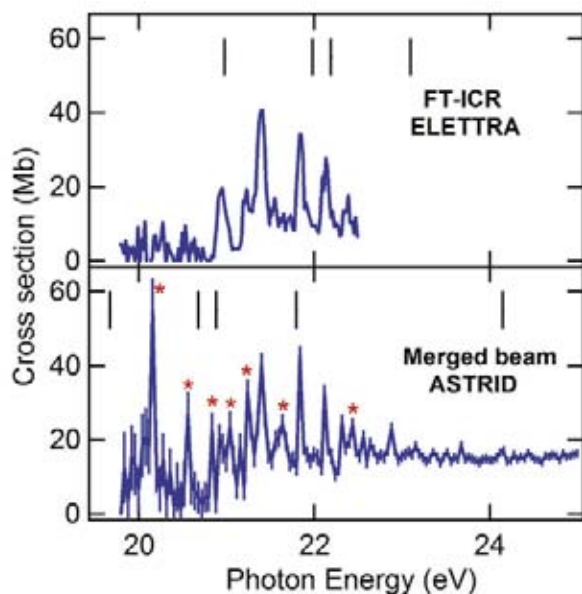
Figure 1.
Variation of the photoionization cross sections of Xe+ ion (blue lines). Upper panel: with ion trap result; lower panel: the merged beam experiment. The vertical bars give the position of the various ionization thresholds for ions in the ground and metastable levels. The asterisks correspond to transitions from the metastable level.

The target ions are first produced by electron ionization of Xe atoms, producing the Xe^+ ions in both fundamental $^2P_{3/2}$ and metastable $^2P_{1/2}$ state. After a 1 s delay for relaxation, the Xe^+ ions are irradiated for 1.3 s and the mass spectrum of ions in the trap is recorded. The resulting photoionization (Xe^{2+} signal) spectrum is shown as the thick curve on the upper panel of Figure 1. The spectrum clearly shows a rise of the signal at 20.9 eV, the energy of the first threshold for the direct photoionization process:

$$Xe^+ \, 5p^5 \, ^2P_{3/2} + h\nu \rightarrow Xe^{2+} \, 5p^4 + e^-$$
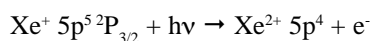
The positions of the thresholds for the various terms of the Xe^{2+} $5p^4$ configuration are shown as vertical bars. Above the continua produced by process (1), prominent lines are observed. In our spectrum, the absence of signal below 20.9 eV demonstrates that the ions in the trap are in the ground level at the moment of the irradiation.

The measurement was reproduced using the merged beam experiment at ASTRID [4]. The spectrum obtained is shown in the lower panel of Figure 1. In addition to the previously observed lines, new ones, marked with an asterisk, appear. The most intense is below 20.9 eV and reveals an overwhelming contribution of Xe^+ ions in metastable levels.

This work shows that an ion trap coupled to synchrotron radiation allows for the measurement of a pure ionic population. Further developments are foreseen, since the possibility of doing in-cell chemistry with mass selected ions opens new opportunities for studies in fields including spectroscopic and dynamic studies on molecular or cluster ions, multiply charged molecular ions, bio molecules, etc.

References

[1] J.B. West, *J. Phys. B* **34**, R45 (2001).
[2] R. Thissen, J.M. Bizau, C. Blancard, M. Coreno, C. Dehon, P. Franceschi, A. Giuliani, J. Lemaire and C. Nicolas, *Phys. Rev. Lett.* **100,** 223001 (2008).
[3] J. Lemaire *et al.*, *Phys. Rev. Lett.* **89**, 273002 (2002).
[4] H. Kjeldsen *et al.*, *Nucl. Instrum. Meth. B* **234**, 349 (2005)

THE UMBRELLA MOTION OF CORE-EXCITED CH$_3$ AND CD$_3$ METHYL RADICALS

U. Ekström[1], V. Carravetta[2], M. Alagia[3,4], M. Lavollée[5], R. Richter[6], S. Stranges[3,4,7]

[1] *Department of Physics, Chemistry and Biology (IFM), Linköping University, Sweden*

[2] *Institute of Chemical Physical Processes, CNR, Pisa, Italy*

[3] *Istituto per lo Studio dei Materiali Nanostrutturati, CNR, Roma, Italy*

[4] *Laboratorio Nazionale TASC, INFM-CNR, Trieste, Italy*

[5] *CNRS, Université Paris-Sud, LIXAM UMR 8624, Orsay-Cedex, France*

[6] *Sincrotrone Trieste S.C.p.A., Trieste, Italy*

[7] *Dipartimento di Chimica, Università La Sapienza, Roma, Italy*

**E-mail: Carravetta@ipcf.cnr.it; stefano.stranges@uniroma1.it**

Figure 1.
The potential energy surface for core excited CH$_3$. Contour lines have been drawn with 0.1 eV interval and starting from the minima which are marked with dots; an extra contour at 0.05 eV has also been drawn with a dotted line. The umbrella motion is shown in the insert.

Since 1934, when it was first observed in ammonia, the umbrella nuclear motion (insert of Figure 1) has been widely investigated both from a theoretical and an experimental point of view in a number of molecules. Such nuclear motion, which is typically characterized by a particularly large amplitude, occurs if the molecule can exist in two stable geometrical configurations, which are related by an inversion of the molecular structure and correspond to two symmetric local minima separated by a potential barrier. In a double well potential, such as the one presented in Figure 1 for the electronically excited methyl radical CH$_3$, the potential barrier prevents classical oscillations between the two energy minima, but barrier penetration, a strictly quantum effect known as "tunneling", can produce large umbrella-like oscillations. Such motion leads to a "tunneling splitting" of the vibrational levels that is directly related to the characteristic time needed by the molecule to go from one minimum energy configuration to the other [1].

The umbrella-like motion caused by a core-electron excitation at the central atom of an AX$_3$ molecule could be studied only recently for the methyl free radicals CH$_3$ and CD$_3$ [2,3]. Its observation by x-ray absorption spectroscopy (XAS) [4] is rather difficult, for the intrinsic problems that make vibrationally resolved XAS spectra quite rare in the literature for polyatomic molecules. Due to their fast Auger and radiative decay, core excited states have a very short lifetime that is comparable to the typical time of a molecular vibration. As a consequence the vibrational structure of an XAS spectrum can be easily masked by the large lifetime broadening of the electronic band.

A detailed study of the umbrella-like vibration in inner-shell molecular spectroscopy has been carried out by a joint theoretical and experimental investigation on the lowest-lying planar to non-planar core excitation in the CH$_3$ and CD$_3$ methyl radicals. The high resolution XAS has been recorded for both isotopomers by combining a pyrolytic supersonic jet source (to generate efficiently the radicals) with an intense and high-resolution SR source. The complex vibrational structure observed in the spectra has been theoretically predicted in terms of the excitation of the symmetrical stretching and the symmetrical out of plane bending (the umbrella mode) accompanying the core electron excitation. The strong anharmonicity of the potential energy surface of the excited
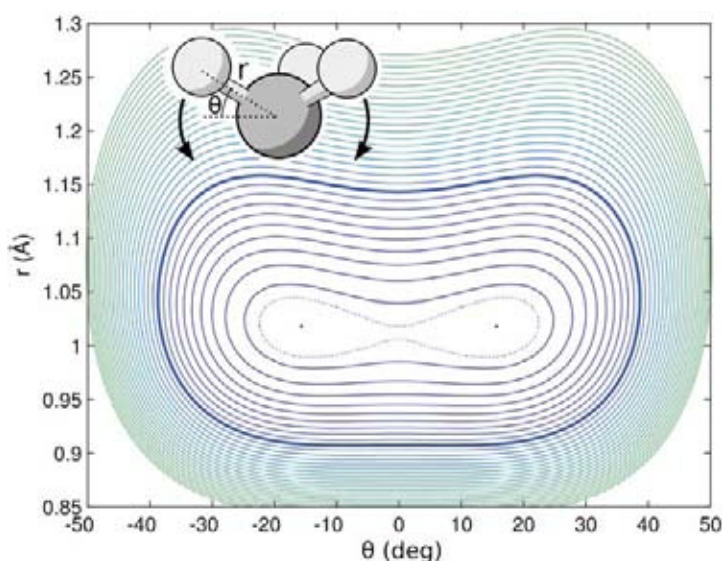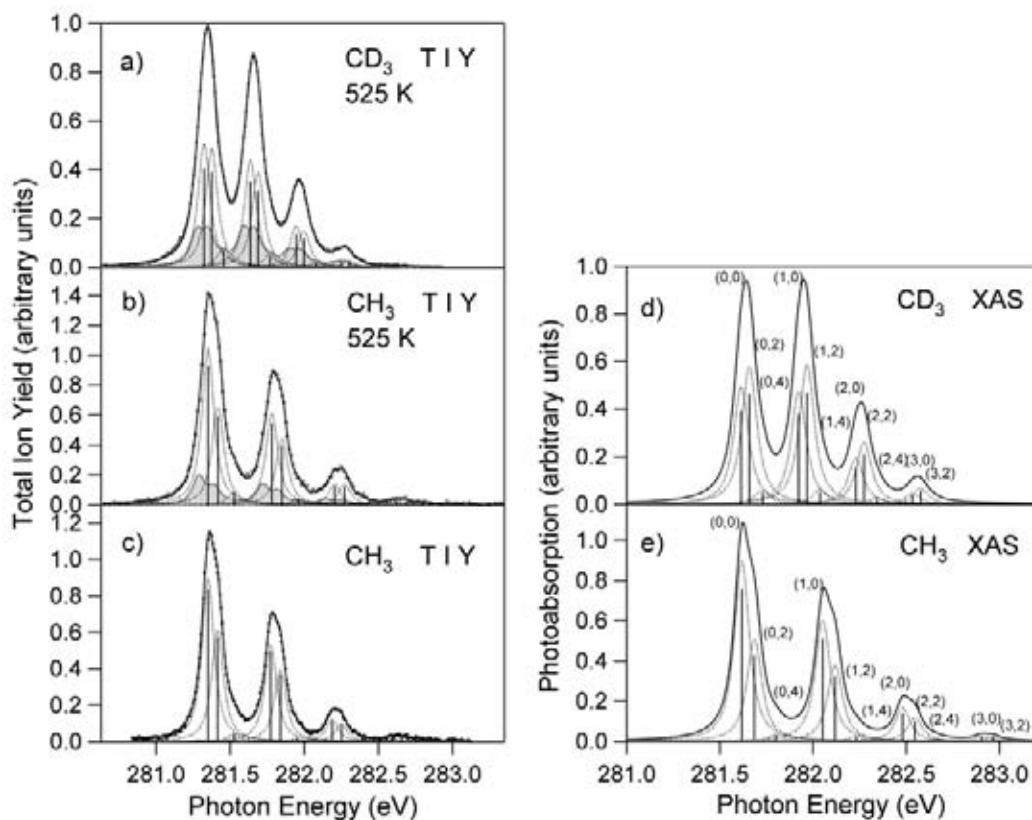
Figure 2.
Left: experimental XAS spectrum of CD_3 and CH_3 recorded with 30 meV photon bandwidth. The spectra of the radical generated in a seeded beam are reported in curves a) and b) where the small hot band contribution is shown in grey. Curve c) reports the spectrum of internally cold CH_3 radicals [1].
Right: calculated XAS spectra; the theoretical relative intensities (Franck-Condon factors) of the symmetrical stretching and bending vibrational progressions are presented as bar diagrams and convoluted (line), using the experimental natural and photon bandwidths, for a better comparison to the experiment.

state (Figure 1) along the bending coordinate has a profound effect on the energy and relative intensity patterns of the bending vibrational progression, with a remarkable isotopic effect. By a detailed theoretical characterization of the double well potential energy surface of the excited state a rather small potential barrier of 45 meV, with a consequently short umbrella inversion time of 149 fs for CH_3 and 375 fs for CD_3 was here estimated, for the first time, for a core excited state.

The excellent agreement between the experimental and theoretical XAS spectra observed in Figure 2 proves that, in the case of the methyl radical, it is possible to calculate high quality potential energy surfaces for core-hole states using spin-restricted Kohn-Sham DFT, and that the adopted model for the vibrational motion including the explicit coupling of only the two symmetrical modes, that allow the molecule to move from the planar to the pyramidal equilibrium geometry, is valid. Extending the study of CH_3 to the isotopomer CD_3 has improved our understanding of the XAS vibrational structure and provided additional information on the accuracy of the theoretical-experimental approach used in this work. This kind of investigation is planned to be also extended to the low symmetry methyl radicals CH_2D and CD_2H.

References

[1] E. Merzbacher, "*Quantum Mechanics*", New York: John Wiley & Sons, Inc. (1970).

[2] M. Alagia, M. Lavolee, R. Richter, U. Ekstrom, V. Carravetta, D. Stranges, B. Brunetti and S. Stranges, *Phys. Rev. A* **76**, 22509 (2007).

[3] U. Ekstrom, V. Carravetta, M. Alagia, M. Lavolee, R. Richter, C. Bolcato and S. Stranges, *J. Chem. Phys.* **128**, 44302 (2008).

[4] J. Stöhr, "*NEXAFS Spectroscopy*", Berlin: Springer-Verlag (1992).

SYNCHROTRON-LASER TWO-COLOR EXPERIMENTS AT THE GasPhase BEAMLINE: EXPERIMENTAL SETUP AND FIRST RESULTS

A. Moise[1], M. Alagia[2,3], L. Banchi[1], M. Ferianis[1], K. C. Prince[1,3], R. Richter[1]

[1] *Sincrotrone Trieste S.C.p.A., Trieste, Italy*

[2] *ISMN-CNR, Sez. Roma 1, Roma, Italy*

[3] *Laboratorio Nazionale TASC, INFM-CNR, Trieste, Italy*

E-mail: robert.richter@elettra.trieste.it

Two color experiments are used in many laboratories to study the dynamics of atomic and molecular processes. Usually the experiments are performed using two (or more) synchronized lasers, to prepare the target in a particular well defined state and probe the products of the process. The large range of wavelengths and pulse lengths available, together with the high sensitivity guaranteed by the high number of photons per pulse allows the detailed study of even very low cross section processes. Due to progress in high harmonic generation those studies now extend even to the attosecond time scale and into the soft x-ray region [1]. A natural extension of the laboratory multi-color studies is the application of synchrotron-laser experiments, especially in the range of ionizing radiation processes. Synchrotrons are widely tunable, and provide high average flux over the whole range of energies. They also provide relatively short pulses, allowing the study of dynamics. The typical pulses of third generation storage rings are in the low picosecond range, although techniques like laser slicing are now employed to generate short x-ray pulses. The coupling of lasers and synchrotrons was started already in the eighties at second generation light sources. Those pioneering studies were very important to show the potential of such experiments. With the development of third generation light sources the available photon flux and resolution have improved, but the main experimental difficulties have remained unchanged [2]. Although synchrotrons are

Figure 1.
(a) Direct and resonant two-color photoionization of noble gases.
(b) Lifetime measurement of the 1s3p $^1P^o$ state of helium (dots). The graph includes a simulation of the signal (red line) using the Elettra bunch structure (blue line) and the known lifetime of the state (black dotted line).
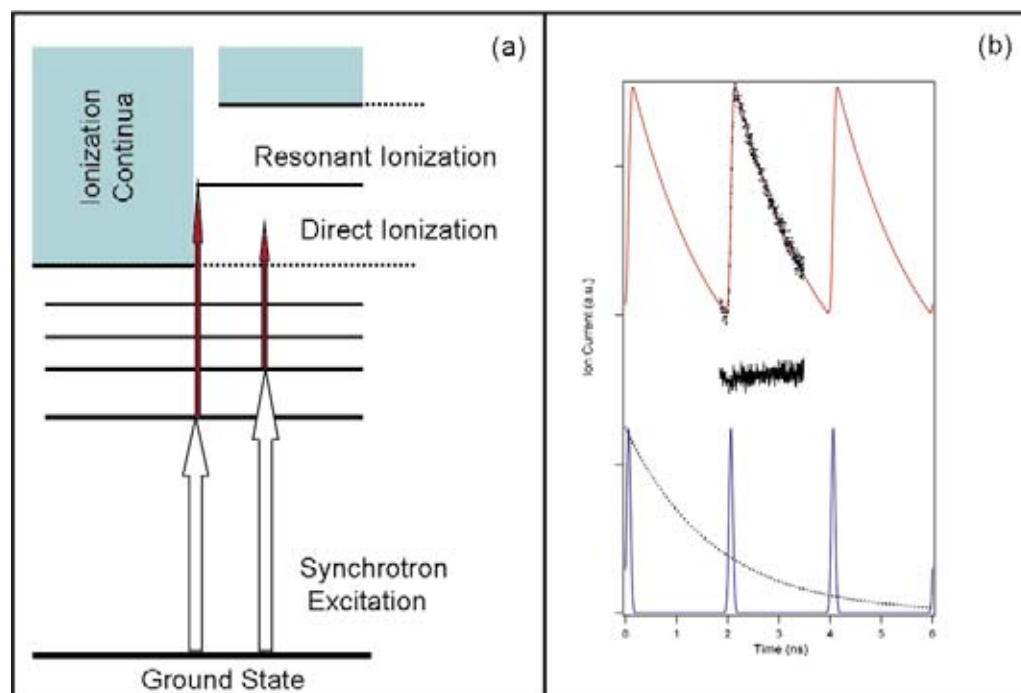
pulsed light sources, the time structure is very different from typical laser sources, as it depends on the electron bunch structure of the storage ring. The other main difference is that, although the average numbers of photons of the two sources are becoming more similar, the photons available per laser pulse or synchrotron bunch are widely different. The most common mode of operation for many light sources is multibunch – the ring is filled with many electron packets, and in the case of Elettra the separation between the pulses is ~ 2 nanoseconds. This high repetition rate cannot be matched by the lasers, causing additional difficulties in synchronization and data acquisition.

We describe experiments carried out using a tunable mode-locked Ti:Sapphire oscillator and synchrotron light pulses in the EUV range [3]. Synchrotron radiation was used to prepare the target (here noble gas atoms) in a well defined quantum state, which was then ionized directly into the continuum, or via an autoionizing state, by the laser. A schematic picture of the processes is shown in Figure 1a.

In the first case – the ionization into the continuum – the use of a pulsed laser permits the determination of the lifetime of the excited state by varying the delay between the laser and synchrotron light pulse. A measurement performed in this way does not rely on the time resolution of the detectors, but depends entirely on the synchronization of the laser and synchrotron light pulses. Results obtained for the 1s3p state of helium are shown in Figure 1b. The setup is suitable to study the dynamics from a few nanoseconds down to 10s of picoseconds during multibunch operation of the storage ring [3].

Ionization via autoionizing states embedded in the ionization continuum allows the exploration of highly excited states of the target. In noble gases the single photon ground state absorption spectra are dominated by the ns and nd series. The widths, positions and shapes of the autoionizing resonances strongly depend on electron correlation and have been the subject of many theoretical investigations. Rydberg series of even parity are not accessible in transitions from the atomic ground state due to selection rules, but can be studied via double-resonance schemes. We show an overview of the neon nf' Rydberg series using a combination of laser and synchrotron radiation. The synchrotron wavelength has been fixed to one of the 3d resonances detected by VUV fluorescence (Figure 2a). Then the laser was scanned in the wavelength range 810…890 nm to cover the energy between the two spin-orbit states of Ne+. Two series of Rydberg states are allowed,
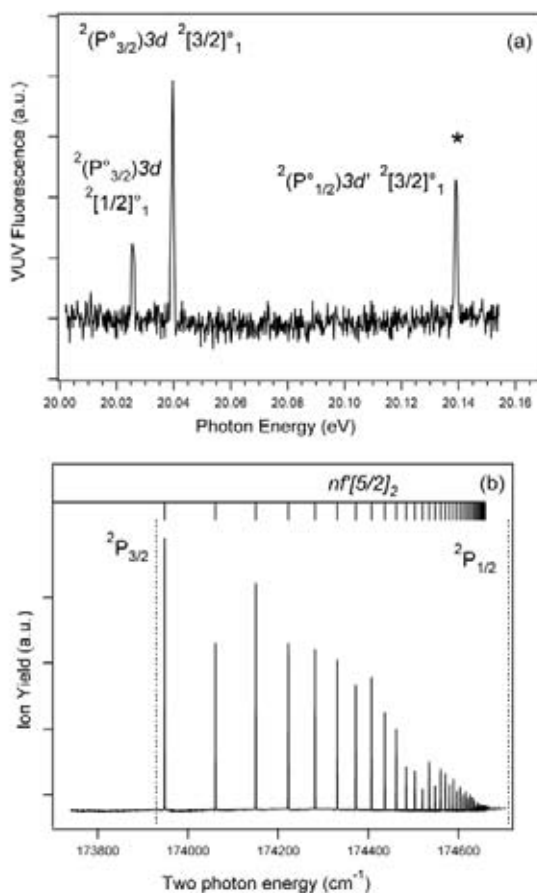
Figure 2.
(a) Part of the neon single photon VUV fluorescence spectrum showing the *3d* group of states. The transition used to record the two-photon spectrum is marked (*). (b) The two color neon ionization spectrum recorded via the ($^2P^\circ_{1/2}$) *3d'* $^2[3/2]^\circ_1$ state. The two-photon ionization thresholds are marked.

but within our signal-to-noise ratio only the nf' has been observed. In the dipole approximation, under field free conditions only transitions to J=2 states are allowed from the J=0 ground state. Thus the series is mainly the nf' $[5/2]_2$ series of Rydberg states. The two color neon spectrum is shown in Figure 2b.

In the described experiment the laser has been used together with a PEPICO mass spectrometer, but signal levels have demonstrated that experiments using other configurations available at the beamline are possible.

References

[1] M. Drescher, M. Hentschel, R. Kienberger, M. Uiberacker, V. Yakovlev, A. Scrinzi, Th. Westerwalbesloh, U. Kleineberg, U. Heinzmann, and F. Krausz, *Nature (London)* **419**, 803 (2002)

[2] F. J. Wuilleumier and M. Meyer, *J. Phys. B: At. Mol. Opt. Phys.* **39**, R425(2006)

[3] A. Moise, M. Alagia, L. Banchi, M. Ferianis, K. C. Prince and R. Richter, *Nucl. Instrum. Methods A* **588**, 502 (2008)
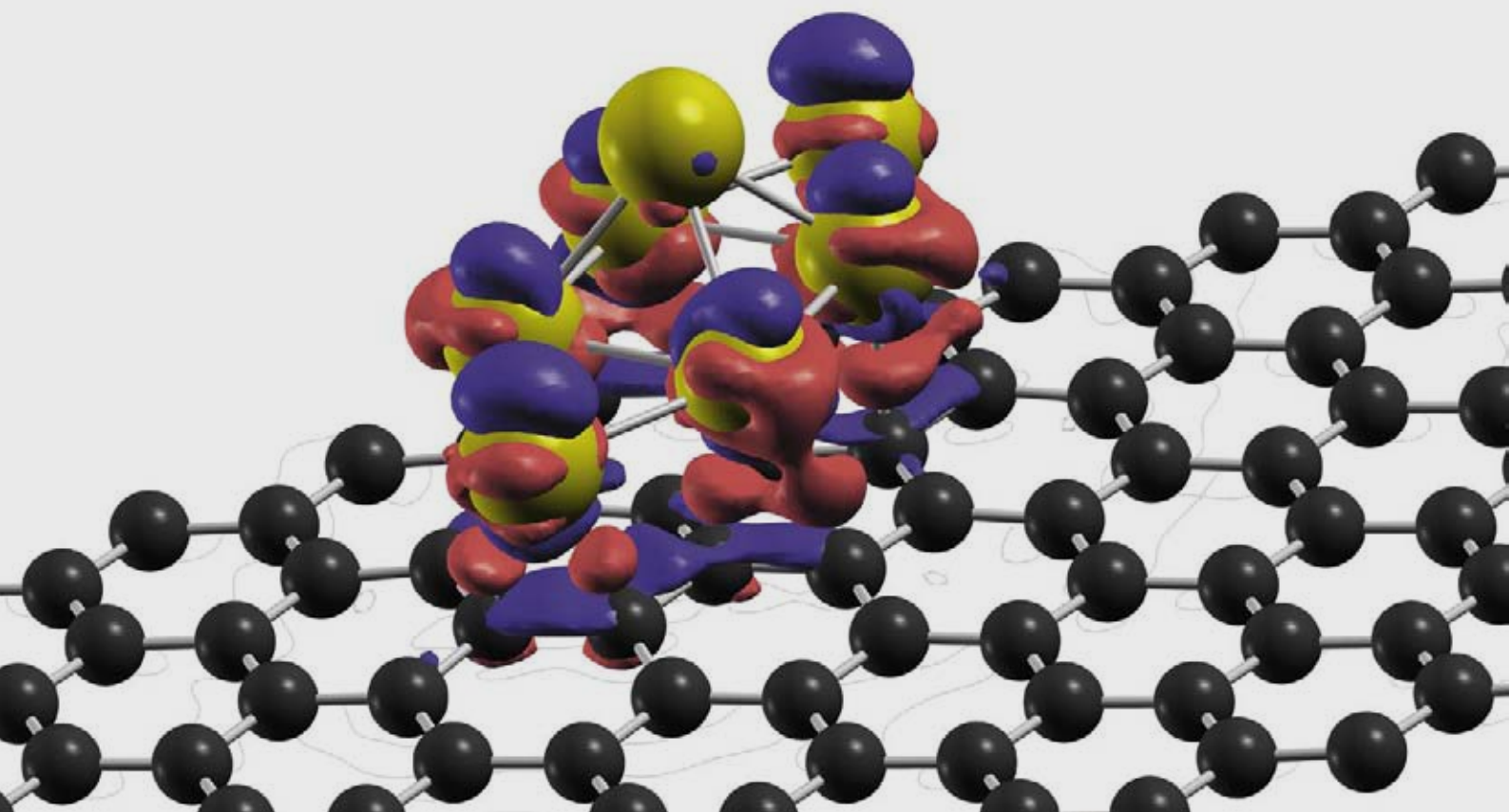
The numerical simulation of matter at the nanometric scale is proving to be the missing link between experiment and theory. The role of computers in science is twofold. On the one hand, they allow one to solve equations that could not be tackled by any analytical methods. On the other hand, computers give access to virtual experiments in which the representation of the physical reality, though necessarily schematic and simplified, can be tuned and varied at will down to atomic details. When real experiments can be done, simulations give predictions, interpretations, as well as a very accurate assessment of theories and models. In other cases (actually the most interesting), by means of virtual experiments, computers permit investigation of properties and processes that cannot be directly observed in real experiments, thus providing a unique insight into the system being studied, complementary to that obtained in the laboratory.

Large-scale facilities are the ideal environment for the development of a multi-disciplinary approach to complex problems in the physics and chemistry of matter at the nanometric scale, and for the nucleation of collaborations between theorists, experts in computer simulation, and experimentalists. These collaborations result in a scientific output that is way superior to the sum of the inputs from the individual disciplines.

The Theory@Elettra group is a joint initiative of the Elettra Synchrotron Radiation Laboratory and the DEMOCRITOS National Simulation Center of INFM-CNR. The group is located in the premises of the Elettra laboratory and aims at i) providing direct support to the scientists at the laboratory as well as to the international community active in the field of synchrotron radiation research; ii) developing new theoretical and simulation methods particularly targeted to the problems investigated in synchrotron radiation laboratories; iii) fostering the collaboration between local experimentalists and external theorists, and iv) promoting access to the laboratory by external users.

The first two papers reported in this section, by Umari and Pasquarello and by Stojic et al., are examples of the ongoing effort to extend the scope of first-principles calculations based on density-functional theory to an ever increasing range of processes and properties. In the first paper it is shown how the hyper-Raman spectrum of materials can be simulated on a computer, a task that will allow a thorough characterization of complex systems, such as glasses, by comparing the detailed features of the simulated spectra with those observed in the laboratory. In the second paper N. Stojic extends a technique previously adopted to calculate transmission coefficients in quantum point contacts to a totally different process, namely photoemission from valence electrons at metal surfaces. The other two papers, by Huang et al. and by Ding et al., are examples of fruitful collaborations between scientists of the Theory@Elettra group and experimentalists operating at synchrotron beamlines.

Stefano Baroni

Stefano Baroni is a condensed matter theorist, mostly known for his contributions to the field of quantum simulations of materials. He is full professor of physics at the Scuola Internazionale Superiore di Studi Avanzati (SISSA), head of the condensed matter theory sector of SISSA, and founding director of the CNR-INFM DEMOCRITOS National Simulation Center in Trieste, and former director of CECAM, the Centre Européen de Calcul Atomique et Moléculaire at the École Normale Supérieure in Lyon, France. SB is a fellow of the American Physical Society and a corresponding member of the Accademia Peloritana dei Pericolanti in Messina. He is the deviser and founder of the Theory@Elettra group.

FIRST-PRINCIPLES HYPER-RAMAN SPECTRUM OF VITREOUS SILICA

P. Umari[1], A. Pasquarello[2,3]

[1] Theory@Elettra group INFM-CNR DEMOCRITOS, Trieste, Italy
[2] Ecole Polytechnique Fédérale de Lausanne, Institute of Theoretical Physics, Lausanne, Switzerland
[3] Institut Romand de Recherche Numérique en Physique de Materiaux, Lausanne, Switzerland

E-mail: umari@democritos.it

Hyper-Raman scattering (HRS) is a non-linear three-photons process in which two in-coming photons are scattered into a photon and a phonon. Although the HRS signal is typically ~10^6 times smaller than that for linear two photons Raman scattering (RS), new experimental set-ups permit the achievement of comparable resolutions. The interest in addressing HRS is that there are different selection rules from RS and infrared (IR) spectroscopies. Moreover, there are modes that are inactive both in RS and IR but become visible in HRS. As vitreous materials lack space periodicity, the analysis of their vibrational spectra can provide access to valuable structural information. In particular, in vitreous silica, which is a disordered material formed by a network of corner-sharing SiO_4 tetrahedra, the analysis of the Raman spectrum could provide estimates for the concentration of small ring structures [1]. This was possible through the analysis and comparison of experimental RS spectra with theoretical density-functional results for a model structure previously obtained by a first-principles molecular dynamics simulation. Indeed, it is now possible to calculate within the density-functional framework a large variety of vibrational spectra such as inelastic neutron scattering (INS), IR and the RS in the non-resonant regime. When applied to crystalline materials, for which the structure is known, agreement with the experimental results within a few percent is usually obtained. In our work [2] we introduce a method for calculating within the density-functional framework the HRS in the non-resonant limit and we present results for a model of vitreous silica.

In analogy with linear non-resonant RS processes, non-resonant HRS cross sections are determined by the HRS tensors. These are composed of two terms: the first accounts for the modulation of the first hyper-susceptibility tensor directly by atomic displacements; the second term accounts for the modulation due to electric fields which accompany longitudinal modes. In contrast to RS, this requires also for isotropic vitreous materials consideration of the particular scattering geometry realized in the experimental setups. The scheme requires the Born effective charges, the derivatives of the hyper-susceptibility tensor with respect to atomic displacements and the second hyper-susceptibility tensor which can be easily calculated through an approach based on finite electric fields [3].

We apply our method to a model structure of vitreous silica previously generated by first-principles molecular dynamics which consists of 72 atoms at the experimental density. For this model a large variety of spectra such as the INS response, the neutron weighted vibrational density of states, the IR and RS response, has been previously calculated. We show in Figure 1 the HRS spectra for a scattering angle of 90 degrees in the VV and VH configurations. In the insets the spectra are compared to measured results [4] in the frequency range 350-650 cm^{-1} and excellent agreement is found both for the position and intensity of the main peak. We analyze the VH spectra in terms of separate contributions from the first and second term in the HRS tensors. In Figure 1 we show that in the VH configuration most of the spectrum and in particular the main features at ~500 and ~1200 cm^{-1} originate from the modulation due to longitudinal modes. Moreover, this component strongly resembles the energy loss infrared spectrum. In the VV configuration only the first-term in the HRS tensor contributes, and the spectrum resembles the vibrational density of states.
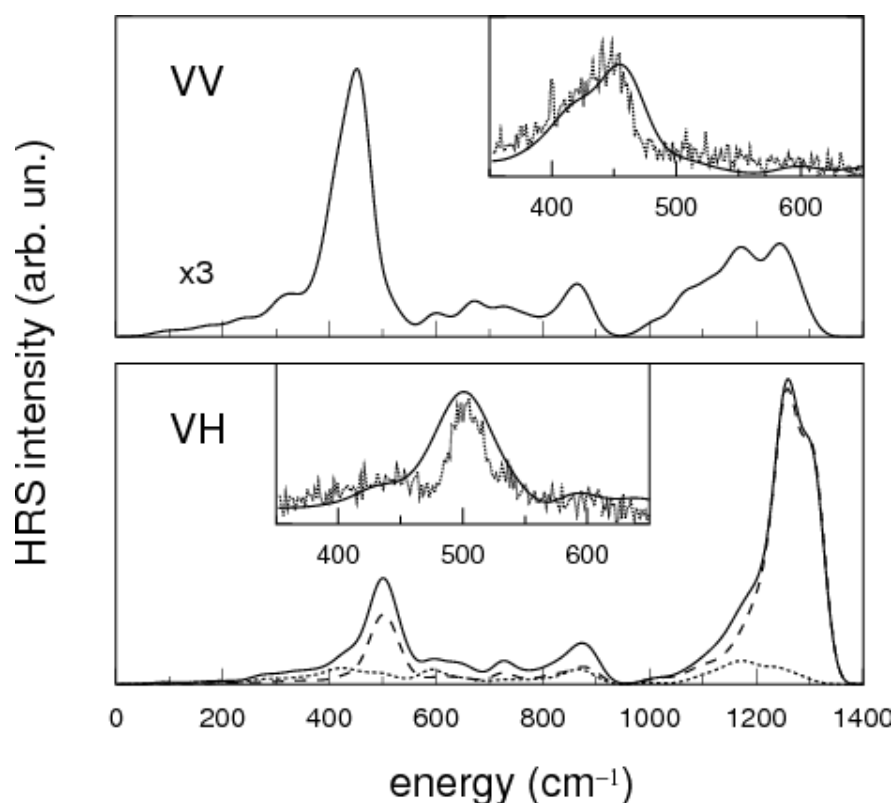
Figure 1.
Reduced HRS spectra of vitreous silica for a scattering angle of 90 degrees. Upper panel: in-coming and out-going photons, vertically polarized. Theory: total (solid line). Lower panel: in-coming and out-going photons, vertically and horizontally polarized, respectively. Theory: total (solid line), contribution from first- (dotted line) and second- (dashed line) term in the HRS. A Gaussian broadening of 16 cm^{-1} has been used. Insets: calculated (solid line) and measured (dashed line) spectrum. The experimental lines are from Ref. [4].

In conclusion, we provided a scheme for the calculation of HRS spectra in the non-resonant regime and could obtain for the first time the HRS spectrum of a disordered material from first-principles. This methodology will open new opportunities for the study of vibrational properties in disordered and complex materials.

References
[1] P. Umari, X. Gonze, and A. Pasquarello, *Phys. Rev. Lett.* **90**, 027401 (2003).
[2] P. Umari and A. Pasquarello, *Phys. Rev. Lett.* **98**, 176402 (2007).
[3] P. Umari and A. Pasquarello, *Phys. Rev. Lett.* **89**, 157602 (2002).
[4] B. Hehlen, E. Courtens, R. Vacher, A. Yamanaka, M. Kataoka, and K. Inoue, *Phys. Rev. Lett.* **84**, 5355 (2000).

AB INITIO SIMULATION OF PHOTOEMISSION SPECTROSCOPY IN SOLIDS: NORMAL-EMISSION SPECTRA OF CU(001)

N. Stojić[1,2], A. Dal Corso[1,2], B. Zhou[3], S. Baroni[1,2]

[1] *Scuola Internazionale Superiore di Studi Avanzati, Trieste, Italy*

[2] *Theory@Elettra group INFM-CNR DEMOCRITOS, Trieste, Italy*

[3] *Laboratorio Nazionale TASC, INFM-CNR, Trieste, Italy*

E-mail: stojic@sissa.it

Photoemission spectroscopy (PES) is one of the most basic techniques for investigating the electronic properties of solids. In practice, however, it is difficult to extract information directly from the observed spectra and theoretical considerations are necessary for a precise determination of the underlying transitions. In the energy range of ultra-violet photoemission spectroscopy (UPS, between 5 and 100 eV), the spectra are dominated by wavevector-conserving transitions (direct transitions) with transition matrix elements differing significantly for any pair of initial and final states. Hence, in UPS, final-state effects play a major role. In empirical approaches these final states are often modelled by free-electron bands, but, in reality, they are influenced by the crystal potential especially at low photon energies and, therefore, their proper description requires detailed calculation.

Despite the wide use of *ab initio* approaches based on density-functional theory (DFT), there have been only few attempts to apply them to the calculations of UPS. In contrast to X-ray PES, for which measured spectra are routinely compared to the *ab initio* density of electronic states, the simulation and interpretation of UPS spectra is highly nontrivial. Using DFT, it is not easy to account for the non-periodic nature of electronic states involved in PES and to accurately describe self-energy effects on the quasiparticle states. We address the first problem by calculating the transmission of electrons from the crystalline medium into the vacuum, using an approach specially developed for our plane-wave-based pseudopotential implementation of DFT [1]. Self-energy effects are accounted for semi-empirically: the real part of the self-energy shifts of DFT bands is described by applying

Figure 1.
An example of all the allowed direct transitions for the Cu(001) spectrum, $\hbar\nu$=23 eV, p-polarization and θ=65˚ (panel a). Panel b) shows the effect of the dipole matrix elements. Panel c) shows the effects of the transmission factors.
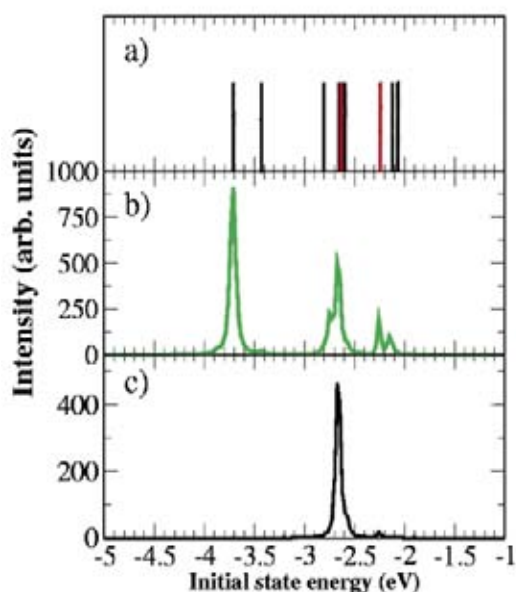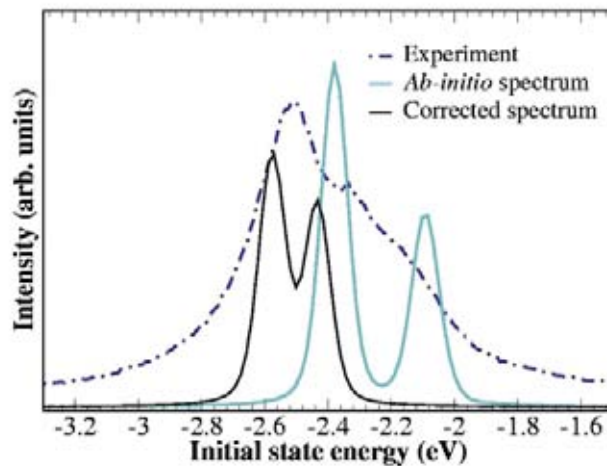
the LDA+U method, while the imaginary part (lifetime effects), is added as an empirical parameter. In our approach, we calculate dipole matrix elements completely *ab initio* and describe the effects of the change of the dielectric function upon crossing the surface (surface-optics effects), by Snell's and Fresnel's equations.

Our approach [2] is based on the bulk three-step model, which breaks the photoemission process into three independent steps: excitation of the photoelectron, its transport through the crystal up to the surface, and its escape into the vacuum. In this model, the photoemission current is proportional to the product of the probability that an electron is excited from an initial bulk state to an intermediate bulk state, times the probability that the electron in the intermediate state is transmitted into the vacuum. The energy and the component of the momentum parallel to the surface are conserved.

In Figure 1 we illustrate the influence of the dipole matrix elements and of the transmission factors on the shape of the spectrum. In panel *a* we show all the direct transitions regardless of the symmetry, their dipole matrix elements, and the transmission coefficients. In panel *b* we calculate the photoemission spectrum setting the transmission factor to be maximum (one) for all the bands. After introducing the dipole matrix elements, only few peaks remain. The addition of the transmission factor (panel *c*) selects the intermediate states with the correct symmetry, imposing the selection rules, and also modulates the peak intensities.

Figure 2 compares our *ab initio* and corrected (LDA+U and surface optics) spectra, with a recently measured spectrum on the Cu(001) single crystal surface at the APE beamline (TASC). The *ab initio* spectrum has the correct number of peaks, but their positions are somewhat shifted and the peak ratio is overestimated. This is improved in the corrected spectrum which shows better agreement with experiment. However, we cannot reproduce the high-energy broad structure present in the experimental spectrum. We explain it by non-direct transitions, allowed due to a small broadening of $k_{//}$ in the experiment.

We have introduced a new method for the *ab initio* low-energy photoemission calculations based on pseudopotentials and plane-waves, which has an advantage in its simplicity and unbiased basis-set, with the possibility to significantly reduce the number of empirical parameters. Our results are in reasonable agreement with experiment for low photon energies. Empirical corrections, including the LDA+U and surface-optics, give significant improvements.

References

[1] A. Smogunov, A. Dal Corso, and E. Tosatti, *Phys. Rev. B* **70**, 045417 (2004).
[2] N. Stojić, A. Dal Corso, B. Zhou, and S. Baroni, *Phys. Rev. B* **77**, 195166 (2008).

LOOKING UNDERNEATH FULLERENES ON Au(110): FORMATION OF DIMPLES IN THE SUBSTRATE

M. Huang[1], S. Fabris[1], M. Hinterstein[2,3], X. Torrelles[2], R. Felici[4], J. Rius[2], H. Fuess[3], M. Pedio[5]

[1] *Theory@Elettra group INFM-CNR DEMOCRITOS, Trieste, Italy*

[2] *Institut de Ciència de Materials de Barcelona, ICMAB-CSIC, Barcelona, Spain*

[3] *Technische Universität Darmstadt, Darmstadt, Germany*

[4] *European Synchrotron Radiation Facility (ESRF), Grenoble, France*

[5] *Laboratorio Nazionale TASC, INFM-CNR, Trieste, Italy*

E-mail: fabris@democritos.it

The adsorption of large organic molecules on metal surfaces can lead to complex nano-structuring of the supporting substrate. The mechanisms driving the substrate reconstruction are controlled by an interplay between intermolecular and of molecule-substrate interactions involving a large number of sites. This can result in either displacive substrate reconstructions, yielding extensive mass transport, and/or in complex structural deformation of the adsorbed molecules. In this context the interaction of fullerenes with surfaces can be seen as a model system. The presence of strong directional π molecular states, together with the capability of being an acceptor or donor of electrons allows fullerene to establish different kinds of interaction ranging from van der Waals to ionic and covalent bonding, through the C atoms that are in direct contact with the substrate.

The interaction between fullerene C_{60} molecules and the Au(110) surface induces a massive *p(6x5)* substrate reconstruction and leads to the formation of surface nanoscale pits [1]. The dimples are one and two layers deep, host the fullerene molecules and allow for a large increase in the metal/molecule contact area. In this study [2] we show that this new configuration alters the electronic properties of the molecule+substrate system as detected by Photoemission (UPS) and Inverse Photoemission (IPE). Our numerical simulations based on density functional theory (DFT) shows that the driving force for the surface reorganization is provided by the formation of strong directional C-Au bonds resulting from the hybridization between the molecular π orbitals and the surface *s* metal states.

DFT calculations based on plane-waves pseudopotentials, and periodic supercells provide insight into the molecular bonding mechanism inducing the nanopit formation at the C_{60}/Au(110) interface. The electronic ground state was calculated for the local geometry of the fullerene adsorbed in the Au nanopits; this geometry was obtained experimentally from synchrotron radiation surface x-ray diffraction data [2]. The calculated bonding charge, the density of electronic states (DOS), and the partial DOS (C p-DOS, resulting from projecting the wave functions on the atomic C-2p states) provide evidence of strong directional C-Au bonding (Figure 1).

The bonding charge density is mostly localized between the lateral C atoms in contact with the nanopit edges, while the interstitial region directly underneath the C_{60} is not primarily involved in bond formation. The degree of directional electronic contribution to the bonding is showed in Figure 1A by charge accumulation (red pockets) localized along the shortest C-Au bond lengths (marked by dashed lines and ranging between 3.1-3.3 Å). Moreover, molecular adsorption induces the polarization of the C_{60} molecule, involving mostly the C atoms on the lower half of the molecule.

Any ionic contribution to the C_{60}/Au(110) bonding would result in new molecular features at the Fermi level due to the population of the C_{60} LUMO, like those measured in the C_{60}/Ag and C_{60}/Cu systems. In the present case, both the photoemission spectrum and the calculated DOS (Figure 1B) do not present any new feature between the Fermi level and the C_{60} HOMO. The same conclusion can be drawn from the analysis of the unoccupied states (conduction band inverse photoemission
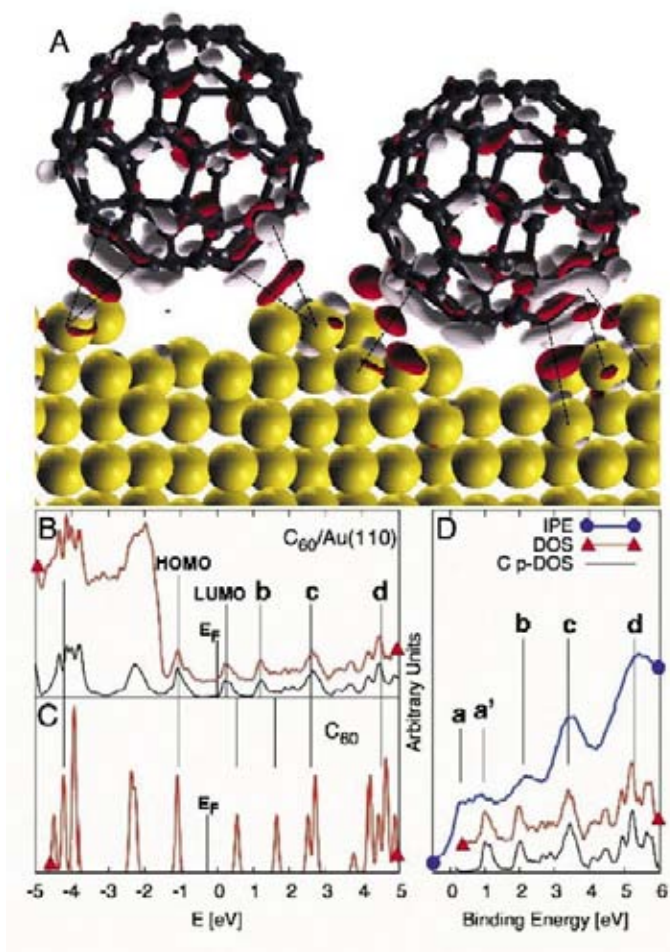
Figure 1.
(A) Bonding charge density obtained from DFT. Positive and negative electron density isosurfaces ($|0.006|$ e/Å^3) are displayed in red and light gray areas, respectively.
(B) Experimental PE spectrum (red), calculated DOS (black) for C_{60}/Au(110) and (C) C p-DOS for an isolated C_{60} molecule. (D) Conduction band IPE data and C p-DOS for C_{60}/Au(110).

data [3], IPE, and DOS in Figures 1B and C). With respect to an isolated C_{60} molecule (Figure 1C), the LUMO and LUMO+1 states (labeled b) are shifted to lower energies upon adsorption (Figure 1B) but no significant fraction of the C_{60} LUMO is transferred below the Fermi level.

Moreover, the HOMO and the higher energy molecular states (labeled c and d in Figure 1b and c) are not affected by the molecular adsorption. This allows us to align the calculated energies of the c and d states to the corresponding features in the IPE (Figure 1d). By doing so, we conclude that the broad feature above the Fermi level (a and a`) results from two different origins: a flat contribution from the gold *s* states (a) and the molecular LUMO (a'). At higher energies, the spectrum is dominated by the three distinct molecular peaks (b, c, and d in Figure 1d).

The additional charge available after C_{60} adsorption is redistributed in the contact interfacial region and substrate mass transport takes place in order to form and maximize the number of strong directional bonds. In *fcc* metals, the hexagonal structure of the (111) surfaces allows the formation of 12 C-metal

bonds by surface vacancy formation, as in the case of C60/Pt(111) [4]. Mass transport is facilitated on more open substrates, like the Au(110) surface, where the number of bonds can be maximized according to size and shape of the nanopit. In the present case, the measured fullerene corrugation is determined by the presence of two different adsorption sites related to different depths.

This study demonstrates that the 6x5 reconstruction of the Au(110) surface upon fullerene adsorption yields the formation of nanopits at the interface which are one and two layers deep. The larger fullerene/metal contact area allows for the formation of a large number of C-Au covalent bonds.

References

[1] M. Pedio *et al.*, *Phys. Rev. Lett.* **85**, 1040 (2000).
[2] M. Hinterstain *et al.*, *Phys. Rev. B* **77**, 153412 (2008).
[3] M. Pedio *et al.*, *J. Electron Spectrosc. Relat. Phenom.* **76**, 405 (1995).
[4] R. Felici, M. Pedio, and F. Borgatti, *Nat. Mater.* **4**, 688 (2005).

CARBON DIOXIDE ACTIVATION AND HYDROGENATION ON Ni SURFACES FOR ORGANIC SYNTHESIS

X. Ding[1], M. Peressi[1,2], A. Baldereschi[2,3], E. Vesselli[4,5], L. De Rogatis[5,6], A. Baraldi[4,5], G. Comelli[4,5] , R. Rosei[4,5], P. Fornasiero[6], L. Savio[7], L. Vattuone[7], M. Rocca[7]

[1] *Theory@Elettra Group, CNR-INFM DEMOCRITOS, Trieste, Italy*

[2] *Department of Theoretical Physics, University of Trieste, Italy*

[3] *CNR-INFM DEMOCRITOS, Trieste, Italy and EPFL, Lausanne, Switzerland*

[4] *Department of Physics, University of Trieste and CENMAT, Trieste, Italy*

[5] *Laboratorio Nazionale TASC, INFM-CNR, Trieste, Italy*

[6] *Department of Chemistry, University of Trieste, Italy*

[7] *Department of Physics, University of Genova, Italy*

E-mail: maria.peressi@ts.infn.it

There is a great interest in carbon dioxide (CO_2) chemistry, not only for its capture to reduce greenhouse effects, but also for its storage and recycling in useful technological applications as a synthesis feedstock. As an example, it is a key compound for the synthesis of methanol, according to the reaction $CO_2 + 3H_2 \leftrightarrow CH_3OH + H_2O$, a promising candidate as energy carrier to feed internal combustion engines or fuel cells.

CO_2, however, is a closed shell, stable, and poorly reactive molecule, making difficult the development of low-cost and efficient catalysts for its conversion. Cu-based catalysts are normally used, but recent experimental findings indicate that model Ni/Cu catalysts are 60 times more active for CO_2 hydrogenation than traditional pure Cu ones. Formate (HCOO) has been identified as the first intermediate in the methanol synthesis. However, not only the details of the reaction path are unknown and the promoting role of Ni is obscure, but, surprisingly, there is a lack of knowledge concerning even more basic questions, such as the CO_2 interaction with Ni and other transition metal surfaces.

Although available techniques, both experimental and theoretical, do not allow us to follow in detail the evolution of the catalyst and the whole reaction under standard temperature and pressure conditions, investigations performed on model systems for simplified reaction schemes can contribute to a deeper comprehension of heterogeneous catalytic organic synthesis processes involving carbon dioxide as a reactant and therefore can suggest the design of new and more efficient catalysts.

The comprehensive study of the mechanism of chemisorption, activation and hydrogenation of CO_2 on Ni by characterizing the stable intermediates of the reaction and by identifying the relevant reaction paths has been made possible by a close collaboration between theoreticians and experimentalists, covering several complementary competences [1-4]. Geometries, adsorption energies, and vibrational frequencies of adsorbed CO_2, HCOO and related transition states as well as reaction/diffusion energy barriers are obtained by atomic-scale quantum mechanical numerical simulations, providing a guide for experiments and for the interpretation of experimental data and allowing us to propose a full description of the mechanism.

Ni(110) is the only transition metal, low Miller index surface to which CO_2 chemically binds. The molecule receives electronic charge from the metal, bends, and binds to the surface with the carbon atom in a "V" configuration. When adsorbed H approaches CO_2, the H-CO_2 complex flips and binds to the surface with the two oxygen atoms and H binds to the carbon atom, thus yielding the formate intermediate which is known to exist in such a "reversed Y" configuration and to be present also under real catalyst working conditions. The resulting energy barrier for CO_2 hydrogenation is relatively small (0.43 eV) and, most importantly, smaller than that for CO_2 desorption and that for dissociation into CO + O. The presence of hydrogen steers the
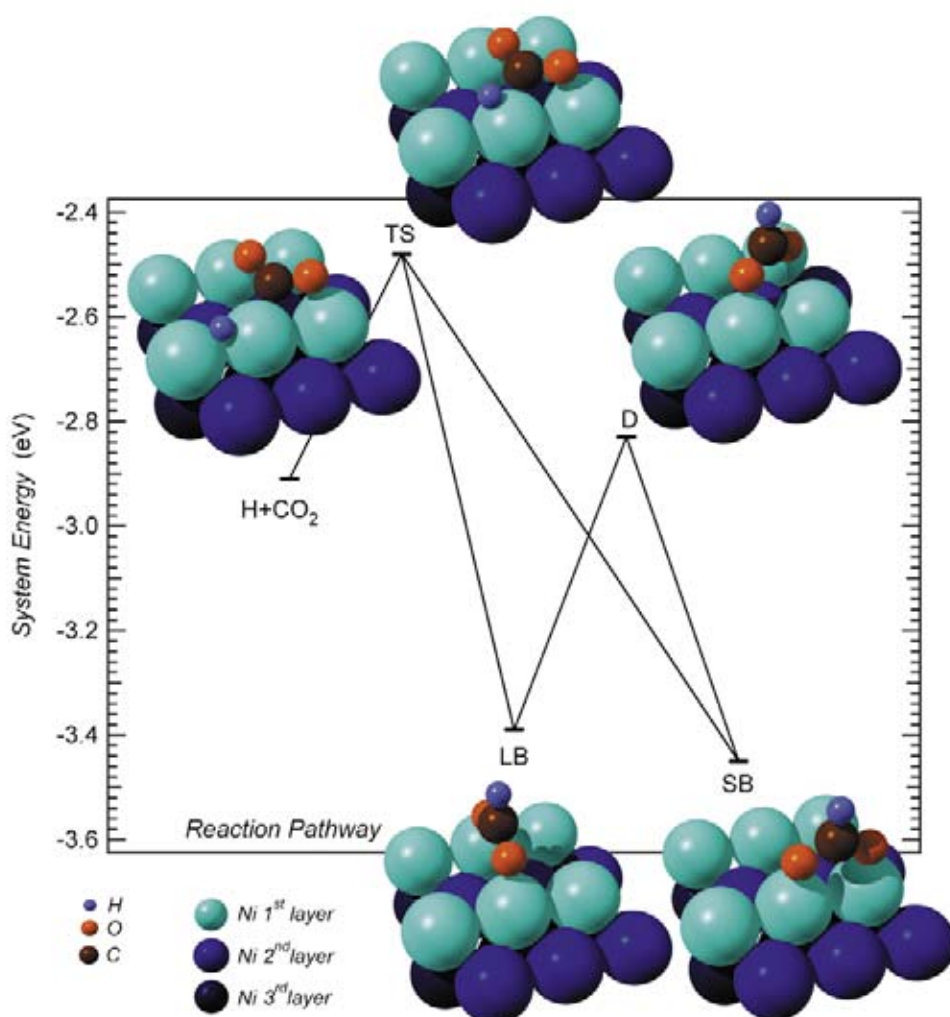
Figure 1.
Results of numerical simulation for the CO_2 + H → HCOO reaction. Energies (with respect to gas-phase H and CO_2) and geometries are given for the most relevant states, starting from coadsorbed H and CO_2, with CO_2 charged, bent and bonded to metal in a "V" shaped configuration. LB and SB indicate the long- and short-bridge adsorption sites of the "reversed Y" HCOO, respectively, which are both possible and almost energetically equivalent. TS indicates the transition state of the reaction, responsible of the hydrogenation energy barrier, while D is that of formate diffusion between the two possible states. Only the outer three Ni layers are shown, but a thicker slab has been used in the calculations.

reaction in the desired direction and prevents the formation of CO which is unreactive. This is the key point of CO_2 + H chemistry on Ni(110), since the charge transfer from the metal to the molecule yields an activated state which is reactive with hydrogen via an induced flip of the complex. This does not occur on Cu, where CO_2 is not activated by the metal, interacting only very weakly, remaining neutral, linear and unreactive: its first hydrogenation requires therefore a much higher reaction barrier (~1 eV). This provides possible explanations for the promoting role of Ni in Ni/Cu catalysts.
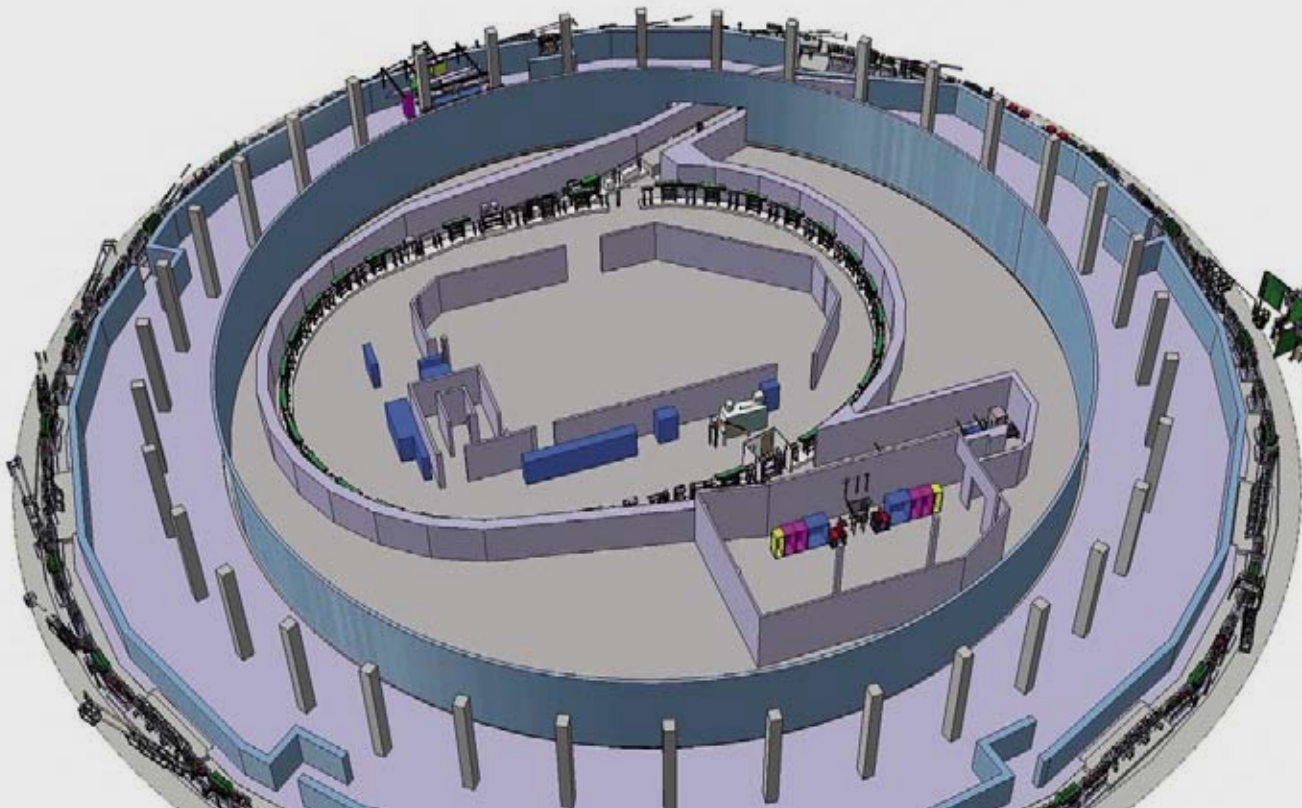
References
[1] E. Vesselli *et al*., *J. Am. Chem. Soc*. **130**, 11417 (2008).
[2] X. Ding *et al*., *Phys. Rev. B* **76**, 195425 (2007).
[3] X. Ding *et al*., *Mat. Sci. Eng. C* **27**, 1355 (2007).
[4] X. Ding *et al*., *AIP Conference Proceedings* **1018**, 197 (2008).

FACILITY HIGHLIGHTS

ELETTRA AND INSTRUMENTATION
RESEARCH

Scientific breakthroughs very often or perhaps normally are not the result of a linear process of development. They result from some form of jump in our understanding of a subject. They can be catalyzed by a theoretical leap forward in which an entirely new concept is developed, or by new measurements methodologies, capable of giving an entirely new level of information. Developments of new measurement methodologies have often led to scientific breakthroughs, for example and perhaps most famously, the development of the Scanning Tunneling Microscopy (STM). This example gives us many interesting clues to how revolutionary ideas are developed. Firstly, the problem that Binnig and Rohrer originally were trying to solve was really quite disconnected from the eventual uses of STM in surface science; they needed to find a way to image defects in the oxide layers in a Josephson junction. Secondly, although the brilliant realization that tunnel currents from atomically sharp tips could lead to scanned atomic resolution images was made in 1978, it took 4 years for the first breakthrough result to be achieved in the imaging of single atomic steps in Au(111) in 1982, followed by the iconic images of the Si(7x7) reconstruction in 1983. Their first paper on the topic was also rejected. Clearly in instrumentation, brilliant concepts usually have to be followed by years of persistence! Thirdly, inventions can lead in unexpected directions. Although the STM was a breakthrough in surface science, the closely connected invention of the AFM by Binnig, Quate and Gerber in 1986 arguably has spawned many more discoveries, due to its amazing variety of imaging modalities. In synchrotron radiation research, if we look for potentially revolutionary breakthroughs, we can perhaps point to x-ray imaging as an example. Although x-ray holography was first described decades ago, it has only been with the development of very high brightness x-ray sources, good detectors, fast computer algorithms and sophisticated sample environments has the field started to take off. For example, experiments at the FLASH FEL by Chapman *et al.* have demonstrated fsec pump probe imaging and very recent experiments at ALS by Marchesini *et al.* have shown how it is possible to use a uniformly redundant array as a reference object, speeding up acquisition by factors of thousands. These instrumentation developments potentially will have enormous scientific impacts, from nanoscience to biology. Although considered to be 'science fiction' only a few years ago, with vision, persistence, patience and the ability of those involved to pick the right targets for their work, diffractive x-ray imaging is now rapidly developing. One of the things that made this field possible was the availability of good detectors. These happened to be available based on advances in other fields, but unfortunately, this is usually not the case. The area of detectors still stands as one that has huge potential to push forward x-ray science. Not only can new detector technologies speed acquisition, they can give us access to measurements that were previously impossible. The advent of time stamping pixel detectors will be one development that will clearly spawn many new discoveries.

Finally we should not neglect the machines that give us photons. Important incremental advances in brightness and beam stability are still possible with 3rd generation machines, such as through topoff operation, in-vacuum undulators, and shorter bunches. Of course the largest performance jump is now arriving with the advent of VUV-soft x-ray FELs, and soon hard x-ray FELs, but there will always be a place for the high average power, high repetition rate, and easy tunability of conventional synchrotron sources. The advance of science and the advance of instrumentation are intrinsically linked. With the increasingly sophisticated range of instrumentation tools available today, it is indeed an exciting time to contemplate the advances in science that will be made possible in the next few years.

Howard Padmore

Howard Padmore started out in synchrotron radiation at Daresbury Laboratory, working from the start of SRS operations in 1982 in the surface science group. He became head of the soft x-ray group in 1987, and then moved to Berkeley in 1993 to head the Experimental Systems Group (ESG) at the ALS where he became a Division Deputy in 2003. He leads the ESG in running 10 of the facility beamlines, and in developing new techniques in synchrotron radiation research. His personal work currently is in low energy photoemission and PEEM, applied to photocathodes and solar energy conversion devices as well as ultra-fast studies of material dynamics using x-ray streak camera techniques.

ELETTRA STATUS, ACCELERATOR PHYSICS ACTIVITIES AND PROJECTS

E. Karantzoulis
Sincrotrone Trieste S.C.p.A., Trieste, Italy

E-mail: Emanuel.Karantzoulis@elettra.trieste.it

During 2007 Elettra operated for 5 runs of 4 to 8 weeks each for a total of 5424 hours, of which 3888 (71.7%) scheduled to user experiments with a user uptime (Figure 1) of 90.4% (94.1% excluding beam losses due to storms and external electricity supply interruptions). In addition to storms and external electricity supply interruptions (36.2% of the downtime) the other major causes of downtime were due to delays during the refill phase (18.9%), to the Linac systems (11.3%) and to water-cooling systems (9.4 %) faults. The storage ring operated at 2 GeV for 74.4% of its user time whereas the 25.6% was at 2.4 GeV. The prevailing user operation's mode was multi bunch (97.5% of the time) consisting in filling 415 of the 432 available RF-buckets with 330 mA at 2 GeV and 140 mA at 2.4 GeV with 48 (24 at 2.4 GeV) hours between refills. The remaining 2.5% of user time was dedicated to 4 bunch mode, with 4 equidistant bunches of 32 mA total current at 2 GeV and 8 hours between refills.

A long shutdown of three months during autumn was required for the installation of the new transfer line and septum necessary for the transportation of the electrons from the new Elettra injector to the storage ring. During the other 5 shutdowns of 1 to 2 weeks duration maintenance work was mainly made on the vacuum system, cooling and electrical system, power supplies and radiofrequency. The old RF-plant in section 9 was moved to the booster to be used as the booster RF-plant. Some minor installation concerning the new LIBERA beam position detectors went on to completion during 2007 and so the Global Orbit Feedback that stabilizes the electron orbit to an accuracy of a few microns rms, started operating. Finally, beam loss monitors that show the radiation created when the electron beam hits the vacuum chamber were also installed prior to booster commissioning.

Each of the 5 runs started with a few days dedicated to accelerator physics whereas the total accelerator physics and machine time for developments/projects was 1242 hours or the 23.8% of the total. In Figure 2 the percentage of time distribution can be seen. Thus the SR-FEL (storage ring free electron laser) had the 43% of the Accelerator physics time,
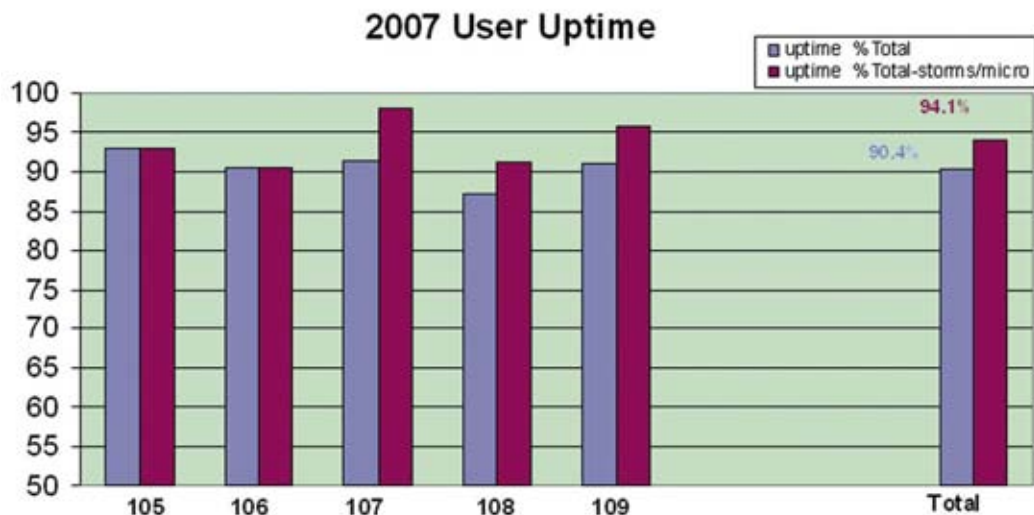

Figure 1.
Blue: user uptime in 2007 with partial uptime during the five runs of the year (105÷109). Red: user uptime excluding beam losses due to storms.

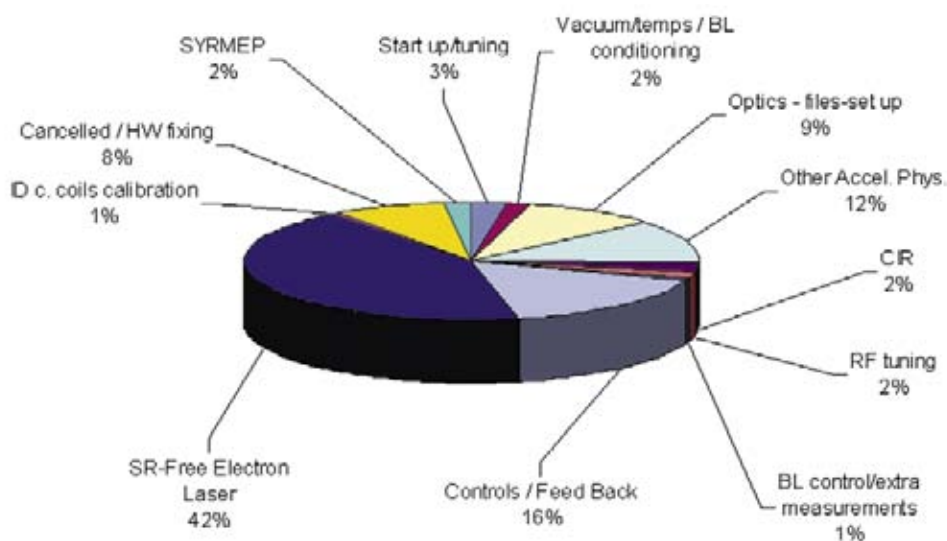## 2007 accelerator physics and project shifts distribution

Figure 2.
Accelerator physics and project beam time distribution for 2007.

feedback systems 16%, optics tuning 10%, other accelerator physics issues 12% whereas an 8% was sacrificed in repairs.

The beam quality is the measure of the "goodness" of a light source. This depends not only upon the up time but also from the lifetime, beam stability and optics amongst other. Thus the third harmonic cavity that triples the beam lifetime at 330 mA allowing 48 hours continuous operations between refills when at 2 GeV operated with practically no problems (only 2.5% of the total downtime). The systems that suppress instabilities (the longitudinal multi bunch instabilities controlled by the third harmonic cavity and those transverse controlled by the transverse multi bunch feedback systems) operated well in improving the beam quality, which is monitored and registered with specially developed software. The Global Orbit Feedback that keeps the beam position and angle stable within a few microns at the source points started operating too with promising results.

The Accelerator physics activities have as objective to improve the functioning of the accelerator complex and its beam quality; to find new modes for beam use and to optimize the new projects and developments ensuring thus the high performance. With the exception of accelerator time dedicated to projects

such as storage ring free electron laser (and its success in the harmonic generation experiment on 19th of April), global orbit feedback tests, optics tuning, the 12% (other accelerator physics in Figure 2) was dedicated to bunch purity and cleaning studies that are of great importance for the few bunch operation, preliminary studies for the top-up which is scheduled to start after the completion of the new Elettra injector, measurements of the machine longitudinal resistive impedance and finally investigating the THz range of coherent radiation in collaboration with the SISSI infrared beam line.

6624 hours of operations are foreseen in 2008, of which 4032 (75.4%) dedicated to the user experiments of which the 77% at 2 GeV and the 23% at 2.4 GeV. The multi bunch mode prevails with 100% of the user scheduled time; no dedicated time for the 4 bunch mode was requested. The machine development time amounts to 2160 hours (25% of total) of which almost 1000 hours are dedicated to booster commissioning. The user uptime for the first half of 2008 is 91.6% (94.1% excluding beam losses due to storms). The Elettra team effort in 2008 is focused mainly on the booster commissioning, the Elettra operations with the new injector and the preparatory work for the top-up.

THE NEW ELETTRA BOOSTER IS IN OPERATION

M. Svandrlik on behalf of the Elettra Booster Project Team
Sincrotrone Trieste S.C.p.A., Trieste, Italy

E-mail: michele.svandrlik@elettra.trieste.it

The new Elettra booster injector is in operation since March 3rd, 2008, as planned in the original time schedule. Elettra was shutdown for 5 months between October 2007 and February 2008 to allow the installation of the new 2.5 GeV transfer line connecting the Booster to the storage ring and to carry out the final part of the booster commissioning.

The Booster Project started in March 2005 and lasted therefore exactly 3 years. The allocated budget over this period was 13.9 M€. Of that amount about 60% went into the accelerator hardware, 40% in building and services. As for manpower, 79 people of the Elettra staff contributed to the project, mostly part time. The manpower employed was 100 man-years for the 3 years duration of the project.

The main project challenge was to replace the existing Linac injector with the new full energy Booster, located in a new building inside the storage ring main building, affecting as less as possible the users' operation of the facility. This required careful planning of both installation and commissioning, foreseeing the consequences of possible delays and programming appropriate back-up plans. Strong overlap between hardware and beam commissioning phases was needed to mitigate the effect of unexpected issues.

Commissioning activities were focussed to get a working injector, in order to avoid delays that would compromise the timely restart of the facility for users. Beam commissioning was performed in three different phases. During the first phase, between September 7th and October 13th, 2007, the beam was first extracted from the gun, accelerated through the linac pre-injector to the nominal energy, 100 MeV, and then injected into the booster. First 100 turns in the booster were obtained on September 26th, while in the following days the beam could be ramped in energy up to 800 MeV and extracted from the Booster. The maximum achievable energy was at that time limited by the booster main magnets power converters, not yet performing to specification.

On December 11th the BTS transfer line installation was completed. During the same shutdown the new injection septa magnets, capable of operating up to 2.5 GeV, were also installed in Elettra. Meanwhile, also improvements on various booster sub-systems were carried out. In particular one of the limiting factors on the power converters, a distortion of the output current waveform at low currents, could be removed. Just prior to the Christmas shutdown, during the second beam commis-

Figure 1.
Frequent injection mode tests performed in February 2008, at 2.0 GeV, insertion devices at maximum gap and beamline shutters closed. Beam current in the storage ring is kept constant between 300 ± 1 mA.
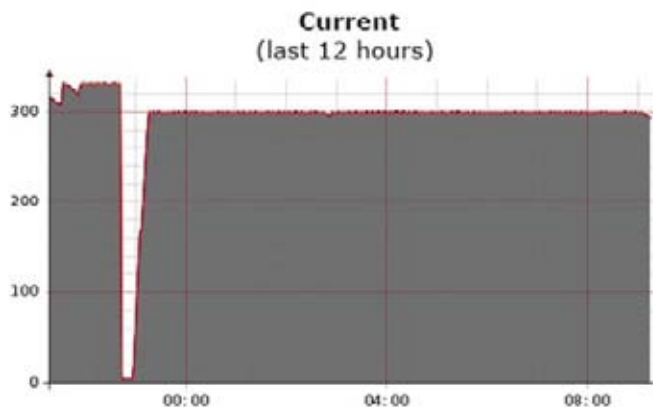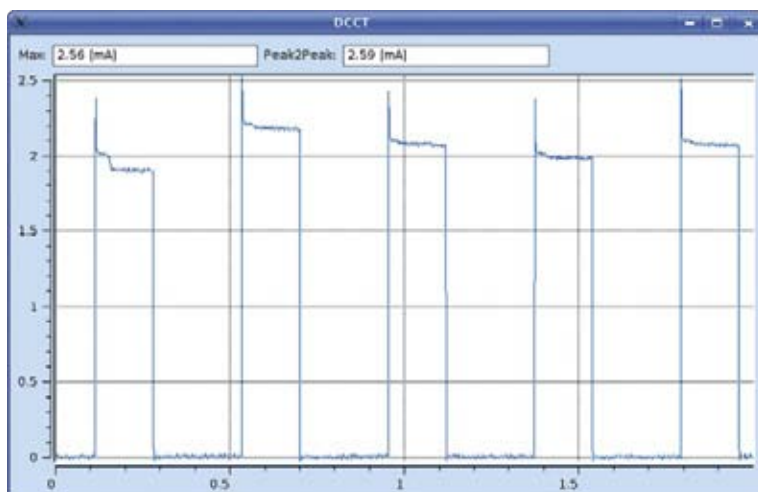
Figure 2.
Booster cycles in August 2008: energy is 2.0 GeV, repetition frequency 2.4 Hz, beam current at extraction 2.0 mA.

sioning phase, the beam could then be extracted from the booster for the first time at 2.0 GeV, in single shot mode.

The Christmas shutdown allowed a further improvement in the performance of the power converters. During the third and final commissioning phase, booster operation at 2.0 GeV, 1 Hz repetition rate, could be established. On February 11th it was finally possible to inject for the first time into Elettra at full energy, i.e. 2.0 GeV. In order to quickly recover good vacuum conditions in the storage ring, after the new septum installation, the beam current intensity in the Storage Ring was kept as high as possible, by successfully testing the frequent injection mode, as shown in Figure 1.

Users' operation at 2.0 GeV started on March 3rd, 2008, with routine full energy refills on top of the stored current. On the 13th of April the beam was then injected in Elettra at 2.4 GeV, the other user operation energy. In May, single bunch operation of the injector was established for Storage Ring FEL users at 0.9 GeV.

In the timeframe between April and August 2008 injection for users has been performed at 0.9 GeV, due to a harmful fault on one of the cabinets of the bending magnets power converters, occurred on April 17th. The repair of this cabinet has been included in a general refurbishing program which is being carried out by the supplier of the converters to finally meet their original specified performance. After the intervention scheduled during the summer shutdown in August, booster operation at 2.0 GeV, 2.4 Hz, 2mA of extracted beam current has been established (Figure 2) with good reliability and improving reproducibility. Injection rates of 1.5 mA/s have then been achieved, with best injection efficiencies measured to be close to 100%.

Reliable operation at full energy allows now to start the top-up mode experiment campaign.

The Booster inauguration ceremony was held on March 28th, 2008. The project was concluded on time and on budget. Key performance achievements are:
- Users' operation at 2.0 GeV established
- Overall efficiency larger than 80%

BEAM EMITTANCE MEASUREMENT FOR THE NEW FULL ENERGY INJECTOR AT ELETTRA

G. Penco[1], L. Badano[1], S. Bassanese[1], G. Ciani[1], P. Craievich[1], S. Di Mitri[1], M. Ferianis[1], M. Veronese[1], M. Predonzani[1], A. Lutman[2]

[1] Sincrotrone Trieste S.C.p.A., Trieste, Italy
[2] DEEI, University of Trieste, Italy

E-mail: giuseppe.penco@elettra.trieste.it

The Elettra new full energy Booster was commissioned and it is now in routinely operation at ELETTRA. During the commissioning of the 100 MeV pre-injector linac, the Twiss functions and the normalized beam emittance was measured in order to match the optics with the transfer line. The diagnostic station, which was installed at the end of straight-on line after the first transfer line bending magnet, is equipped with three types of screens: a YAG:Ce scintillation screen, an OTR and a CHROMOX (Al_2O_3:CrO_2) screen, imaged by a CCD digital camera. To measure the emittance of the beam a quadrupole scan of the QF (for the x-plane) and QD (for the y-plane) was performed. Moreover a four electrode pick-up prototype, designed at DESY, is installed to detect the beam longitudinal structure. A global sketch of this equipment is shown in Figure 1 and readers are referred to [1] for more details.

The phase space coordinates (x, x') of a single particle and the Twiss vector (β, α, γ) are transformed through a beam transport channel $\mathbf{R}$ as following:

$$X_f = \begin{pmatrix} R_{11} & R_{12} \\ R_{21} & R_{22} \end{pmatrix} X_i ;$$

$$T_f = \begin{pmatrix} R_{11}^2 & -2R_{11}R_{12} & R_{12}^2 \\ -R_{11}R_{21} & 2R_{12}R_{21} & -R_{12}R_{22} \\ R_{21}^2 & -2R_{21}R_{22} & R_{22}^2 \end{pmatrix} T_i$$

1)

Defining $\mathbf{Q}$ the quadrupole transfer matrix and $\mathbf{S}$ the lattice transfer matrix up to the screen, the global transfer matrix $\mathbf{R}$ can be written as:

$$\begin{pmatrix} S_{11} + S_{12}K & S_{12} \\ S_{21} + S_{22}K & S_{22} \end{pmatrix},$$

where K is the quadrupole field strength. When the scan is performed on the quadrupole QD to measure the horizontal emittance, $\mathbf{S}$ is the transfer matrix of a drift, while when the scan is on the quadrupole QF, $\mathbf{S}$ becomes

$$\begin{pmatrix} 1 + K_{QD}D & \delta q + K_{QD}\delta qD + D \\ K_{QD} & K_{QD}\delta q + 1 \end{pmatrix}$$

where K_{QD} is QD quadrupole strength, δq is the distance between QD and QF, D is the drift between QD and the screen. The mean square of the bunch transverse size is $\sigma^2 = \varepsilon\beta$, where ε is the geometric emittance: after some calculation σ^2 can be written as a quadratic function of K, with the coefficients as function of the Twiss parameters:

$$\sigma^2 = (S_{11}^2 \varepsilon\beta + 2S_{11}S_{12}(-\varepsilon\alpha) + S_{12}^2(\varepsilon\gamma))$$
$$+ (2S_{11}S_{12}\varepsilon\beta + 2S_{12}^2(-\varepsilon\alpha))K + S_{12}^2\varepsilon\beta K^2$$

Thus the optical functions and finally the geometric emittance is obtained by quadratic fitting the measured mean square of the beam size σ^2 as function of the quadrupole field strength.

A great effort was spent in the images analysis, in order to obtain a reliable estimation of the σ^2 of the bunch. Readers are referred to [2] to have more details. Single bunch simulation performed during the Booster project design phase predicted a normalized emittance at 90% (ε_{90}) of about 70 µrad. Booster requirements specified a single bunch charge of 50-150pC and a ε_{90} of about 200 µrad at 100 MeV, therefore simulation results had a safety margin. Measurements were performed in single bunch mode, at 107 MeV, varying the bunch charge from 50 pC up to 150 pC and optimizing the bunching system. The transport efficiency between the thermo-
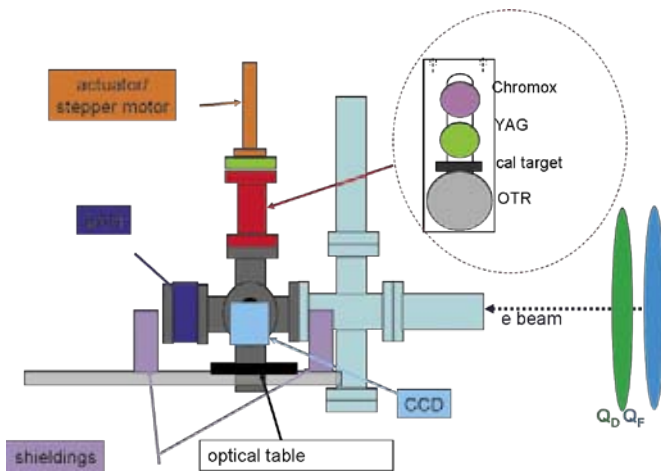
Figure 1.
Schematic layout of the emittance measurement station installed at the end of straight-on line after the first transfer line bending magnet.
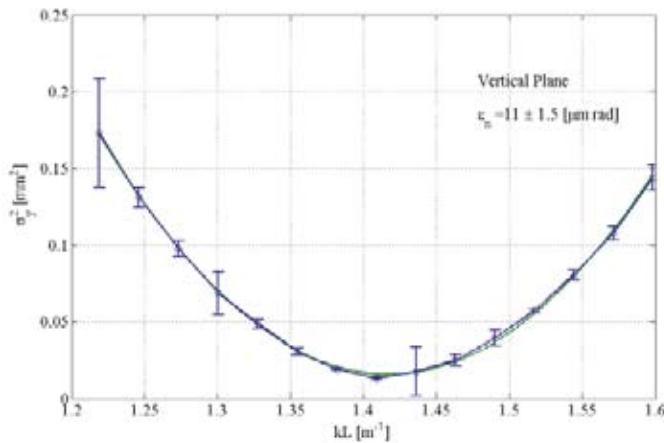

Figure 2.
QD quadrupole scan results for the RMS normalized vertical emittance measurements.

ionic filament and the diagnostic station is about 50%. A scan on the quadrupole QD was performed, acquiring five images for each K values. The experimental data obtained and the quadratic fit is shown in Figure 2. The value of 11 μrad refers to the normalized RMS vertical emittance, which corresponds to 39% of the bunch particles in phase space if one assumes a Gaussian distribution [3]. The ε_{90} is 4.6 times larger than the RMS emittance, so we can estimate a ε_{90} of about 51 μrad. This value is in good agreement with the simulation. Similarly, a scan on the quadrupole QF was performed, providing a normalized RMS horizontal emittance of about 23 μrad (ε_{90} =110 μrad). The asymmetry between the two planes can be due to an asymmetry in the emission or to a horizontal misalignment of the pre-injector, which can introduce dipole

components in the accelerating structures RF fields, leading to a horizontal emittance grow up. Increasing the charge per bunch up to 150 pC, as expected we obtained an increment of the normalized RMS emittance in both planes: $\varepsilon_{RMS,y}$=17 μrad ($\varepsilon_{90,y}$=78 μrad) and $\varepsilon_{RMS,x}$=31 μrad ($\varepsilon_{90,x}$=142 μrad).

References
[1] S. Bassenese *et al.*, *"The Diagnostic Line of Elettra Booster 100MeV Pre-injector"*, Pro-ceeding of the EPAC 2008 Conference.
[2] G. Penco *et al., "Beam emittance measu-rement for the new full energy injector at ELETTRA"*, Proceeding of the EPAC 2008 conference.
[3] M. Martini and H.Schonauer, CERN PS 97-18.

LOW ENERGY X-RAY FLUORESCENCE MICROSPECTROSCOPY DOWN TO THE C EDGE WITH SUB-MICRON OPTICAL RESOLUTION

A. Longoni[1], R. Alberti[1], T. Klatka[1], A. Marcello[2], A. De Marco[2], D. Bacescu[3], A. Gianoncelli[3], B. Kaulich[3], M. Kiskinova[3]

[1] Politecnico di Milano, Dipartimento di Elettronica e Informazione and INFN sezione di Milano, Milano, Italy
[2] ICGEB - AREA Science Park, Trieste, Italy
[3] Sincrotrone Trieste S.C.p.A., Trieste, Italy

E-mail: burkhard.kaulich@elettra.trieste.it

X-ray micro-fluorescence (μ-XRF) has been recognized as one of the best methods for element specific analysis with chemical sensitivity to low concentrations, much superior than that of XANES. However, the μ-XRF stations operating in the synchrotron facilities work in multi-keV (>2 keV) range, lacking the access to the K-absorption edges of low-Z elements as C, N, O, F, Na, Mg, Al and Si that are of particular interest for many domains of life science, environmental and geochemistry, cultural heritage and new materials.

The TwinMic station [1], hosting x-ray transmission microscopes operating at 200 – 2000 eV photon energies with sub-100 nm optical resolution with classical XANES anal-ysis mode, is the first to have implemented a soft X-ray fluorescence (LEXRF) spectrometer with sub-micron resolution. The developed modular LEXRF instrument can host up to eight Silicon drift detectors (SDD). The data acquisition and read-out electronics [2] have specifically been designed and adapted to the photon flux and geometrical constraints of the TwinMic station (Figure 1a).

Pilot experiments with only 2 of eight SDDs demonstrate the potential of element specific analysis down to C edge with a detector and electronics limited energy resolution of down to 80 eV at C K-edge (Figure 1b).

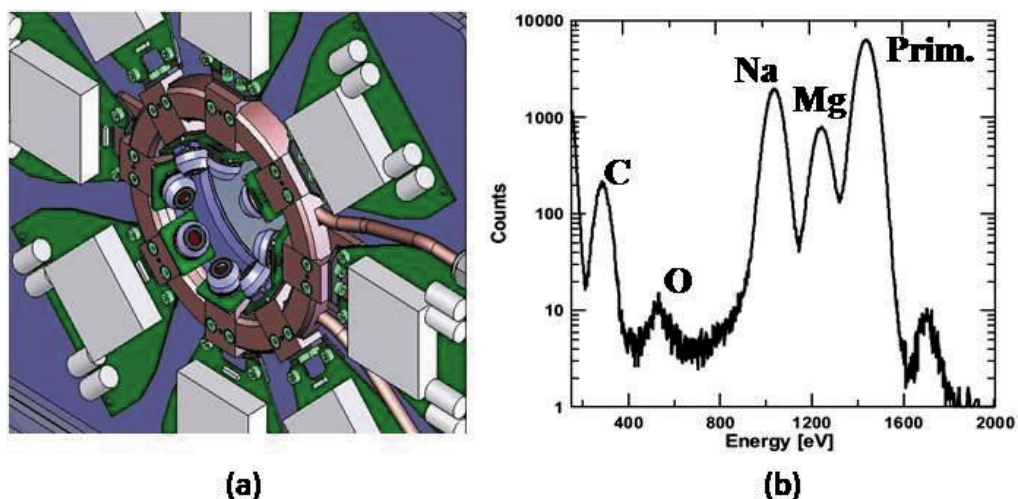Figure 2 depicts the first feasibility experiments in collaboration with ICGEB, illustrat-

(a)

(b)

Figure 1. (a) Low energy X-ray fluorescence (LEXRF) setup with up to at SDD detectors in angular configuration facing toward the microprobe of the TwinMic microscope operated in scanning transmission mode. Customized designed multi-channel read-out electronics including a custom pulsed-reset preamplifier system are mounted close to the detectors for optimum performance of the LEXRF spectrometer.
(b) Unfocused beam LEXRF spectra of human epatocyte cells from liver; LEXRF peaks can clearly be resolved down to the C absorption edge.

Figure 2. Scanning transmission and LEXRF maps of epatocyte cells from human liver simultaneously acquired with the TwinMic station in scanning transmission mode: BF is the brightfield or absorption map, DPC the corresponding differential phase contrast map. The image size is 40 x 40 µm^2 with 40 x 40 pixels of the raster scan and an exposure time of 10s per pixel.
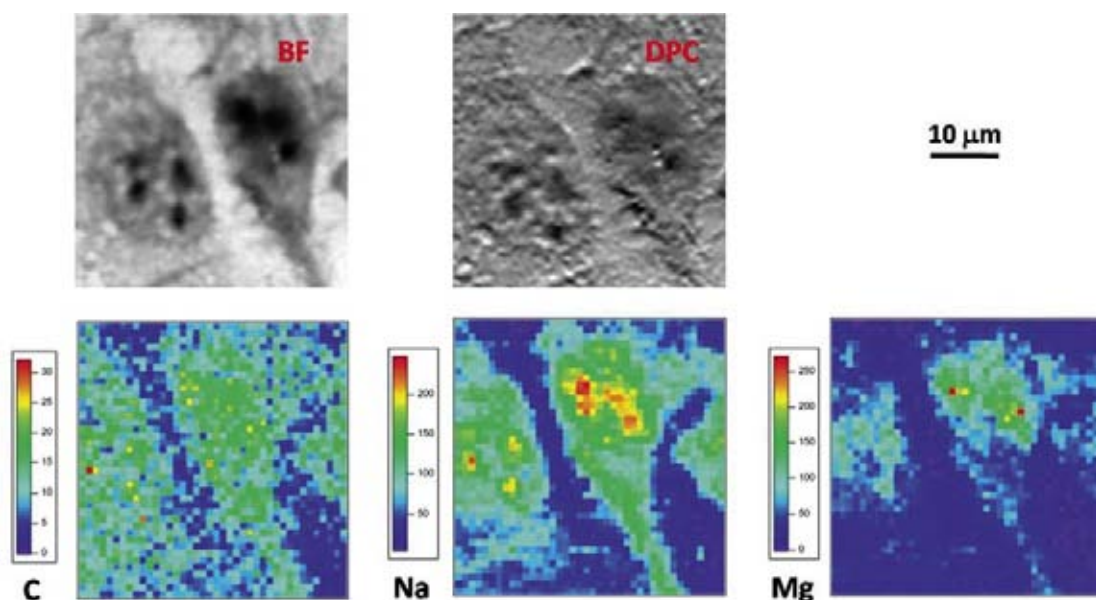
ing the potential of the set-up for applications in human biology and virology. They aim at fostering the development of novel genetically encoded contrast labels for the detection of sub-cellular processes and bio-functions through specific targeting of externally administered probes.

A spatial resolution with the current setup of two detectors (<700 nm) has been achieved. The full potential of the LEXRF, resolution of 100 nm with chemical sensitivity in the range of a few 100 ppm range instrument is expected when all 8 detectors are purchased and implemented.

The developed XRF system is coupled with the STXM (Scanning X-ray Transmission Microscope) operation mode of TwinMic, allowing to simultaneously collect brightfield (absorption) images, phase contrast images and XRF maps, providing morphological and chemical information at the same time.

References

[1] B. Kaulich *et al.*, in Proc. 8th Int. Conf. X-ray Microscopy (IPAP, Tokyo, 2006) **7**, 22 (2006).

[2] R. Alberti *et al.*, IEEE Trans on Nucl. Sci. **54**, 751 (2007).

A TWO-DIMENSIONAL DETECTOR FOR PUMP-AND-PROBE AND TIME RESOLVED EXPERIMENTS

G. Cautero[1], R. Sergo[1], L. Stebel[1], P. Lacovig[1], P. Pittana[1], M. Predonzani[1], S. Carrato[2]

[1] Sincrotrone Trieste S.C.p.A., Trieste, Italy
[2] D.E.E.I., University of Trieste, Trieste, Italy

E-mail: carrato@units.it

Objective of time resolved experiments is to measure the dynamics of chemical/physical reactions. When an external excitation (pump) is used to excite a non equilibrium state and the dynamic evolution is monitored through one or more light pulses (probes), the technique is called "pump&probe analysis" and the time resolution is limited only by the used pulse width.

In pump&probe experiments that combine laser and synchrotron radiation pulses, the time resolution is limited by the SR pulse width and, with the upcoming FEL, is foreseen to be in the tens of femto seconds.

When also spatial and energy resolutions are required, it is possible to combine pump&probe with electron spectromicroscopy techniques, where electron analyzers and suitable focalizing tools allow meV and below micrometer resolutions.

A typical approach in order to perform pump and probe or, more generally, "time resolved" experiments consists in associating to each single count received by the detector the "exact time" it was acquired or, alternatively, other external events.

Usually the detectors available on electron analyzers are not suited to front this job. For this reason in the Instrumentations and Detectors Laboratory of Elettra a new bidimensional detector setup has been developed specifically for time resolved acquisition.

It consists in a (cross) delay lines detector, where the delay anodes are two orthogonal microstrip lines; the position is obtained by calculating the time between the start and stop signals coming from the anodes ends; it is evident that this detection approach is intrinsically suitable for highly resolved timing information.

The time decoding is based on a digital TDC chip that provides up to 10 ps time resolution, with a time window ranging up to 40 ms, and is able to handle up to 40 Mcounts/s.

Main features are:
- Two-dimensional acquisition with spatial resolution better than 100 μm and 150 μm in the two directions
- The count rate (more than 4 Mcounts/s) exceeds the performances of the best count-mode two-dimensional detectors presently available on electron analyzers.
- It is able to correlate each count with external events and/or with the time it has occurred.

Figure 1.
(a) Experimental setup for the first time resolved acquisition;
(b) histograms of counted events for three different delays (with reference to the ramp generator), e.g. for three different electron energies.
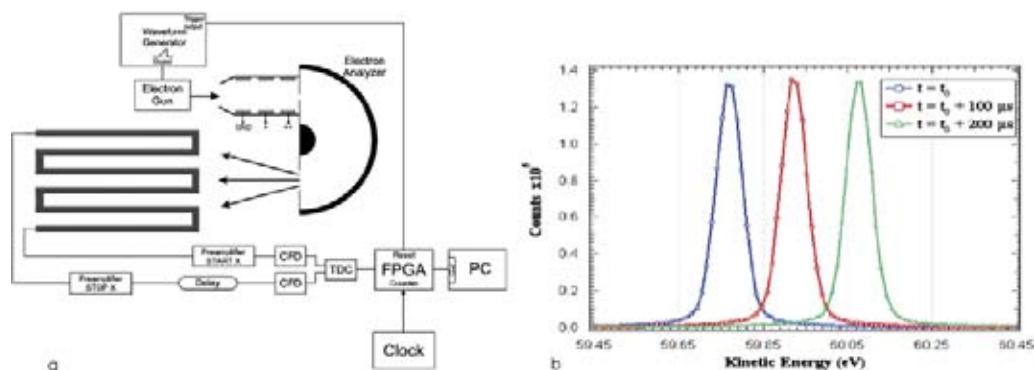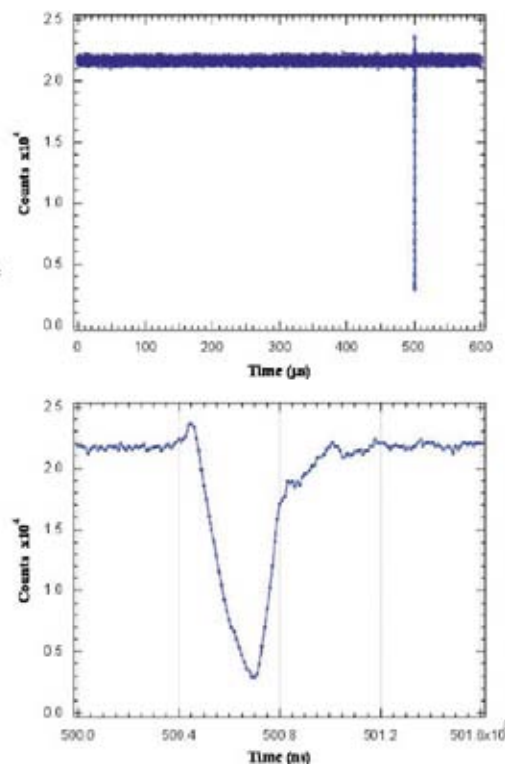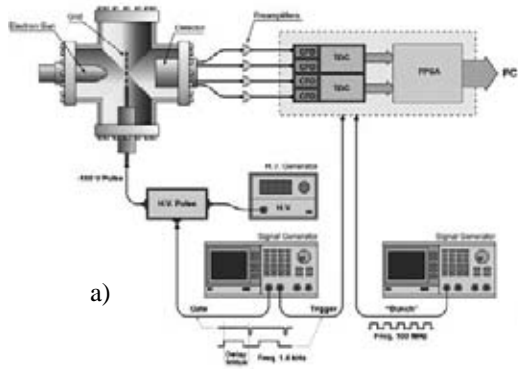
Figure 2.
(a) Second UHV test for time resolved experiments: experimental setup; (b) effect on the count rate of a negative 200 ns pulse applied to the grid (the lower figure is a zoom of the upper one).

Two simple time resolved tests in UHV are reported in this document in order to

a) illustrate one use of the detector combined with the energy dispersion properties of electron analyzers

b) underline the fact that the possibility to associate at each event the time it was received allows to follow the reaction dynamics, regardless of the availability of analyzers or SR pulses

In the first test (Figure 1a) the detector is mounted on an electron analyzer; an electron gun, controlled by a waveform generator, simulates the variable kinetic energy (KE) of the electrons emitted from a sample. The output of the waveform generator is 1 kHz ramp with 1ms rise time connected to both the electron gun (to set the KE of the electrons) and to the detector (to trigger the acquisition).

Each detected event is "time – stamped" and data are stored in frames identified by the time. The time resolution is set to meet the experiment requirements – in this case in the μs scale. When it is necessary to follow events in the time scale of ms down to ns it is possible to use a clock counter inside the detector electronics, otherwise the TDC intrinsic time resolution (27 ps) is available. The histograms of the number of observed events versus KE have been plotted in

Figure 1b, where equally spaced—on the horizontal axis—peaks are correctly obtained for electrons with linearly increasing delay and, consequently, increasing kinetic energy.

In the second test (Figure 2a) an electron gun is placed in front of the detector, with a grid in between the two.

Every 0.6 ms, a 200 ns pulse is supplied to the detector trigger and, delayed by 500ms and amplified to 150 V, to the grid in order to stop the electrons (KE is set to 75 eV) coming from the electron gun; finally, 100 MHz clock is used to "time stamp" the events. In Figure 2b the counts relative to an acquisition are reported; with 10 ns time resolution it is possible to follow the effect of the voltage barrier on the electrons and to appreciate the correspondence with what is reasonable to foresee. It is apparent that, in the same way, it is possible to follow any kind of experiment where dynamics in the order of ns are expected.

FERMI@ELETTRA
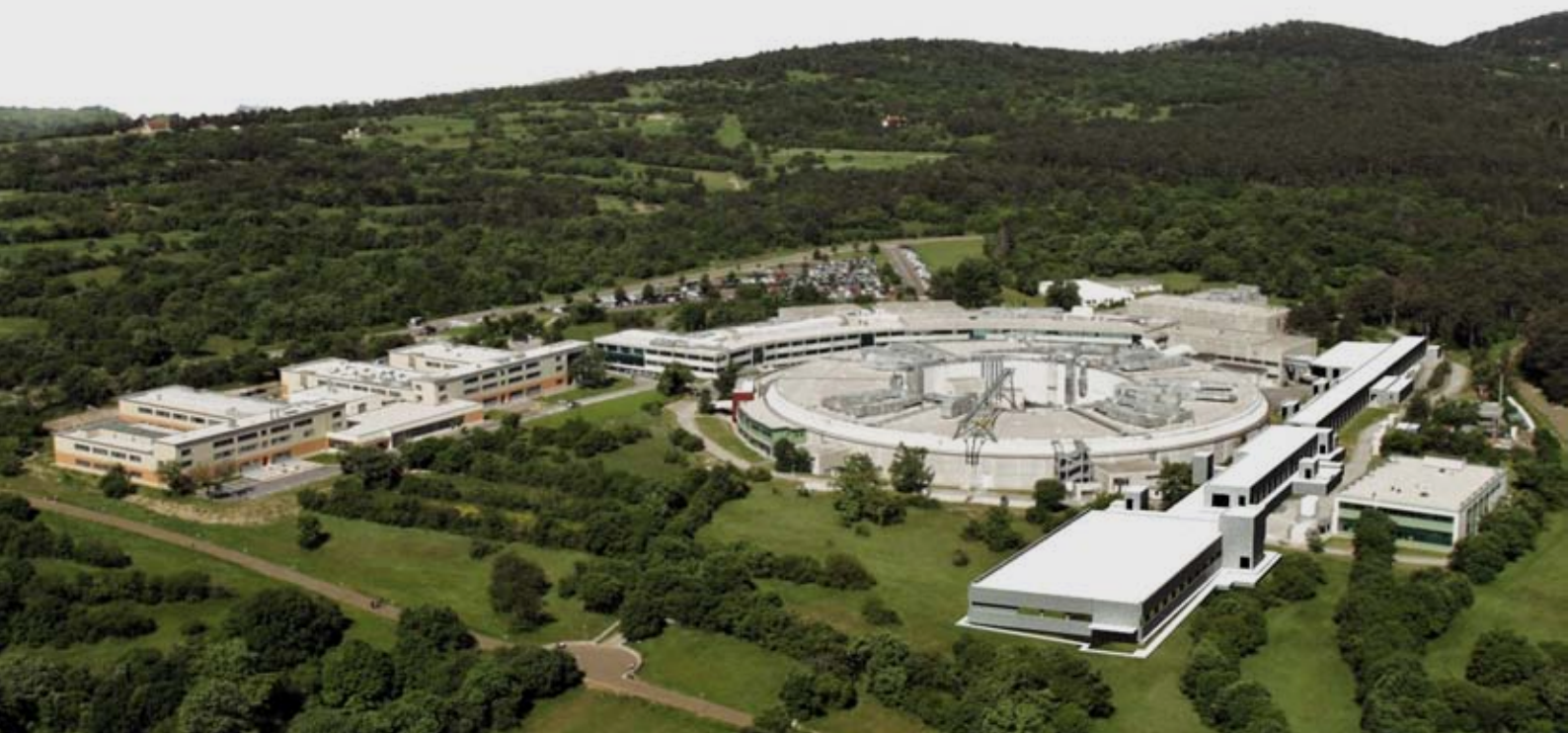
T his last year has been very busy for the FERMI@Elettra project, but looking forward, next year will be even busier as we continue ramping up to deliver the project in the relatively short time remaining. During last year we continued to refine the overall design and performance parameters in order to bring more to the users for the same cost, as well as ramping up to start production on many of the major systems.

Certainly the biggest and most noticeable progress was in the area of civil engineering. One needs only to visit the linac area to see that there is work occurring by the contractors as they build up the linac extension. Even more significant is the work that occurred in the offices of the infrastructure team and design/architecture firm. Together the completed completed the entire detailed design work of the FERMI civil engineering.

An improvement in FEL I has lead us to reconsider FEL II and its primary design and potential wavelength reach. In short, together the linac and undulators are capable of reaching shorter wavelengths than what is listed in the CDR, and we will exploit that capability in the build up of FEL II.

Key to the overall operation of the FEL is a high-brightness electron beam, and the best way to generate such a high-quality beam is to study in detail what others have done and then set about to do the same and better. The FERMI project has done just that by using a proven photocathode rf-gun system for the generation of the high-quality electron beam.

To gain experience with this rf-gun system we formed a collaboration with MAX Lab in Lund Sweden to allow us to perform the initial commissioning of the rf-gun while we wait for the linac tunnel extension to be completed. This commissioning is now well advanced with initial measurements of the electron beam emittance already performed.

The linac is next to accept the beam from the rf gun, and it is the next major system that must be ready for operations, but it is also the one that must undergo the most significant rebuild. In October/November 2007 we removed the entire linac in preparation for the linac tunnel rebuild. Now we need to reinstall the linac in its new configuration.

Sincrotrone Trieste has teamed with a newly the formed company Kyma S.r.l. to produce the undulators for the FERMI@Elettra project. Through interaction with the Kyma S.r.l. partners ST has transferred essential technology to Kyma S.r.l. and this has allowed the new company to produce its first high-quality undulator. These undulators will be installed, beam will be passed along their length, and we will have produced FEL light.

Once one has generated an FEL pulse it must be transported and focused onto the samples of the various experimental end stations. The FERMI@Elettra program has chosen three primary areas of research: Low-Density Matter (LDM), Diffraction and Projection Imaging (DiProI), and Elastic and Inelastic Scattering (EIS). This will constitute our initial core experimental programs.

In concluding, the FERMI@Elettra project is beginning to move forward rapidly and starting to accelerate. This next couple of years will be very intense, but as things start to materialize and tests get underway it should also prove to be an intensely satisfying couple of years.

Stephen Val Milton

Stephen Val Milton is the Director of the FERMI@Elettra project at Sincrotrone Trieste. From 1998 until 2002 he led the APS free-electron laser project, LEUTL. This project was the first to achieve full saturation of a self-amplified spontaneous emission free- electron laser in the visible to ultraviolet wavelength range. Following the completion of the LEUTL project he took over as Director of the ANL component of the Linac Coherent Light Source (LCLS) where he was responsible for the delivery of the 130-m long undulator system of the LCLS at the Stanford Linear Accelerator Center.

SINGLE BUNCH BEAM BREAK UP INSTABILITY IN NORMAL CONDUCTING LINACS

M. Borland[1], P. Craievich[2], S. Di Mitri[2], A. A. Zholents[3]

[1] *Argonne National Laboratory, Argonne, IL, U.S.A.*
[2] *Sincrotrone Trieste S.C.p.A., Trieste, Italy*
[3] *Lawrence Berkeley National Laboratory, Berkeley, CA, U.S.A.*

E-mail: simone.dimitri@elettra.trieste.it

The electron beam for the FERMI FEL must be extremely collimated and with a very small beam size; these properties are formally described by the transverse emittance parameter that is proportional to the width of the particle position and angular divergence distribution in the transverse plane of interest. The Single Bunch Beam Break Up (SBBU) instability is one of the main source of emittance degradation. In practice, the high current electron beam travelling off axis through the FERMI linac generates an image charge on the inner surface of the accelerating sections; in turn, this excites an electromagnetic field called geometric transverse wake field that interacts with the real beam by perturbing its transverse dynamics [1]. In fact, the wake field effect is an angular kick distributed along the bunch that forces the bunch tail to deviate from the bunch head axis. As the beam travels, the bunch tail oscillates in the transverse planes; if the oscillation amplitude is very large, the transverse emittance blows up. In this case the bunch assumes a typical distortion in the *(t,x)* and *(t,y)* plane called "banana shape" [2]. Figure 1 shows the jitter (shot-to-shot variation) of the banana shape in both transverse planes in presence of trajectory jitter.

Figure 1 demonstrates how the wake field effect is related to the transverse off axis position of the bunch inside the accelerating sections: if the bunch position changes, the wake field effect changes as well. Notice that a

Figure 1.
Banana shape (slice centroid lateral deviation vs. Time coordinate in the bunch in 100 fs unit) at the linac end affected by trajectory jitter. The bunch head is on the left. The maximum head-tail deviation is 180 μm in the horizontal plane and 240 μm in the vertical plane, close to the rms unperturbed beam size.
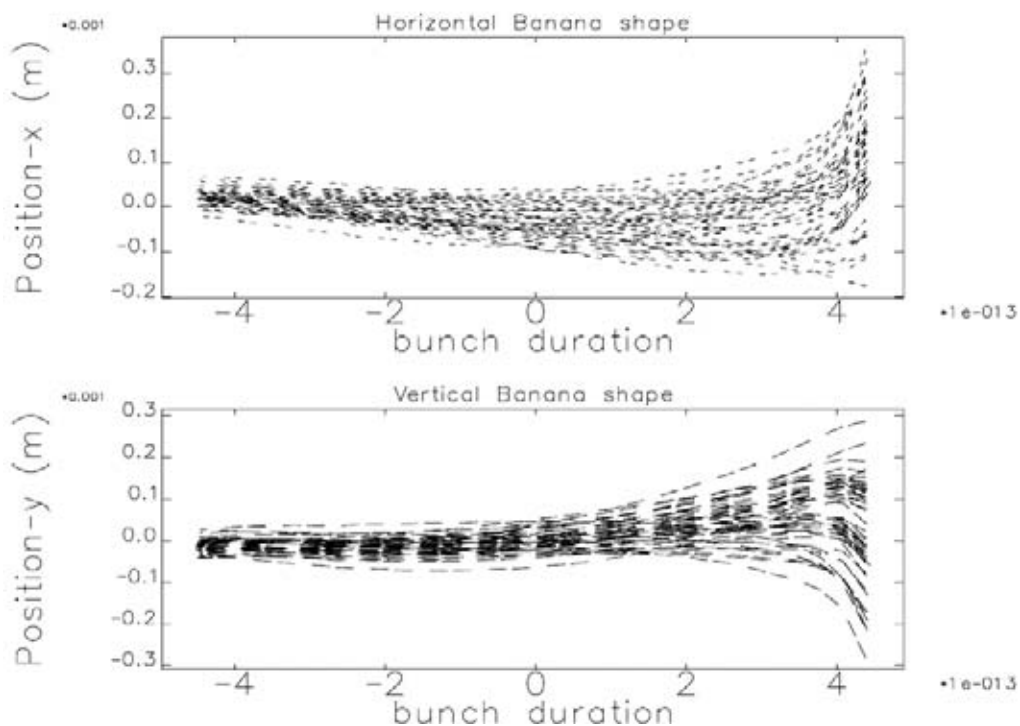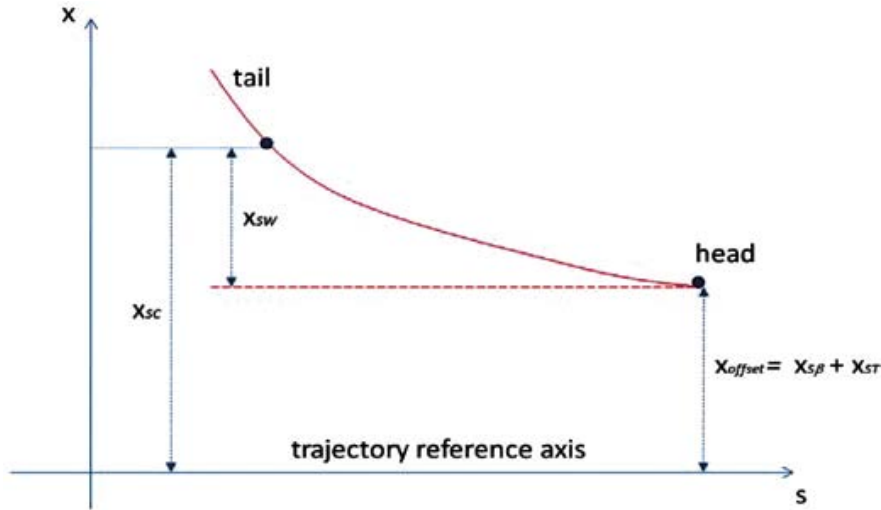
similar behavior of that in Figure 1 concerns the particle angular divergence along the bunch.

Let us assume the electron bunch is longitudinally divided into several slices, whose length much smaller than the total bunch length. The amplitude of the slice centroid transverse motion x_{sc} is the linear superposition of three main contributions, as shown in Figure 2: i) the betatron motion, $x_{S\beta}$, generated by the external focusing; ii) the trajectory distortion, x_{ST}, generated by machine errors; iii) the transverse wake field effect, x_{SW}, that induces the SBBU instability. Regarding the SBBU instability, only the motion relative to the bunch head is of interest.

The total effect of the SBBU instability on the particle position and angular divergence distribution, even in presence of trajectory jitter, can be evaluated by looking at the shot-to-shot variation of each slice centroid emittance ε_{SW} calculated relatively to the bunch head centroid emittance. In fact, we require that the rms (over all jittered runs) slice lateral deviation be less than the rms (over all particles) beam size σ_x:

$$\frac{\sqrt{<x^2_{SW}>}}{\sigma_x} \leq 1 \qquad (1)$$

Since $\sqrt{<x^2_{SW}>} \sim \sqrt{<\varepsilon_{SW,x}>}\sqrt{\beta_x}\cos\varphi_x$

and $\sigma_x = \sqrt{\varepsilon_x \beta_x}$, the previous equation is

made more stringent by:

$$\sqrt{\frac{<\varepsilon_{SW,x}>}{\varepsilon_x}} \leq 1 \qquad (2)$$

where ε_x is the beam projected emittance.
Same considerations apply to the vertical plane.

References

[1] A. W. Chao, *"Physics of Collective Beam Instabilities in high energy accelerators"*, Ed. John Wiley & Sons Inc., (1993).
[2] P. Tenenbaum, *"Effectiveness of emittance bumps on the NLC and US cold LC main linear accelerators,"* SLAC-TN-04-038 (2004).

LOW-ENERGY TRANSVERSE RF DEFLECTOR CAVITY

P. Craievich[1], S. Biedron[1], C. Bontoiu[1], S. Di Mitri[1], M.Ferianis[1], A.Rubino[1], M. Veronese[1], M. Petronio[2], D. Alesini[3], L. Palumbo[3], L. Ficcadenti[4]

[1] Sincrotrone Trieste S.C.p.A., Trieste, Italy
[2] DEEI, University of Trieste, Italy
[3] INFN/LNF, Rome, Italy
[4] University La Sapienza, Rome, Italy

**E-mail: paolo.craievich@elettra.trieste.it**

FERMI@Elettra is a soft X-ray fourth generation light source under development at the Elettra laboratory. The single bunch beam is produced by a photo-injector, then accelerated up to 1.2 GeV by a linear accelerator, and finally transported to the undulators, where the free electron lasing occurs. In order to completely characterize the beam phase space by means of measurements of the bunch length and of the transverse slice emittance two deflecting cavities will be positioned at two points in the linac. One will be placed at 1.2 GeV (high energy), just before the FEL process starts; the second at 250 MeV (low energy), after the first bunch compressor (BC1). The description of the low-energy bunch deflection, which allows the efficiency of the first bunch compressor to be measured, together with the RF design are here presented.

Complete characterization of the beam phase space by means of measurements of the bunch length and of the transverse slice emit-

tance are important tasks for the FERMI FEL project. The deflector following BC1 will operate in a vertical deflecting mode to allow measurements of the horizontal slice emittance and bunch length. Figure 1 sketches the bunch vertical deflection when the centroid remains on the trajectory axis while the beam is stretched in the transverse direction and collides with an optical transition radiation (OTR) screen. The deflector will be followed by a multi-screen emittance measurement station with quadrupole magnets in-between the screens.

If the finite transverse emittance of the bunch is taken into account, then the beam size at the screen after the deflection can be estimated by the quadratic summation of the RMS non-deflected particle transverse size distribution and of the RMS beam size in the pencil beam approximation. Finite emittance contribute to the increase of the beam size measured at the screen, but if the deflecting

Figure 1.
Deflector operating mode: the centroid remains on axis while the beam is stretched in the transversal direction and collides to an OTR screen.
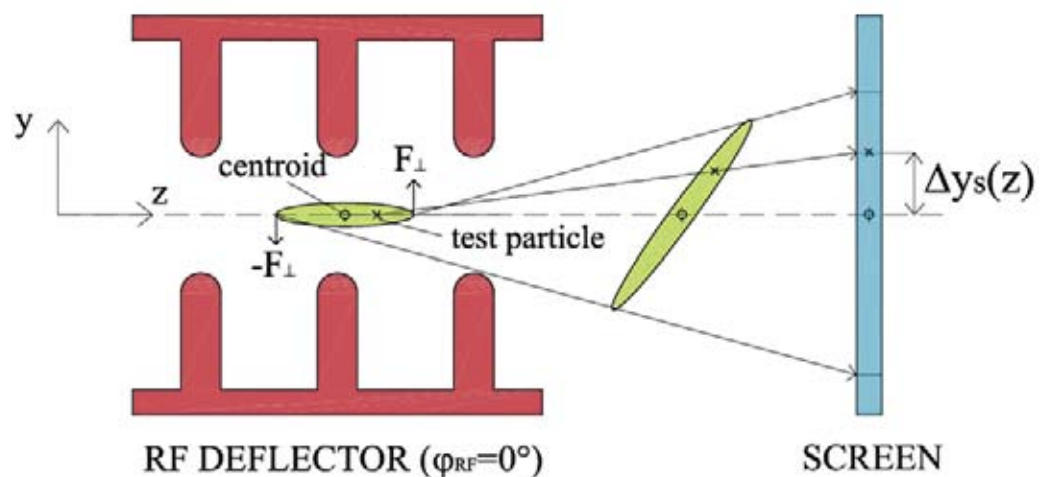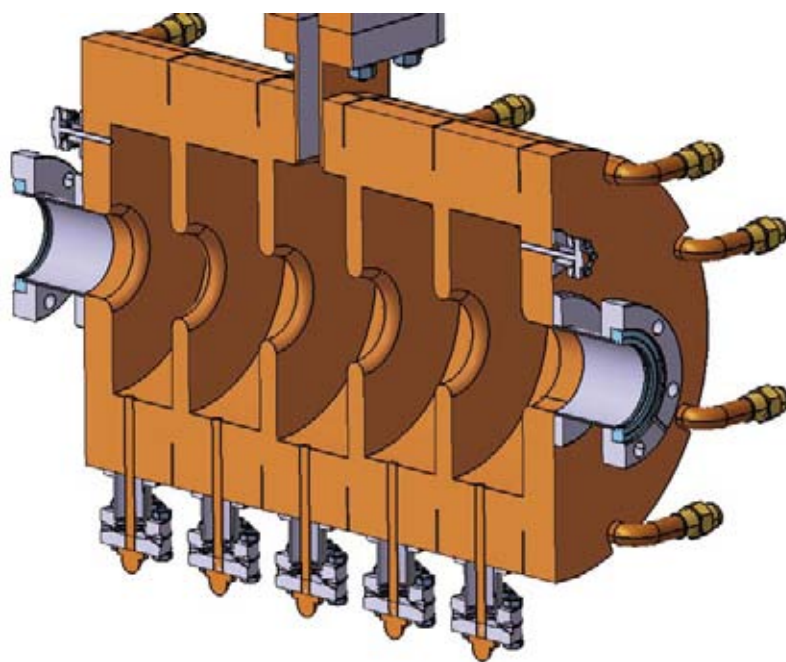
voltage is sufficiently large the relative error due to finite emittance can be reduce, i.e. a relative error less than 3% requires a deflecting voltage $V_\perp \geq 1.6$ MV. The measurement of the transverse slice emittance requires short portions of the bunch length to be resolved at the screen after the bunch is deflected. Considering a division into 30 slices of the whole bunch (about 700 µm for the medium bunch length option) and assuming 10 µm RMS resolution of the screen, then a contrast of 70% allows the detection of the 40 µm slice length. In the approximation of a uniform bunch current distribution, a minimum peak voltage of 2.3 MV is required to achieve the desired vertical deflection of the bunch in the worse case optical condition.

The RF design and the choice between different options was done taking into account the following constraints: a minimum peak voltage of 2.3 MV, a working RF frequency of 2998 MHz, an RF pulse length less than 3 µs, and a maximum available RF power of 5 MW. Deflecting cavities, such as iris loaded travelling wave (TW) guide or multi cell standing wave (SW) structures, are a powerful tool to reach this aim. The minimum peak voltage can be achieved by both traveling wave or standing wave structures. In particular the deflector at low energy will work at maximum beam energy of 250 MeV. We have chosen to scale the deflecting SW structure developed for the SPARC project [1] to the FERMI operating frequency. Such a choice allows us to reach

the desired resolution with full flexibility. This could become important if one contemplates use of an even shorter bunch as in the single bunch compressor scheme which was proposed as a possible option for FERMI@Elettra. The deflector is a standing wave structure composed of 5-cells operating on the π-mode. The design is shown in figure 2. The main RF parameters of the deflector are the quality factor Q=15600, the transverse shunt impedance $R_\perp$=2.4 MΩ, the filling factor τ=0.8 µm at coupling coefficient β=1, and the working frequency f_r=2.998 GHz. The total length of the RF structure is 0.5m and the maximum integrated deflecting voltage is 4.9 MV with 5 MW of input power [2].

As a conclusion, a peak voltage of 2.3 MV for the RF deflector is completely satisfactory for the bunch length measurement. The same specification allows for a resolution of 30 slices over the medium bunch length of the FERMI@Elettra project with an intensity contrast of about 70%. The 5-cell SW structure being built will achieve this peak voltage requirement and also allow us flexibility to explore adequately even shorter bunch length.

References

[1] D. Alesini *et al.*, *Nucl. Instr. Meth. A* **568** 488 (2000).

[2] P. Craievich *et al.*, *"Fermi Low-Enegy Transverse RF Deflector Cavity"*, Proceedings of EPAC08, Genoa, Italy, (2008).

THE 100-MeV BEAM DIAGNOSTIC STATION

S. Spampinati[1,2], S. Di Mitri[1], G. Penco[1]

[1] *Sincrotrone Trieste S.C.p.A., Trieste, Italy*
[2] *University of Nova Gorica, Nova Gorica, Slovenia*

E-mail: simone.spampinati@elettra.trieste.it

The FERMI Free Electron Laser (FEL) will be a 4th generation light source in which powerful and coherent VUV, X-radiation is generated by the passage of the high energy electron beam through an undulator chain. A very high quality, high density electron beam is needed to produce the high brightness FEL. The electrons are extracted by a Cu target illuminated by a UV laser and accelerated by the high voltage electric field of the RF Gun. Then, the beam will be further accelerated to 1.2 GeV in the main linac and its length will be compressed in magnetic chicanes (bunch compressors) to achieve a high peak current. The electron beam characteristics will be controlled and tuned by a lot of 'knobs' distributed along the machine. The passage from the injector to the linac is a critical point since the beam coming from the Gun shall be matched with the optics of lattice downstream. In order to do this, a beam diagnostic station will be placed there, where the beam energy is approximately 100 MeV. This diagnostic station is placed across the so called Laser Heater area. This is constituted an undulator placed in a small magnetic chicane where the electron beam interacts with an external laser. This interaction provides an increase of the electron beam energy spread in order to prevent the development of succeeding instabilities. The 100 MeV diagnostic station is equipped with quadrupoles and Optical Transition Radiation (OTR) screens to measure and correct the beam optics and to evaluate the transverse emittance. A Beam Position Monitor (BPM) and a spectrometer (dipole magnet) are downstream the laser heater chicane. Figure 1 shows sketch of the FERMI@Elettra layout.

Small transverse emittance is one of the peculiarities of an electron beam driving a single pass VUV, X-ray FEL and it is provided by the photo-injector. Many parameters have to be optimized there to reach the required normalized emittance value (<2 μm rad for FERMI). A precise emittance measurement is then an important topic for this kind of machine. A multi-screens technique [1] will be implemented to measure the beam emittance and the beam Twiss parameters at the end of the photo-injector. The screens are placed at a relative betatron phase advance of 60 degree, in both x and y plane. The second screen is in the laser heater chicane, just after the laser heater undulator, in correspondence of the beam waist. To avoid emittance degradation, the incoming electron beam optics has to be matched to the linac optics; the matching will be performed by the four quadrupoles at the beginning of the diagnostic section.

The last part of the 100 MeV energy diagnostic station is represented by a spectrometer line. The knowledge of the beam energy at this point is required for two reasons: to satisfy a resonance condition (provide the exact amount of beam heating) in the undulator between the electron beam energy and the wavelength of the external laser; to optimize the injection into the main linac. For this purpose, the beam average energy has to be known with an accuracy of 100 keV rms. The maximum dispersion in the centre of the laser heater chicane is 3.1 cm. Theferore a BPM with < 5 micron rms resolution placed there will permit to resolve a shot-to-shot relative energy variation of 0.1%. This BPM will be part of the FERMI longitudinal feedback system. The correlated beam energy spread in the laser heater chicane is mainly due to the off-crest acceleration provided by the upstream injector. Then, a scan of the average beam energy and energy spread as function of the injector RF phase and voltage will be performed to characterize the longitudinal beam dynamics.

Alignment and transverse matching between the laser and the electron beam is very important in order to have the correct

interaction between the two beams and therefore the desired heating. The relative alignment between the photon and electron beam has to be better than 50 μm. To achieve this, two screens, capable of recording the image of the two beams, are placed in the laser heater chicane before and after the undulator. The layout of the laser heater chicane foresees some space for the future integration of an optical replica synthesizer [2] that could be able to measure the beam current profile with 10 fs rms resolution of the bunch duration. A dispersive section and an additional undulator are needed for this diagnostics. The additional dispersive section and an Optical Transition Radiation (OTR) screen are then sufficient to detect the beam energy modulation provided by the laser/electron interaction.

References

[1] H. Widemann, *"Particle Accelerator Physics"*, Spriger, II ed., (1999)

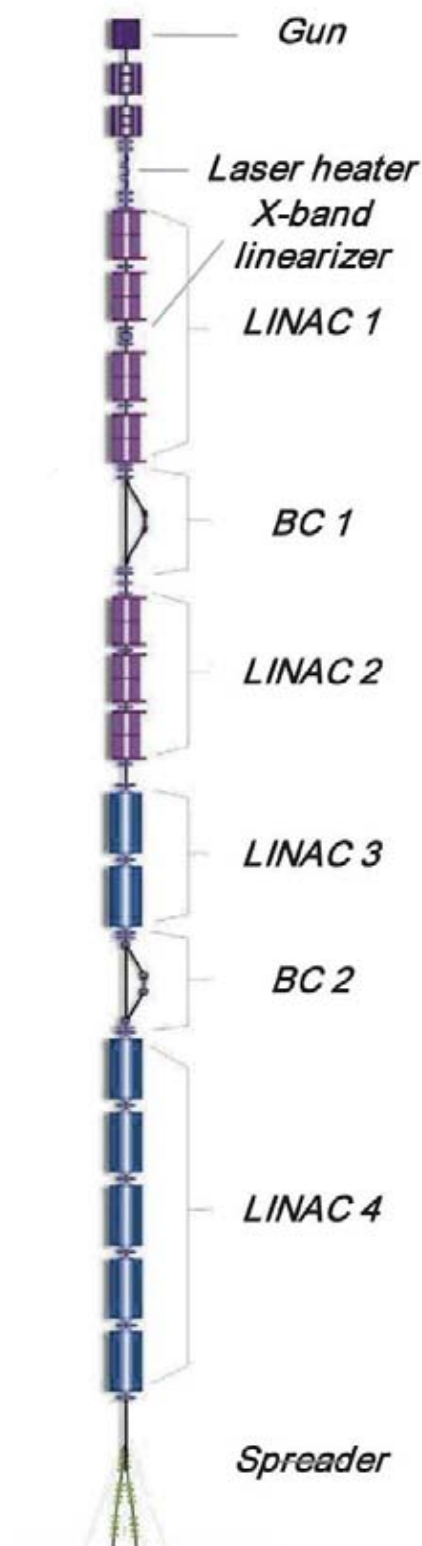[2] T E. Saldin E.A. Schneidmiller, and M.V. Yurkov, *Nucl. Instr. Meth. A* **539**, 499 (2005).

Figure 1.
Sketch of the FERMI@Elettra layout

BEAM BASED ALIGNMENT IN THE FERMI@ELETTRA UNDULATOR CHAINS AND FEL PERFORMANCE

S. Di Mitri[1], B. Diviacco[1], S. Spampinati[1,2]

[1] *Sincrotrone Trieste S.C.p.A., Trieste, Italy*
[2] *University of Nova Gorica, Nova Gorica, Slovenia*

E-mail: simone.dimitri@elettra.trieste.it

The FERMI FEL is going to generate coherent light by the passage of the high energy electron beam through an undulator chain. The continuous interaction of the electrons with the induced radiation in the undulators amplifies the FEL light power. This interaction is guaranteed by the transverse overlap of the electron beam and the photon beam in the undulator chain. Therefore it is very important to steer the electron beam on a straight path, in spite of all trajectory perturbations that can be introduced by the undulator misalignment, quadrupole misalignment and beam launching error. The Beam Based Alignment (BBA) is a technique that uses 1 μm resolution Beam Position Monitors to calculate the trajectory offsets; then, steerers (dipole correctors) and quadrupoles are used to steer the electron beam on an ideal straight path.

The FERMI FEL will be a variable polarization user facility that implies a changing undulator light polarization. When the phases of the devices are changed, their focusing changes as well and the quadrupole gradients between the undulators shall be changed accordingly to maintain the beam optics fixed. Unfortunately, if a quadrupole is traversed off axis, a dipole field component is excited and it will kick the electron beam by modifying its trajectory. Thus, we need to centre the quadrupoles on the straight path identified by the BBA algorithm because when the undulators change their polarization, the new focusing setting must not perturb the reference trajec-

Figure 1.
Electron beam straight path constructed through the BBA algorithm (solid line). The realistic beam trajectory (dotted line) is affected by distortion inside the undulators. According to the statistic provided by the BBA algorithm applied to Fermi FEL1 at 60 nm resonance FEL wavelength, the relative displacement of the electron beam from the undulator axis (dashed line) is in the range 200 – 600 μm.
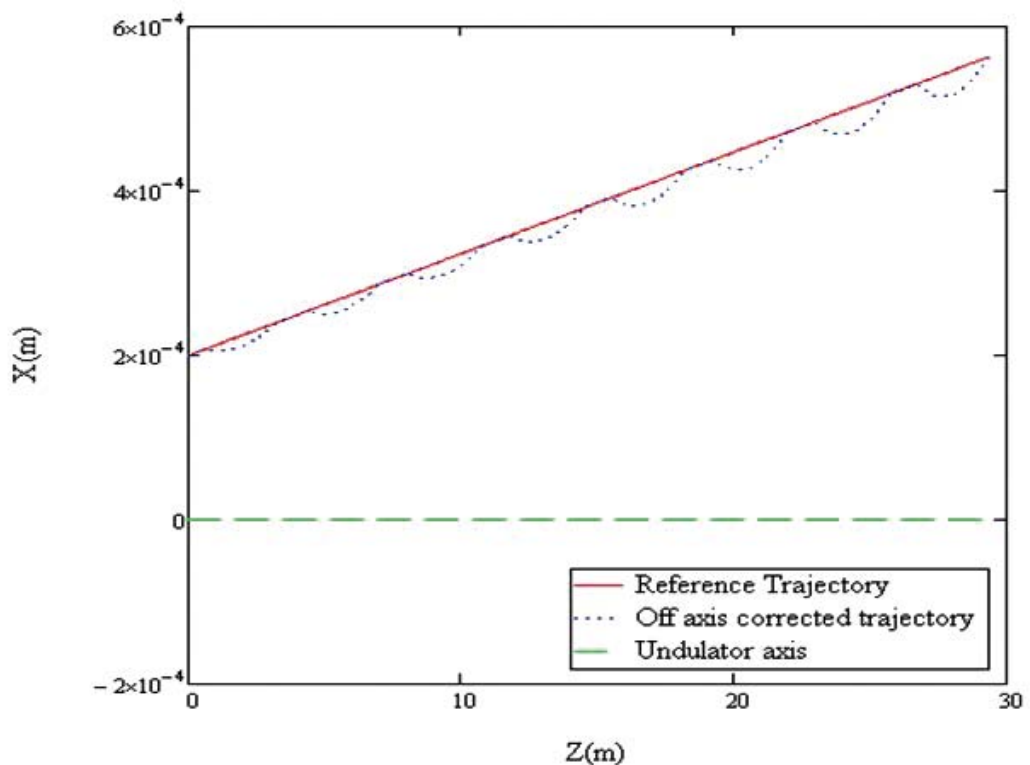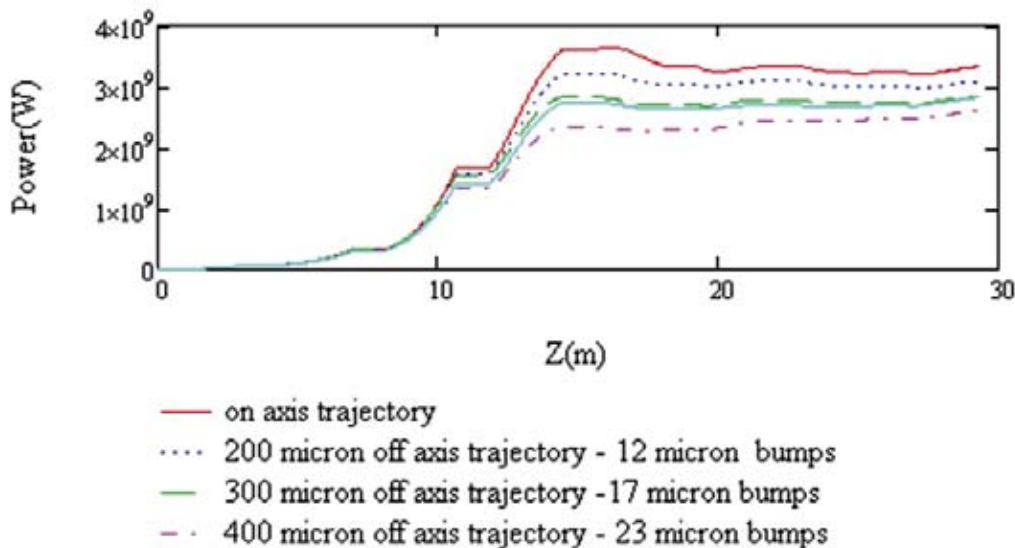
tory. The quadrupoles will be moved on the reference trajectory with remotely controlled micro-movers in the horizontal and vertical plane. A similar option could be adopted for the undulators, but it is not strictly required for the FERMI FEL at the cost of a small reduction of the final FEL peak power.

Once the undulators are closed to the nominal gap, they will contribute to the trajectory distortion in two ways:
1) an error of the first field integral will be compensated by correction coils mounted at the undulator edges;
2) the focusing of the undulator traversed off axis induces an angular kick error. The relative displacement of the electron beam and of the undulators has in turn two sources: first, the static alignment of the undulators with respect to the machine reference axis has a finite accuracy. Second and more important, the straight path determined by the BBA algorithm is not necessary on the same line of the machine reference axis. Simulations actually show that it is far from the linac axis by several 100's micron and that it is dependent on the beam launching error and on the accuracy of the initial machine alignment.

The evolution of the FEL radiation peak power is plotted in Figure 2. It shows that the off axis motion of the electrons with respect to the undulator magnetic axis makes the FEL to saturate at a lower power level (compare the solid line with the others); however, this remains within the FEL tolerances and users requirements.

References
[1] P. Emma, R. Carr, H. D. Nuhn, *Nucl. Instr. Meth. A* **429**, 407 (1999).
[2] U. Hahn, J. Pflüger, G. Schmidt, *Nucl. Instr. Meth. A* **429,** 276 (1999).
[3] T. Tanaka, H. Kitamura, T. Shintake, *Nucl. Instr. Meth. A* **528**, 172 (2004).

THE GUN SPECTROMETER FOR THE FERMI@ELETTRA PROJECT

G. Penco[1], D. Castronovo[1], D. Zangrando[1], M. Trovò[1], G. Loda[1]

[1] Sincrotrone Trieste S.C.p.A., Trieste, Italy

E-mail: giuseppe.penco@elettra.trieste.it

The FERMI photo-injector gun has been built and it is now in the MAX-lab, at Lund, in order to perform RF high power tests and a preliminary commissioning with the driven laser [1]. Diagnostics have been designed and inserted in the gun-to-first accelerating section in order to tune the injector parameters and achieve the specified performance. In this framework the spectrometer at the gun exit plays an important role to accurately know the peak field of the gun accelerating gradient and the injection phase. The energy of the bunch has to be known with an error less than 0.1 %. The gun spectrometer diagnostic beam line is mainly composed by the bending magnet and a Yag screen, that combining with a Cerenkov radiator allow the investigation and characterization of eventual deterioration of the longitudinal profile due to the space charge forces and microbunching instabilities [2].The beam energy measurements will be performed generally at low charge, but it could be interesting to operate the spectrometer even at high charge, to investigate the effects induced by the space charge forces. Thus to compensate the blow up of the bunch due to the space charge defocusing an additional quadrupole is inserted just at the exit of the bending magnet.

The bending magnetic design has been the result of the optimization and balance of physics requirements and layout constraints. In order to accommodate all diagnostics in between the gun and the first accelerator structure, the trajectories cross is placed at about 1 m from the cathode. One of the main physics request is that particles with the same energy but having a transversal displacement have to be bended in the same way. This means that the quadrupole integrated field along the beam trajectory is specified to be very small, in details of the order of 0.2% with respect to the integrated field on the nominal trajectory. Since the bunch energy is about 5 MeV, an accurate study of the quadrupole components even in the fringe fields was carried on. The choice of a bending angle of 60° is a good compromise between high resolution and low peak magnetic field and consequently low fringe fields. Acting on the chanfer of the iron yoke we minimized the variation between the integrated field sampled by particles on the nominal trajectory and particles on parallel trajectories with a horizontal displacement up to 20 mm.

The optimized magnet design is reported in figure 1.

The magnetic design was carried on in parallel and in strong interaction with 3D tracking code of electron bunches in order to simulate the bunch energy measurement and optimize the performance of the spectrometer beamline. Figure 2 shows the horizontal profile at the spectrometer screen and the energy distribution along the bunch when a low charge flat-top bunch is launched with different RF gun phase and consequently different energy and energy spread. In this case there is a good linearity between the screen images and the energy spread.
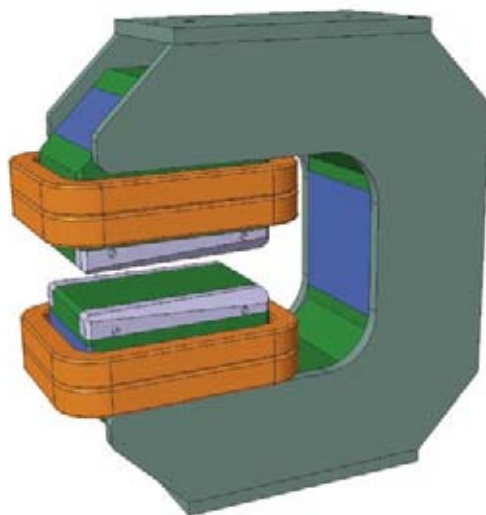
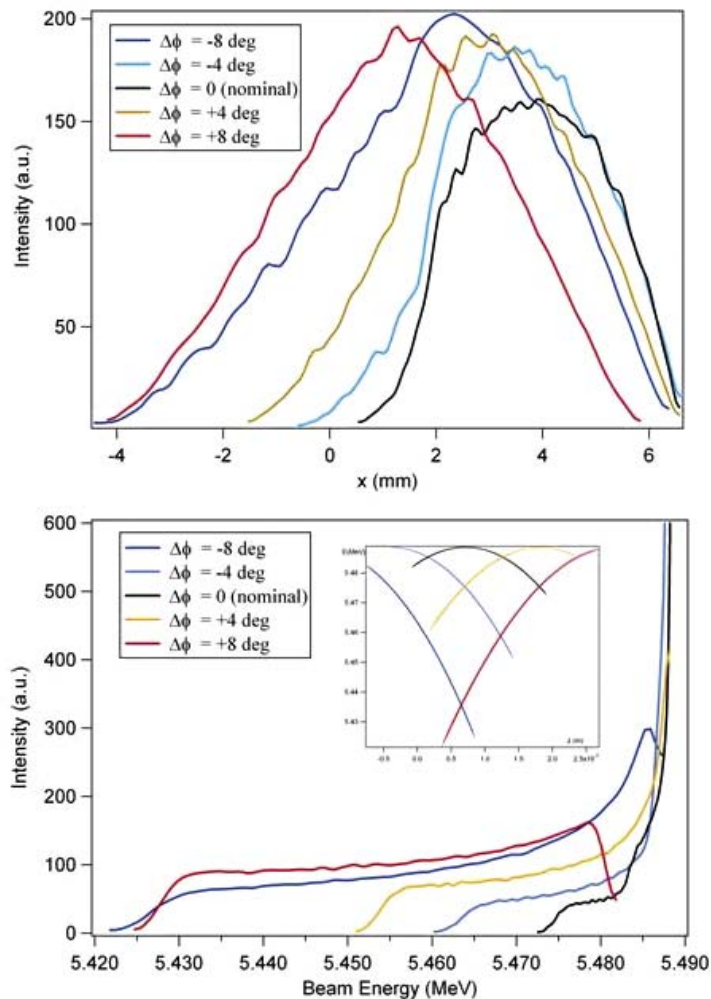**Figure 1.**
3D bending magnet design.

Figure 2.
Horizontal profile at the spectrometer screen (top) and bunch energy distribution (bottom) for a low charge flat-top bunch tracked through the spectrometer beam line for different RF gun phase.

If the bunch charge is increased up to the nominal value of 800 pC, the space charge forces introduce a large defocusing effect and change the energy distribution in the bunch. In order to contain the large defocusing it is necessary to switch on the quadrupole of the spectrometer beamline. The same happens even at low charge when in some configuration the relative energy spread of the bunch can assume values around 10%. In this condition when the bunch passes thought the quadrupole, chromatic effects have to be taken into account during the screen images analysis, to accurately evaluate the energy spread.

The nominal electron bunch produced by the FERMI photoinjector is a 800 pC - 10 ps bunch with a ramped longitudinal profile [3] and the spectrometer can be very useful to check and control the efficiency in producing the desired ramping current distribution. In fact setting the RF gun phase far off crest to superimpose a very linear energy correlation along the bunch, particles on the head of the bunch are bended less than particles on the tail, so the ramped longitudinal profile can be reproduced at the spectrometer screen. Since the high resolution of the screen, this measurement resolves the longitudinal profile better than 0.2 ps, which is better than a commercial streak camera.

References
[1] M. Trovò *et al.*, Proc. of the EPAC 2008 conference.
[2] G. Penco *et al*., Proc. of the EPAC 2008 conference.
[2] G. Penco *et al*., *"Ramping longitudinal distribution studies for the FERMI@ELETTRA injector"*, Proc. of the FEL 2006 conference.

FERMI@ELETTRA PHOTOINJECTOR HAS STARTED ITS COMMISSIONING!

M. Trovò[1], L. Badano[1], F. Cianciosi[1], P. Craievich[1], F. Curbis[2], N. Cutic[2], M. Danailov[1], A. Demidovich[1], R. Gobessi[1], D. Kumbaro[2], F. Lindau[2], G. Penco[1], L. Pivetta[1], L. Rumiz[1], G. Scalamera[1], D. Wang[1], F. Zudini[1]

[1] Sincrotrone Trieste S.C.p.A., Trieste, Italy
[2] MAX-lab, University of Lund, Lund, Sweden

E-mail: mauro.trovo@elettra.trieste.it

The new FERMI@Elettra photoinjector is presently undergoing high-power testing and characterization at MAX-Lab in Lund Sweden. This effort is a collaboration between Sincrotrone Trieste, MAX-lab and UCLA. The 1.6-cell RF gun cavity and the focusing solenoid [1] were successfully designed and built by the Particle Beam Physics Laboratory at UCLA, delivered to Sincrotrone Trieste (ST) at the beginning of 2008, and installed in the linac tunnel at MAX-Lab. Use of the MAX-Lab facility will allow the FERMI project to progress significantly with the photoinjector while waiting for the completion of the new linac building extension at Sincrotrone Trieste.

The experiments in MAX-lab aim to perform the acceptance test of the FERMI Gun and to start its commissioning using the existing S-band 25 MW klystron and the operating photoinjector UV laser (262 nm, 10 ps duration and 500 J pulse energy available) regularly used during the FEL operation of the MAX-lab injector [2].

The crucial elements of the FERMI photoinjector (RF cavity, magnets, laser beam diagnostics and transport and electron beam diagnostics) have been installed by the ST staff in the injector tunnel of MAX-lab, as shown in Figure 1, during the Easter shutdown [3]. The system was completely set up in situ by assembling the different components (supports, vac-

Figure 1.
FERMI gun back-view with RF waveguide and cavity and pumping system in the MAX-lab tunnel.
Left: FERMI gun picture.
Right: 3D cad rendering as designed.
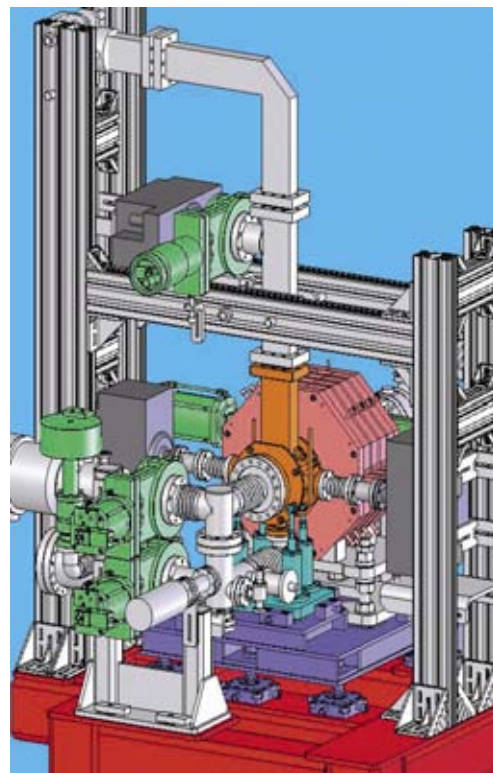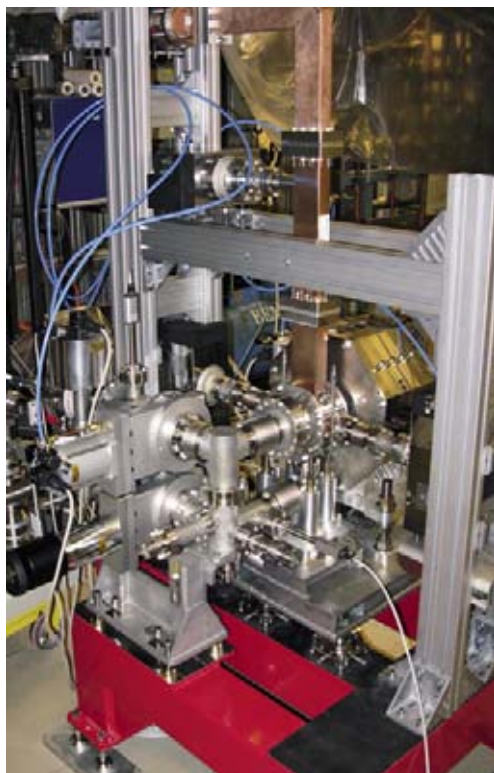
uum components, wave guides, pumping system and diagnostics). The photoinjector has also been equipped with its own control system that interfaces in an effective manner to all the devices, allowing the development of the specific high-level software to tune the photoinjector.

During the allocated beam time of week 21, the RF gun was conditioned to full specifications, achieving, in four nights, the nominal values of 10 MW input peak power (corresponding to a maximum gradient of the electrical field at the photocathode of about 120 MV/m), 3 μs pulse duration and 10 Hz repetition rate. Electrons accelerated by this filed gain, upon reaching the exit of the gun, an energy of about 5 MeV.

On the night of May 28, the RF gun's copper cathode was illuminated by a UV laser operating at 262 nm and delivering 50 μJ per pulse and the first FERMI photoelectrons were clearly detected on both the integrating current transformer (ICT) and YAG:Ce scintillation screen. Figure 2 shows the time behaviour of the RF power at the gun input measured by means of a directional coupler, the laser time arrival as measured with a photodiode signal, and the electron beam current signal as measured with the ICT. The photoelectron peak, superimposed on the dark current background, is clearly visible on the ICT trace in correspondence of the laser shot. The photoelectron beam charge was measured to be equal to 180 pC, corresponding to a quantum efficiency QE = $1.7 \cdot 10^{-5}$.

During the third allocated beam time of weeks 27 and 28, the Gun commissioning advanced and achieved new crucial results. The photoelectron extraction and the gun tuning were performed in a more systematic way. Moreover the dedicated gun diagnostics were integrated in the photoinjector control system thus enabling a full set up of the gun facility.

In conclusion, the FERMI photo-cathode gun commissioning has been successfully started in the MAX-lab tunnel with encouraging results: the cavity conditioning went on smoothly, the first photoelectrons were extracted and measured, the first quantum efficiency measurement indicates a good cathode surface cleanness and, more importantly and in general, the system behaves according to specification.

Further activities are planned at MAX-lab to continue the characterization of the FERMI gun e-beam and to proceed the system commissioning. This will allow us to reduce the
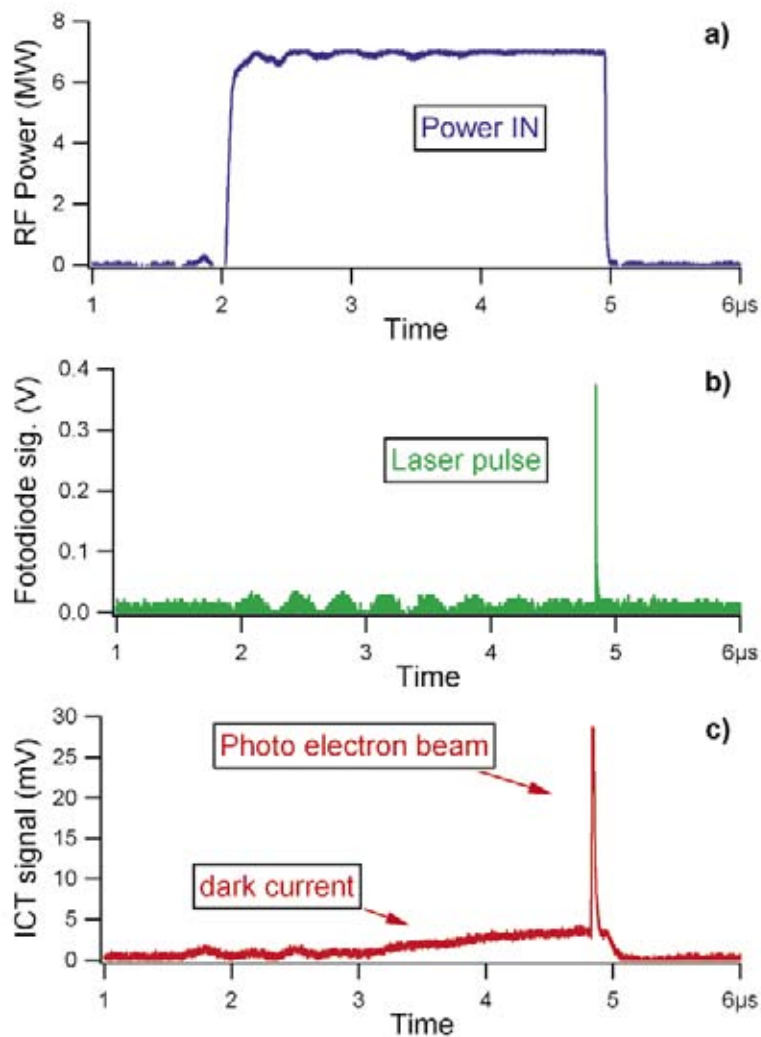
commissioning time at Trieste. The system will be moved back to Trieste as soon as the FERMI site will be completed.

References

[1] G. D'Auria *et al.*, "The new Photoinjector for the FERMI Project", PAC'07, Albuquerque, TUPMN028, 974 (2007).
[2] S. Thorin *et al.*, "Start-to-end simulations for a seeded harmonic generation free electron laser", Phys. Rev. ST Accel. Beams **10**, 110701 (2007)
[3] M. Trovò *et al.*, "Status of the FERMI@Elettra Photoinjector", EPAC 08, Genova, MOPC080, 247 (2008).

Figure 2.
Time behaviour of the RF power at the input of the gun (a), of the photodiode signal of the laser (b) and of the ICT signal (c).

FACTS & FIGURES

Sincrotrone Trieste S.C.p.A. began operations in 1987: it is a **non-profit Share Company** (Società Consortile per Azioni) recognised as being of national interest by a State Law, which manages the **Elettra Laboratory**. Elettra continues to update itself and grow. In addition to significant modernisation projects relating to beamline sources and other components, a new fourth generation light source, **FERMI@Elettra**, is under construction alongside the original one.

Elettra is an Associate Laboratory of the International **Atomic Energy Agency (IAEA)** of Vienna, and forms a key node in the science and technology network of the **Central European Initiative (CEI)**.

It participates in more than twenty projects within the EU Framework Programme for Research and Development, and co-ordinates **project I3 (IA-SFS)**, which encourages transnational access to and technological development in European synchrotron light laboratories.

On its site Elettra hosts the **National Laboratory TASC** (INFM-CNR), a facility for micromanufacturing and nanoscience. It has also established enduring working relationships with important Italian and foreign institutions, including various **CNR** (National Research Council) bodies, the **Academies of Science of Austria** and the **Czech Republic**, UNESCO's International Centre of Theoretical Physics **(ICTP)**, the International School of Advanced Studies **(SISSA)**, and the **Universities** of Milan, Trento, Trieste and Udine. These partners are actively contributing to the construction and operation of beamlines and support laboratories.

Elettra's scientific and technical quality and developments are constantly monitored by Board-appointed international Committees which advise on all relevant aspects of the general and development policy, scientific programs, accelerator development, technology transfer and industrial applications.

SHAREHOLDERS
> AREA Science Park Consortium (51%)
> Autonomous Region of Friuli Venezia Giulia (40%)
> INFM-CNR (National Institute of Material Physics of the Italian National Research Council) (5%)
> The national Agency for inward investment promotion and enterprise development (4%)

ALLIANCES AND PARTNERSHIPS
> IAEA (International Atomic Energy Agency)
> CEI (Central European Initiative)
> IRUVX (European Consortium for FELs up to the UV/softXray)
> Austrian Academy of Sciences
> Academy of Sciences of the Czech Republic
> CNR (Consiglio Nazionale delle Ricerche – National Research Council)
> CNRS (Centre National de la Recherche Scientifique)
> ICTP - UNESCO (International Centre for Theoretical Physics)
> INSTM (Consorzio Interuniversitario Nazionale per la Scienza e Tecnologia dei Materiali – National Inter-University Consortium for Materials Science and Technology)
> INFN (Istituto Nazionale di Fisica Nucleare National Institute of Nuclear Physics)
> ISAS (International School of Advanced Studies)
> Charles University, Prague
> University of Nova Gorica
> University of Milan – Bicocca
> University of Trento
> University of Trieste
> University of Udine

Sincrotrone Trieste S.C.p.A. is managed by a **Board of Directors**, assisted by a shareholder-appointed **Board of Auditors**, and advised by Board-appointed international committees such as the **Council of Partners** for general and development policy, the **Scientific Advisory Council** for scientific programs, the **Machine Advisory Committee** for accelerator development, and the **Industrial Advisory Panel** as far as technology transfer and industrial applications are concerned.

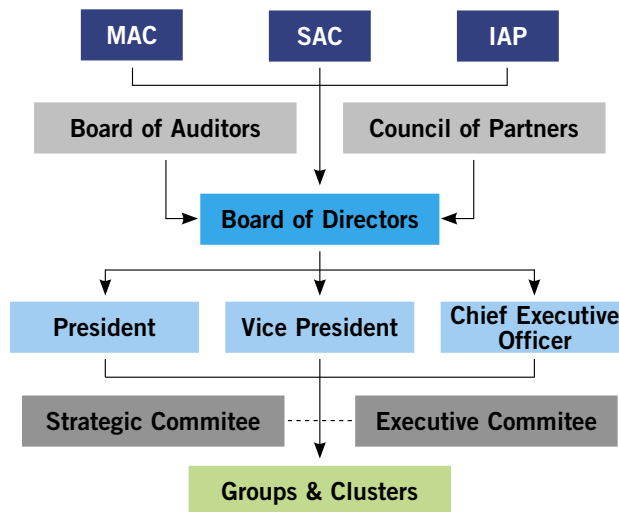## Machine Advisory Committee (MAC)

Chairman: Richard P. Walker
Paul J. Emma
Mikael Eriksson
Jerome Hastings
Carlo Pagani
Claudio Pellegrini
Mike Poole
Robert W. Schoenlein
Hans Weise

Scientific Advisory Council (SAC)

Chairman: Ingolf Lindau
David Attwood
Gordon Brown
Charles S. Fadley
Robert Huber
Sine Larsen
Dietrich Menzel
Charles V. Shank
Friso van der Veen

Industrial Advisory Panel (IAP)

Chairman: Alberto Sangiovanni-Vincentelli
Carlo Castellano
Enrico Albizzati
Maurizio Arienzo
Mauro Ferrari

```
MAC        SAC        IAP

Board of Auditors    Council of Partners

        Board of Directors

President   Vice President   Chief Executive Officer

Strategic Commitee ---- Executive Commitee

        Groups & Clusters
```

Board of Auditors

Chairman: Fabio Matarazzo
Nicola Archidiacono
Claudio Sambri
Paolo Marchesi
Ugo Braico

Board of Directors

President: Carlo Rizzuto
Vice President: Giovanni Comelli
Chief Executive Officer: Alfonso Franciosi
Roberto Della Marina
Marcello Fontanesi
Gemma Ravizza
Giorgio Rossi
Giorgio Sulligoi
Alessandro Trovarelli

Council of Partners

President: Carlo Rizzuto
Fabio Barbone
Stefano Fantoni
Alain Fontaine
Marcello Fontanesi
Dante Gatteschi
Peter Laggner
Vladimir Matolin
Fabio Ruzzier
Claudio Tuniz

THE STAFF

S incrotrone Trieste has adopted a matrix-type of organization. The four Strategic Initiatives correspond to and are implemented through four **Clusters** of different **Projects**, grouped together based on the complementarity of the different project goals. The human and instrumental res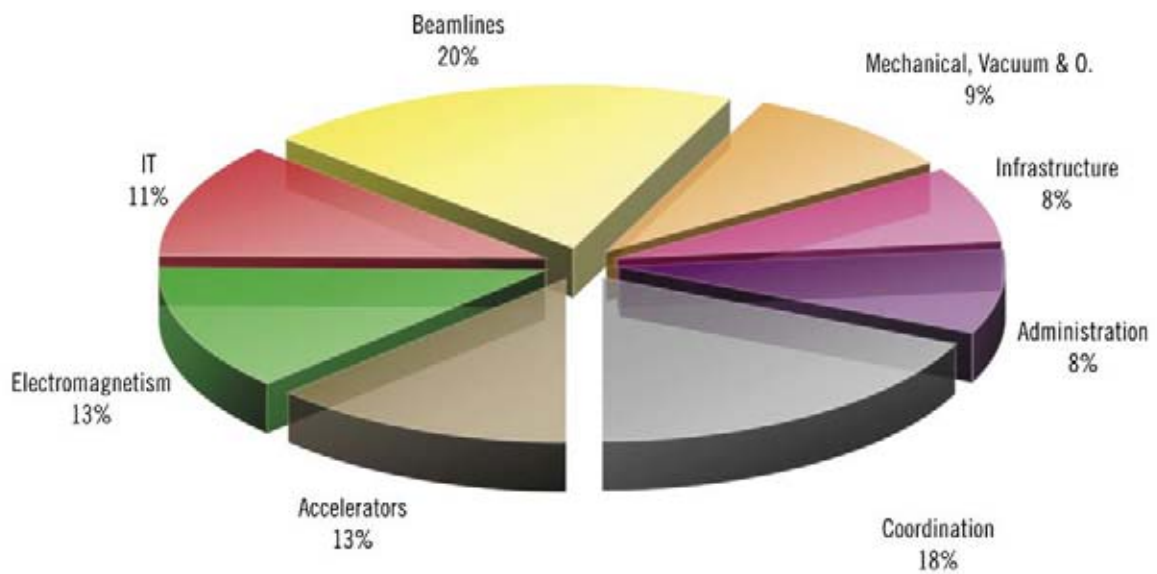ources required by the different projects are managed within eight **Groups** of staff members with similar or related expertise.

CLUSTERS

	Elettra	Fermi	Research	Technology Platform

Scientists and Reseachers ■ **Technical Personnel** ▢ **Administrative and clerical Personnel** ▨

GROUPS

Group	Total
Accelerators	40
Electromagnetism	40
Information Technology	36
Beamlines	62
Mechanical, Vacuum and Optical Engineering	29
Infrastructure	25
Administration	27
Coordination	56

TOTAL 315
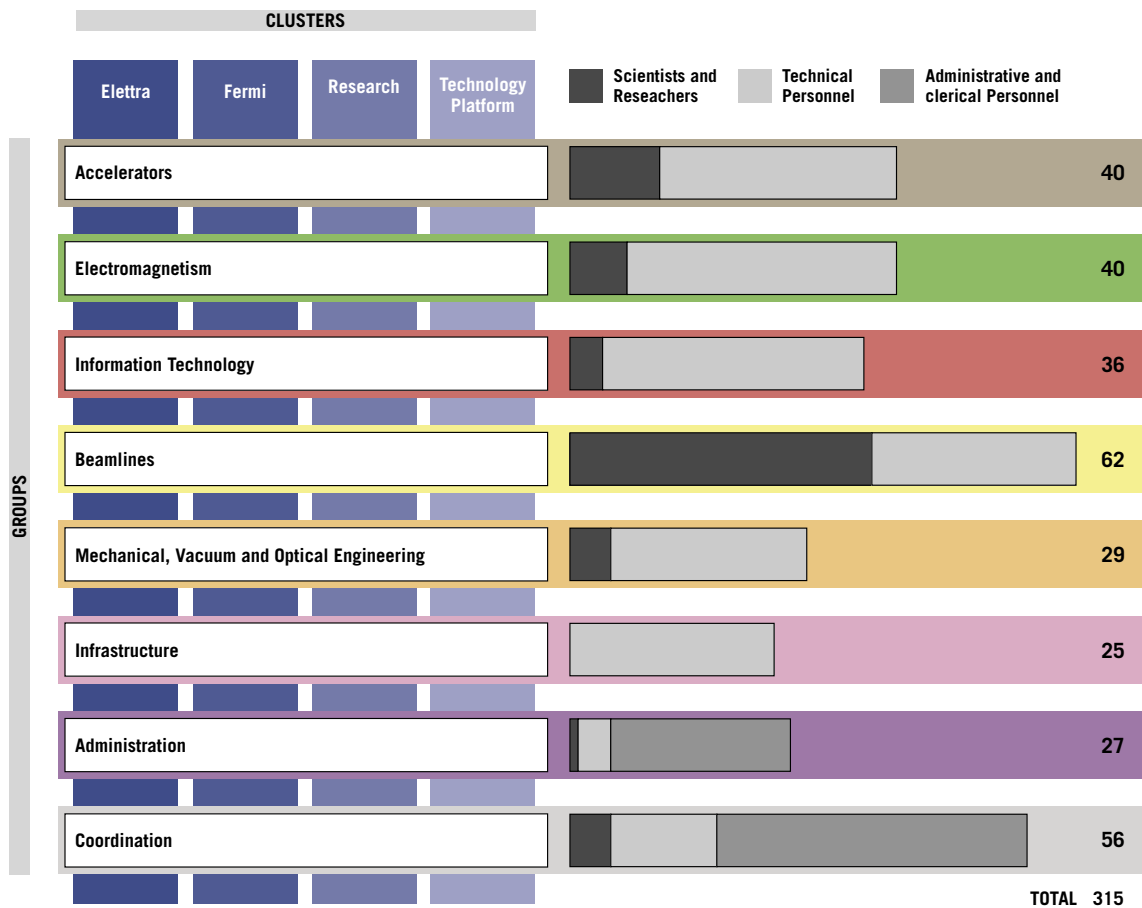
STAFF DISTRIBUTION BY GROUP

Beamlines 20%
Mechanical, Vacuum & O. 9%
Infrastructure 8%
Administration 8%
Coordination 18%
Accelerators 13%
Electromagnetism 13%
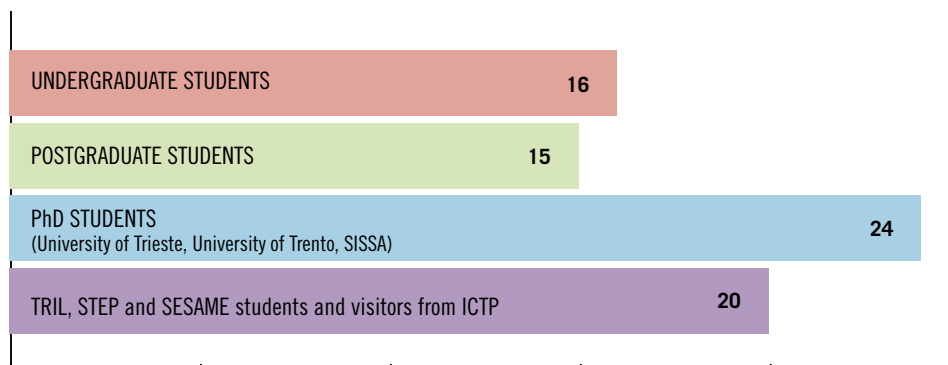IT 11%

TRAINING AND CAREER DEVELOPEMENT (July 2007 - June 2008)

Elettra provides support for training and education of university students, hosting courses, lectures, stages ranging from Physics to Engineering and support for scientific activities. A collaboration with the International Centre of Theoretical Physics has been established with the aim of giving the opportunity to junior representatives of scientific institutes in developing countries to participate in Elettra's projects.

UNDERGRADUATE STUDENTS	16
POSTGRADUATE STUDENTS	15
PhD STUDENTS (University of Trieste, University of Trento, SISSA)	24
TRIL, STEP and SESAME students and visitors from ICTP	20

	BEAMLINES		source*	energy range (eV)	partner institutions
1.1L	TWINMIC	A multipurpose twin X-ray microscopy beamline for improving life conditions and human health	short id	250 - 2000	ESRF, PSI, SLS, CNR-INFM, King's Coll. London, RheinAhrCampus Remagen, Göttingen Univ., ITPO Ljubljana
1.2L	Nanospectroscopy	SPELEEM (Elmitec GmbH) and LEEM-PEEM end-station	id	50 - 1000	CNRS
1.2R	FEL	European Free-Electron Laser project	id	1,8 - 9,5	
2.2L	ESCA Microscopy	Scanning photoelectron microscopy (SPEM)	id	200 - 1400	
2.2R	SuperESCA	Fast X-ray photoemission experiments on surfaces	id	85 - 1500	
3.2L	Spectro Microscopy	Angle-resolved photoemission microscope	id	27 - 95	
3.2R	VUV Photoemission	Angle-resolved photoemission in the VUV range	id	16 - 1000	CNR
4.2	Circularly Polarised Light	Circularly Polarised Photoemission and X-ray absorption spectroscopy	id	5 - 1000	CNR
5.2L	SAXS	Small Angle X-Ray Scattering	id	8000 - 16000	Austrian Academy of Science
5.2R	XRD1	X-ray Diffraction	id	4000 - 22000	CNR
6.1L	Materials science	Photoemission and X-ray absorption	bm	40 - 800	Czech Academy of Science, Charles University, Prague
6.1R	SYRMEP	SYnchrotron Radiation for MEdical Physics	bm	8000 - 35000	University of Trieste
6.2R	Gas Phase	Research on gaseous systems	id	14 - 1000	CNR, CNR-INFM, INSTM
7.1	MCX	Powder Diffraction Beamline	bm	2100 - 23000	University of Trento, INSTM
7.2	ALOISA	Advanced Line for Overlayer, Interface and Surface Analysis	id	120 - 8000	CNR-INFM
8.1L	BEAR	Bending magnet for Emission Absorption and Reflectivity	bm	4 - 1400	CNR-INFM
8.1R	LILIT	Laboratory for Interdisciplinary LIThography	bm	1000 - 5000	CNR, CNR-INFM
8.2	BACH	Beamline for Advanced DiCHroism	id	35 - 1600	CNR-INFM
9.1	SISSI	Source for Imaging and Spectroscopic Studies in the Infrared	bm	0,001 - 3	CNR-INFM, Univ. of Rome "La Sapienza"
9.2	APE	Advanced Photoelectric-effect Experiments	id	10-2000	CNR-INFM
10.1L	X-ray microfluorescence	X-ray microfluorescence	bm	4000 - 20000	
10.1R	DXRL	Deep-etch Lithography	bm	2000 - 20000	
10.2L	IUVS	Inelastic Ultra Violet Scattering	id	11-2008	
10.2R	BAD Elph	Photoemission with low energy photons	id	4 - 25	Wuerzburg Univ.
11.1R	XAFS	X-ray Absorption Fine Structure	bm	2300 - 25000	ICTP
11.2	XRD2	X-ray Diffraction	id		

source*   id = insertion device (wiggler or undulator)
           bm = bending magnet

The allocation of **beamtime** to proposing users occurs via international committees and referees and the users have their own representative body to assess the quality of the service (**Scientific Review Committee**).

Atoms, Molecules & Plasmas

Svante Svensson (Chairman)
Vincenzo Aquilanti
Uwe Becker
John M. Dyke

Scattering

Paolo Mariani (Chairman)
Stephanie Finet
Daniele Fioretto
Hermann Franz
Giulio Monaco

Catalytic Material/Surface Science

Carlo Mariani (Chairman)
Philip Hofmann
Falko P. Netzer
Petra Rudolf
Michèle Rose Sauvage-Simkin
Robertino Zanoni

Hard condensed matter - Structures

Maurizio Benfatto (Chairman)
Robert Joseph Cernik
Paola D'Angelo
Marco Milanesio

Scientific Review Committee

Dipankar Das Sarma
(Chairman)

Condensed matter
Electronic & Magnetic Structure

Dipankar Das Sarma (Chairman)
Hermann Dürr
Mark Golden
Giorgio Margaritondo
Maurizio Sacchi

Protein & Macromolecular
Crystallography

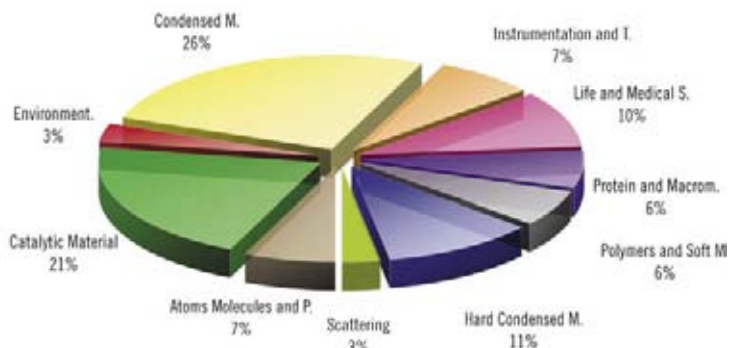Giuseppe Zanotti (Chairman)
Tilman Schirmer
Dusan Turk
Luigi Vitagliano

Instrumentation & Technological materials
Life and Medical Sciences
(excluding Crystallography)
Polymers and Soft Matter

Graeme Morrison (Chairman)
Paul Dumas
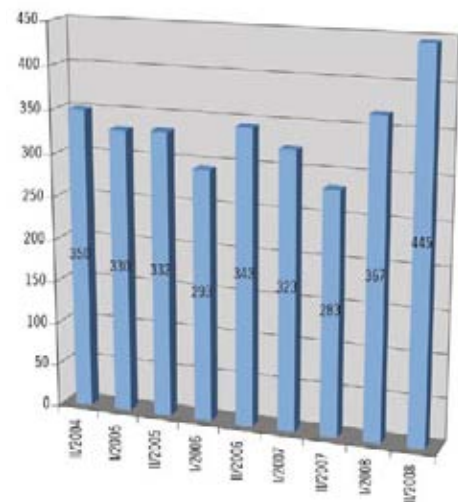Christopher Hall
Lisa Miller
Günther Schmal
Steve Wilkins

USERS AT ELETTRA: TOT = 750 (July 2007 - June 2008)

Norway
2

Switzerland
13

Canada
4

Usa
22

Brazil
6

Argentina
2

South Africa
1

Moldova
15

Croatia
15

Japan
5

China
6

Australia
8

India
48

Iran
2

Map values: 2, 6, 4, 49, 6, 44, 30, 101, 12, 39, 7, 31, 265, 5

ALLOCATED PROPOSALS BY RESEARCH AREA: TOT = 288 (July 2007 - June 2008)

Condensed M.
26%

Instrumentation and T.
7%

Life and Medical S.
10%

Environment.
3%

Protein and Macrom.
6%

Catalytic Material
21%

Polymers and Soft M
6%

Atoms Molecules and P.
7%

Scattering
3%

Hard Condensed M.
11%

2004 - 2008 PROPOSALS SUBMITTED BY SEMESTER

Bar chart values: 350, 330, 332, 293, 343, 323, 283, 367, 445

From October 1st, 2007 to March 2nd, 2008 the Elettra light source was closed due to the booster installation.

FINANCIAL FIGURES

BUDGET ALLOCATION FOR 2008

Running costs	
General costs	€ 6.046.920
Personnel	€ 13.981.938
Utilities	€ 5.024.115
Accelerator group	€ 279.953
Administration group	€ 261.536
Beamlines group	€ 866.151
Coordination group	€ 1.799.596
Electromagnetism group	€ 478.285
IT group	€ 369.051
Infrastructure group	€ 1.070.664
Mechanical, Vacuum and Optical engineering	€ 355.982
Industrial Liason Office operation	€ 607.602
Scientific partnerships	€ 350.000

Development projects	€ 6.817.338

TOTAL ORDINARY OPERATION	€ 38.309.131

Special projects	
Booster	€ 55.305
Fermi	€ 58.392.360

TOTAL SPECIAL PROJECTS	€ 58.447.665

GENERAL TOTAL	€ 96.756.796

PROJECTS / SPONSORED RESEARCH

The recent shift in the Company activities to a project-based approach has had a very positive effect on the ability to propose projects to external funding institutions and thus attract resources: the last two calendar years, 2007 and 2008 (not yet concluded), were extremely successful in this respect. As for the FERMI project, in December 2007 we were officially notified of the signing of the program agreement "FERMI@Elettra – Phase II" with the Ministry of University and Research, that assigns to the Company a contribution of 11.7 million Euro.

Apart from this main project, the Company has been able to win research contracts with public entities on the European, Italian and Regional levels, acquiring contributions equivalent to 8.8 million Euro in 2007 and 3.1 million Euro in the first half of 2008. At the time of this writing, submitted applications for external funding presently under evaluation by the Region of Friuli Venezia Giulia and by the European Commission (EC) total in excess of 4 million Euro, while the further requests for funding in the applications that are presently being drafted, in view of the deadlines in autumn 2008, total about 10 million Euro more.

Particularly relevant is the acquisition of a Starting Grant assigned by the European Research Council (ERC) to the project for the construction of an inelastic scattering beamline for the FERMI source, coordinated by Dr. Claudio Masciovecchio, scientist of the Beamlines Group of the Company. The selection process by the ERC has been particularly strict: less than 3% of the submitted projects have obtained funding. This success testifies the absolute excellence at the European level of the personnel and of the programmes of the Company.

The consolidated presence of national and international partners has in the past brought in significant investments. Various new initiatives have been undertaken to increase this presence and to consolidate the transformation of the Company into an international institution. The most important ones are the definition and constitution, with EC funding in the preparatory phase, of a European Consortium of FELs (with Germany, United Kingdom and Sweden as the original founders and Switzerland, France, The Netherlands and Poland adhering subsequently). This Consortium is the possible base for a transformation of the Company into an international foundation (or some other form of institution).

Other important achievements have been obtained within the I3 project IA-SFS (Integrating Activity on Synchrotron and Free Electron Laser Science). Elettra has been the coordinator of this project since March 2004: this is the most significant FP6 (Sixth European Union Framework Programme) project in the field of synchrotron radiation and free electron lasers (see http://www.elettra.trieste.it/i3/). The EC finances a total of 27 million Euro within the project for user access to the European network of synchrotron light sources, not to mention the joint development of various specific technologies. Elettra has proved itself with a precise, timely and transparent management of the assigned funding and excellently coordinated the manifold activities of this project. The other international institutions that participate in the project have voted unanimously for Elettra to coordinate the new integrated initiative that will continue IA-SFS in FP7, namely the ELISA project (European Light Sources Activities – Synchrotrons and Free Electron Lasers) that is presently under negotiation. Furthermore, the IA-SFS has been selected as one of the 40 "success stories" of FP6 to be included in a publication, edited by the European Commission, that will be distributed to the general public, National and Regional authorities, European Parliament, Delegations and Representations of the European Union all over the world.

During the last 12 months, Elettra participated in 31 research contracts (see table) funded by the following external agencies: European Commission, Italian Ministry of Research, Region Friuli Venezia Giulia, International Centre for Theoretical Physics, Indian Department of Science and Technology.

EUROPEAN/INTERNATIONAL RESEARCH CONTRACTS

NAME	SHORT NAME	COORDINATOR
Biocrystallography on a Highly Integrated Technology Platform for European Structural Genomics	BIOXHIT	EMBL Germany
Integrating Activity on Synchrotron and Free Electron Laser Science	IA-SFS	Elettra
European FEL Design Study	EUROFEL	DESY Germany
European Design Study Towards a Global TeV Linear Collider	EUROTeV	DESY Germany
Enabling Grids for E-sciencE - II	EGEE-II	CERN Switzerland
Light Source Theory Network	LighTnet	STFC United Kingdom
ICTP-Elettra Users Programme		Elettra
Transnational access of the Indian scientists to the Elettra beamlines		Elettra
Conservation materials for stained glass windows-assessment of treatments, studies on reversibility, and performance of innovative restoration strategies and products	CONSTGLASS	Fraunhofer-Institut für Silicatforschung Germany
Deployment of Remote Instrumentation Infrastructure	DORII	PSNC Poland
Preparatory Phase of the IRUVX-FEL Consortium	IRUVX-PP	DESY Germany
TIME-Resolved Spectroscopy of Nanoscale Dynamics in Condensed Matter Physics	TIMER	Elettra

NATIONAL RESEARCH CONTRACTS

NAME	SHORT NAME	COORDINATOR
Nano- and micro-spectroscopy by synchrotron radiation integrated with advanced STM/AFM systems to study manmade atomic scale functional materials	Integrated nanospectroscopies	Elettra
BOOSTER-Elettra		Elettra
Post-Genomic Structural Biology: Developing Infrastructures for Protein Crystallography	Structural biology	Elettra
FERMI@Elettra - Phase I		Elettra
High efficiency innovative light sources for solid state illumination devices with civil and automotive applications	LUCI	CNR
FERMI@Elettra - Phase II		Elettra

REGIONAL RESEARCH CONTRACTS

NAME	SHORT NAME	COORDINATOR
Development of a 3D detector with micrometer space resolution and picosecond time resolution	3D detector	Elettra
Desorption measurements from photoresists for the Extreme UltraViolet Lithography	EUVL photoresists	Elettra
X-ray diffraction from polycrystalline materials in controlled environment	XRD polycrystalline materials	Elettra
Monitoring station for PM10 particles	PM10	Elettra
The Elettra storage-ring FEL: a multi-purpose light source	EUFOS	Elettra
Realization of a technological platform for the crystallographic analysis of biological macromolecules of biomedical interest for the industrial research	DAGEAS	Elettra
Study of hybrid organic/inorganic interfaces for strategic applications in the field of flexible displays and biochips	Nano-BioSOLEd	Elettra
Study and realization of prototype platforms for plane and helical undulators		Elettra
Convalidation of LiFArte activity	INVISIBLE	AREA Science Park
Development and realization of solid state ultrafast laser amplifiers optimizd for FEL applications	FEL Laser Amplifiers	Elettra
Distributed environment monitoring based on Grid	MADBAG	Elettra
Anti Counterfeiting Tags	ACT	Elettra
Development of chemical sensors for environmental and biological diagnosis based on nanowires and nanotubes	Nanowire/nanotube sensors	Elettra

TECHNOLOGY TRANSFER AT ELETTRA

The Industrial Liaison Office (ILO) was set up in 2004 to promote the exceptional body of skills and technical expertise resulting from the experience accumulated in the construction and running of the Elettra facilities over a long period of time. This know-how is of particular interest to other Synchrotron facilities, suppliers of advanced instrumentation and private industrial companies operating in different fields: mechanical, optical, pharmaceutical, microelectronics, energy, chemistry etc.

Products and services are sold throughout the world. 2007 turnover is reported on the next page together with the trend over the years, and show an increase in consultancies and instrumentation business.

In 2007, in order to supply the world market and, initially, the FERMI@Elettra project with undulators, a partnership of an entrepreneurial nature was established and a spin-off company (Kyma srl) was created to set up an industrial scale production structure. After launching the production of undulators for FERMI@Elettra, Kyma will operate in the international market as an expert and qualified supplier of accelerator components.

In 2008 ILO, for the first time, presents itself to industry through a catalogue that describes Sincrotrone Trieste technologies and services. The catalogue has been specifically conceived for this target and describes various examples of the great variety of studies, skills and technological resources to be found in the Laboratory. For enterprises that must innovate continuously, access to this valuable source of knowledge can provide useful support to R&D activity and a genuine competitive advantage in the international marketplace.

Furthermore, in terms of market share, ILO has proved its capability to sell Elettra-developed scientific instrumentation to other synchrotron facilities and research laboratories worldwide, so that in 2008 another catalogue concerning Elettra products has been released.

The catalogue includes: photon or charged particle detectors, based on centroid finding techniques – such as (cross) delay anode detectors – or based on multi-channel acquisition, employed in several of Elettra's beamlines (See the technical paper on page 110); high voltage bipolar power supply systems especially suited for benders of X-ray biomorph mirrors; picoammeters with a sampling frequency of 10 kHz on 4 independent channels; ionisation chambers and beam position monitors used to characterise and monitor photon and electron beams and other devices developed in our Instrumentation and Detectors Laboratory such as multi-point strain gauges; charge pulse amplifiers; high voltage pulse generators; RF filters etc.

As far as accelerator parts that are still provided directly by Elettra are concerned, resonant cavities are illustrated, whose purpose is to accelerate electrons passing through them by the application of accelerating voltages ranging from tens to hundreds of kilovolts, with a resonant frequency of 500 MHz.
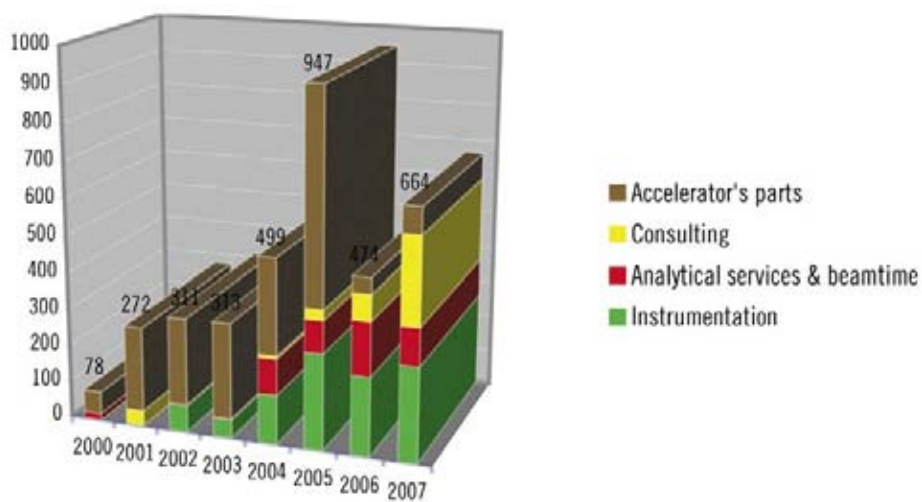
2007 ORDERS AMOUNT BY CUSTOMER COUNTRY

COUNTRY	NUMBER OF ORDERS	AMOUNT (Thousands of Euro)
Switzerland	1	1,00
Italy	10	238,56
Germany	7	355,90
France	3	33,38
United States	5	36,30
United Kingdom	1	36,80
Spain	2	795,40
Canada	1	31,05
TOTAL	30	1.528,38

2007 ORDERS AMOUNT BY COMMERCIAL ACTIVITY
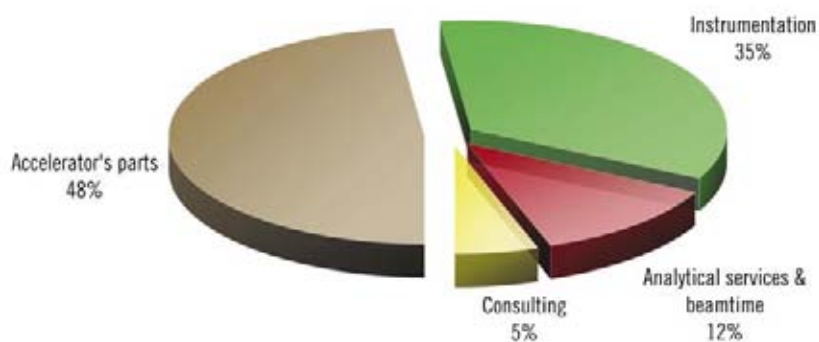
2007 TREND IN TURN OVER OF COMMERCIAL ACTIVITY (Thousands of Euro)

EVENTS

Official visit of Giorgio Napolitano, President of the Republic of Italy

(March 28, 2008)

Carlo Rizzuto and local Authorities receive the President of the Republic Giorgio Napolitano: the President of FVG Region Riccardo Illy, the President of the Province of Trieste Maria Bassa Poropat and the Mayor of Trieste Roberto Dipiazza (1, 2). After the speech of Carlo Rizzuto (3, 4), President Napolitano visits the Syrmep beamline for mammography (5) and watched the 3D simulation of the new free electron laser FERMI@Elettra (6). In the Control Room, he activates the injection of the new Booster (7) and signs the visitors book (8). Finally he receives the Elettra medal (9).

6

7

8

9

Visit of the Friuli Venezia Giulia Region' President

(December 19, 2007)
Riccardo Illy, President of the Friuli Venezia Giulia Region, attends the ceremony for the opening of the first FERMI building (1, 2). On the occasion of the visit, the "Gianfranco Rados" Scholarship was awarded to Francesca Iannelli (3).

Official visit of Bartholomew I of Constantinople

(March 4, 2008)
The highest religious authority of the Orthodox Church, His All Holiness Bartholomew I, Archbishop of Constantinople, New Rome and Ecumenical Patriarch, visits Trieste in occasion of the 225th anniversary of the Greek-oriental community.

Open Day at Elettra

(May 10, 2008)
808 persons visit the Elettra and TASC labora-
tories in 23 tours, guided by 58 volunteers.

Elettra Spring Party

(May 22, 2008)
A social event for the Elettra staff, with music and games. The party takes place in the hall of the Linac Underground, where the laboratories of FERMI@Elettra project will be built.

events

Israeli Ambassador in Italy

(March 10, 2008)
H. E. Gideon Meier visits Elettra

TV interview

(April 17, 2008)
TG Leonardo - RAI 3 and RAI International - video-tape at the ESCA Microscopy beamline. TV broadcast of a special report on the new technology for anti-counterfeiting of art works, the project "Leaf Art".

Press Tour

(July 12, 2008)
The Press Tour organized by Area Science Park to show the scientific park. The journalists, from local and national newspapers and agencies, during the vist at the Elettra laboratory.

InnovAction

(Udine, February 14-17, 2008)
Elettra and FERMI@Elettra at the Udine
Fair of knowledge, ideas and innovation.
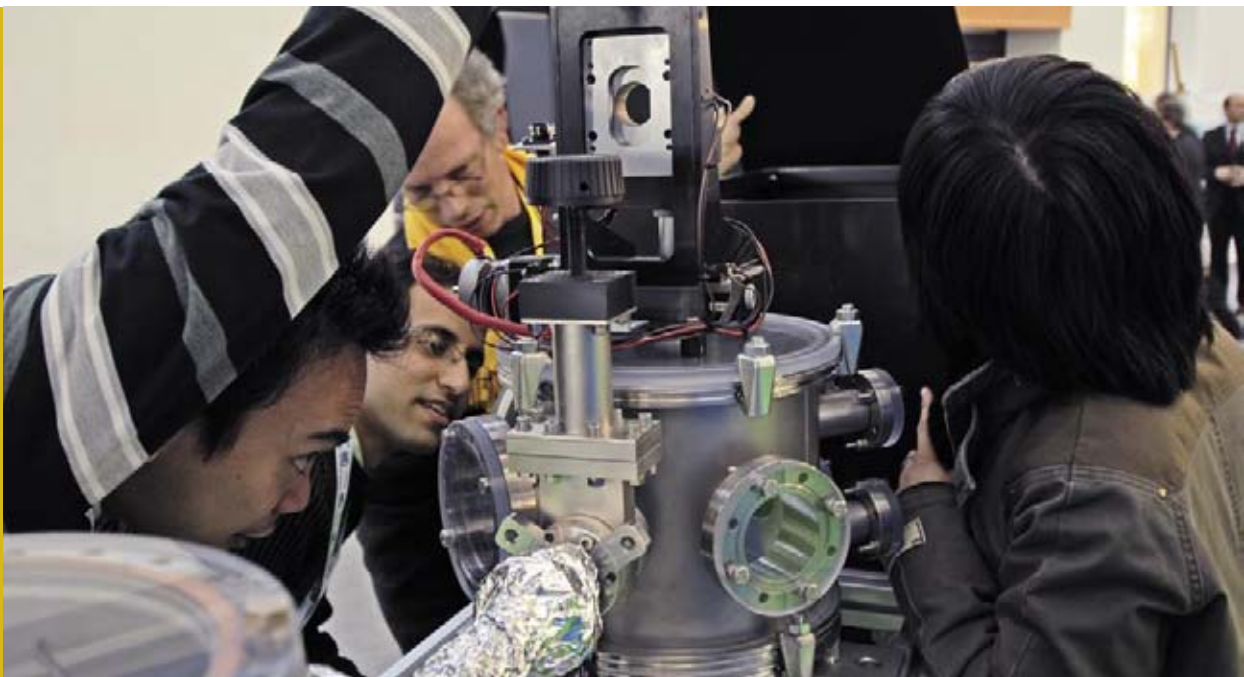
Festival della Scienza - Festival of Science

(Genoa, October 25 - November 6, 2007)
The particulate monitoring unit set up at Elettra to collect PM10 samples is displayed at the Festival of Science.

FEST

(Trieste, April 17-22, 2008)
The virtual tour of FERMI@Elettra (1) is presented at the 2008 edition of FEST, International Science Media Fair (2).

Meetings dedicated to orientations, schools and training

(Bologna, November 8-9, 2008) (Padova, May 22, 2008)
Sincrotrone Trieste's stands at Bologna - Incontro Aziende-Studenti Companies-Students Meeting (1) - and Padova "Università aperta" incontro aziende-studenti "University Open Day" companies-students meeting (2).

The new catalogue "Services and Technologies for Industry"

(Trieste, June 19, 2008)
Press conference for the presentation of the new Sincrotrone Trieste catalogue: Carlo Rizzuto, President of ST, and Renzo Tondo, President of Friuli Venezia Giulia Region (1) and the catalogue cover (2).

Introduzione all'ottica - In Viaggio con la luce / Introduction to Optics - Travelling with light

(Trieste, November 5-7, 2007)
The Optic School organized by Sincrotrone Trieste: the poster of the school (1) and some students attending lessons at the Elettra Laboratory (2).
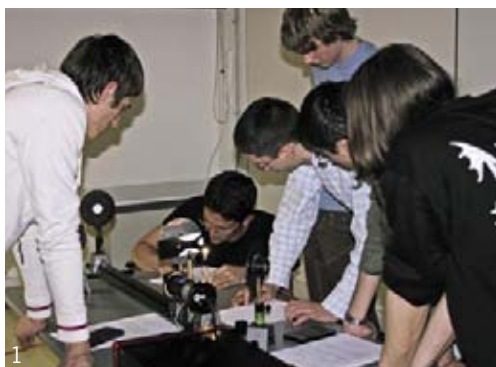
Timing and Synchronization Workshop

(Trieste, March 26-28, 2008) The participants at the workshop

EPAC 2008 - 11th European Particle Accelerator Conference

(Genoa, June 23-27, 2008)
Sincrotrone Trieste's stand at the conference. ST is one of the organizers of the event.

6th International Workshop on LEEM-PEEM

(Trieste, November 7-11, 2008)
Poster of the workshop (1) and picture of the participants during the visit to Miramare Castle (2). The workshop was organized by Sincrotrone Trieste.

## WORKSHOPS, CONFERENCE, MEETING AND SCHOOLS (October 2007 - September 2008)

| EVENT	PLACE	DATE	ORGANISERS / COLLABORATORS
Introduzione all'ottica - In Viaggio con la luce Introduction to Optics - Travelling with light	ST	5-7/11, 2007	Sincrotrone Trieste
XV Users' Meeting	Trieste	3-4/12, 2007	Sincrotrone Trieste
Solid State Modulator Workshop	Trieste	6-7/12, 2007	Sincrotrone Trieste
Timing and Synchronization Workshop	ST	26-28/03, 2008	Sincrotrone Trieste / INFN / Enea
EUROTeV/GANMVL All hands Meeting	ST	31/03-01/04, 2008	Sincrotrone Trieste
Tavola Rotonda "Ricercatori stranieri in Italia"	Trieste	01/04, 2008	SISSA / Sincrotrone Trieste
PiezoWalk Drives" NanoPosition with Millimiter Travel, Workshop	ST	02/04, 2008	PI Physik Instrumente / Sincrotrone Trieste
Tango collaboration meeting	ST	17-18/04, 2008	Sincrotrone Trieste
Advanced School on Synchrotron and Free Electron Laser Sources and their Multidisciplinary Applications	Trieste	7-25/04, 2008	Sincrotrone Trieste / ICTP / IAEA
POCPA Workshop - 1st Workshop on POwer Converters for Particle Accelerator	ST	19-21/05, 2008	Sincrotrone Trieste / CERN
EPAC 2008 - 11th European Particle Accelerator Conference	Genova	23-27/06, 2008	Sincrotrone Trieste / INFN / EPS
1st Internal Elettra Workshop on Time-Resolved Experiments	ST	21/07, 2008	Sincrotrone Trieste
6th International Workshop on LEEM-PEEM	TS	7-11/09, 2008	Sincrotrone Trieste

VISITS

VISITORS DISTRIBUTION PER INSTITUTE (September 2007 - August 2008)
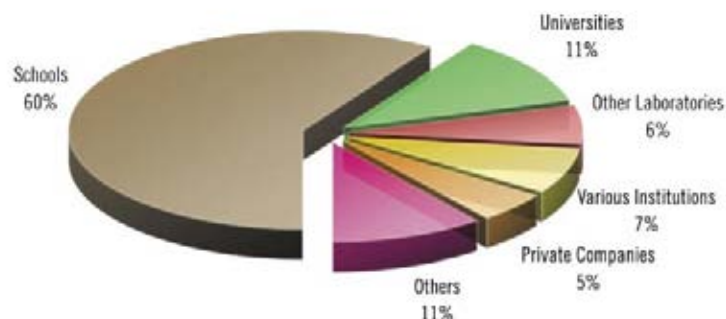
VISITORS DISTRIBUTION PER COUNTRY (September 2007 - August 2008)
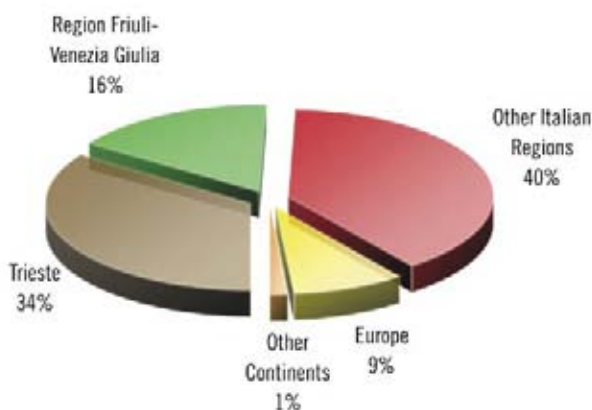
VISITORS - PERIOD 2006-2008
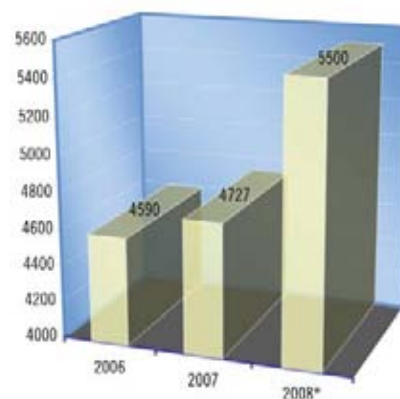
* estimated visitors at December 2008
(effective visitors at September 2008: 4908)

Sincrotrone Trieste

Elettra Laboratory

Power Supplies

New families of intelligent (DSP or PC embedded) power supplies, which cover many types of applications (high voltage/current, four-quadrant, etc.) and configurations are forthcoming. Epics of Tango interface are often already included and custom-built solutions are possible.

Detectors

Photon and charged particle detectors, based on cross delay anodes, multi anodes and centroid finding techniques are continuously developed. 3D information (x, y, time) with spatial and time resolutions in the order of tens of micro- and pico-seconds are available through many custom-built solutions.

Lab Instrumentation

Fast picoammeters, multi-point strain gauges, charge pulse amplifiers, ion chambers, pulse generators, RF filters, etc. Every tool is intelligent and in sole cases Epics/Tango interfaces are already included.

Accelerator Components

Elettra, over the years, has acquired wide experience in developing and realizing accelerators components, such as undulators, resonant cavities, etc. For the production of Insertion Devices a specific spin-off company has been set-up.

Sincrotrone Trieste S.C.p.A.

Industrial Liaison Office
www.elettra.trieste.it/ilo
ilo@elettra.trieste.it
Phone: +39 040 375 8303
Fax: +39 040 375 8623

KYMA

Equipment for Light Sources

Design and Manufacturing of Pure Permanent Magnet (PPM) Undulators

Instrumentation for Magnetic Measurements

Large Climate Chamber Test Services

A spin-off company of Sincrotrone Trieste s.c.p.a. in partnership with Euromisure s.r.l. and Cosylab d.d.

KYMA

Il Consorzio per la gestione di
AREA Science Park è Ente Nazionale di
Ricerca che opera sul territorio regionale
e nazionale per favorire la competitività
delle imprese e del territorio, fornendo
supporto qualificato per il trasferimento
tecnologico, occupandosi di formazione
imprenditoriale e internazionalizzazione.

Gestisce il primo Parco Scientifico e
Tecnologico multisettoriale italiano, con
87 realtà insediate, dove si svolgono da
30 anni attività di ricerca, sviluppo e
innovazione tese al raggiungimento di
risultati d'eccellenza per migliorare la
qualità della vita.

Ecco AREA Science Park, un luogo dove la
formazione di alta qualità, la ricerca e il
fare impresa si incontrano e si convertono
in una fondamentale risorsa per la crescita
economica e occupazionale del Paese.

The Consortium for the management of
AREA Science Park is a National Research
Body which operates on a local and national
level to foster territorial and business
competitiveness, by supporting the technology
transfer and encouraging entrepreneurial
training and internationalisation.

It manages the first multi-sector Science and
Technology Park in Italy, where the tenants,
now 87, have been operating for 30 years in
the field of scientific research, development
and innovation, with a view to achieving
excellence and improving quality of life.

AREA Science Park is the place where highly
specialised training, research and business
meet and turn into an essential resource
for boosting the economic and employment
growth of Italy.

AREA Science Park

Una risorsa per il territorio

A resource for territorial competitiveness